Interrogating Nonadiabatic Molecular Dynamics using Ultrafast Nonlinear Optics

Magdalena Martha Zawadzki

Dipl.Phys.

Submitted for the degree of

Doctor of Philosophy

Heriot - Watt University

School of Engineering and Physical Sciences

Institute of Photonics and Quantum Sciences

May 7, 2017

For my family

Supervisor: Dr. Dave Townsend

Second Supervisor: Prof. Daniele Faccio

Day of submission: May 7, 2017

Abstract

The field of femtochemistry seeks to comprehend the fundamental underlying mechanisms of the interaction between light and molecules and to study the ultrafast timescales on which these processes occur. In particular, the photoresistance of biologically relevant molecules to potential damage caused by absorption of ultraviolet radiation is of great interest. The so called "building blocks" of life use ultrafast non-radiative relaxation pathways for the dissipation of the high excess UV energy as vibrational energy into the surroundings, which is the key of their photoprotective function. The use of a "bottom-up" methodology for such investigations is applied to understand basic model UV chromophores, which are molecular sub-units of various bio-molecules such as, for example, the DNA bases and the melanin pigmentation system.

The photophysics of the basic model chromophores, indole and the aniline derivatives N,N-dimethylaniline and 3,5-dimethylaniline, were investigated in the gas phase to understand the link between their molecular structure, the ultrafast non-adiabatic dynamics and thus their potential photoprotection function. This study was done with the powerful time-resolved photoelectron imaging (TRPEI) technique, which provides temporal, energy- and angle-resolved information related to the non-adiabatic relaxation dynamics operating within each molecular system. TRPEI is a highly differential pump-probe spectroscopic technique providing a detailed picture of the underlying processes, since it is sensitive to both electronic and nuclear motion within the molecule.

The observation of the complete dynamical process using the TRPEI method is however restricted by the energy of the utilised probe pulse. For this reason the spectroscopic technique was improved with the integration of a newly built femtosecond vacuum ultraviolet (VUV) light source. The VUV laser pulses are generated in a four wave frequency mixing process in third order nonlinear media, such as noble gases. First results from this instrument are presented for the butadiene molecule. The combination of the new VUV laser light and the already powerful spectroscopic technique enables, in principle, the detection of the complete non-radiative relaxation process of a large variety of molecular systems.

Acknowledgements

First and foremost I would like to express my sincerest gratitude to my supervisor, Dr. Dave Townsend, for his never ending enthusiasm, his continuous support and guidance and the interesting conversations about science and life. He created a perfect atmosphere throughout my PhD study for me to independently develop ideas and grow as a scientist. I am very grateful for being Dave's student in the last three and a half years. Secondly, I would like to thank all past and present *Ultrafast Dynamics Group* members for their helpful discussions in the lab and their contributions to this work. In particular, I would like to thank Dr. Marco Candelaresi, with whom I had the pleasure to build the VUV light source, Lisa Saalbach and Dr Nikoleta Kotsina, with whom I obtained the very recent result. Special thanks goes to Ashley Lyons for the innumerable awesome conversations and his English humour. I was very fortunate to share an office with him. Furthermore, I owe Prof. Martin Paterson thanks for all the theoretical calculations that support the experimental results of my work and Prof. Daniele Faccio for his helpful and in depth discussions and the valuable guidance on several hikes in the Scottish Highlands. Additionally, my sincere thanks goes to Prof. Albert Stolow for giving me the unique opportunity to perform scientific studies at the National Research Council in Ottawa, Canada. The inspiring scientific discussions and very kind hospitality were greatly appreciated. I also would like to thank the whole NRC group for making my visit to Canada a truly great experience. This PhD thesis would have not been possible without the support and solidarity of all my friends all around the world. I am genuinely grateful for all the amazing, warm-hearted and inspiring friends from Germany, Scotland, England, Canada, Italy, Portugal, Ireland, India, Poland, Russia, Denmark, Spain, France, Iran, New Zealand and Australia.
To my partner in life and in this particular endeavour David Vocke, I am truly grateful to be able to share my life with you. Your love, the continuous, creative and uplifting conversations and the wonderful moments we collected on this long journey are most precious to me. I would like to dedicate this work to my family, Theresia, Peter and Patrick, the most important and wonderful people in my life. You are my foundation and the source of enormous positivity, creativity, never ending support and love. I am exceedingly grateful for everything you have done for me.

List of papers and conference contributions

Peer-reviewed papers

- **Magdalena M. Zawadzki**, James O. F. Thompson, Emma A. Burgess, Martin J. Paterson and Dave Townsend, Time-resolved photoionization spectroscopy of mixed Rydberg-valence states: indole case study, *PCCP*, 17, 26659, 2015 [1]

- **Magdalena M. Zawadzki**, Marco Candelaresi, Lisa Saalbach, Stuart W. Crane, Martin J. Paterson and Dave Townsend, Observation of multi-channel non-adiabatic dynamics in aniline derivatives using time-resolved photoelectron imaging *Faraday Discuss.*, 194, 185-208, 2016 [2]

- Stuart W. Crane, **Magdalena M. Zawadzki**, James O. F. Thompson, Nikoleta Kotsina, Omair Ghafur, and Dave Townsend, Caveats in the interpretation of time-resolved photoionization measurements: A photoelectron imaging study of pyrrole, *J. Chem. Phys.*, 145 (23), 2016 [3]

- **Magdalena M. Zawadzki***, Marco Candelaresi*, Nikoleta Kotsina, Lisa Saalbach, Martin J. Paterson, Daniele Faccio, Dave Townsend, Non-adiabatic intramolecular dynamics of butadiene and isoprene exciting with vacuum ultraviolet pulses, *in preparation*, 2017

- **Magdalena M. Zawadzki**, Martin A. B. Larsen, Andrey E. Boguslavskiy, Lisa Saalbach, Martin J. Paterson, Albert Stolow, Dave Townsend, Ultrafast deactivation mechanisms in formamide and its derivatives using time-resolved photoelectron imaging, *in preparation*, 2017

Awards

- 1st Year Postgraduate Research Prize in Recognition of Outstanding Research Performance, Heriot-Watt University, Edinburgh, UK, 2014

Oral and poster conference contributions

- RSC Spectroscopy and Dynamics Group Conference, Jan. 2015
  M. M. Zawadzki, M. Candelaresi, J. O. F. Thompson and D. Townsend, *poster contribution*, Nottingham, UK

- XXVI International Symposium on Molecular Beams, Jun. 2015
  M. M. Zawadzki, M. Candelaresi, J. O. F. Thompson and D. Townsend, *poster contribution*, Segovia, Spain

- RSC Spectroscopy and Dynamics Group Conference, Jan. 2016
  M. M. Zawadzki, M. Candelaresi, J. O. F. Thompson, E. A. Burgess, M. J. Paterson and D. Townsend, *oral presentation*, Warwick, UK

- 2nd COST XLIC WG3 Meeting - Control of Chemical Reactivity, Apr. 2016
  M. M. Zawadzki, M. Candelaresi, J. O. F. Thompson and M. J. Paterson, D. Townsend, *poster contribution*, Belfast, UK

- IONS conference, May 2016
  M. M. Zawadzki, *oral presentation*, Quebec City, Canada

- Gordon Research Conference - Multiphoton Processes, Jun. 2016
  M. M. Zawadzki, M. Candelaresi, J. O. F. Thompson, M. J. Paterson, D. Townsend, *poster contribution*, Andover, NH, USA

- 2nd COST XLIC WG1 Meeting, Aug. 2016
  M. M. Zawadzki, N. Kotsina, L. Saalbach, M. Candelaresi, M. J. Paterson, D. Townsend, *poster contribution*, Edinburgh, UK

- Faraday Discussion - Ultrafast Imaging of Photochemical Dynamics, Aug. 2016
  M. M. Zawadzki, N. Kotsina, L. Saalbach, M. Candelaresi, M. J. Paterson, D. Townsend, *poster contribution*, Edinburgh, UK

ACADEMIC REGISTRY

Research Thesis Submission

Name*:*			
School:			
Version: *(i.e. First, Resubmission, Final)*		Degree Sought:	

Declaration

In accordance with the appropriate regulations I hereby submit my thesis and I declare that:

1) the thesis embodies the results of my own work and has been composed by myself
2) where appropriate, I have made acknowledgement of the work of others and have made reference to work carried out in collaboration with other persons
3) the thesis is the correct version of the thesis for submission and is the same version as any electronic versions submitted*.
4) my thesis for the award referred to, deposited in the Heriot-Watt University Library, should be made available for loan or photocopying and be available via the Institutional Repository, subject to such conditions as the Librarian may require
5) I understand that as a student of the University I am required to abide by the Regulations of the University and to conform to its discipline.
6) I confirm that the thesis has been verified against plagiarism via an approved plagiarism detection application e.g. Turnitin.

* *Please note that it is the responsibility of the candidate to ensure that the correct version of the thesis is submitted.*

Signature of Candidate*:*		Date:	

Submission

Submitted By *(name in capitals):*	
Signature of Individual Submitting:	
Date Submitted:	

For Completion in the Student Service Centre (SSC)

Received in the SSC by *(name in capitals):*			
Method of Submission *(Handed in to SSC; posted through internal/external mail):*			
*E-thesis Submitted (**mandatory for final theses)***			
Signature:		Date:	

Please note this form should be bound into the submitted thesis.

Contents

Chapter 1

Introduction

Life is fragile but resistant, due to nature's creativity and innovations. Understanding the fundamental interactions and reactions of important biological molecules to sunlight, in particular ultra violet (UV) radiation, is crucial to ultimately understanding the evolution of life on planet earth. The absorption of UV light by organic molecules can cause potentially harmful reactions to biomolecular systems, since the high energy of UV photons provides access to molecular decay pathways that are otherwise inaccessible. These harmful reactions, including bond breaking, can lead eventually to harmful mutations [4, 5, 6]. Thus over billions of years of evolution, nature has chosen certain molecules as the so called "building blocks of life" which include, for example, the DNA bases, the melanin pigmentation system, various amino acids, and phenylpropanoids in plants [6, 7]. They are extremely efficient at dissipating this potentially harmful UV radiation on an ultrafast time scale as harmless heat into the surrounding environment via non-destructive pathways. Due to their photoprotective function these photostable molecules are one of natures great innovations.

A fundamental question one may ask of biomolecular systems is: "What is intrinsically special about them and how do they achieve the photostability and photoprotection?" The ultrafast photodynamics of these polyatomic molecules is key to the deactivation mechanisms, which involve complex intramolecular redistribution processes of charge and vibrational energy. These processes include radiationless transitions, internal conversion, isomerization, proton and electron transfer and intersystem crossing [8, 9, 10, 11]. Of particular interest to the work described in this thesis, internal conversion is based on the non-adiabatic coupling between different electronic potential energy surfaces leading to the formation of so called "conical intersections", which mediate the relaxation dynamics. The coupling between the electronic and the nuclear degrees of freedom results in the break down of the Born-Oppenheimer approximation, which allows the definition of electronic and vibrational energy states due to the adiabatic separation of electronic and nuclear motions. This will be expanded upon in Chapter 2.

The observation and investigation of the highly complex and ultrafast relaxation mechanisms in polyatomic molecules in "real time" require highly developed femtosecond time-resolved spectroscopy techniques. The development of the first laser by Maiman in 1960 [12] and the generation of the first femtosecond pulses from a Ti:Sapphire laser in 1991 by Sibbett and co-workers [13] enabled the evolution of the required temporal resolution for these spectroscopic studies.

The development of femtosecond spectroscopic methods to study time-resolved nonadiabatic molecular dynamics in the gas-phase was pioneered by Prof. Ahmed Zewail and co-workers, resulting in the award of the Nobel Prize 1999 in Chemistry [14, 15, 16]. Some of the primary questions that the field of Femtochemistry seeks to answer are: Firstly, "How and on what time scale is incident energy redistributed among the various degrees of freedom of a molecular system?" Secondly, "How and with what speed do reactants turn into products connected via individual quantum states?" Thirdly, "What are the specific nuclear motions that drive the dynamics via transition states and on what time scale do they operate?" [16].

In the scope of this work the "reactant" is a molecular system absorbing a UV photon, which will then undergo a certain ultrafast deactivation process. This might be an efficient rapid non-radiative decay process resulting in the photostability of the bio-molecule. In order to study this dynamical process, femtosecond time-resolved spectroscopic techniques require a "pump" and a "probe" pulse. Here the first ultrafast laser pulse starts the reaction by generating a nonstationary state, known as a wave packet, and therefore defining a reference time labelled "time zero". The second ultrafast laser pulse probes the temporal evolution of this created wave packet by projecting onto a final set of states [17]. There has been a variety of pump-probe techniques which have been developed, such as transient absorption spectroscopy and nonlinear optical spectroscopy in condensed phase, as well as laser-induced fluorescence, resonant multiphoton ionisation and H-atom photofragment translational spectroscopy in the gas phase [18, 19]. Each of these experimental techniques provide different information which complement each other to reveal the full dynamical processes.

In this work, the gas-phase time-resolved photoelectron imaging (TRPEI) technique is used to investigate the nonadiabatic dynamical processes in small polyatomic molecules, some of which provide good starting approximations to chromophores found in larger biomolecules. This state-of-the-art pump-probe spectroscopic method is very well suited for the dynamical studies of molecular systems, since it can observe electronic configurations and vibrational dynamics with its highly differential temporal, energy and angle-resolved information. TRPEI is used to study the photophysics of model biomolecular systems in order to understand the link between their structure, their dynamical behaviour and thus (in principle) their photoprotective function. In the time-resolved spectroscopic experiments the probe

pulse generates a free electron via photoionisation, which exhibits time dependent kinetic energy and an angular distribution.
In addition to the aforementioned highly differential information provided by TRPEI, this spectroscopic technique possesses further advantages. Using photoionisation as a probe is advantageous since the ionisation of any molecular state participating in the dynamical relaxation process is always ensured based on symmetry arguments of the outgoing photoelectron (i.e. there are no "dark" states in the ionisation process). Furthermore, the detection of charged particles, such as electrons or ions, is very sensitive [18]. The experimental principles of TRPEI will be explained in detail in Chapter 2 and the practical infrastructure and considerations are outlined in Chapter 3. Chapters 4 and 5 will then present in depth analysis of TRPEI data obtained from the model biological chromophores aniline and indole, respectively.

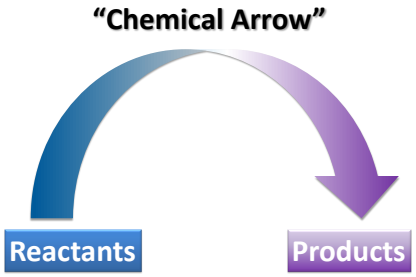

Figure 1.1: *The "chemical arrow" symbolising the evolution of reactants towards products along the connecting reaction coordinates.*

Despite the fact that TRPEI is a highly differential technique, its "view" along the reaction coordinate (illustrated in Figure 1.1) is often restricted by the probe photon energy. For a transition between a given initial and final electronic state the transition strength is governed, in part, by the square of the overlap between the associated vibrational wavefunctions (the so-called Franck-Condon factor). In the case of photoionisation, the probe photon may lack sufficient energy to sample the region of the ionisation continuum that gives rise to large Franck-Condon factors. As such, no significant photoionisation signal is observed. A specific example of this is in the ionisation of a highly vibrationally excited electronic ground state formed via non-adiabatic relaxation from energetically higher lying electronic states. So, in order to map the whole dynamical process (including any ground state recovery), a high energy photon in the deep UV is the preferred choice. Generating the so called vacuum ultra violet (VUV) radiation with nonlinear optical processes was a crucial part of this work and will be discussed in detail in Chapter 6. The existing time-resolved spectrometer was enhanced by building a new VUV light source, which can be used as a pump or a probe pulse for the experiment depending on the molecular system of interest. This opens up several new avenues of experimental investigation that will be outlined along with an overall summary of the thesis in Chapter 7.

Chapter 2

The foundations of ultrafast molecular physics

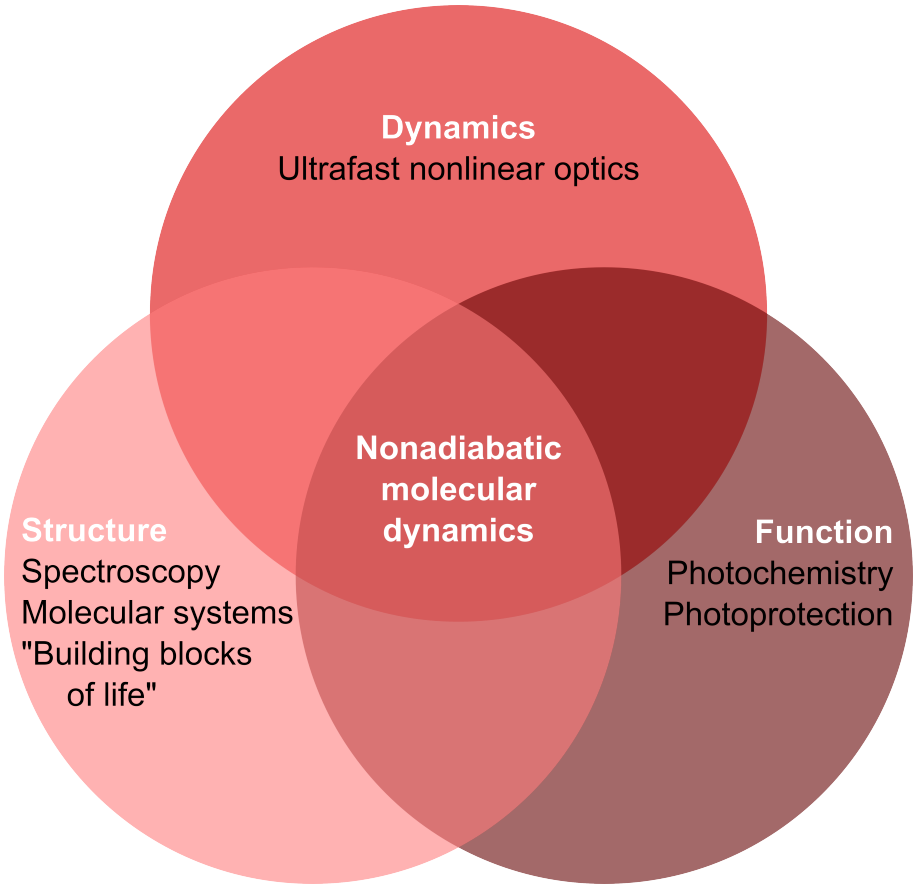

2.1 Excited state landscape and molecular transitions

The complex dynamical mechanisms operating in polyatomic molecules following UV excitation lie at the very heart of molecular physics and quantum chemistry. Here it is of great interest to understand how the energy partitioning within a molecular system is influenced by electronic and nuclear changes. Certain reaction coordinates of the molecule determine the potential energy landscape and therefore also molecular transitions. In the quantum mechanical formulation the time-independent Schrödinger-Equation allows one to determine the molecular potential energy.

$$\hat{H}\Psi(\mathbf{r},\mathbf{R}) = E\Psi(\mathbf{r},\mathbf{R}) \tag{2.1}$$

Here $\hat{H}$ is the full Hamiltonian of the molecular system, $\Psi(\mathbf{r},\mathbf{R})$ is the whole molecular wavefunction dependent on the electronic and nuclear coordinates $\mathbf{r}$ and $\mathbf{R}$, respectively. The eigenvalue E is the total energy of the molecular system.
Unfortunately it is not analytically possible to solve the Schrödinger-Equation for a system bigger then two particles. For this reason the well known Born-Oppenheimer approximation (BOA) can be used to separate the motions of the electrons from the nuclei.

2.1.1 Born-Oppenheimer approximation and molecular orbitals

The simple but powerful approximation, established by Max Born and J. Robert Oppenheimer in 1927 [20], assumes that the electronic motion is extremely fast compared to nuclear motion, due to their great mass difference ($m_p \cong 1836 \cdot m_e$ [21]). The derivation of the BOA outlined in this section can be found in textbooks, such as [22], and only a short summary is provided here. The Hamiltonian $\hat{H}$ in Equation 2.1 can be written as a sum of the kinetic energy operator of the electrons $\hat{T}_e$, the nuclei $\hat{T}_N$ and the potential energy operator of the system $\hat{V}$.

$$\hat{H} = \hat{T}_e(\mathbf{r}) + \hat{T}_N(\mathbf{R}) + \hat{V}(\mathbf{r};\mathbf{R}) \tag{2.2}$$

The electrons can instantaneously react to any change in the nuclei geometry $\mathbf{R}$, therefore the electronic energy $E_e(\mathbf{R})$ is only parametrically dependent on the nuclear motion and the total wavefunction $\Psi(\mathbf{r},\mathbf{R})$ can be written as the product of the electronic $\psi_e(\mathbf{r};\mathbf{R})$ and the nuclear $\psi_N(\mathbf{R})$ wavefunction.

$$\Psi(\mathbf{r},\mathbf{R}) = \psi_e(\mathbf{r};\mathbf{R}) \cdot \psi_N(\mathbf{R}) \tag{2.3}$$

The nuclear wave function is a product of the vibrational and rotational wavefunctions. If the total wave function formulation in Eq. 2.3 is substituted into the Schrödinger-Equation, it follows:

$$\hat{H}\psi_e\psi_N = \psi_N\hat{T}_e\psi_e + \psi_e\hat{T}_N\psi_N + \hat{V}\psi_e\psi_N + W = E\psi_e\psi_N. \tag{2.4}$$

The term W is a quantity containing mixed kinetic energy terms, since the electronic wave function depends on the nuclear coordinates. In the adiabatic approximation this term is zero, it only plays a role in non-adiabatic effects, where electronic states influence each other. This so-called breakdown of this approximation will be discussed below.
On the basis of Equation 2.4 the electronic Schrödinger-Equation can be written for fixed nuclear coordinates as

$$\hat{T}_e\psi_e + \hat{V}\psi_e = E_e(\mathbf{R})\psi_e \tag{2.5}$$

Here $\hat{V}$ is the Coulomb potential originating from the nuclei at fixed coordinates. The eigenvalue of this electronic equation $E_e(\mathbf{R})$ is the contribution to the total energy of the molecule comprising the kinetic energy of the electrons, the electron nuclei Coulomb interaction energy and the nuclei repulsive Coulomb potential energy at fixed nuclei distances [22].
The solutions of the electronic Schrödinger-Equation evaluated at different nuclear coordinates results in a potential energy surface (PES) of a polyatomic molecule based on its nuclear geometry. For this reason the Born-Oppenheimer approximation allows the description of molecular structure as well as the observation of nuclear trajectories. By substituting Equation 2.5 with the calculated eigenvalue $E_e(\mathbf{R})$ into Equation 2.4, the nuclei Schrödinger-Equation can be obtained

$$\hat{T}_N\psi_N + E_e\psi_N = E\psi_N \tag{2.6}$$

The eigenvalue E is the total energy of the molecular system based on the BOA. Solving this equation enables one to study the vibrational and rotational motion of the nuclei, thus the BOA provides the foundation for the investigation of molecular dynamics.
The eigenfunctions ψ_e of Equation 2.5 are the electronic wavefunctions of the molecule called the molecular orbitals. These molecular orbitals can be expressed as a linear combination of atomic orbitals (LCAO) within the system, which are the basis set for the calculation.

$$\psi_e = \sum_i c_i\phi_i \tag{2.7}$$

In Equation 2.7 linear combinations of the atomic wavefunctions can interfere constructively (in phase), which means that electron density is accumulated in the

internuclear space. The result is a bonding molecular orbital, which can exhibit a σ or a π character. If the atomic waves are out of phase causing destructive interference, the electronic density will be close to zero in the internuclear region causing a repulsion of the nuclei. This is called an anti-bonding molecular orbital, which can be either a σ^* or a π^* orbital. The creation of non-bonding molecular orbitals occurs, if the phases of the contributing atomic orbitals cancel to zero. In that case the generated MO neither stabilises nor destabilises the molecule. In Figure 2.1 the basic ideas of the formation of molecular orbitals are displayed [23].

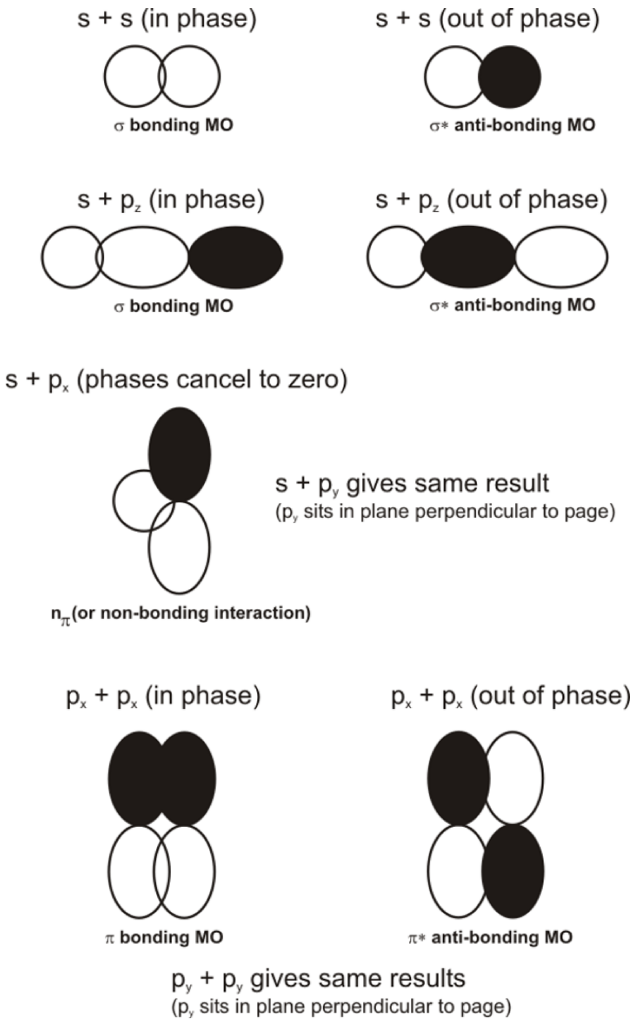

Figure 2.1: *Fundamental idea of molecular orbital generation using the linear combination of atomic orbitals [23].*

For bigger polyatomic molecules, the molecular orbitals become increasingly complex. Nevertheless these orbitals can be assigned with labels, such as σ or π due to symmetry arguments. Within the scope of this work the molecule indole has been studied using time-resolved photoelectron imaging, which is discussed in detail in Chapter 5. To illustrate the idea in Figure 2.2 the molecular orbitals of indole are displayed and were calculated at fixed nuclei coordinates in the ground state minimum geometry. On the left hand side of Figure 2.2 the π bonding molecular

orbitals are shown exhibiting an extended area of in phase wavefunctions. On the right hand side of the picture the anti-bonding orbitals are displayed, calculated at the same nuclei coordinated configuration. The whole shape of the molecular orbital comprises more nodes, which is a signature of destructive interference of the wavefunctions leading to a repulsion of the nuclei. The label $\pi\pi^*$ denotes a transition between a π bonding orbital to a π^* anti-bonding orbital. This then defines the excited state label as shown in Figure 2.2. The figure also contains the values of the oscillator strength, a quantity that describes the probability of electronic dipole transition between the energy states.

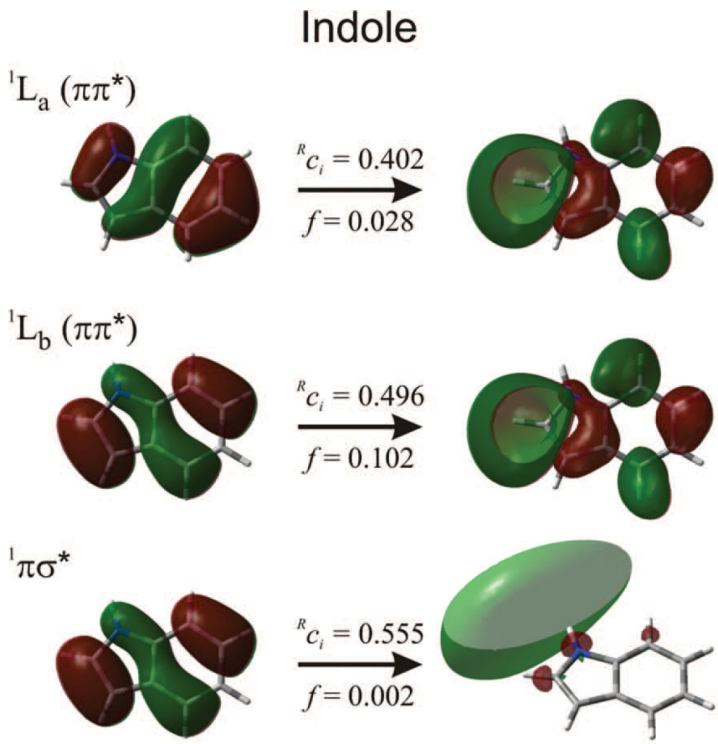

Figure 2.2: *Bonding (left side) and antibonding (right side) molecular orbitals of Indole in the minimum energy nuclei configuration [24].*

2.1.2 Franck-Condon principle and vibronic transitions

An electronic transition between two energy states, caused by i.e. the absorption of a photon, leads to the redistribution of the electronic wavefunction. Based on this electronic redistribution the nuclei experience a different coulomb interaction, which causes a geometry change of the nuclei resulting in vibrational (and rotational) motion of the molecule.

In the framework of the Born-Oppenheimer approximation the potential energy surface of the ground state S_0 and the electronic exited state S_1 are dependent on the internuclear separation R as plotted in Figure 2.3. Each electronic state exhibits several vibrational states ν, with ν'' defining the initial and ν' the final vibrational state of the transition, displayed in Figure 2.3.

The combination of electronic and vibrational transitions are called vibronic transitions and can be explained with the Franck-Condon principle. Based on the large mass difference of electrons and nuclei, a electronic transition takes place instantaneously at a rigid nuclear geometry from an initial equilibrium energy state $|\epsilon''\nu''\rangle$ to a final exited state $|\epsilon'\nu'\rangle$ and is symbolised by a vertical transition in Figure 2.3. Once the electronic wavefunction reaches its final distribution and the transition is complete, the former frozen nuclei wavefunction starts to readjust causing a vibrational motion of the molecule.

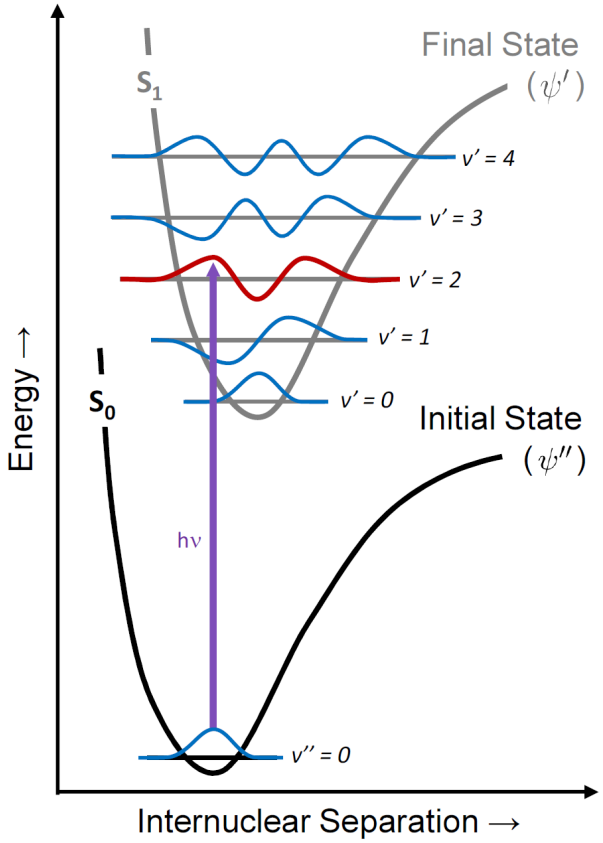

Figure 2.3: *The quantum mechanical Franck-Condon principle showing the highest transition probability for the biggest vibronic wavefunction overlap between the initial ground state and the final exited state [25].*

The Franck-Condon principle specifies that the highest transition probability occurs at the biggest wavefunction overlap between the initial and final state. This can be quantum mechanically described with the electric dipole transition moment of the vibronic ground and excited state, with the electric dipole moment oparator $\hat{\mu}$ that is based on the position of the electrons and nuclei.

$$\hat{\mu} = \hat{\mu}_e + \hat{\mu}_N \tag{2.8}$$

Based on the Born-Oppenheimer approximation and the specific calculated electronic wavefunctions for each different nuclear geometry, the total electric dipole transition moment can be written as:

$$\langle \epsilon' \nu' | \, \mu \, | \epsilon'' \nu'' \rangle = \int \psi^*_{\nu'} \left(\int \psi^*_{\epsilon'} \mu_\epsilon \psi_{\epsilon''} d\tau_e \right) \psi_{\nu''} d\tau_N. \tag{2.9}$$

Here the factors are integrated over the electronic $d\tau_e$ and nuclear $d\tau_N$ coordinates. To a reasonable approximation the transition moment is independent of the nuclear geometry and therefore the electronic integral can be expressed with a constant $\mu_{\epsilon'\epsilon''}$ and Equation 2.9 can be written in the following way:

$$\langle \epsilon' \nu' | \, \mu \, | \epsilon'' \nu'' \rangle = \mu_{\epsilon'\epsilon''} S(\nu', \nu''). \tag{2.10}$$

The propensity rules for electronic transitions are based on $\mu_{\epsilon'\epsilon''}$. $S(\nu', \nu'')$ is called the Franck-Condon factor and the relative intensities for vibrational transitions are proportional to the square of the Franck-Condon integral.

$$S(\nu', \nu'') = \int \psi^*_{\nu'} \psi_{\nu''} d\tau_N \tag{2.11}$$

2.1.3 Jablonski diagram and relaxation processes

In polyatomic molecules the photophysical processes that may occur after absorption of a photon, accompanied by the aforementioned vibronic transition, manifest themselves in a variety of possible relaxation pathways. Here radiative as well as non-radiative pathways and bond dissociation are possibilities to dissipate the absorbed excess energy, and these compete on various time scales with each other.
In biologically important molecules, the "building blocks of life", nature has chosen non-radiative and non-dissociative relaxation solutions in order to stabilise the system upon radiation impact. The nature of photostability and thus photoprotection is an open question in molecular physics and is discussed within the scope of this thesis. As such, the driving relaxation processes for photoprotection have to occur on ultrafast timescales to out-compete any potentially harmful mechanisms.
The Jablonski diagram, displayed in Figure 2.4, shows a model molecular system with the electronic ground state S_0 of singlet character exhibiting vibrational energy levels (grey lines). Several electronic excited energy states with their vibrational energy levels of singlet multiplicity S_2 and S_1 as well as of triplet multiplicity T_1 are also depicted in the diagram.

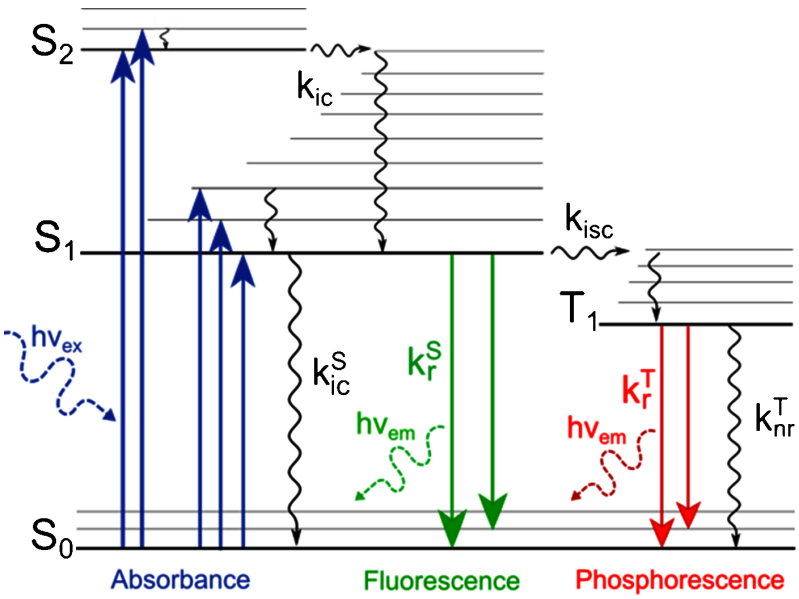

Figure 2.4: *Jablonski diagram illustrating the possible relaxation pathways of a molecule after initial absorption of a photon with the energy $h\nu_{ex}$ [26]. The molecule can emit energy $h\nu_{em}$ via fluorescence after internal conversion (k_{ic}) and/or IVR. Phosphorescence can occur after intersystem crossing (k_{isc}) to a triplet state.*

Absorption

The initial starting point of the relaxation processes discussed within the scope of this work is the absorption of a UV photon of energy $h\nu_{ex}$ from the equilibrium electronic ground state S_0 (vibrational energy level $\nu'' = 0$) to an energetically higher lying electronic state on a ultrafast timescale $< 10^{-15}$ s. This process is symbolised with the blue arrows in Figure 2.4 and occurs on a sub-femtosecond timescale, based on the Born-Oppenheimer approximation. In heteroaromatic biomolecules the absorption of visible/ultraviolet light takes place at chromophores. Typical examples are carbonyl-, nitro-groups and carbon-carbon double bonds, where the electronic transition takes place from a bonding n-orbital or a π-orbital to a non-bonding π^*-orbital. These are called the $n\pi^*$ or $\pi\pi^*$ transitions, which will be used throughout this work. An example of the $\pi\pi^*$ electronic transition in indole can be seen in Figure 2.2. In the laboratory this process is realised with the "pump" pulse of the pump-probe spectroscopic technique, which starts the dynamical process and defines time zero.

Non-radiative decay

Intramolecular Vibrational Redistribution - Once the molecular system is situated in its electronical and vibrational excited state, the energy may be dissipated non-radiatively on that electronic energy surface via intramolecular vibrational redistribution (IVR). The small vertical wavy arrows symbolise the energy and population flow from a higher vibrational energy level to the lowest one on the same

electronic energy potential [27, 28]. IVR is a very fast non-radiative relaxation process and occurs at a timescale of $10^{-14} - 10^{-11}$s depending on the molecular system. Since energy has to be conserved, the arrows symbolise a redistribution and not an energy loss across the vibrational modes. In nature's biomolecules these vibrational modes are coupled to the solvent (i.e. water molecules) and the energy is transformed into harmless heat within the surroundings.

Internal Conversion - An important relaxation process for photostabilisation of organic biomolecules is internal conversion (IC), where vibrational levels of different electronically excited states couple together on a ultrafast timescale of $10^{-14} - 10^{-11}$ s allowing a radiation-free energy and population transfer back to the electronic ground state of the molecular system [29]. The non-adiabatic coupling between two vibronic energy levels is dependent on their energy difference and in the special case the two energy levels become degenerate. This coupling between two potential energy surfaces forms conical intersections (CI), areas of (near) energetic degeneracy, that are responsible for the ultrafast relaxation processes in biomolecules. These CI cause the breakdown of the adiabatic separation of the Born-Oppenheimer approximation, which will be discussed in detail in Section 2.2.

Intersystem Crossing - Non-radiative energy and population transfer between two electronic states of different multiplicity is normaly "spin-forbidden", since the conservation of total angular momentum has to be satisfied. In certain cases intersystem crossing (ISC) from a singlet excited energy state S_1 to a triplet state T_1 (see Figure 2.4) becomes possible due to molecular spin-orbit coupling in the presents of heavy atoms, like sulphur and phosphor [30]. The timescales for ISC of $10^{-8} - 10^{-3}$ s are considerably slower then the other non-radiative processes.

Radiative decay

After the initial absorption of photon energy into a electronic and vibrational excited state and the subsequent intramolecular vibrational redistribution to the lowest vibrational level, the molecule can release energy in form of fluorescence and return into its electronic ground state. The spontaneously emitted photon energy matches the energy difference between the two electronic states S_1 and S_0, as symbolised with green arrows in Figure 2.4. The emitted photon energy by fluorescence is usually smaller than the absorbed photon energy, since the IVR process dissipated already energy in the form of vibration into the surrounding. The timescale of the radiative decay within the same spin manifold is on the order of $10^{-9} - 10^{-7}$s [31, 32].

Phosphorescence is another radiative decay process by which the molecule can release its absorbed excess energy. In this case the molecular system is situated in a excited triplet state after ISC. It relaxes back into the singlet electronic ground state on a timescale of $10^{-4} - 10^{-1}$ s by emitting a photon of the energy corresponding to the T_1 and S_0 energy difference [31].

2.2 Conical intersections and wave packet dynamics

The temporal evolution of excited states of polyatomic molecules is significantly complex, since it comprises intricate coupling between electronic and nuclear motion. This non-adiabatic coupling of the formerly adiabatically separated electronic and nuclear degrees of freedom, results in the breakdown of the Born-Oppenheimer approximation. As a consequence, ultrafast non-radiative decay processes can occur on a timescale of femtoseconds allowing the relaxation of the molecular system into its equilibrium ground state or a energetically lower excited state.
In more detail, the photochemical reactions of polyatomic molecules progress on multidimensional energy states. In the Born-Oppenheimer picture an electronic energy state and the nuclear motion associated with it are relatively isolated from all other electronic states. For this reason small nuclear perturbations cause only minor perturbations in the electronic energy.
If electronic states get in close energetic proximity, any small nuclear change leads to a drastic qualitative change in the electronic distribution, which can result in a simultaneous electronic coupling between the electronic energy states. These states become energetically degenerate. In polyatomic molecules a certain set of nuclear motions can linearly lift the degeneracy of two multidimensional energy states around the area of equal energy. This is called a conical intersection and can be defined by these two nuclear motions, which form the branching space or **g**-**h**-space. [33, 34]. The nonadiabatic coupling vector $\mathbf{h}_{S_iS_j}$ is responsible for the breakdown of the Born-Oppenheimer approximation (by defining the coupling between two electronic states) and can be written as [35]

$$\mathbf{h}_{S_iS_j} = \left\langle \psi_{e,i} \left| \frac{\partial}{\partial \mathbf{R}} \right| \psi_{e,j} \right\rangle , \tag{2.12}$$

where $\mathbf{R}$ are the nuclear coordinates and $|\psi_{e,i}\rangle$ is the electronic wave function for the S_i electronic state at a fixed nuclear geometry. The integral is performed with only the electronic coordinates. The function of this coupling vector is the generation of off-diagonal elements of the nuclear kinetic energy operator, which facilitates electronic transitions [36, 37]. Using the electronic part of the Hamiltonian $\hat{H}_e$, Equation 2.12 can be written as

$$\mathbf{h}_{S_iS_j} = (E_j - E_i)^{-1} \left\langle \psi_{e,i} \left| \frac{\partial \hat{H}_e}{\partial \mathbf{R}} \right| \psi_{e,j} \right\rangle . \tag{2.13}$$

Here E_i and E_j are the electronic energies of state S_i and S_j, respectively.

The second vector, which is responsible for lifting the degeneracy in the area of a conical intersection, is the energy difference gradient $\mathbf{g}_{S_iS_j}$ and is defined as [35]

$$\mathbf{g}_{S_iS_j} = \frac{\partial}{\partial \mathbf{R}} \left(\langle \psi_{e,i} | \hat{H}_e | \psi_{e,i} \rangle - \langle \psi_{e,j} | \hat{H}_e | \psi_{e,j} \rangle \right). \tag{2.14}$$

Conical intersections are not single points of energetic degeneracy, but an infinite number of points or seams [38]. This subspace has got $3N-8$ degrees of freedom, with $3N-6$ being the internal degrees of freedom of the molecular system. The seam is, at first approximation, perpendicular to the branching space. Figure 2.5 shows the three potential energy states in cytosine that form conical intersection in the branching space defined by the aforementioned branching vectors $\mathbf{g}$ and $\mathbf{h}$. The intersection between two electronic energy surfaces, i.e. S_1 and S_0, form a cone-like structure that can clearly be seen here.

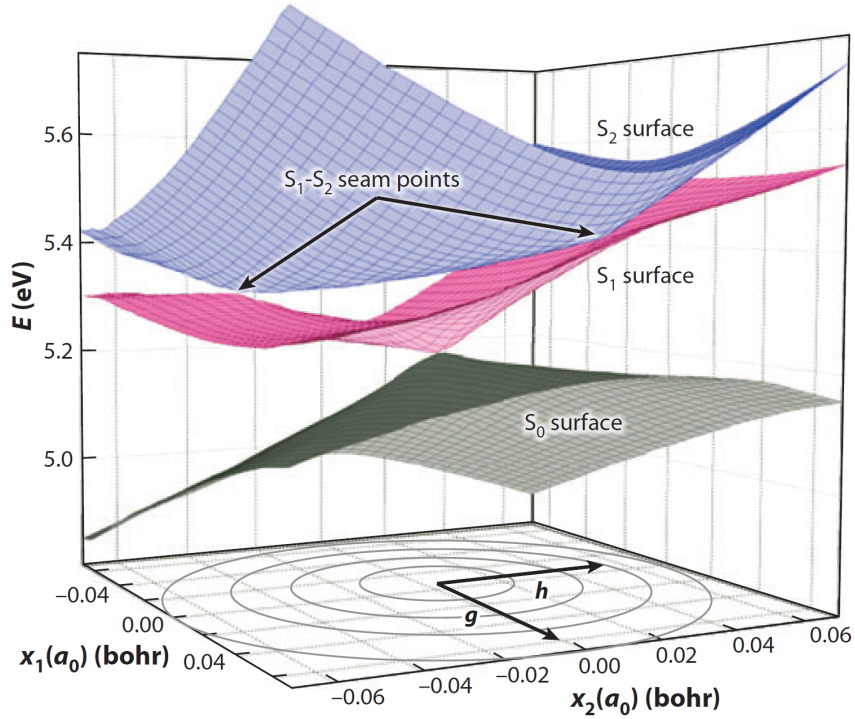

Figure 2.5: *Sketch of multiple electronic states S_2, S_1 and S_0 and the common conical intersections in the g-h branching space [38]. By way of example, the conical shape of the S_1/S_0 intersection is clearly visible.*

The prominence of conical intersections for radiationless nonadiabatic molecular relaxation is well known, but their mechanisms still not fully understood. E. Teller investigated the important role of CI already in 1937 [39]. He showed that fast non-radiative decay can be mediated by conical intersections using a classical approach for the analysis of nuclear motion.

Time-resolved spectroscopic experiments of isolated molecular systems rely on the preparation of an initially coherent wave packet, which dynamically evolves in time and the detection of its nonstationary superposition states. The wave packet creation is dependent on the frequencies and amplitudes of the pump pulse, a broadband femtosecond laser pulse, which excites an initial set of eigenstates [40, 41].
The wave packet $|\Psi(t)\rangle$ is a linear combination of time-independent exact molecular eigenstates $|\psi_n\rangle$ and can be expressed as

$$|\Psi(t)\rangle = \sum_n A_n e^{-i(E_n t/\hbar + \phi_n)} |\psi_n\rangle \,. \tag{2.15}$$

The exact eigenstates $|\psi_n\rangle$ are the solutions to the time-dependent Schrödinger-Equation and are, by definition, stationary [40]. Once the pump pulse is temporally over and the excitation process is terminated, the wave packet can progress freely on the potential energy surface.
The dynamical evolution of the wave packet is expressed by the time-dependent phase $e^{-i(E_n t/\hbar+\phi_n)}$, which contains the energy of the eigenstate E_n and the initial phase ϕ_n at the time of preparation. The amplitudes A_n for each individual eigenstate $|\psi_n\rangle$ are for an isolated molecule normally time-independent, since no couplings occur between the states. However, the exact solutions of the Schrödinger-Equation are usually not known and the simplified Born-Oppenheimer wavefunctions are used to express the wave packet.
Following excitation of the molecule from the electronic ground state in the vertical Frank-Condon region, the wave functions will cause constructive interference and generate a localised vibrational wave packet, as can be seen in Figure 2.6 [42]. The time-dependent phase of the wave functions leads to a change in the local constructive interference, resulting in a dynamical motion of the wave packet on the potential energy surface along a critical reaction coordinate R_{AX-H}. In the case of a relatively isolated electronic state the dephasing and rephasing of a wave packet motion was observed on very fast fs-timescales by A. Stolow and co-workers. These dynamical processes are called revivals [43, 44]. A very famous example of a wavepacket revival was done by Zewail on NaI [16].
In general, as the wave packet explores the potential energy surface the coupling between vibrational states results in the intramolecular redistribution of the wave packet, as mentioned in the previous section. During the dynamical process the BO-eigenstates can also couple non-adiabatically, which leads to the temporal evolution of the amplitudes A_n [40]. Here population and energy is transferred between the interacting states, which takes place in particular at the aforementioned conical intersections [34, 45, 46]. In Figure 2.6 these nonadiabatic molecular dynamics of the wave packet are shown occuring between a bound $^1\pi\pi^*$ state and a dissociative $^1\pi\sigma^*$ state along the reaction coordinate. A second conical intersection between the $^1\pi\sigma^*$

excited state and the electronic ground state S_0 completes the radiationless decay pathway. This will be discussed in more detail in Section 2.4. It can be concluded that the dynamical energy conversion process in polyatomic molecules is extremely complex and involves intramolecular vibrational distribution, internal conversion on a ultrafast timescale and in some cases also dissociation along certain reaction coordinates.

Along the whole relaxation pathway the nonstationary superposition state of the initial prepared wave packet can be, theoretically, observed with a suitable probe pulse (also preferably in the fs regime). The primary aim of the TRPEI experiment is to learn more about which nuclear motions are important for bringing molecules to conical intersections and which motions are effectively "spectators" to these processes.

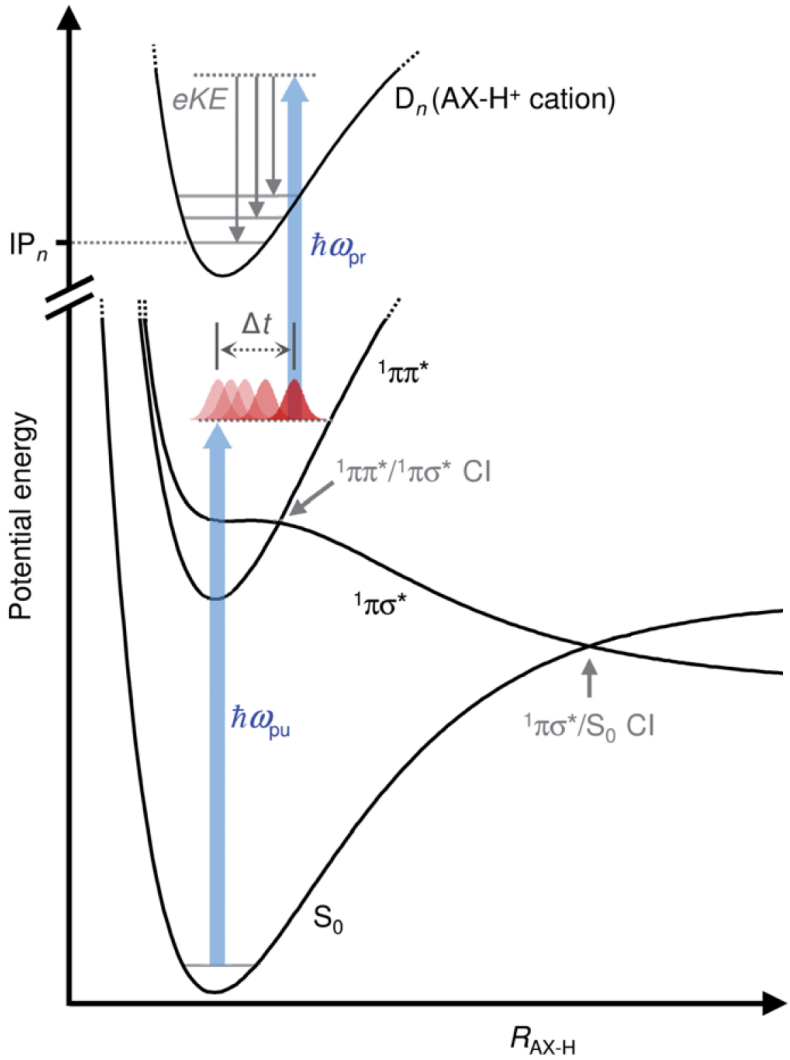

Figure 2.6: *Sketch of electronic ground state S_0, electronic excited states $^1\pi\pi^*$ and $^1\pi\sigma^*$ and cation state D_N and the conical intersections CI between the electronic states. By way of example, the wave packet motion during an evolution time Δt is taking place on the higher excited state surface [42].*

2.3 Photoionisation and observables

Time-resolved photoelectron imaging is a highly differential pump-probe spectroscopic technique that uses photoionisation to remove an electron from the previously excited molecule. The time, energy and angle resolved information that is provided by the spectroscopic imaging measurement yields a great deal of insight about the studied molecular system, which provides the great advantage to disentangle the highly complex and potentially coupled dynamical information.
The probe pulse can be delayed with respect to the pump pulse, which initially prepares the wave packet. For this reason the excited state dynamics can be studied on a fs time scale. The investigated electronic states are coupled by the probe pulse to specific final ionic states, with the biggest vibrational Franck-Condon overlap between them [18]. Under the assumption of a pertubative light matter interaction (weak field regime) the time dependent photoionisation matrix element $d_{if}(t)$ can be expressed as

$$\begin{aligned} d_{i,f}(t) &= \langle \Psi_f(\mathbf{R},\mathbf{r}); \Psi_{e^-}(\mathbf{k},\mathbf{R},\mathbf{r}) | \, \hat{\mu} \cdot \mathbf{E}_{probe} \, | \Psi_i(\mathbf{R},\mathbf{r},t) \rangle \\ &= \sum_n A_n e^{-i(E_n t/\hbar + \phi_n)} \, \langle \Psi_f; \Psi_{e^-} | \, \hat{\mu} \cdot \mathbf{E}_{probe} \, | \psi_n \rangle \end{aligned} \tag{2.16}$$

Here $\hat{\mu}$ is the dipole operator, which acts together with the incident radiation field $\mathbf{E}_{probe}$ on the N-electron initial state $\Psi_i(\mathbf{R},\mathbf{r},t)$. The (N-1) final state is $\Psi_f(\mathbf{R},\mathbf{r})$, removed by one electron, and the ejected electron can be characterised by the wave vector $\mathbf{k}$ and wavefunction $\Psi_{e^-}(\mathbf{k},\mathbf{R},\mathbf{r})$. A_n, E_n and ϕ_n are the wavepacket parameters amplitude, energy and phase, which have been described in the previous section. As already outlined, the dynamical behaviour of the wavepacket motion can be extremely complex. Further simplification can be done using the Born-Oppenheimer picture, where the electronic motion can be separated from the vibrational motion of the molecule. Equation 2.16 can be now written with the initial wavefunction ψ_{e_α} of the electronic state α and the initial vibrational wavefuntion ψ_{ν_α}. The final ionic states are described with $\psi_{e_\alpha +}$ and $\psi_{\nu_\alpha +}$.

$$d_{i,f}(t) = \langle \psi_{e_\alpha +} \psi_{\nu_\alpha +}; \Psi_{e^-} | \, \hat{\mu} \cdot \mathbf{E}_{probe} \, | \psi_{e_\alpha} \psi_{\nu_\alpha}(t) \rangle \, . \tag{2.17}$$

Upon non-adiabatic coupling of two electronic states and the energy and population transfer from one vibronic state α to another vibronic state β, the splitting of the wave packet and its dynamical behaviour can be mapped from these two initial states onto two final ionic states $\alpha+$ and $\beta+$, respectively.

The complementary ionisation correlations are defined as the Koopman's correlations (Type I) [47] and Equation 2.17 changes to

$$d_{i,f}(t) = \sum_{e_\alpha,\nu_\alpha} A_{e_\alpha,\nu_\alpha}(t) e^{-i(E_{e_\alpha,\nu_\alpha}t/\hbar+\phi_{e_\alpha,\nu_\alpha})} \langle\psi_{\nu_\alpha+}|\psi_{\nu_\alpha}\rangle \langle\psi_{e_\alpha+};\Psi_{e^-}|\,\hat{\mu}\cdot\mathbf{E}_{probe}\,|\psi_{e_\alpha}\rangle + \sum_{e_\beta,\nu_\beta} A_{e_\beta,\nu_\beta}(t) e^{-i(E_{e_\beta,\nu_\beta}t/\hbar+\phi_{e_\beta,\nu_\beta})} \langle\psi_{\nu_\beta+}|\psi_{\nu_\beta}\rangle \langle\psi_{e_\beta+};\Psi_{e^-}|\,\hat{\mu}\cdot\mathbf{E}_{probe}\,|\psi_{e_\beta}\rangle \tag{2.18}$$

This complex looking matrix element and the theoretical approach of photoionisation can be explained with the corresponding observables, visualised in Figure 2.7. The observed photoelectron intensity $I(E, \Delta t)$ is dependent on the kinetic energy of the electrons and the temporal delay between the pump and the probe pulse [47].

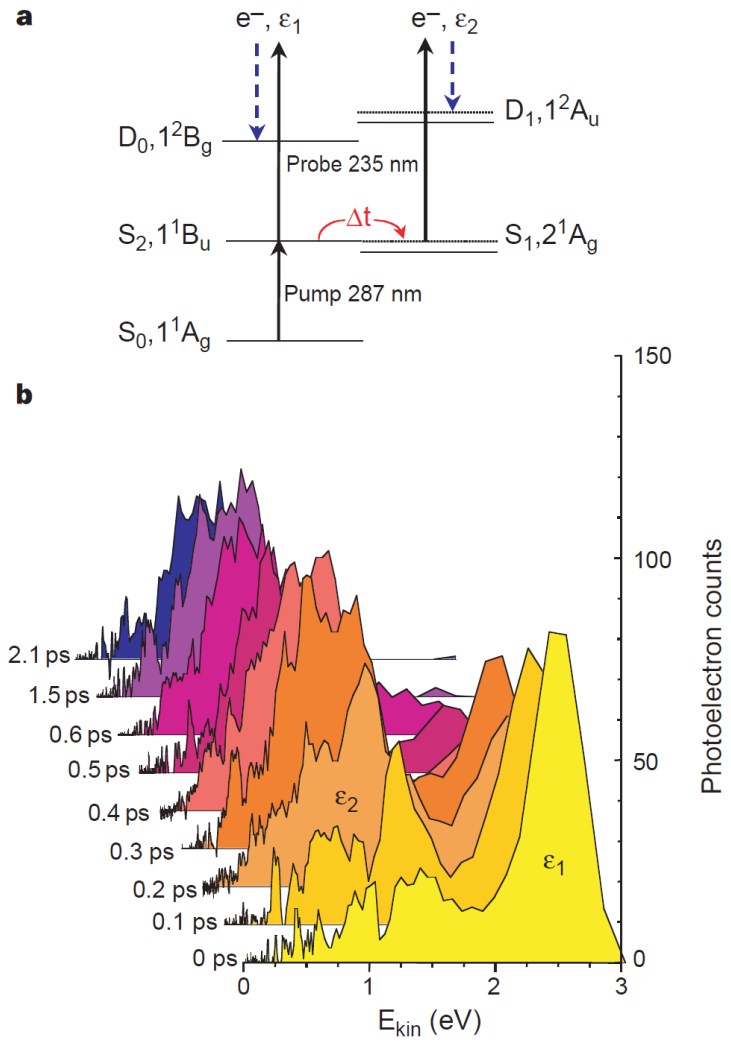

Figure 2.7: *Explanation of Koopmans correlations Type I by the means of non-adiabatic molecular dynamics of a linear polyene, decatetraene DT, studied with time-resolved photoelectron spectroscopy. The initially excited S_2 state undergoes internal conversion to the vibrationally excited electronic state S_1. Individual photoionisation of both states reveals the dynamical process of both states in a spectrally resolved manner [47].*

In Figure 2.7 the time-resolved photoelectron spectroscopic study of a linear polyene, decatetraene DT, is visualised with the energy level diagram [47]. Here the non-adiabatic coupling of the initially excited S_2 electronic state takes place on an ultrafast timescale. The dynamical process of internal conversion from S_2 to the higher vibrationally excited S_1 electron state can be interrogated at different pump-probe delay times via the photoionisation process. The propensity rules for ionisation are $S_2 \rightarrow D_0 + e^-(\epsilon_1)$ and $S_1 \rightarrow D_1 + e^-(\epsilon_2)$ [47]. This projection onto the ionisation continuum is called the Koopmans correlation Type I. It can be clearly seen that both excited states evolve on similar timescales. Therefore a simple ion yield measurement would not be able to decode all the dynamical information.
The TRPES technique provides both the time and energy resolved information about the participating excited states, dependent on the kinetic energy E_{kin,e^-} of the ejected photoelectron. This can be obtained by the subtraction of the ionisation state energy D_0 or D_1 from the total provided energy of the pump and the probe pulse $E_{pump} + E_{probe}$.
In addition, Koopmans correlations Type II are defined as the photoionisation from two electronic excited states α and β to the same cation electronic state. This is defined as corresponding ionisation correlations and is more explicitly described in [48]. Also in the Type II case, the temporal information of the non-adiabatic molecular dynamics can be disentangled from the spectral information. Here the internal conversion from an energetically higher lying electronic state α to a vibrationally excited lower lying electronic state β can be detected by purely the vibrational propensities [18].

Time-resolved photoelectron imaging provides, in addition to the temporal and energy resolved information, also angle-resolved information. This is based on the complex wavefunction Ψ_{e^-} of the outgoing electron after ionisation. So far it has been treated like a simple weighting factor in the time and energy resolved data [18]. For polyatomic molecules the photoelectron wavefunction is highly complex, correlated to the energy and angular momentum and defines the photoelectron angular distribution (PAD) of the TRPEI experiment [49]. The general formula for the intensity I of the PAD, based on symmetry arguments [50], can be written as [51]

$$I(\theta, \phi) = \sum_{L=0}^{L_{max}} \sum_{M=-L}^{L} \beta_{LM} Y_{LM}(\theta, \phi) \tag{2.19}$$

Here spherical harmonic functions are expressed by Y_{LM} and β_{LM} are the anisotropy expansion parameters. Both variables are dependent on L, the rank and M, the order of the spherical harmonic. β_{LM} is in general dependent on the dynamics of the photoionisation, the experimental probe (energy and polarisation of the pulse) and the orbital geometry of which the electron originated from [51].

In the lab frame the maximal number L_{max} is double the number of photons of the overall pump + probe ionisation process. A linearly polarised $(1 + 1')$ pump-probe ionisation measurement (for which $L_{max} = 4$) simplifies photoelectron angular distribution analysis, as a couple of assumptions can be made. Based on reflection symmetry, the values for L have to be even. The ϕ angle dependence vanishes for cylindrical symmetry, which results in M being restricted to a value of zero. These symmetry considerations are valid when both linear pump and probe polarisation vectors are parallel. Equation 2.19 can therefore be simplified to

$$I(\theta) = \sum_{L=0,2,4} \beta_L P_L(\cos(\theta)) \tag{2.20}$$

Here θ defines the angle between the ejected photoelectron direction and the laboratory frame z axis, which is given here by the polarisation direction of the laser pulses. As mentioned before, the angular distribution exhibits a cylindrical symmetry around the z axis. The harmonic wavefuntion $Y_{L0} \propto P_L(\cos(\theta))$, with $P_L(\cos(\theta))$ being the Legendre polynomials in $\cos(\theta)$ [40].

The PADs originating from ionisation of polyatomic molecules, which have various contributing molecular orbitals to the dynamical process, can be quite complex and convoluted. Nevertheless the temporal evolution of the PAD as a function of pump-probe delay still provides a powerful signature of the electronic dynamics that a given system of interest undergoes. The detection of the PAD will be expanded upon in more detail in Section 3.3.3.

2.4 Photoprotection - the role of $\pi\sigma^*$ states

Over the last decades the underlying photochemical mechanisms of bio-molecules became of increasing interest in the field of femtochemistry. The aim is to reveal and understand why DNA bases, melanins and amino acids are extremely resistant to potential damage caused by UV radiation impact. Life on earth is dependent on sunlight, nevertheless high exposure of biological systems to UV light can result in damaging effects, such as genetic mutations. In particular, the photoprotective function of DNA, that is defining the genetics of living organisms, was developed over the course of billions of years of evolution. Another example of nature's adaptation to environmental conditions is eumelanin, a pigment that determines the human skin and hair colour. Although UV sunlight is necessary for photosynthesis of vitamin D, eumelanin acts as the body's front line defence system against the potential harmful processes induced by UV radiation [52, 53]. In order to understand the underlying operating defence mechanisms in e.g. eumelanin, the field of ultrafast molecular physics seeks to study the photophysical processes of its base molecule, indole. The non-adiabatic dynamics in indole are studied in detail in Chapter 5.

In general, the role of the molecular sub-units of biological systems were the focus of comprehensive experimental and theoretical research studies over recent years. Here a "bottom up" methodology of investigation has been used to primarily understand the photoresistant function of basic model UV chromophores. Figure 2.8 illustrates this idea of the stepwise exploration of biologically relevant molecules and excellent overviews of the research can be found in [42, 54]. The photoprotective function is dependent on the molecular structure and the photophysical dynamics, such as the efficient conversion of excess UV energy into vibrational energy that can be dissipated as heat into the surroundings.

The role of $\pi\sigma^*$ states as a mediator for ultrafast non-radiative decay processes for photoexcited electronic states back to the ground state was first theoretically investigated by Sobolewski and Domcke [55, 56, 57]. The $\pi\sigma^*$ states, which are dissociative along a specific X-H bond extension coordinate, are found in a variety of molecular UV chromophores. For example, the calculated energy states along the aforementioned reaction coordinate in phenol, indole and pyrrole are displayed in Figure 2.8, showing the $\pi\sigma^*$ states. Usually the optically "bright" states of the molecular systems, e.g. $\pi\pi^*$ states, are excited upon UV photon absorption. These states can couple non-adiabatically to the repulsive $\pi\sigma^*$ states, forming a conical intersection and facilitating energy and population transfer. A second CI between the $\pi\sigma^*$ states and the electronic ground state S_0 potentially enables the efficient and ultrafast non-radiative transfer of energy back to the equilibrium state. One key element to comprehend the complex photoprotective functions of biological important systems is the understanding of these $\pi\sigma^*$ states.

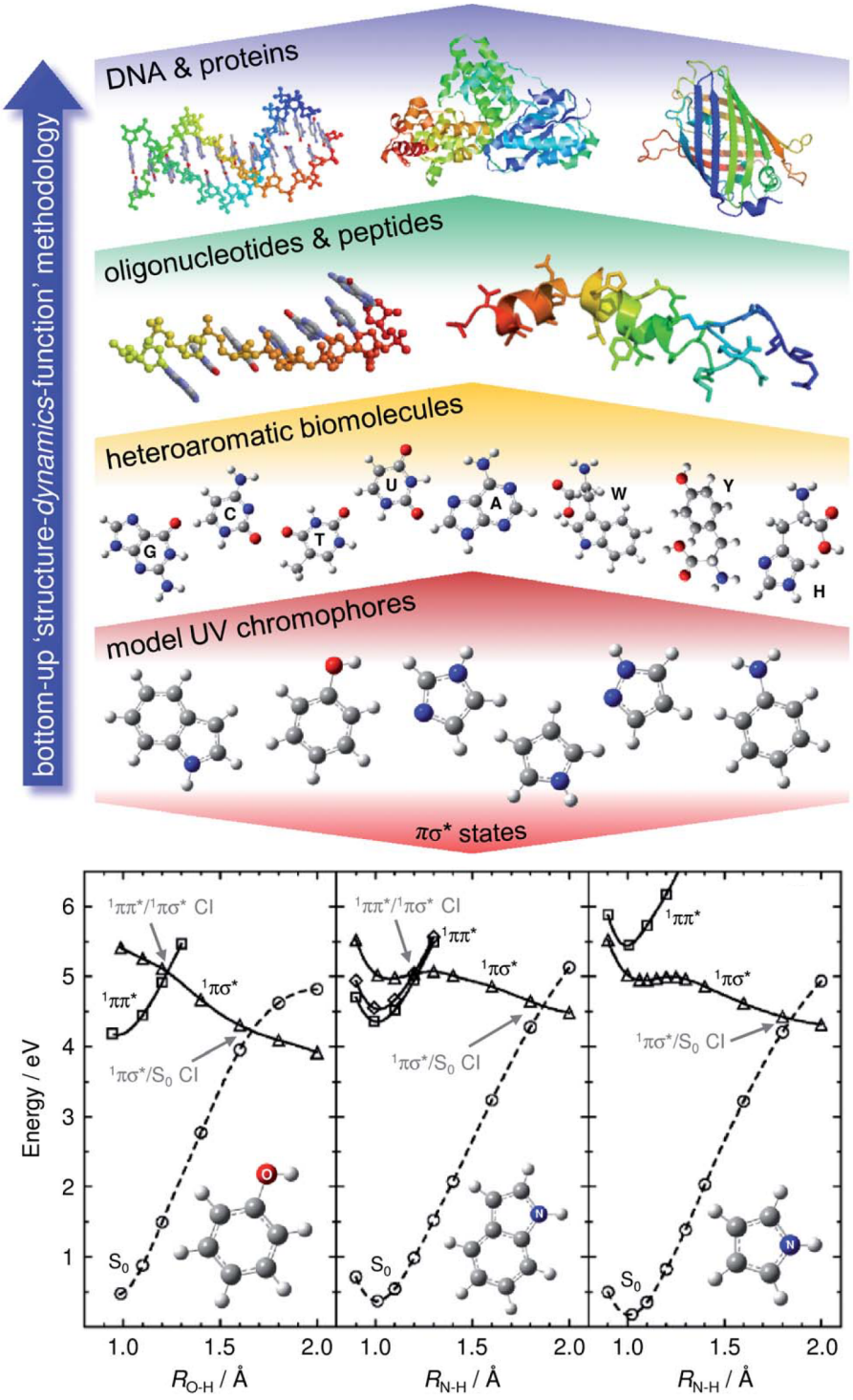

Figure 2.8: *Illustration of a "bottom-up" approach from model UV chromophores to DNA and proteins to investigate their dynamical behaviour and therefore the photostability of the molecular systems. A key feature of the photoprotection might be the $\pi\sigma^*$ states. The bottom half of the picture shows the calculated energy cuts of phenol, indole and pyrrole as a function of X-H nuclear stretching coordinate. All three molecules exhibit a $\pi\sigma^*/S_0$ CI, mediating potential ultrafast relaxation pathways [42].*

2.5 Nonlinear optics

The field of nonlinear optics explores the physical phenomena caused by intense light modifying the optical properties within a material. In 1961 Franken *et al.* discovered the effect of second harmonic generation [58], shortly following the demonstration of the first laser by Maiman in 1960 [12]. The term "nonlinear" optics pertains to the response of a dielectric medium under the influence of an applied intense optical field. The comprehensive work by Boyd, summarised in the book "Nonlinear Optics", is recommended to the interested reader, since most of the theory in this section originates from it [59].

The concept of the optical nonlinearity can be mathematically described with the dipole moment per unit volume, also called the polarisation $\mathbf{P}(t)$ of a medium, which is in the presence of a electromagnetic field with an electric field strength $\mathbf{E}(t)$. If the intensity of the applied optical field is low, the induced polarisation can be described with the well known linear relationship, where the vacuum permittivity ϵ_0 and the linear susceptibility $\chi^{(1)}$ are the proportionality constants.

$$\mathbf{P}(t) = \epsilon_0 \chi^{(1)} \mathbf{E}(t) \tag{2.21}$$

The utilisation of a strong laser field with a high intensity causes a nonlinear optical response of a medium and its polarisation is now dependent on higher order terms of the electrical field strength $\mathbf{E}(t)$. Based on this, Equation 2.21 has to be extended expressing $\mathbf{P}(t)$ as a power series of $\mathbf{E}(t)$.

$$\begin{aligned} \mathbf{P}(t) &= \epsilon_0 \left[\chi^{(1)} \mathbf{E}(t) + \chi^{(2)} \mathbf{E}^2(t) + \chi^{(3)} \mathbf{E}^3(t) + \ldots \right] \\ &\equiv \mathbf{P}^{(1)}(t) + \mathbf{P}^{(2)}(t) + \mathbf{P}^{(3)}(t) + \ldots \end{aligned} \tag{2.22}$$

In this equation $\chi^{(2)}$ and $\chi^{(3)}$ are the second- and third-order nonlinear optical susceptibilities. Typically $\mathbf{P}^{(2)}(t)$ and $\mathbf{P}^{(3)}(t)$ are much smaller than the linear polarisation $\mathbf{P}^{(1)}(t)$. Higher order terms ($n > 3$) are small and therefore rarer, since they would require an intensity much greater than the damage threshold of most media. Due to this they have a negligible contribution to the polarisation of a material.

2.5.1 Second order nonlinear processes

This section will cover the second order nonlinear processes which are important within the scope of this work, such as second harmonic generation (SHG) and also sum and difference frequency mixing (SFM and DFM). The second order nonlinear susceptibility, $\chi^{(2)}$, is only non zero for materials that possess a non-centrosymmetric crystal structure. Nonlinear media such as gases, liquids and amorphous solids are centrosymmetric and, as a result, have a vanishing second order nonlinearity.

It can be mathematically shown that using a crystal with a centre of symmetry

$\mathbf{P}(\mathbf{E}) = -\mathbf{P}(-\mathbf{E})$ and a finite electric field leads to a vanishing nonlinear susceptibility $\chi^{(2)}$.

$$\mathbf{P}(\mathbf{E}) = \chi^{(2)}\mathbf{E}(t)^2 = -\mathbf{P}(-\mathbf{E}) = -\chi^{(2)}\mathbf{E}(t)^2 \Rightarrow \chi^{(2)} = 0 \tag{2.23}$$

On this basis $\chi^{(2)}$ nonlinear effects are only present in non-centrosymmetic media.

Second harmonic generation

The simplest example of a nonlinear optical process is second harmonic generation, which is illustrated in Figure 2.9.

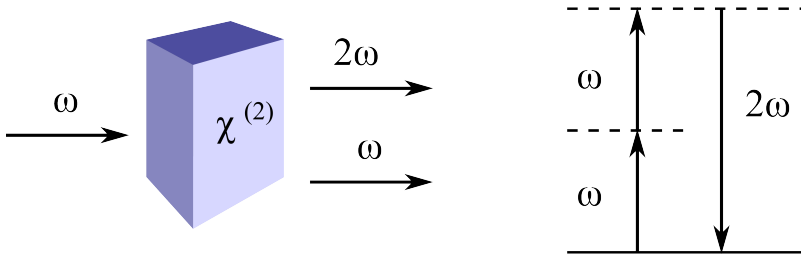

Figure 2.9: *Sketch of second harmonic generation in a non-centrosymmentric crystal with its corresponding energy level diagram, where the solid line is the atomic ground state and the dashed lines symbolise virtual energy states.*

In this sketch the incoming laser light can be expressed with its electric field strength

$$\mathbf{E}(t) = \mathbf{E}e^{-i\omega t} + c.c. \tag{2.24}$$

The second order nonlinear polarisation $\mathbf{P}^{(2)}(t)$ of the non-centrosymmentric material can be written accordingly using Eq. 2.22 and Eq. 2.24.

$$\mathbf{P}^{(2)}(t) = 2\epsilon_0\chi^{(2)}\mathbf{E}\cdot\mathbf{E}^* + \left(\epsilon_0\chi^{(2)}\mathbf{E}^2e^{-i2\omega t} + c.c.\right). \tag{2.25}$$

It can be seen that the $\mathbf{P}^{(2)}(t)$ is composed of two terms. The first one is a frequency independent component, which just adds a static field in the nonlinear crystal and is called optical rectification. The second term contains a frequency component of 2ω and can be understood as the source of the second harmonic radiation. Equation 2.25 is applicable to lossless and dispersionless media only.
In a particle interaction picture, shown on the right hand side of Figure 2.9, SHG can be described as a exchange of photons in a single quantum mechanical mechanism. The destruction or absorption of two photons of a fundamental frequency ω takes place simultaneously with the creation of one photon of the frequency 2ω. Figure 2.9 shows the process that occurs from an atomic ground level to two virtual levels symbolised by the dashed lines.

The process of second harmonic generation is used in different applications, e.g. doubling the fundamental frequency of an Nd:YAG laser or in autocorrelation measurements. In the scope of this thesis SHG was used to convert the fundamental output of the Ti:Sapphire laser output from 800 nm to 400 nm, which is then used in further frequency mixing processes in order to access otherwise unavailable frequencies. These processes are described in detail subsequently.

General frequency mixing

In a generalised second order nonlinear process, two waves of frequencies ω_1 and ω_2 can interact within the $\chi^{(2)}$ nonlinear crystal resulting in multiple different frequency mixing effects. In this case the electric field strength is

$$\mathbf{E}(t) = \mathbf{E}_1 e^{-i\omega_1 t} + \mathbf{E}_2 e^{-i\omega_2 t} + c.c. \tag{2.26}$$

The generalised second order term of the nonlinear polarisation is

$$\mathbf{P}^{(2)}(t) = 2\epsilon_0 \chi^{(2)} \mathbf{E}(t)^2 \tag{2.27}$$

Combining Equations 2.26 and 2.27 shows all components of the nonlinear polarisation

$$\begin{aligned}
\mathbf{P}^{(2)}(t) = {} & \epsilon_0 \chi^{(2)} \mathbf{E}_1^2 e^{-2i\omega_1 t} + c.c. && \text{(SHG)} \\
& + \epsilon_0 \chi^{(2)} \mathbf{E}_2^2 e^{-2i\omega_2 t} + c.c. && \text{(SHG)} \\
& + 2\epsilon_0 \chi^{(2)} \mathbf{E}_1 \cdot \mathbf{E}_2 e^{-i(\omega_1+\omega_2)t} + c.c. && \text{(SFM)} \\
& + 2\epsilon_0 \chi^{(2)} \mathbf{E}_1 \cdot \mathbf{E}_2^* e^{-i(\omega_1-\omega_2)t} + c.c. && \text{(DFM)} \\
& + 2\epsilon_0 \chi^{(2)} \left(\mathbf{E}_1 \cdot \mathbf{E}_1^* + \mathbf{E}_2 \cdot \mathbf{E}_2^*\right) && \text{(OR)}
\end{aligned} \tag{2.28}$$

The first two terms in Equation 2.28 are the second harmonic generation (SHG) of the first frequency at ω_1 and of the second at frequency at ω_2, respectively. The third and the forth term describe the processes of sum and difference frequency generation (SFM and DFM). The fifth term is the previously mentioned direct current electric field within the medium, called optical rectification (OR).
Normally only one of the aforementioned nonlinear optical processes will take place inside a nonlinear crystal and produce radiation with a significant intensity. This is based on the fact that each of these created output signals also requires a specific phase-matching condition in order to build up to a measurable intensity. The concept of phase-matching will be explained below in Section 2.5.2.
In both sum frequency generation and difference frequency generation, two distinct input frequencies ω_1 and ω_2 interact with the nonlinear $\chi^{(2)}$ material producing a third optical field at a frequency of ω_3 due to the conservation of energy. The sec-

ond order nonlinear polarisation in Equation 2.28 can be expressed with following notation

$$\mathbf{P}^{(2)}(t) = \sum_n \mathbf{P}(\omega_n) e^{-i\omega_n t}. \tag{2.29}$$

Consequently SFG and DFG can be written with the following convenient expressions respectively:

$$\mathbf{P}(\omega_1 + \omega_2) = 2\epsilon_0 \chi^{(2)} \mathbf{E}_1 \cdot \mathbf{E}_2 \tag{2.30}$$

$$\mathbf{P}(\omega_1 - \omega_2) = 2\epsilon_0 \chi^{(2)} \mathbf{E}_1 \cdot \mathbf{E}_2^*. \tag{2.31}$$

Sum frequency generation uses two incoming pump frequencies ω_1 and ω_2 that induce, within the nonlinear $\chi^{(2)}$ medium, an oscillating field of a new frequency, ω_3, equal to the sum of the incident frequencies. This concept is shown in the top half of Figure 2.10. Here, the right hand side explains the process with the photon picture, where the two incoming photons get absorbed by the material while a third photon is simultaneously emitted. SFG can be used to generate tunable ultraviolet laser light, which is used in many spectroscopic techniques.

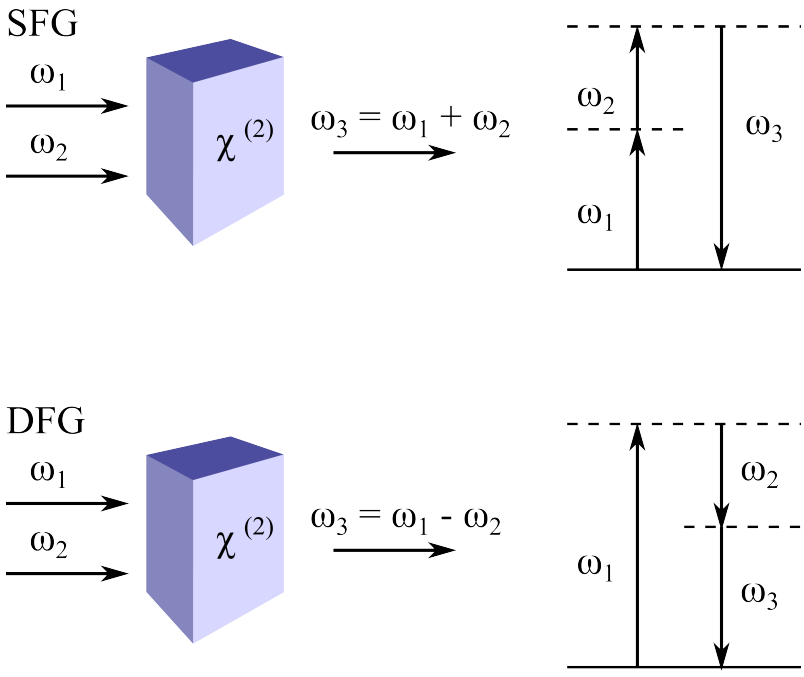

Figure 2.10: *Sketch of SFG and DFG in a non-centrosymmentric crystal with its corresponding energy level diagram, where the solid line is the atomic ground state and the dashed lines symbolise virtual energy states.*

Difference frequency generation is, at first glance quite similar to SFG, since the process also involves two incoming frequencies producing a third outgoing frequency. Thus, this time it is the difference between ω_1 and ω_2 in order for energy to be conserved.

However, DFG has one significant difference that can be explained with the photon energy level picture on the right hand side in Figure 2.10. In case of DFG, one

pump photon, of frequency ω_1, is absorbed to a high virtual energy level. This energy level decays instantaneously by emitting two photons with frequencies ω_2 and ω_3, stimulated by the presence of the second photon at ω_2. This nonlinear process is therefore also called optical parametric amplification (OPA).

Optical parametric amplification

The purpose of optical parametric amplification is to amplify a seed input wave at ω_2, which is called the *signal*, by pumping the nonlinear material with a *pump* wave at a frequency of ω_1. The latter of these fields pumps the crystal with the required energy for the amplification of the seed wave. Since conservation of energy has to be satisfied, a third frequency ω_3 is generated, which is called the *idler*.
The process of OPA is used in the scope of this work to convert the fundamental frequency of the Ti:sapphire laser into a tunable infrared wave, which can be frequency converted into a tunable ultraviolet wave using several nonlinear processes.

2.5.2 Phase matching

In order for efficient nonlinear processes (such as those described above) to occur the conservation of both energy and momentum must be maintained. In this photon interaction picture, $\hbar\omega$ is the energy and $\hbar\mathbf{k}$ is the momentum of an individual photon of frequency ω and wavevector $\mathbf{k}$.

$$\sum_{i=1}^{n} \hbar\omega_i = \hbar\omega_{n+1} \tag{2.32}$$

$$\sum_{i=1}^{n} \hbar\mathbf{k}_i = \hbar\mathbf{k}_{n+1} \tag{2.33}$$

A constant phase relationship between the incoming interacting waves and the outcoming, generated wave has to be achieved. This can be explained by the means of the elementary example of SHG. The incoming electric field travelling in z-direction can be represented with a plane wave approximation described in Eq. 2.24:

$$\mathbf{E}(z,t) = \mathbf{E}_i e^{-i\omega_i t} + c.c., \quad \text{with} \quad \mathbf{E}_i = \mathbf{A}_i e^{i\mathbf{k}_i \cdot \mathbf{z}}. \tag{2.34}$$

The wavevector is defined as

$$|\mathbf{k}_i| = \frac{n_i \omega_i}{c_0}. \tag{2.35}$$

Where chromatic dispersion is present in media, the group velocities of the pump and the second harmonic waves will be different leading to a phase mismatch between the contributing $\mathbf{k}$-vectors in SHG, which can be described using Eq. 2.33

$$\Delta\mathbf{k} = \mathbf{k}_2 - 2\mathbf{k}_1. \tag{2.36}$$

In order for efficient SHG to take place, both waves have to travel in phase for a certain coherence length L_c, which means that $\Delta\mathbf{k} \approx 0$ or very close to zero. The phase matching is achieved in most cases with the utilisation of birefringent optical nonlinear crystals [60], which directly compensate for the dispersion. Mathematically it can be described such that the extraordinary refractive index, n_e, of the wave with the frequency ω equals the ordinary refractive index, n_o, of the wave of frequency 2ω, while both waves travel collinearly at an angle θ with respect to the optical axis through the crystal [61].

$$n_e(\theta, \omega) = n_o(2\omega) \tag{2.37}$$

This is a type I mixing process, since the two incoming waves possess the same polarisation direction and the generated outcoming wave is polarised in perpendicular direction (SHG using type I: e-e-o waves).

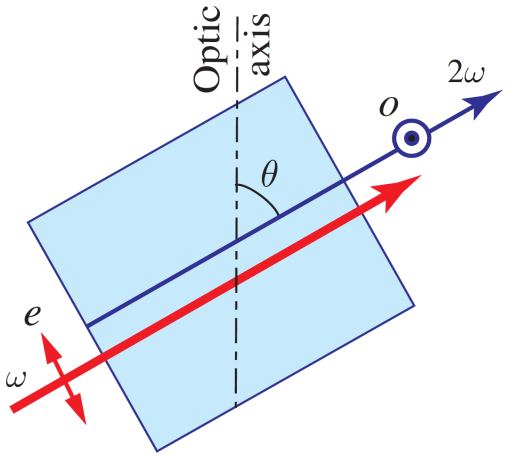

Figure 2.11: *Sketch of efficient SHG in a nonlinear birefringent crystal. The incoming extraordinary wave of frequency ω travels at an angle θ with respect to the optical axis matching the velocity of the generated ordinary wave of frequency 2ω [61].*

There are many different types of phase matching. For second order nonlinear processes the two conditions used within this work were type I and type II. A type II second order nonlinear process uses two perpendicular polarised collinear propagating waves to generate a third wave with the same polarisation as the first one (i.e. SFM using Type II: o-e-o waves). The most commonly used nonlinear crystals for second order nonlinear phenomena are β barium borate (BBO), potassium dihydrogenphosphate (KDP), lithium triborate (LBO) and lithium niobate ($LiNbO_3$).

2.5.3 Third order nonlinear processes

Third order nonlinear processes occur in all types of optical media, also in a variety of centrosymmetric materials such as solids, liquids and gases. It's still dependent on the spatial symmetry (as it arises from the crystal structure), but it does not disappear like the $\chi^{(2)}$ nonlinearity for centrosymmetric media. On the condition that the intensity of the optical field is high enough, the third order nonlinearity is the lowest non-vanishing order in the aforementioned media and gives rise to a range of nonlinear phenomena. By way of example are the four wave mixing processes that enable efficient frequency conversion performed throughout my PhD work and explained in detail in Chapter 6. Further examples of third order nonlinear phenomena, such as the Kerr effect, will be mentioned briefly hereafter since they are used for many photonic devices including the mode locking of femtosecond laser and optical compression.

Four wave mixing - the general case

The four wave mixing (FWM) process is a $\chi^{(3)}$ nonlinear process, where three incident laser waves of frequencies ω_1, ω_2 and ω_3 create a fourth laser wave of the frequency $\omega_4 = \omega_1 \pm \omega_2 \pm \omega_3$. The third order nonlinear polarisation is defined in Eq. 2.22 as the nonlinear response of a $\chi^{(3)}$ medium

$$\mathbf{P}^{(3)}(t) = \epsilon_0 \chi^{(3)} \mathbf{E}^3(t) \tag{2.38}$$

produced by the incident electric field strength, which is composed of three frequency components

$$\mathbf{E}(r,z,t) = \mathbf{E}_1 e^{-i\omega_1 t} + \mathbf{E}_2 e^{-i\omega_2 t} + \mathbf{E}_3 e^{-i\omega_3 t} + c.c., \quad \text{with} \quad \mathbf{E}_i = \mathbf{A}_i e^{i\mathbf{k}_i \mathbf{z}} \tag{2.39}$$

Calculating the third order nonlinear polarisation results in 44 different frequency components, if the positive and the negative frequencies are viewed to be distinct and can be expressed with the complex amplitudes for each of the different frequencies:

$$\mathbf{P}^{(3)}(t) = \sum_n \mathbf{P}(\omega_n) e^{-i\omega_n t}. \tag{2.40}$$

In accordance with this work, only some of the processes will be explained in detail such as the four wave difference frequency mixing (FWDFM) process, which is utilised for the fifth harmonic generation of the Ti:Sapphire laser (λ = 160 nm). This third order nonlinear process can be expressed with the according complex amplitude used in Equation 2.40

$$\mathbf{P}(\omega_4 = 2\omega_1 - \omega_2) = 3\epsilon_0 \chi^{(3)} \mathbf{E}_1^2 \cdot \mathbf{E}_2^* \tag{2.41}$$

In this FWDFM process the fundamental frequency and the third harmonic frequency interact with each other within the nonlinear medium thereby producing radiation at the fifth harmonic frequency. This will be explained in detail in Chapter 6.
Furthermore, other third order nonlinear phenomena can occur in a FWFM process such as the special case of third harmonic generation where a fourth wave of the frequency $3\omega_i$ is created by three incident interacting waves of the same fundamental frequency ω_i. This can be described with one of the polarisation terms of Equation 2.40.

$$\mathbf{P}(3\omega_i) = \epsilon_0 \chi^{(3)} \mathbf{E}_i^3 \tag{2.42}$$

Additionally the initial pump wave ω_i can also be influenced by intensity dependent effects caused by itself or other present waves and expressed with the following polarisation amplitude

$$\mathbf{P}(\omega_i) = \epsilon_0 \chi^{(3)} \left(3\mathbf{E}_i \cdot \mathbf{E}_i^* + 6\mathbf{E}_j \cdot \mathbf{E}_j^* + 6\mathbf{E}_k \cdot \mathbf{E}_k^*\right) \mathbf{E}_i \tag{2.43}$$

It can be seen that the product of the electric field strength with its complex conjugate leads to a intensity dependent manipulation of the initial wave $\mathbf{E}_i$. These intensity dependent third order nonlinear effects are called Kerr effects. The first term on the right hand side expresses the influence of the self-manipulation of the initial wave and result in the processes of "self phase modulation" and "self focusing". The second and third terms illustrate the intensity influence of the other pump wave (either $\mathbf{E}_j$ or $\mathbf{E}_k$) onto the first wave $\mathbf{E}_i$, this phenomena is known as "cross phase modulation".

Nonlinear Kerr effect phenomena

The $\chi^{(3)}$ nonlinearity also gives rise to an intensity dependent refractive index, n. This modulation of n is called the optical Kerr effect and is caused by a driving laser of high intensity. The refractive index, n, is defined in the presence of this intense laser field in the following way:

$$n = n_0 + n_2 I \tag{2.44}$$

Here n_0 is the normal linear refractive index, that is dominant at low laser intensities. The nonlinear refractive index n_2 can be expressed with third order susceptibility $\chi^{(3)}$

$$n_2 = \frac{3}{2n_0^2 \epsilon_0 c} \chi^{(3)} \tag{2.45}$$

and the intensity I of the driving wave is defined as

$$I = \frac{1}{2} n_0 \epsilon_0 c |E|^2 \tag{2.46}$$

The optical Kerr effect leads to several intensity dependent third order nonlinear phenomena. Self phase modulation (SPM) is caused by the time-dependant change in the refractive index n. The pump wave, an initially transform limited Gaussian, experiences a intensity dependent phase shift $\Phi(t)$ as a function of propagation distance, L.

$$\Phi(t) = \frac{\omega}{c} n_2 I(t) L, \tag{2.47}$$

which leads to a spectral broadening of the pump pulse

$$\Delta\omega = \frac{\omega}{c} n_2 L \frac{I_0}{\tau}, \tag{2.48}$$

with I_0 being the intensity of the laser pulse and τ representing the pulse duration [62]. Cross phase modulation (XPM) is based on the same principles, but now the phase modulation of a second pulse with different characteristics (i.e. frequency, polarisation) is based on the refractive index change due to the intensity of the first pump pulse. Self focusing of a Gaussian beam occurs due to the transverse intensity profile $I(r)$ influencing the nonlinear refractive index change in the same way, based on Equation 2.44. The maximal refractive index change occurs in the region of highest intensity at $r = 0$, resulting in the so called Kerr lensing. This is relevant to the principles of femtosecond laser operation, which will be discussed in Section 3.1.1.

Chapter 3

The experimental techniques - useful tools in the lab

This chapter comprises the key tools used throughout my PhD work and explains the method of data processing and analysis. Time-resolved photoelectron imaging is a comprehensive experimental technique consisting of several highly developed parts.

The optical setup includes the laser source for the "pump" and "probe" beams of the spectroscopic method, a titanium-sapphire femtosecond pulsed laser. This laser light is partitioned into several beam lines with nonlinear crystals for the frequency up-conversion. It also pumps two optical parametric amplifiers (OPA) and a high harmonic box generating the third and fourth harmonic frequencies of the fundamental laser output in the ultraviolet spectral region. Furthermore, an optical compressor is utilised for the re-creation of ultrashort fs pulses.

The photoelectron spectrometer consisting of a source and a main vacuum chamber (which are separately pumped) is the other key tool in the lab. Within the main chamber, ion optics composed of specially designed electrodes ensure the perfect velocity map imaging (VMI) of electrons or ions onto the detector after ionization by the UV laser light. An image accumulated over many laser shots providing information about energy and angular distribution of the charged particles is recorded at different "pump-probe" time delays. This series of images is then processed and analysed with software built in Matlab. Each of the above steps will be expanded upon in detail.

3.1 Optical tools

Advanced spectroscopic techniques such as TRPES benefited enormously from the development in femtosecond laser technology (see Section 3.1.1) based on the realisation of several general requirements. In nature most molecular systems involved in photobiological processes absorb in the wavelength range of the electromagnetic solar spectrum from around 140 nm - 400 nm. In the laboratory these wavelength are generated with nonlinear optical processes like harmonic generation, frequency mixing and parametric generation and therefore the laser output pulse energy has to be high enough to begin with in order to drive these nonlinear processes. The theory of nonlinear processes is described in Section 2.5. Another important requirement for time-resolved spectroscopic experiments is the reliable and stable operation of the laser system over many hours. The reasons for this are the general potentially low signal levels of one photoelectron spectrum and the need to obtain spectra at different time delays with the same photon energy to begin with. Hence accumulation of data to improve statistics is affected by any fluctuations, such as laser power and temperature. The laser setup, which was used for most of the experiments, is shown in Figure 3.1 including the laser system, two optical parametric amplifiers (OPA) and the important optical elements such as nonlinear crystals, mirrors and prisms for the compression of ultrashort pulses.

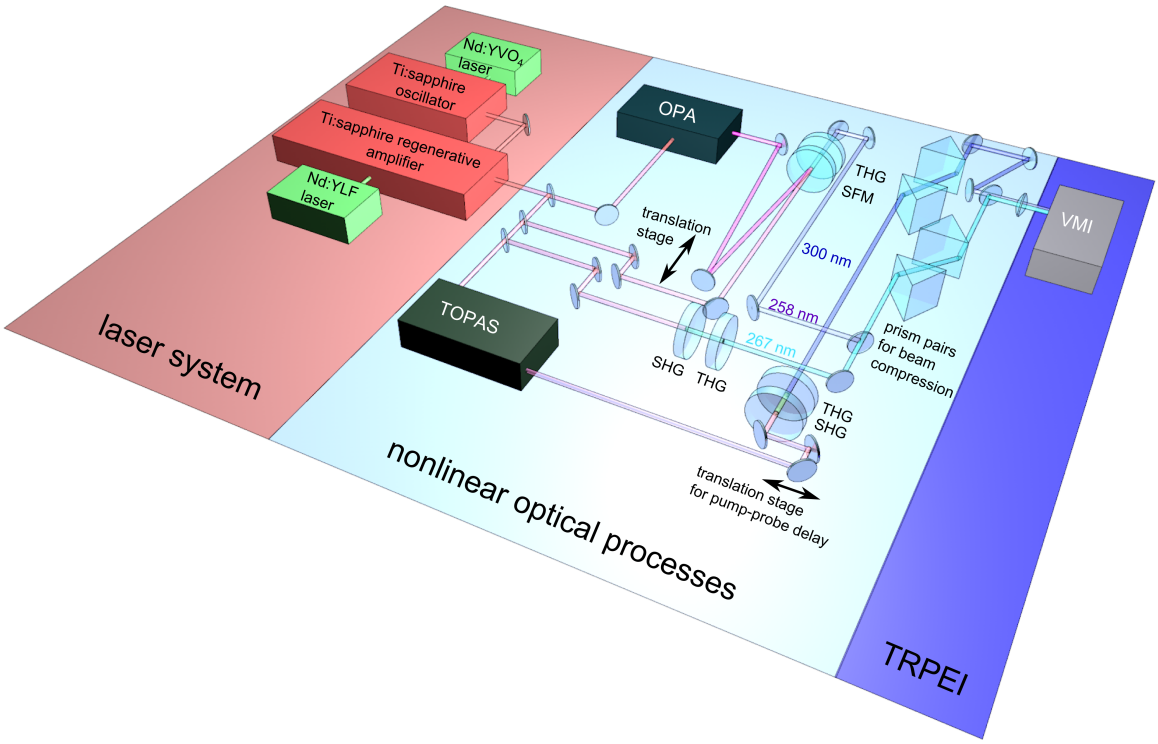

Figure 3.1: *Schematic of the femtosecond laser setup in our lab including the Ti:sapphire oscillator and amplifier with both respective pump lasers, two optical parametric amplifiers (OPA, TOPAS) and the most important optics used for nonlinear frequency conversion and pulse compression.*

Since most of the molecular systems of interest absorb in the visible (VIS) and ultraviolet (UV) electromagnetic spectral region, but every molecule has got its unique absorption spectrum, an infrared (IR) laser output can be exploit to begin with. This IR pulse can be frequency converted to almost any requested VIS to UV pulse via nonlinear processes such as second/third harmonic generation (SHG/THG) or sum/difference frequency mixing (SFM/DFM) (explained in detail in Section 2.5). These UV pulses are compressed using single pass configuration prisms before they are used as a pump and probe beams in the VMI spectrometer (see subsection 3.1.3).

3.1.1 Femtosecond lasers

Since the first successful optical laser was invented by Theodore Mainman in 1960 the techniques in this research area have developed rapidly [63]. Today pulsed laser systems with a pulse duration in the femtosecond domain are commercially available. There are several options to generate an ultrashort femtosecond pulse, for instance with gas lasers using active mode locking, dye lasers (of which the so-called colliding pulse mode-locked (CPM) dye laser is a popular example), or solid state lasers working with different types of mode locking techniques [64, 65].
In our lab ultra-short laser pulses are achieved with a Ti:sapphire laser using a modelocked oscillator and chirped-pulsed amplifier. The titanium-sapphire laser has got a sapphire crystal (Al_2O_3) doped with titanium ions Ti^{3+} as its active medium, the spectroscopic properties of which are well understood [66].
A regeneratively amplified solid state Ti:Sapphire laser system from Spectra Physics is used to generate ultrafast femtosecond laser pulses in the infrared wavelength regime. The Ti:Sapphire oscillator (Spectra Physics, Tsunami) is pumped by a 5 W Nd:YVO_4 diode-pumped laser (Spectra Physics, Millennia Pro) and produces an output power of 0.4 W, a central wavelength of 800 nm with a pulse duration of 50 fs and a repetition rate of 80 MHz, which is used to seed the regenerative amplifier (Spectra Physics, Spitfire). The Spitfire, which is pumped by a 20 W Nd:YLF laser (Spectra Physics, Empower), generates an output power of 4 W operating with a repetition rate of 1 kHz, a pulse duration of 50 fs and a central wavelength of 800 nm (see Figure 3.1).
The following sections explain the underlying physical principles responsible for the efficient operation of the Ti:Sapphire oscillator and amplifier of the whole laser system.

Titanium-sapphire oscillator

Mode locking and Kerr effect

The creation of ultrafast femtosecond laser pulses requires a broad bandwidth and intra cavity mode locking. The longitudinal modes in a continuous wave (cw) laser are independent of each other due to cavity fluctuations unlike in a pulsed laser where the longitudinal modes are locked in phase. This locked phase relationship between the modes leads to constructive interference at their peaks and a reduction of random fluctuations creating a single circulating pulse within the cavity.
In case of the Ti:Sapphire laser a passive self mode locking technique based on the Kerr effect can be used. Here the gain medium acts due to Kerr lensing as an artificial saturable absorber [13, 67, 68].
The optical Kerr effect occurs when intense laser light propagates through a nonlinear media, such as a crystal, and is an intensity dependant nonlinear modification of the refractive index with $\Delta n = n_2 I$, where Δn is the modification, n_2 the nonlinear refractive index and I the optical intensity, as described in Section 2.5.3. This nonlinear effect leads to a phase delay between the more intense peak of the Gaussian beam and the less intense wings outside of the optical axis, which can be compared to a optical lens. This results in the deformation of the wavefronts and therefore the self-focusing of the laser beam. Only the high intensity pulsed laser beam experiences the self-focusing effect shown in Figure 3.2. The initiation of Kerr lens mode locking, caused by power fluctuations inside the cavity that are high enough for the nonlinear focusing effect to occur, allows just the focused light to pass through the aperture and therefore the amplification of phase locked modes.

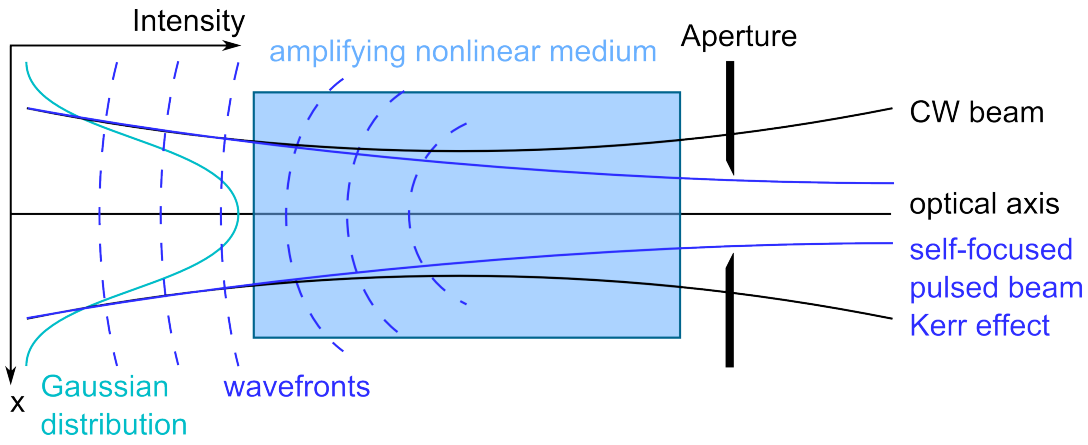

Figure 3.2: *Sketch of the nonlinear optical Kerr effect originating due to intensity dependent nonlinear modification of the refractive index in a amplifying nonlinear media. The distortion of the wavefronts and the self-focusing effect are the results and can be seen here.*

Titanium-sapphire amplifier

Group velocity dispersion

In ultrafast optics dispersion in space and time of ultrashort laser pulses plays a major role, which is called angular dispersion and chirp respectively and will be explained hereafter. Optical dispersive devices can alter the temporal duration of a ultrashort laser pulse, whereas the spectrum in the frequency domain remains unchanged. This characteristic is called group velocity dispersion (GVD) and is defined as the derivative of the inverse group velocity v_g with respect to the angular frequency ω [59, 69].

$$\mathrm{GVD} = \frac{d}{d\omega}\frac{1}{v_g} = \frac{d}{d\omega}\left(\frac{dk}{d\omega}\right) \tag{3.1}$$

In Equation 3.1 the parameter $k(\omega)$ stands for the frequency-dependent wavenumber. The group velocity v_g is defined as

$$v_g = \left(\frac{dk}{d\omega}\right)^{-1} = \frac{v_{phase}}{\left(1 + \frac{\omega}{n}\frac{dn}{d\omega}\right)} \tag{3.2}$$

Since the refractive index n is more commonly thought of in terms of the wavelength, the group velocity v_g can be calculated by using the vacuum wavelength $\lambda_0 = \frac{2\pi c_0}{\omega}$, the refractive index n and the phase velocity $v_{phase} = \frac{c_0}{n}$:

$$v_g = \frac{c_0}{n - \lambda_0 \frac{dn}{d\lambda_0}} \tag{3.3}$$

Different wavelength components of an ultrashort laser pulse propagate with distinct velocities through dispersive materials based on its wavelength dependent refractive index n. Thus the group velocity dispersion, which is defined as the group delay dispersion per unit length, can be expressed dependent of the wavelength λ_0:

$$\mathrm{GVD} = \frac{\lambda_0^3}{2\pi c_0^2}\frac{d^2 n}{d\lambda_0^2} \tag{3.4}$$

For an ultrashort transform-limited Gaussian laser pulse (used as a seed beam in the chirped pulse amplification setup described below) the fundamental relationship between its pulse duration dt and bandwidth $d\nu$ is given by:

$$d\nu \times dt > 0.441 \tag{3.5}$$

This transform limited laser pulse that travels though a “normal” dispersive medium experiences a positive chirp, which means that the longer wavelength components propagate faster than the shorter wavelengths (red faster then blue) within the same laser pulse. On the contrary, a negative chirped laser pulse has been propagating through a medium with “anomalous” dispersion causing longer wavelengths to prop-

agate slower then the faster ones (red slower then blue). Group velocity dispersion is used for the generation of high power femtosecond laser pulses created with chirped pulse amplification [70].

Chirped pulse amplification

For numerous time-resolved experiments and for nonlinear intensity driven processes the pulse energy provided by the Ti:Sapphire oscillator is not sufficient. For this reason the pulse energy has to be amplified, which proves to be difficult with the pulse energy simultaneously being to high for any amplifying gain medium. The solution is the so-called chirped pulse amplification (CPA) technique that is accomplished in three steps, which are firstly the stretching of the temporally short and transform limited laser pulse, secondly the amplification of the chirped pulse and thirdly the compression of the pulse as close as possible to its initial temporal duration. The amplification and subsequent recompression of an optical chirped laser pulse was firstly demonstrated by Donna Strickland and Gerard Mourou in 1985 [71]. By means of Figure 3.3 all three steps will be explained in detail hereafter.

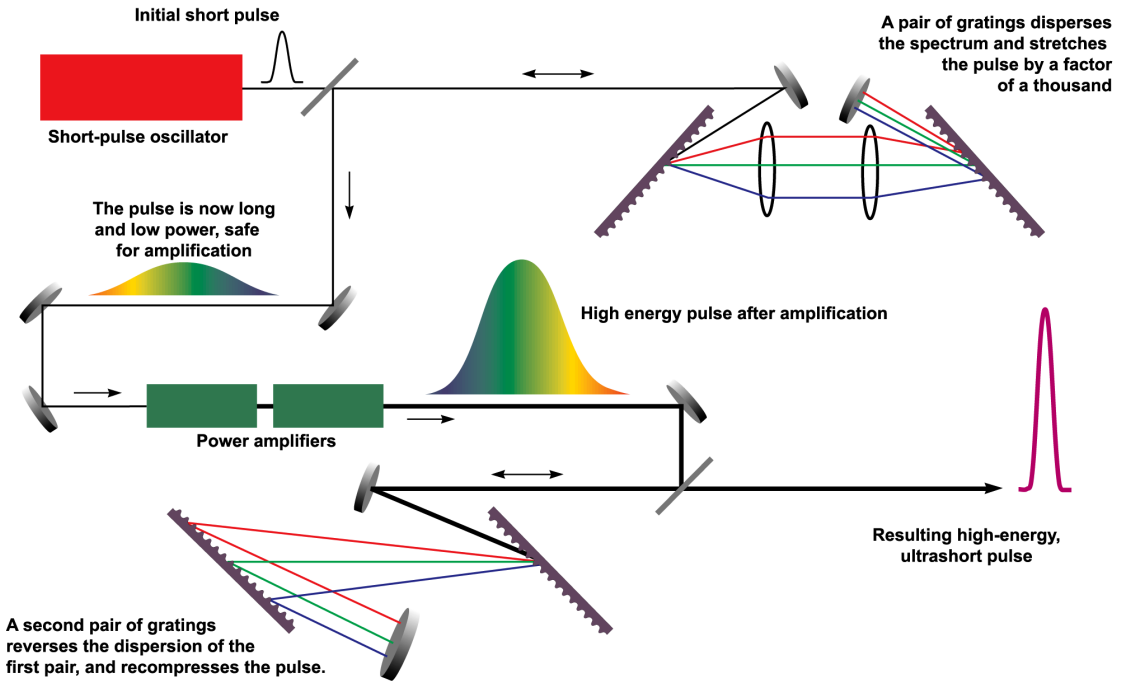

Figure 3.3: *Sketch of chirped pulse amplification setup with the three steps of pulse stretching with a dispersive grating pair, pulse amplification and pulse compression, realised with reverse chirping. [72]*

The chirped-pulsed amplifier is used to magnify the pulse energy of the ultrashort laser pulse from the oscillator by inserting the pulse into the amplifier cavity with an optical high-speed switch, called a Pockels cell and releasing the pulse after it has been efficiently amplified to a high intensity. In order to avoid damage of the optics inside the amplifier, direct amplification of the femtosecond pulse has to

be circumvented. The aforementioned chirped-pulse technique uses three steps to generate the high pulse energy.
Firstly, the initial femtosecond pulse is stretched in time due to group velocity dispersion within the laser pulse, that has been explained in detail before. This chirp allows the energy to distribute over a larger time duration resulting in a lower peak fluence. This is accomplished utilising dispersive optics like a pair of optical gratings, that chirp the original seed pulse up to 10^4 times from the femto- to the pico-second regime. This optically chirped pulse has got a sufficiently reduced peak fluence to enter the optical amplifying medium.
Secondly, this pulse is amplified in the Ti:sapphire crystal, which is the key optical element of the chirped-pulsed amplifier. This amplifying medium is pumped by the frequency doubled Nd:YLF laser in order to accumulate energy. Thereafter the low intensity chirped laser pulse is inserted and locked in the amplifier cavity. Here the pulse travels for many resonator round trips until its intensity is amplified to a certain threshold and finally it is released out of the amplifying resonator. Capture and release of the laser pulse in and out of the cavity is done by the aforementioned Pockels cell, an electro-optical high-speed switch, and a broadband polariser. A high voltage applied to the birefringent crystal of the Pockels cell can turn it into a $\lambda/4$ or a $\lambda/2$ waveplate and therefore alter the polarisation of the laser pulse [73].
Thirdly, the chirped and amplified laser pulse experiences a reverse dispersion and therefore a recompression to its initial temporal duration using a pair of optical gratings. The requirements for the compressor gratings are to match the dispersive properties of the stretching optics and to account for potential unwanted residual nonlinear effects introduced by chromatic dispersion in the amplifying medium. [74, 75].

3.1.2 Nonlinear optical processes

The fundamental physical principles of several second and third order nonlinear processes have been discussed in detail in section 2.5. Here the nonlinear optical tools used in this work, such as the high harmonics box and the optical parametric amplifiers, along with their physical processes will be described from a technical point of view.

High harmonic box

The third and fourth harmonic of the fundamental Ti:sapphire laser output with 800 nm wavelength is generated with the optical setup displayed in Figure 3.4. The p-polarised 800 nm input beam is separated by the first beam splitter BS1. A majority of the beam intensity (80%) is reflected at BS1 and changes its polarisation to s-type by passing through a $\lambda/2$ wave plate. Half of this s-polarised 800 nm beam travels through a 29° cut BBO crystal, which is used to generate p-polarised 400

nm laser light in a second harmonic generation (SHG) nonlinear process. The SHG is explained explicitly in section 2.5. The p-polarised 400 nm beam frequency mixes with the remaining 20% of the initial p-polarised 800 nm beam (reflected of a double mirrored translation stage) within a second 44.3° cut BBO crystal producing a s-polarised 267 nm beam in a third harmonic generation (THG) process. This latter 267 nm laser pulse can be utilised as a UV pump or probe beam in time-resolved photoelectron spectroscopy studies (after its polarisation is rotated to p-type). In the indole study it was used as a pump pulse as described in section 5.1.2.

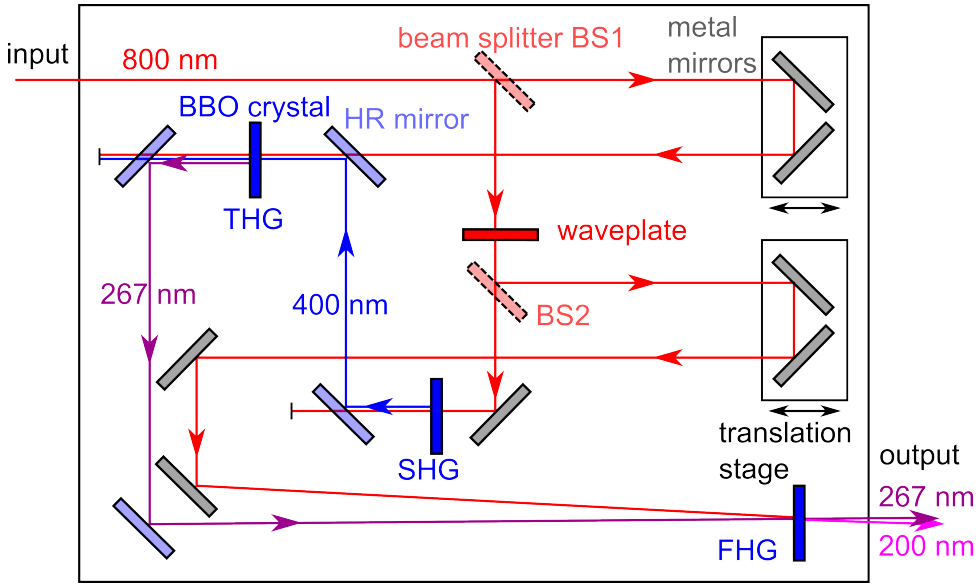

Figure 3.4: *Third and forth harmonic generation of the fundamental laser wavelength using home-built high harmonic box.*

The s-polarised third harmonic can, alternatively, be frequency mixed with the remaining s-polarised 800 nm beam in a 64.7° cut BBO crystal to generate p-polarised 200 nm laser light in a fourth harmonic generation (FHG) process. This new 200 nm output can equally be used as a pump or a probe pulse in a spectroscopic measurement.

For each nonlinear mixing process it is crucial that both laser pulses are spatially and temporally overlapped, therefore it is necessary to finely control and match the length of both beam pathways using translation stages.

The second challenge is the positive chirp of the laser pulses as they are travelling through material such as beam splitters and nonlinear crystals. The temporal lengthening of the pulse results in the reduction of its peak intensity and degrades the frequency conversion efficiency of the nonlinear process. Based on this reason all optics are chosen with an optimal performance/thickness ratio. The BBO crystals have a thickness of 0.5 mm (SHG), 0.1 mm (THG) and 0.1 mm (FHG) to reduce the walk-off between the laser pulses. Furthermore the beam splitters are 3 mm thick and the wave plate has got a thickness of 0.8 mm in order to minimise dispersion.

Optical parametric amplifier

Two optical parametric amplifiers, the OPA 800C (Spectra Physics) and the TOPAS Prime-U (Light Conversion), were used in the lab to generate tunable femtosecond UV laser pulses. The OPA setup uses several nonlinear processes, such as generation of white light continuum, DFG, SFM and SHG.
Starting with the generation of tunable IR amplifier frequencies a supercontinuum is created by focusing a part of the fundamental laser output onto a strong nonlinear material. The generated light exhibits a very broad spectral bandwidth, hence it is called white light generation [76]. A part of this broad spectrum is subsequently amplified in a difference frequency generation process or OPA using the fundamental frequency of the laser as the pump field within the nonlinear medium. This DFG creates a signal and an idler frequency in the tunable near IR spectral region.
Subsequently both generated frequencies are again combined with the fundamental laser frequency and can be used in SFG and SHG nonlinear processes to generate tunable UV laser light, which is utilised as a "pump" or a "probe" beam in the time-resolved spectroscopy technique.

3.1.3 Compression of ultrashort pulses

Normal optical dispersion of a ultrashort laser pulse can be caused by the usage of mirrors and lenses, or even purely propagation through air itself. It results in the redder wavelengths travelling faster then bluer ones. This positive "chirp" can be compensated by using a prism compressor, which introduces negative dispersion due to the fact that longer wavelengths have to travel over a longer distance through the prisms than shorter wavelengths and are effectively slowed down. An original positive dispersed pulse can, in principle, be compressed to its transform limit after passing through a pair of prisms, as shown in Figure 3.5.

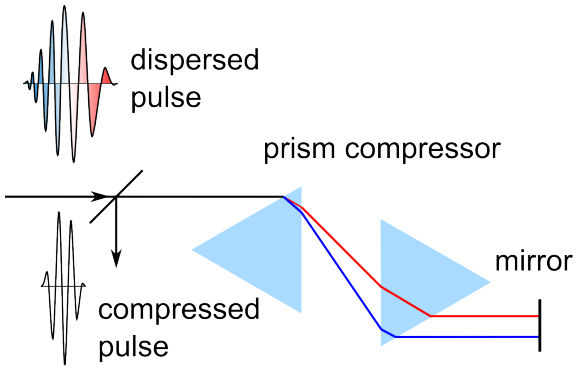

Figure 3.5: *Compression of an incoming positive "chirped" laser pulse with a prism compressor to its transform limit.*

3.2 Photoelectron imaging spectrometer

The general observables in a photoelectron spectroscopy measurement are the distribution of the electron kinetic energy, the photoelectron angular distribution and the scalar and vector correlations between the electron distributions. Time-resolved photoelectron imaging spectroscopic techniques are firstly advantageous, because a 2D position sensitive detection enables the simultaneous measurement of the photoelectron kinetic energy and its angular distribution, and secondly are in demand due to their detection sensitivity and easy implementation [77, 78, 79].

3.2.1 Vacuum system design

In addition to the laser, the other key tool of the experimental setup in our lab is the state-of-the-art photoelectron spectrometer, which uses the velocity map imaging (VMI) technique and consists of two differentially pumped ultra-high vacuum chambers. A detailed sketch of the machine with all its important components is shown in Figure 3.6.

The source chamber at the bottom of the apparatus is connected to the main interaction chamber, which is mounted on top of it. They are both individually evacuated utilising two separate turbomolecular pumps from Edwards Vacuum (2200 l/s and 480 l/s respectively). These are backed by two rotary pumps (Edwards M40 and M28). The source and the main chamber operate under normal conditions at ultra-high vacuum with base pressures on the order of 10^{-8} mbar and 10^{-9} mbar respectively. Both can be separated or connected with a 1 mm skimmer (Beam Dymanics Inc) mounted on a translatable gate-valve assembly [81]. This is an extremely advantageous approach due to two main reasons. The liquid or solid sample that is mounted within the source chamber (as described in more detail below) can be easily refilled by venting of the bottom chamber. Meanwhile the main interaction chamber, separated by the gate-valve, remains under ultra-high vacuum at a base pressure of $p_{base} = 1 \times 10^{-9}$mbar, which protects the sensitive equipment within it and circumvents the time consuming bake-out of the upper chamber before the start of a new experiment. The time scale for a sample replacement and subsequent restart of the data acquisition is consequently substantially reduced to $\sim$ 2 hours (as compared to approximately one day without the valve).

Liquid or solid samples are placed in a cartridge mounted directly within a Even-Lavie (E-L) pulsed valve that is situated in the source chamber [82, 83]. During valve operation the base pressure rises to the order of 10^{-6} mbar in the source chamber. This high intensity, pulsed supersonic molecular beam valve with a 150 μm diameter conical nozzle brings the sample into gas phase by operating a solenoid driver at 1 kHz that raises the temperature of the valve considerably, therefore heating the sample itself. The temperature of the valve is controlled by a Neslab RTE-110

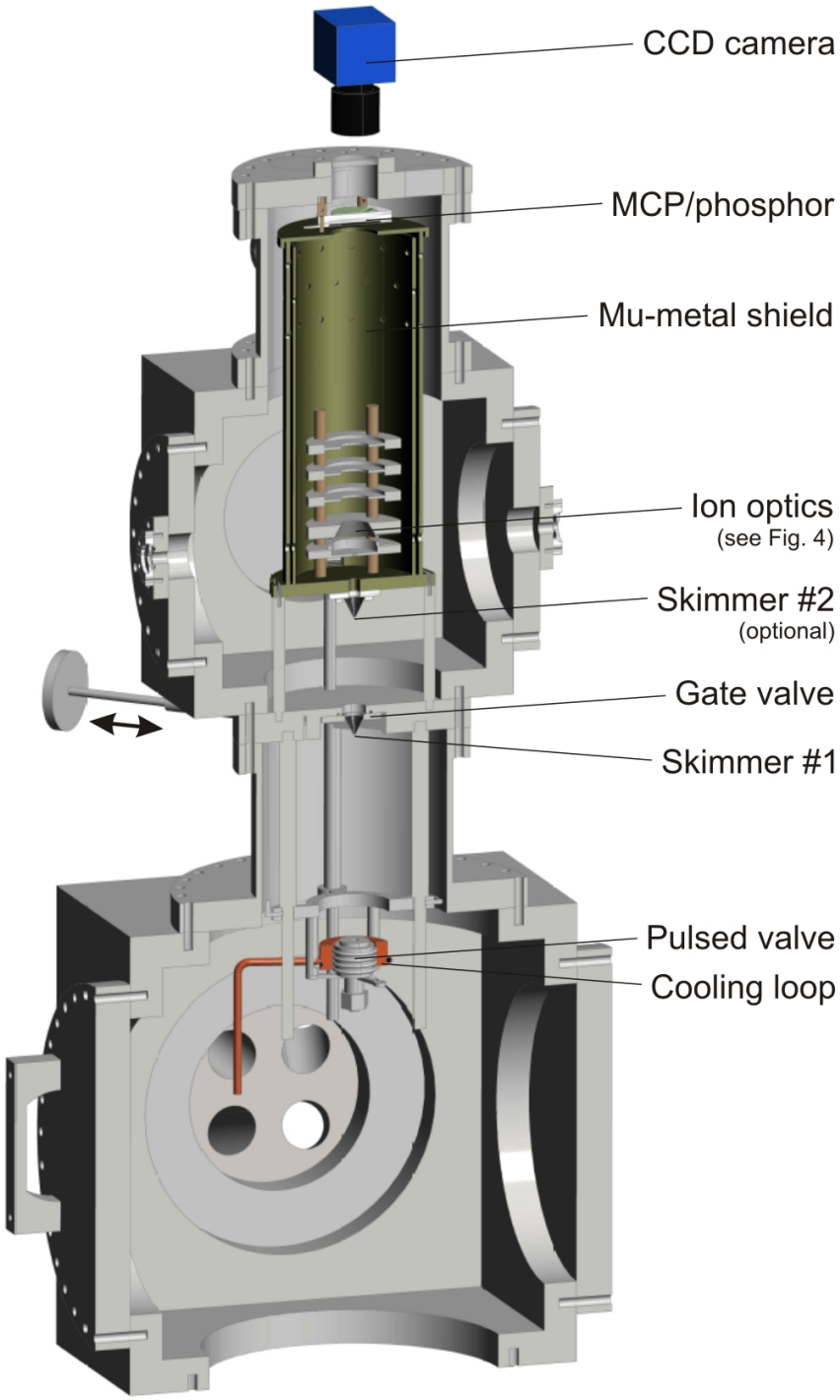

Figure 3.6: *A sketch of the femtosecond photoelectron imaging spectrometer with all the important key tools, used to collect the experimental data. It consists of the source chamber at the bottom and the main interaction chamber containing the ion optics shielded by a mu-metal cylinder at the top. The detector assembly comprises a MCP and phosphor plate and a CCD camera. Some additional details like vacuum pumps, bake-out lamps and vacuum feedthroughs are not displayed here for reasons of clarity [80]. Please see additional information in the main text.*

closed loop chiller that uses a refrigerant of 50:50 water and ethylene glycol and is connected to a copper cooling block surrounding the E-L valve body [80]. A carrier gas (such as helium with a backing pressure of 1 to 5 bar, depending on the sample) then flows over the heated molecular sample and every millisecond a gas pulse is produced of a pulse duration $\sim$ 20 - 25 μs, by the molecular beam value, undergoing a translational and internal cooling via a supersonic expansion into the source chamber.

Depending on physical properties such as vapour pressure and absorption/ ionization cross-section of the molecular sample, an external bubbler can be used as a alternative with a bigger reservoir than the cartridge, which is then connected via stainless steel tubing directly to the pulsed E-L valve. The advantages of this configuration are longer lasting samples due the larger sample storage volume and the reduced exchange time between two samples since only the bubbler and the tubing need ventilation while the complete source chamber remains under vacuum. Likewise in the setup described above a carrier gas picks up the molecular sample, but this time it flows first into the input of the bubbler and on its way out it carries along the molecules of interest towards the pulsed valve and the source chamber.

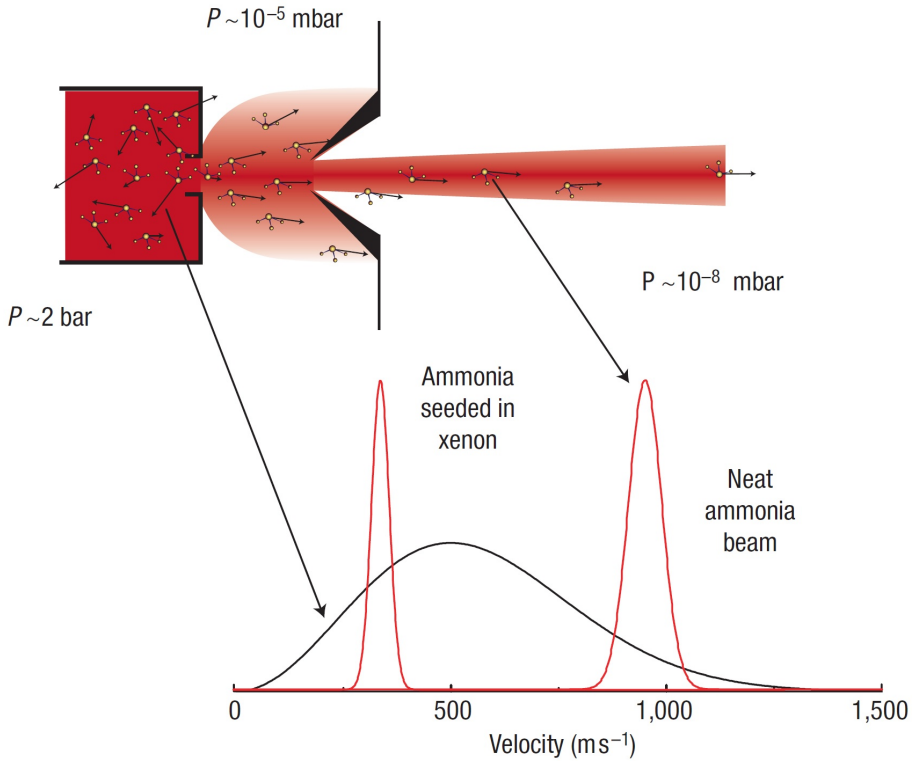

Figure 3.7: *This scheme shows a supersonic expansion of a high pressure gas. The lower part of the picture shows a graph of the velocity distribution of room-temperature ammonia in the box and in the supersonic expending beam. Here the velocity distribution is narrowed due to the utilisation of a narrow distributed carrier gas [84].*

Once passed through the skimmer the molecules of interest within the carrier gas enter the main interaction chamber. The skimmer is designed to allow only the coldest part of the expanding sample to transit through. Figure 3.7 is an illustration of the supersonic expansion of a high pressure gas into the vacuum. It takes place due to the frequent collision of molecules and the adiabatic cooling of all degrees of freedom in the expansion region [84]. The result is a cool gas mixture of sample molecules and the carrier noble gas, which reduces the chance of cluster formation of the molecules. Here a carrier gas with a high ionisation energy, such as He, should be selected in order to prevent a confusion with the resulting photoelectrons of the molecules of interest.
As soon as the upwards propagating molecular beam is inside the main chamber between the ion optic set-up (explained in detail below), it is intersected at 90° with the two co-propagating "pump" and "probe" laser beams, which enter the interaction chamber through a 2.0 mm thick CaF_2 entrance window on the left hand side in Figure 3.6 at the same height as the ion optics. The temporal delay between both laser pulses is precisely controlled utilising a motorised linear translation stage (Physik Instrumente, M-403.62S) and home-built data acquisition software (MATLAB, the Math-Works Inc., R2007b). The first UV laser pulse resonantly excites the molecules and the second pulse ionises them in a so called $(1+1')$ ionisation process. The resultant photoelectrons are generated between the repeller and extractor electrodes of the electrostatic lens assembly, which are optimized for velocity map imaging (VMI) of photoelectrons [85].
These nascent and expanding electron spheres experience a strong electric field, which projects them onto a microchannel plate (MCP) detector, where they induce a electron avalanche on a phosphorescent screen that is detected by a CCD camera. The recorded 2D image comprises both energy- and angle-resolved information, which can be extracted from the 2D projection of a 3D distribution of recoil velocity vectors that are measured. Hereafter VMI, the particle detection and particle image reconstruction technique are explained in greater detail in the following sections.

3.2.2 Velocity map imaging and detection

The state-of-the-art 2D imaging technique is photoelectron velocity map imaging [85, 86], which is a variant of the photofragment imaging method [87] and builds on simple techniques like photolysis mapping, originally demonstrated in 1967 [88].
The main advantages of VMI are twofold. Firstly, it has the potential to measure the full 3D velocity distribution of ejected charged particles (ions or electrons) in a single image. Here all velocities, hence energies, can be mapped simultaneously onto the detector plane and all particles with the same velocity vector will be mapped to the same point on the detector. Secondly, several processes can be involved in the creation of charged particles such multiphoton ionisation, photofragmentation, pho-

toelectron imaging and reaction product imaging. Here the VMI detection method shows its great potential due to its wide range of applications. Based on these reasons velocity map imaging is a highly valuable detecting method in the field of molecular reaction dynamics.
In 1997 Eppink and Parker have shown with their work the advantages of combining ion lens optics and 2D detection [85]. This new velocity map imaging technique now provides essential improvements over other common 2D detection methods using grid electrodes. A comparison between the two methods is shown in Figure 3.8, where O^+ ions were detected resulting from photodissociation of molecular oxygen.

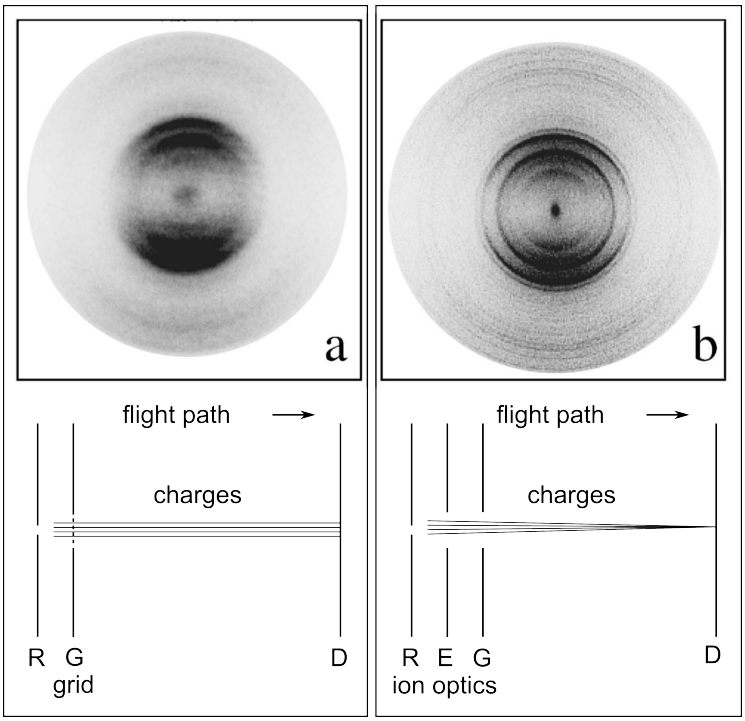

Figure 3.8: *(a) O^+ ions detected with a repeller R and a fine mesh grid G and the sketch of the grid electrodes geometry showing the flight path of the charged particles. (b) Same detected O^+ ions this time with VMI using ion optics, repeller R and extractor E, to map the charges with the same velocity vector on the same point on the detector D (shown is the sketch) [85].*

The charged particles measured with a fine mesh grid are shown in Figure 3.8(a), where the detected image, although using a just one grid with very fine wire spacing, lacks resolution. The reasons are, on the one hand, trajectory deflections as particles pass through the grid and, on the other hand, blurring effects which originate from the non-point source geometry (because every point in the ionization volume can be treated like a point source). These problems can be solved by using open lens electrodes mapping the charges onto the detector, shown in Figure 3.8(b). In this assembly three electrodes, the repeller R, extractor E and an grounded one, are used to create a correctly focused ion image (see Figure 3.8(b)). Here the voltage ratio of repeller and extractor V_E/V_R is crucial and the focusing is not dependent on m/q, the mass-charge ratio [85]. Based on the energy conservation principle and

the initial well defined conditions, the kinetic energy of the charged particles can be described with the following equation:

$$\frac{1}{2}mv^2 = qV_R \tag{3.6}$$

As a result the time-of-flight (TOF) t of the particles, that are released into a field free drift tube of length l, is directly proportional to the repeller voltage V_R and it can be used to identify the mass of the particles.

$$t = l\sqrt{m/(2qV_R)} \tag{3.7}$$

Assuredly the improvements of the detection quality with the VMI method can be seen in Figure 3.8(b), where well defined concentric rings can be allocated conclusively to several different dissociation pathways. The radius r of the rings depends on the expansion speed v and the time of flight t of the charges and can be defined as

$$r = Nvt \tag{3.8}$$

with N being a magnification factor, that is related to the laser focus, the lens geometry and the length of the flight tube and can be calibrated for the whole recorded image. Consequently the kinetic energy can be also written as:

$$E_{kin} = \frac{1}{2}mv^2 = \frac{1}{2}m\left[\frac{r}{Nt}\right]^2 \tag{3.9}$$

In addition, the laser polarisation was chosen to be vertical in both images in Figure 3.8, for this reason a reconstruction of the full 3D distribution utilising the inverse Abel transformation was possible. This will be discussed in more detail in Section 3.3.

In Figure 3.9 (a) the VMI method is illustrated in greater detail with extensive presentation of the equipotential surface between the repeller, extractor and the ground electrode and the simulated ion trajectories resulting from a fixed "focal length" of the ion optics $V_E/V_R = 0.75$ [85]. This focusing effects originates from the open electrode geometry creating the curved equipotential landscape. The laser, that propagates in the y-direction, creates charged electrons and ions with a $(1+1')$ ionisation process in the middle of the repeller and the extractor electrodes. Due to the big ionisation volume the particles are born at different positions (see Figure 3.9 (c)). Although created in various places, the charges with the same direction and velocity will reach the same spot on the detector surface. Figure 3.9 (d) shows position 1, 2 and 3 in the plane of detection corresponding to three distinct ejection angles 0°/180° (x-direction), 45°/135° and 90° (y-direction) respectively (see Figure 3.9 (b)). Looking at Equations 3.6 and 3.9 the great advantage of this lens set-up becomes clear, since the charges trajectories purely depend on the repeller voltage

V_R versus kinetic energy release. Hence if other parameters like particle masses or total size of setup are modified, the shape of trajectories stay the same.

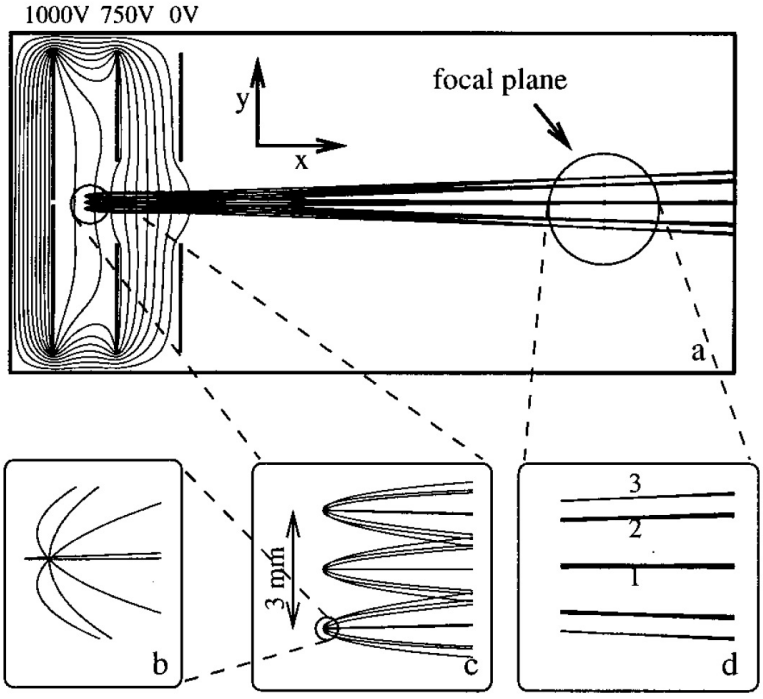

Figure 3.9: *(a) This illustration shows the ion lenses (repeller, extractor, ground), their equipotential surfaces and the simulated ion trajectories [85] following correctly calibrated velocity map imaging. (b - d) show enlargements of picture (a). Particles initially originating from different positions (c) will be mapped onto the same point in the detector plane (d), if they have the same velocity vector.*

In our lab, the lens assembly that was used is shown in Figure 3.10 and consists of two main electrodes on the bottom and three additional ones (C - E), which were grounded in the photoelectron imaging experiments but offer the possibility of "dc slice imaging" measurements in ion detection mode [89]. In this set-up the first and second electrodes are the repeller and the conical extractor between which the molecules and the UV light pulses interact and create both electrons and ions. Depending on the polarity of the electrostatic lens assembly either electrons or ions will be accelerated along the time-of-flight tube towards the detector.
Two crucial features allow an optimised velocity mapping of the particles. Firstly, the extractor electrode is construed conically and maps off-axis ejected charges more effectively to the detector compared to flat and parallel electrodes. Hence this conical geometry greatly reduces coma lens error aberrations [90]. Secondly, the protruding margins of both repeller and extractor act like a potential barrier by shielding the insulating components between the electrodes from electric charges in order to prevent the accumulation of point-charge build up and an resulting field distortion. It is important to protect the generated photoelectrons from external magnetic fields, which was done with a double layer of mu-metal shielding along the time-of-flight axis, the base plate on which the ion optics are mounted and the

the "end-cap" in the front of the detector. Furthermore, it is equally important to prevent any stray electric fields to artificially effect the measurements. Hence all surfaces within the instrument, that are conceivably exposed to generated charges, were coated with colloidal graphite (Acheson Colloids, Aerodag G).

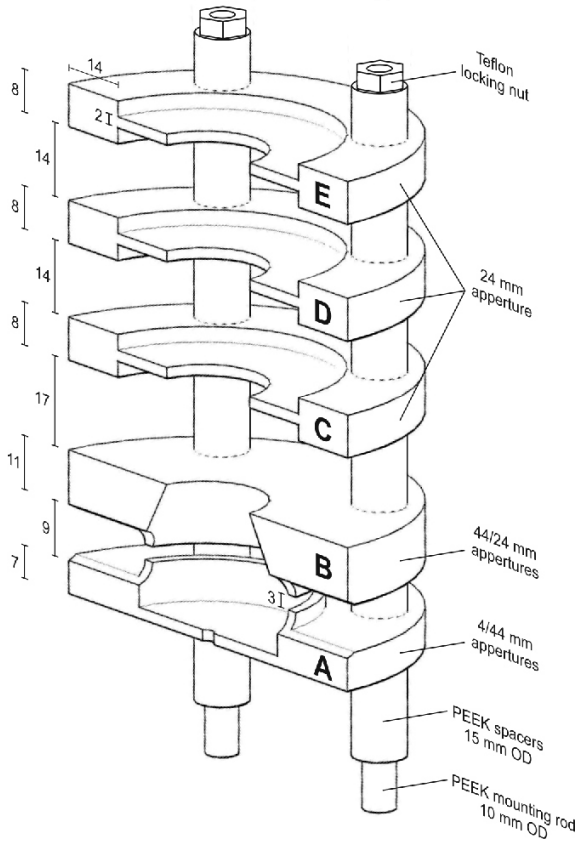

Figure 3.10: *Illustration of the imaging electrode assembly used in our experiments is shown here, where the details are displayed in mm. The optimum VMI conditions where found for a applied voltage ratio of* $V_B/V_A \sim 0.78$ *[80].*

Finally, the detector assembly is positioned at the end of the time-of-flight tube and is composed of 40 mm dual microchannel plate (MCP), which is a many channel electron multiplier, backed up by a P47 phosphor screen that luminesces after the electron avalanche impact. This light is then detected by a monochrome CCD camera (The imaging Source, DMK 21BF04) with a 640 × 480 pixel array. The recorded images are transferred to a PC running acquisition software at 30 frames/s. The data collection is fully automated, which is made possible using home-built software based on MATLAB (The Math-Works Inc, version 7.4.0, 2007a) and a motorised translation stage for a precise overlap of the pump and probe laser beam (definition of time zero) or producing a delay between the two pulses. Furthermore, at each delay point a time-independent one colour signal resulting from the pump and probe respectively may be recorded and used for background subtraction from the two colour pump-probe signal. Two automated shutters SH05 and controllers TSC001 (Thorlabs) made this data acquisition possible.

3.3 Data processing

The overall time-resolved photoelectron imaging setup is summarised in Figure 3.11. Here the molecular sample passes the electrode assembly undergoing a subsequent excitation/ionisation process due to the pump and probe laser pulses. The laser polarisation of the two pulses has to be linear and parallel to the detector plane. This is crucial for the image reconstruction (described below) that requires cylindrical symmetry for the matrix inversion method. The charged particles, generated due to ionisation, expand as so called "Newton spheres" in the TOF tube and get mapped by the detector assembly. A two dimensional projection of the three dimensional particle distribution is recorded as a raw image.

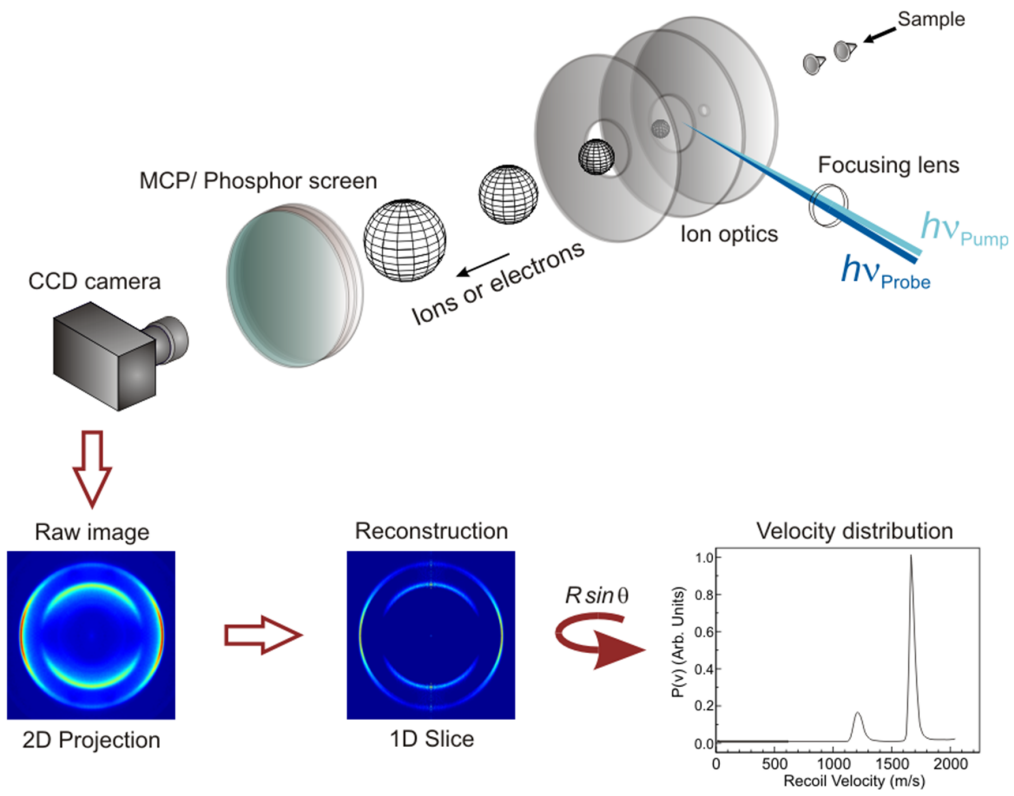

Figure 3.11: *TRPEI setup with expanding particle distribution after $(1+1')$ ionisation by UV laser pulses and sketch of particle reconstruction method [91].*

3.3.1 Particle image reconstruction

In order to reconstruct the original particle velocity distribution, originated from a photoionisation of photodissociation process, a reconstruction method has been applied [80], which uses a matrix inversion method similar to the one applied by Cho and Na [92] and the further developed method by Sussman [93]. The comparison between other reconstruction methods is described in a comprehensive work by Whitaker and co-workers in [94, 95].

The reconstruction method makes use of the assumption that the charge distribution is cylindrically symmetric along the axis parallel to the 2D detector plain. This assumption is valid due to the utilisation of linear polarised pump and probe pulse with a polarisation E-field vector orientation parallel to the 2D detector plane. Based on this, the three dimensional distribution $I(x, y, z) \equiv I(\rho, z)$ of ions or electrons is a cylindrical distribution with radius ρ and altitude along symmetry axis z [80]. The 2D image projection at the detector plane (y, z) is given by

$$P(y, z) = \int I(\rho, z) dx \tag{3.10}$$

with the use of cylindrical coordinates $\rho^2 = x^2 + y^2$ and $dx = \rho d\rho / \sqrt{\rho^2 - y^2}$. On this basis the 2D projection on the detector in Equation 3.10 can be expressed with

$$P(y, z) = \int_y^\infty \frac{I(x, y, z) \rho d\rho}{\sqrt{\rho^2 - y^2}} \tag{3.11}$$

As such the 3D charge particle distribution $I(x, y, z)$ may be reconstructed from $P(y, z)$ using the inverse Abel transformation

$$I(\rho, z) = -\frac{1}{4\pi} \int_r^R \frac{\partial_y P(y, z)}{\sqrt{\rho^2 - y^2}} dy \tag{3.12}$$

The application of this method has the disadvantage that the partial derivative in the numerator causes noise along the centre line of the reconstructed image. Furthermore most reconstruction methods are relatively slow in terms of processing time. Optimisation work on the matrix inversion approach has be done and was published in [80]. Here the particle distribution $I(\rho, z)$ is considered as a discrete distribution I_{ij} by the partitioning of the xy-plane. Here segments, dependent on ρ and y, are used to describe the area with maximum radius i and j as the maximal segment value y, which is displayed in Figure 3.12.

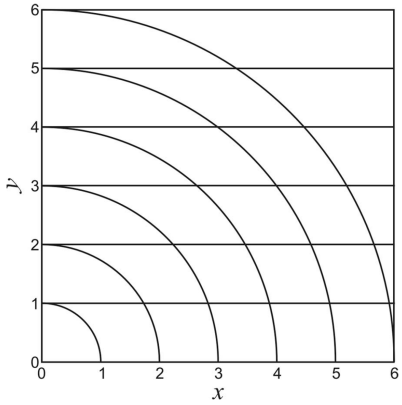

Figure 3.12: *Partitioned area for Abel inversion with segments of A_{ij} [80].*

The area of each segment is defined as A_{ij} and can be expressed for the specific case of $i = j$ as:

$$A_{ij} = \int_{i-1}^{i} \int_{0}^{\sqrt{i^2-y^2}} dxdy \tag{3.13}$$

For all other segment areas the expression is:

$$A_{ij} = \int_{i-1}^{i} \int_{\sqrt{(j-1)^2-y^2}}^{\sqrt{i^2-y^2}} dxdy \tag{3.14}$$

The utilisation of the segment areas allows the 2D data projection on the detector plane for large values of x to be written as $\mathbf{P} = 2\mathbf{AI}$ and therefore the final 3D particle distribution obtained from the inverse Abel transformation is given by

$$\mathbf{I} = \frac{1}{2}\mathbf{A}^{-1}\mathbf{P}. \tag{3.15}$$

The great advantage of using the segmentation inversion method is the enhancement in processing time, which can be potentially implemented in real-time imaging and can be also used to handle large data sets is a reasonable time frame. The processing time of this applied method is 100 times faster than the polar onion peeling method developed by Roberts *et al.* [96].

3.3.2 Analysis of energy resolved information

Time-resolved photoelectron imaging provides the simultaneous measurement of energy and angle resolved information in a single two dimensional image. The charged particles with the same velocity vector (in this case electrons) are mapped to the same point on the detector plane. Based on this, the pixels, which define the radius of the detected rings, can be converted into velocity or energy space. The technique of velocity mapping and image detection was explained in detail in Section 3.2.2.
In Figure 3.11 the reconstructed, Abel inverted image corresponds to the central slice of a 3D "Newton sphere" and has to be weighted by the factor $R\sin\theta$ in order to obtain the full intensity distribution as a function of velocity, kinetic energy of the electron $E_{kin,e}$ or Rydberg binding energy E_{Ryd}. The kinetic energy $E_{kin,e}$ is quadratically dependent on the radius of the recorded rings (see Equation 3.9). The Rydberg binding energy E_{Ryd} is the energy which is needed to remove an electron from an excited electronic state.
The temporal information of the pump-probe spectroscopy technique is established by recording a series of images at different temporal delays between the pump and the probe pulse. In the following section a simple molecular example, N,N-Dimethylisopropylamine (DMIPA) taken from [97], is chosen to illustrate the data analysis.

Figure 3.13 shows a series of Abel inverted data images, which are one-colour background subtracted prior to image reconstruction. The linear polarisation direction of the laser pulses are vertical in the images. At negative delay times the probe pulse arrives before the pump pulse and therefore ideally no two-colour signals will be recorded. At $\Delta t = 0$ both pulses arrive at the same time and the involved energy dependent data features (exited energy states) begin to evolve in time, as can be seen in Figure 3.13.

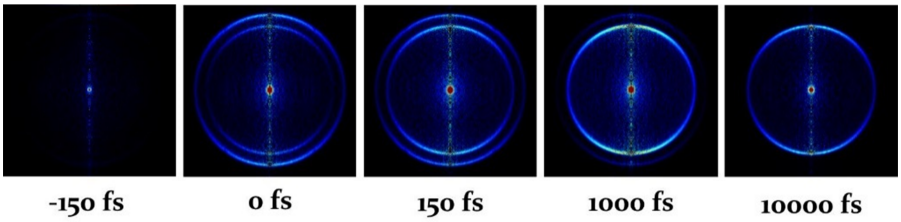

Figure 3.13: *$(1 + 1')$ photoelectron images after Abel inversion of DMIPA [91].*

The time-dependent series of photoelectron data images has to be weighted with the aforementioned factor $R \sin\theta$ in order to obtain the total energy and time dependent photoelectron spectrum of the molecular system, shown in Figure 3.14. Each photoelectron image corresponds to a cut at a specific pump-probe delay time.

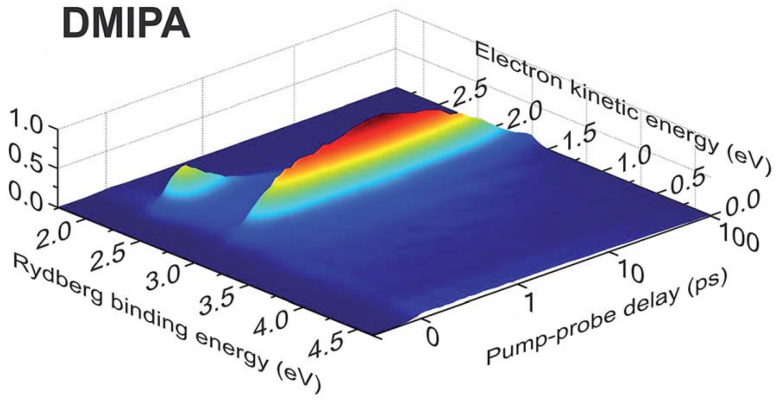

Figure 3.14: *Total 3D photoelectron spectrum of the molecular system DMIPA dependent on the Rydberg binding energy and the delay time between pump and probe pulse [97]. The pump-probe delay is on a lin/log scale.*

In order to analyse the temporal behaviour of the spectral features in the 3D photoelectron spectrum, the data is fitted with the standard Levenberg-Marquardt global fitting function, depending on the energy E and the delay time Δt:

$$S(E, \Delta t) = \left[\sum_{i=1}^{n} A_i(E) \cdot P_i(\Delta t) \right] \otimes g(\Delta t) \tag{3.16}$$

Here $A_i(E)$ are the decay associated photoelectron spectrum of the i^{th} data channel, $g(\Delta t)$ represents the Gaussian cross-correlation function of the pump and probe pulses. The time dependant population $P_i(\Delta t)$ is a series of exponential decay functions, which all originate from $\Delta t = 0$:

$$P_i(\Delta t) = \exp\left(-\frac{\Delta t}{\tau_i}\right) \tag{3.17}$$

The quantity n is the number of exponential functions used in the global fit, which depends on the data set of each specific molecule.
The Levenberg-Marquardt global fitting routine generates a series of transients that may be plotted as a function of time, as can be seen in Figure 3.15. In the example two exponential functions are used to fully describe the photoelectron spectrum of Figure 3.14.

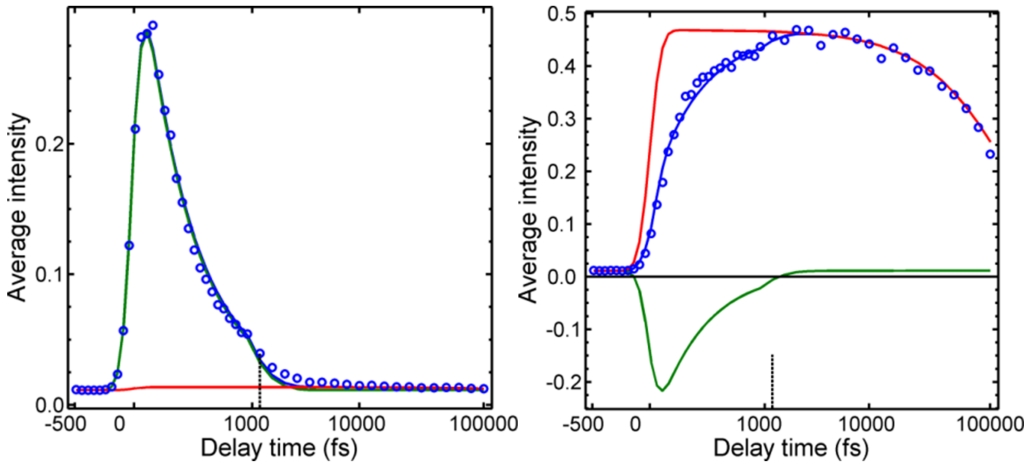

Figure 3.15: *Time dependent functions of two electronic states contributing to the dynamical process in DMIPA [91]. The blue circles are the data points, the red and green curve are the two individual exp. functions and the blue curve is the overall fit.*

On the left hand side of Figure 3.15 the short lived feature at a lower binding energy is plotted and just one exponential function is sufficient to map the decay of the particular temporal evolution of a electronic state. This is set to be the decay time of this state.
On the right hand side of Figure 3.15, the long lived feature at higher binding energy is plotted against pump probe delay time and here two exponential functions are needed to fully fit the data. The longer time constant maps correctly the falling tail of the transient, while the same short time constant of the first state is needed to map the rise time of the second longer lived energy state. This is realised with a negative amplitude of the short time constant, which is effectively subtracted in the fit from the transient. This is an excellent example where the decay time of one state matches the rise time of the other state, resulting in a sequential dynamics of both states, where population and energy is transferred.

The amplitudes $A_i(E)$ of each decay constant of the Levenberg-Marquardt global fitting function can be plotted against energy as shown in Figure 3.16. In this figure the two features are spectrally resolved from each other and since all fit functions originate from $\Delta t = 0$, the already observed negative feature symbolises sequential dynamics from one vibronic state to an other.
In general, the technique of time-resolved photoelectron imaging provides the temporal information and also the ability to spectrally separate dynamical processes via the decay associated spectra, which are potentially convoluted in just a transient data set, since they may occur on similar time scales. This approach allows easier interpretation of complicated non-adiabatic dynamical behaviour in molecular systems.

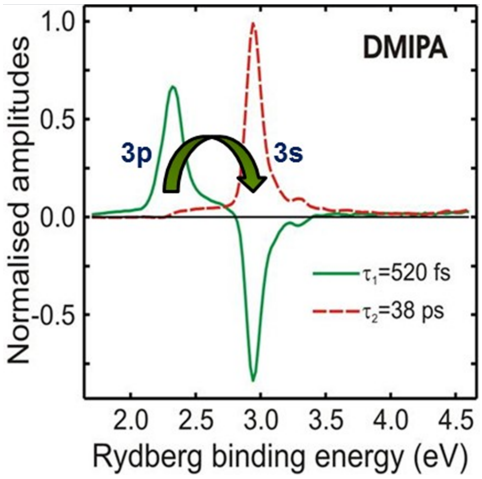

Figure 3.16: *Decay associated spectrum showing the amplitudes of two decaying states dependent on the energy in DMIPA [91].*

3.3.3 Analysis of angle resolved information

The TRPEI technique provides, in addition to the energy- resolved information, also important insights about the electronic character of the dynamically involved energy states and therefore the shape of the molecular orbitals of which the ionised electrons originated from. In some cases the different dynamical processes of polyatomic molecules produce photoelectrons with similar energy and temporal behaviour. The investigation of the photoelectron anisotropy distribution evolves as a function of energy and delay time and is therefore a powerful tool to entangle the underlying photophysical mechanisms.
The PAD can be explained as an interference of different partial waves that is dependent on scattering phase and the amplitude of the angular momentum coupling (e.g. $\Delta l = \pm 1$) and the overlap integral of initial excited and final cation state. Hence the PAD contains direct information about the photoelectron energy and the electronic structure of the initial and final electronic state. In Figure 3.17 this

concept can be explained by a simple picture, where an electron is ionised with a linear polarised photon from an excited state (s-orbital). Due to Koopman's correlations, the excited state of the molecule is mapped onto a final cation state with same electronic structure, therefore the wavefunction of the outgoing electron is a p-function in order to conserve angular momentum. If the initial excited orbital is p-shaped the outgoing partial waves can be s- or d-functions (due to $\Delta l = \pm 1$). The aforementioned interference effects in the PAD, depending on the scattering phases of partial waves, lead to a more complex form of the total wavefunction of the ejected electron.

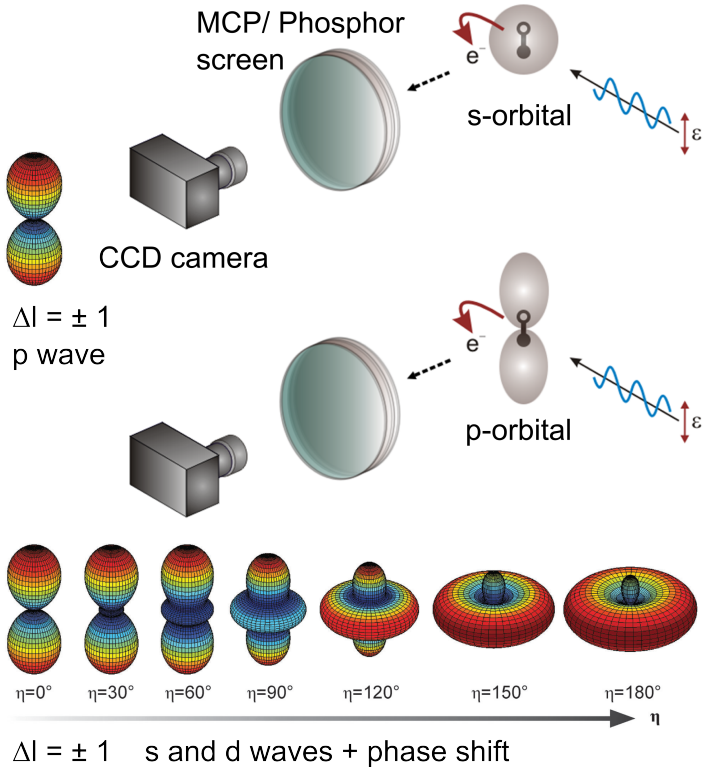

Figure 3.17: *Sketch of angle-resolved detection method [18, 91].*

The photoelectron angular distribution, previously discussed in Section 2.3 and defined by Equation 2.20, can be now specified for the $(1+1')$ ionisation process with linear polarised light in the TRPEI measurement.

$$I(E, \Delta t, \theta) = \frac{\beta_0(E, \Delta t)}{4\pi} \left(1 + \beta_2(E, \Delta t) P_2(\cos(\theta)) + \beta_4(E, \Delta t) P_4(\cos(\theta))\right) \quad (3.18)$$

The parameters in this equation are the above defined n^{th}-order anisotropy parameters β_n and $P_n(\cos(\theta))$ is the n^{th}-order Legendre polynomial. The β_0 parameter relates to the intensity. The dynamical evolution of the PAD is in some cases of greater interest than the absolute value of β itself, since the time dependence is a signature of the non-adiabatic coupling between two electronic excited states. This temporal evolution of the anisotropy parameters can help to establish a more complete picture about the overall relaxation processes in molecules of interest.

Chapter 4

Observation of multi-channel non-adiabatic dynamics in aniline derivatives

In this chapter the deactivation mechanisms operating in the aniline derivatives N,N- dimethylaniline (N,N-DMA) and 3,5- dimethylaniline (3,5-DMA) are presented following excitation at 240 nm, and investigation with time-resolved photoelectron imaging. The findings have been published in M. M. Zawadzki *et al.*, Observation of multi-channel non-adiabatic dynamics in aniline derivatives using time-resolved photoelectron imaging *Faraday Discuss.*, 194, 185-208, 2016 [2].

Aniline, such as other model chromophores, has critical reaction coordinates that drive the non-adiabatic relaxation dynamics. The photochemical dynamics study of site-selective methylated aniline derivatives allows a sophisticated comparison with, and provides new insights into, the existing literature reported for aniline at similar wavelengths.

The energy- and angle-resolved results obtained from the highly differential TRPEI technique reveal new dynamical information about the lower lying excited states and their dynamical behaviour. The first two electronic excited states have been studied previously at an excitation wavelength of 250 nm. The work, presented in this chapter, looks energetically and dynamically further into the excited landscape of the aniline derivatives. Especially the fate of the $2\pi\pi^*$ excited state is of great interest and it can be stated that it is not non-adiabatically coupling to the energetically lower $S_1(\pi\pi^*)$ state or the $S_2(3s/\pi\sigma^*)$ Rydberg/valence state.

4.1 Introduction

4.1.1 The history of aniline and its derivatives

In a variety of biological molecular systems, including DNA bases, amino acids and phenylpropanoids in plants, aromatic amines are a common structural component [98]. Based on this fact, the investigation and full comprehension of the physical and chemical functionality of these heteroaromatic sub-components within the larger biomolecules is of great importance.

After ultraviolet light absorption, this class of molecules exhibits an especially low fluorescence quantum yield, resulting from the very efficient radiationless relaxation dynamics from the electronic excited states to the ground state. The ultraviolet part of the solar spectrum is potentially harmful to living organisms, therefore the proficiency of chromophores to transform the UV energy via non-radiative and ultrafast non-adiabatic pathways into vibrational energy is of great interest.

Various studies find increasing evidence that so-called mixed Rydberg/valence states are correlated with these non-adiabatic couplings between electronic and vibrational degrees of freedom, resulting in a extremely efficient pathway for excess energy dissipation into the molecular surrounding. In their recent reviews Ashfold and co-workers as well as Roberts and Stavros published extensive overviews of non-adiabatic interactions related with mixed Rydberg/valence states in a broad range of biomolecular systems [99, 100].

"Photostability" of biomolecules has evolved as a crucial characteristic of early life 3.5 billion years ago, due to the fact that the surface of the earth was exposed to much higher UV radiation levels due to the not fully developed atmosphere [101].

The simplest aromatic amine is aniline, which is an excellent example of a model system to study and understand the relationship between chemical structure, non-adiabatic dynamics and the photoprotective function of bigger and biologically relevant molecules. Thus, it comes as no surprise that aniline has been experimentally and theoretically studied extensively over the past decade with various methodologies [102]-[110]. Included in this list of literature are the time-resolved photoelectron imaging studies done by Townsend and co-workers, where the dynamical evolution of gas-phase aniline was investigated following UV excitation at 273 nm - 266 nm [105] and furthermore at 250 nm [110]. The latter report investigates N,N-dimethylaniline (N,N-DMA) and 3,5-dimethylaniline (3,5-DMA) in addition to aniline. These species are structurally similar and displayed in Figure 4.1 alongside their UV vapour phase absorption spectra recorded at room temperature.

The potential of site-selective methylation is the ability to reveal additional dynamical information about molecular systems, while maintaining or just marginally changing the spectroscopic properties, such as small red-shifts of absorption bands. The advantages of this approach are used to obtain new insights into the relaxation

pathways and the interplay between the energetically lower lying excited states of aniline and its derivatives, since in the literature there has been no final consensus about the operating dynamical mechanisms in these molecules. Hereafter, a history of the photophysics in aniline and its derivatives will be presented. This mainly focuses on the literature of experimental and theoretical studies performed around 240 nm absorption wavelength, based on the relevance for the present study in this chapter.

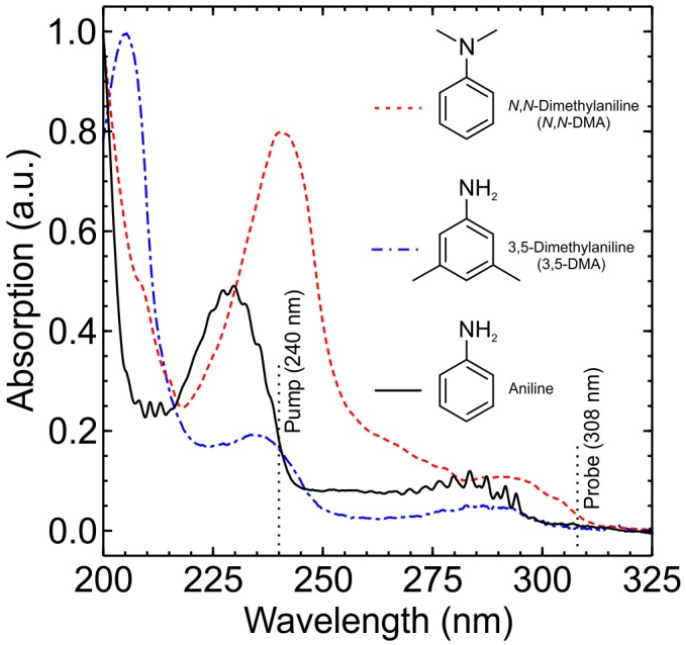

Figure 4.1: *UV vapour phase absorption spectra of N,N-dimethylaniline and 3,5-dimethylaniline was recorded with a commercial bench-top spectrophotometer (Shimadzu UV-2550) at room temperature. The chemical structures of both molecules and the equivalent absorption data for aniline is included for comparison. The pump and probe wavelengths of the TRPEI measurement presented in this chapter are indicated with vertical dashed lines. [2]*

Based on previous studies, the absorption spectrum and the contributing electronic states are well known in the energy region between 4 eV and 6 eV [111, 112, 113, 114]. Here the dominant two bands correspond to the excitations from the ground state to the first two optically bright $\pi\pi^*$ states. In aniline these bands are located at 4.35 eV (285 nm) and 5.39 eV (230 nm). In both N,N-DMA and 3,5-DMA the electronic states are a little lower in energy. Hence the excitation to the first $\pi\pi^*$ excited state in N,N-DMA is 4.25 eV (292 nm) and in 3,5-DMA it is 4.27 eV (290 nm). The absorption maximum of the second $\pi\pi^*$ state is 5.16 eV (240 nm) and 5.27 eV (235 nm) respectively [110].

In this energy region a low-lying $S_2(3s/\pi\sigma^*)$ state has also been observed utilising a (2 + 2) resonance enhanced multiphoton ionisation technique. This is energetically located between the two $\pi\pi^*$ states at around 4.6 eV [115]. The assignment of the 3s

Rydberg contribution to the S_2 state in aniline was also reported based on a quantum defect δ calculation. In general, quantum defect numbers for 3s Rydberg states lie between the values 0.9 and 1.2, based on theoretical calculations. The value for this particular S_2 excited state was calculated to be $\delta = 0.912$, which confirms the 3s Rydberg contribution to the overall excited state [115, 116]. Furthermore, the existence of 3s Rydberg states in aniline and derivatives have been also reported in a similar energy region [117, 118, 119].

Theoretical studies of $\pi\sigma^*$ states in similar molecular systems, such as phenol, performed by Sobolewski and Domcke describe an intramolecular charge transfer pathway via the intersection between the $\pi\sigma^*$ state with a energetically bound $\pi\pi^*$ state at relatively short X-H distances and a second intersection at longer X-H distances of $\pi\sigma^*$ with the electronic ground state S_0 [120]. Based on these findings, Ebata *et al.* proposed a strong coupling between $S_2(3s/\pi\sigma^*)$ and $S_1(\pi\pi^*)$ [115].

The critical reaction coordinates in aniline for the overall relaxation process after UV absorption have been indicated in the literature to be the stretching motion along the N-H coordinate and the aromatic ring structure deformation [102, 104, 121]. In N,N-DMA and 3,5-DMA, just as in aniline, the first two energetically excited electronic singlet states can be attributed to $S_1(\pi\pi^*)$ and $S_2(3s/\pi\sigma^*)$ based on previous work [110].

Instead of just $\pi\sigma^*$, the more correct label $3s/\pi\sigma^*$ is used throughout this work to illustrate the the mixed Rydberg/valence character of the overall S_2 excited state. In the Franck-Condon region S_2 predominantly consists of 3s Rydberg character, whereas at extended N-H bond distances (or N-CH_3 in N,N-DMA) the nature of the state evolves into a repulsive $\pi\sigma^*$ valence character.

After single photon absorption with a wavelength of 250 nm, only the two energetically lowest lying excited states are directly populated in the Franck-Condon region. A time resolved photoelectron imaging study on aniline, N,N-DMA and 3,5-DMA has been reported by Townsend and co-workers at this wavelength [110] and will be now summarised, since it is important for the experimental findings of this work.

After initial excitation with 250 nm, in aniline and N,N-DMA the population of $S_2(3s/\pi\sigma^*)$ decays rapidly via two different and competing pathways. On the one hand, ultrafast internal conversion to the $S_1(\pi\pi^*)$ excited state occurs in < 100 fs and/or on the other hand direct fission of the N-H stretching bond (in aniline) and N-CH_3 bond (in N,N-DMA) also takes place. In the 3,5-DMA molecule, however, no significant internal conversion to the $S_1(\pi\pi^*)$ excited state can be detected. The reason is the methylation of double bond ring system, which slows down the ring deformation motion and therefore increases the time scale of the molecule to reach the conical intersection between $S_2(3s/\pi\sigma^*)$ and $S_1(\pi\pi^*)$. This is why the significant relaxation pathway in 3,5-DMA following 250 nm excitation is N-H bond dissociation. In this study it was also ascertained that all three molecular systems possess

a very similar electronic energy states. In Figure 4.1 a pronounced absorption peak at 240 nm can be ascribed to the second $\pi\pi^*$ excited state. Since there have been several Rydberg states discovered sitting energetically below this second $\pi\pi^*$ state, it will be just designated $2\pi\pi^*$ in order to prevent confusion in the energy state ordering [110, 114]. No work has been done on the aniline derivatives to the best of our knowledge, other than the aforementioned TRPEI study [110], some UV-visible spectra work on N,N-DMA [111, 122] and a theoretical investigation using CASSCF to calculate excited state energies [113]. The photophysical studies undertaken in aniline in general and specifically around the excitation of 240 nm will be summarised.

In a H (Rydberg) atom photofragment translational spectroscopic study Ashfold and co-workers explored H atom loss in aniline along the N-H stretching coordinate of the $S_2(3s/\pi\sigma^*)$ excited state after UV light absorption [102]. A variety of mechanisms responsible for H atom loss were studied over a range of excitation wavelengths 293.9 nm $\geq \lambda_{\text{phot}} \geq$ 193.3 nm. A stepwise decrease in the wavelength gave rise to a significant feature in the total kinetic energy release (TKER) spectra at 240 nm to 230 nm that is assigned to the direct excitation onset of the $2\pi\pi^*$ electronic state. The following non-adiabatic mechanisms were proposed to explain high kinetic energy H atom yields. On the one hand, relaxation dynamics via a $2\pi\pi^*/S_2(3s/\pi\sigma^*)$ conical intersection might occur or, on the other hand, a subsequent non-adiabatic decay through $2\pi\pi^*/S_1(\pi\pi^*)$ and $S_1(\pi\pi^*)/S_2(3s/\pi\sigma^*)$ CIs is the suggested mechanism. Furthermore, the conical intersection between $2\pi\pi^*$ and the S_0 electronic ground state was the explanation for the lower energy TKER data, where this CI is acting as a competing decay pathway for population loss from $2\pi\pi^*$ potential energy surface.

Longarte and co-workers investigated ultrafast relaxation dynamics in jet-cooled aniline with a time-resolved ion-yield study in the wavelength region between 294 nm to 234 nm [109]. The population of the $2\pi\pi^*$ electronic state was observed at around 240 - 235 nm following similar decay pathways to the ones suggested by Ashfold and co-workers. This work also concluded that the population transfer from the $2\pi\pi^*$ potential energy surface to $S_2(3s/\pi\sigma^*)$ seems to be a minor channel.

An ultrafast time-resolved velocity map imaging study of UV photoexcited aniline detecting total kinetic energy release H-atoms undertaken by Stavros and co-workers likewise confirms the direct excitation from the electronic ground state to the $2\pi\pi^*$ state at 240 nm [121]. Based on the detection of ultrafast N-H bond fission the study concluded internal conversion from the $2\pi\pi^*$ potential energy surface to $S_1(\pi\pi^*)$ takes place via an out of plane motion and a subsequent population transfer to the $S_2(3s/\pi\sigma^*)$ state, which is dissociative along the N-H coordinate.

In the energy region close to 240 nm, a comprehensive time-resolved photoelectron imaging investigation of aniline has been done by Fielding and co-workers. The

initial work found a dominant and very efficient non-radiative decay pathway where energy relaxes from the originally excited $2\pi\pi^*$ electronic state on a time scale of 116 fs back to the S_0 ground state. No coupling of $2\pi\pi^*$ to either $S_2(3s/\pi\sigma^*)$ or $S_1(\pi\pi^*)$ was observed [106, 123]. However, in a later experimental [103] study they suggest (based on extensive theoretical work [104]) a non-adiabatic population transfer from the directly excited $2\pi\pi^*$ state in the Franck-Condon region to the S_0 electronic ground state via a three-state conical intersection including $2\pi\pi^*$, $S_2(3s/\pi\sigma^*)$ and $S_1(\pi\pi^*)$. Interestingly, in deuterated d7-aniline the conclusion of the non-radiative decay pathway of the $2\pi\pi^*$ excited state remained to be the ultrafast coupling with the electronic ground state via the $2\pi\pi^*/S_0$ conical intersection.
The TRPEI studies presented in this chapter, which are supported by theoretical calculations, bring new information about the non-adiabatic dynamics operating in the aniline derivatives, especially about the role of the $2\pi\pi^*$ electronic excited state in the overall relaxation. Since aniline has been investigated extensively at 240 nm, this work is concentrating on the double methylated systems N,N-dimethylaniline and 3,5-dimethylaniline, which are specifically chosen to manipulate the critical reaction coordinates involving N-X bond streching (X = H or CH_3) and deformation of the aromatic ring system (see Figure 4.2), while maintaining the other physical properties [102, 121]. In order to circumvent any proximity or symmetry effects changing the NH_2 group geometry according to the aromatic ring system 3,5-DMA is chosen for the current study.

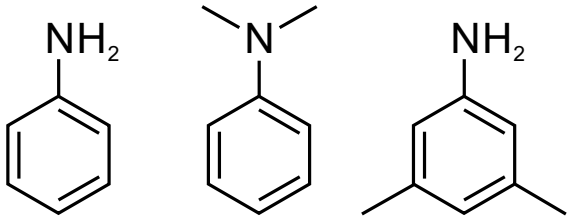

Figure 4.2: *The chemical structures of aniline, N,N-dimethylaniline and 3,5-dimethylaniline.*

4.1.2 Experimental details

In Chapter 3 an extensive overview is given of all key elements used in the time-resolved photoelectron imaging technique. In this Section specific details of the aniline derivatives measurement are provided. The ultra short laser pulses generated by the 1 kHz Ti:sapphire laser system with a central wavelength of 800 nm (FWHM = 30 nm) are frequency converted into UV pump and probe beams with two optical parametric amplifier systems (Spectra Physics, OPA-800c and TOPAS Prime-U).
The pump beam was generated with two consecutive nonlinear optical processes. Initial frequency mixing the fundamental 800 nm laser beam with the OPA signal

beam generates 480 nm and subsequent frequency doubling results in a final pump pulse of 240 nm with a pulse energy of ~ 0.5 μJ. A sequential twice frequency doubling process of the TOPAS signal beam output is generating the 308 nm probe pulse with a pulse energy of ~ 1.6 μJ.

For the second harmonic generation, as well as the frequency mixing processes, thin β-barium borate (BBO) crystals were utilised as nonlinear media. After passing through two single-pass prism compressors (fused silica and CaF_2) the UV pump and probe pulses are combined on a dichroic mirror before being focused with a 25 cm fused silica lens into the main interaction vacuum chamber of the TRPEI spectrometer. As described in detail in Chapter 3, the temporal delay between the two UV pulses is realised with a PC-controlled, motorised linear translation stage. The probe wavelength of 308 nm is selected to guarantee no unwanted "probe-pump" signal towards negative time delays to occur.

The aniline derivative samples were purchased from Sigma-Aldrich (N,N-DMA - 99% and 3,5-DMA - 98%) and without further purification the liquid samples are soaked on filter paper and placed into the cartridge of the 1 kHz pulsed molecular beam valve, behind a exit nozzle ($d = 150$ μm). The carrier gas in this experiment was helium at 1 bar, that flows over and mixes with the molecular sample in the valve, the temperature of which was regulated to be 45 °C.

The gas molecule mix undergoes a supersonic expansion after entering the source chamber and subsequently passes through a 1.0 mm diameter skimmer into the main interaction chamber, where the two parallel propagation UV beams intersect at 90° with the molecular beam in the region between the repeller and lens electrodes. This electrostatic lens assembly is magnetically shielded by mu-metal and optimised for velocity map imaging (for further details please see Section 3.2.2). The photoelectrons are created by a $(1 + 1')$ resonant ionisation process, get accelerated along a time-of-flight tube and were spatially collected with a 40 mm MCP/P47 phosphor screen detector in combination with a CCD camera (640 × 480 pixels). The whole dataset of photoelectron images is recorded repeatedly at incrementally varied pump-probe delay positions covering -300 fs to +500 fs in 25 fs linear increasing time steps and +500 fs to +50 ps in 7 exponential steps. With every repetition a one-colour pump and a one-colour probe photoelectron image is detected in order to background subtract it from the two-colour images.

Before data collection the parameters such as the pulsed valve timing conditions are carefully chosen in ion detection mode to provide cluster free molecular samples. For optimally compressed laser pulses a cross correlation of 130 ± 10 fs was determined by measuring the non-resonant two-colour $(1 + 1')$ ionisation signal of pyrrole. The pyrrole data was also used to energy calibrate the spectrometer.

4.2 Experimental findings

4.2.1 Time-resolved photoelectron spectra

For both molecular systems, N,N-dimethylaniline and 3,5-dimethylaniline, a series of photoelectron images at selected delay times between the pump (240 nm) and probe (308 nm) pulses of the (1 + 1′) photoionisation process are displayed in Figure 4.3. The images, recorded at very short delay times for both molecules, contain a narrow and highly anisotropic outer ring feature, which peaks along the laser polarisation direction (vertical with respect to Figure 4.3). The outer signal is decaying on a fast time scale, where the inner part is longer lived.

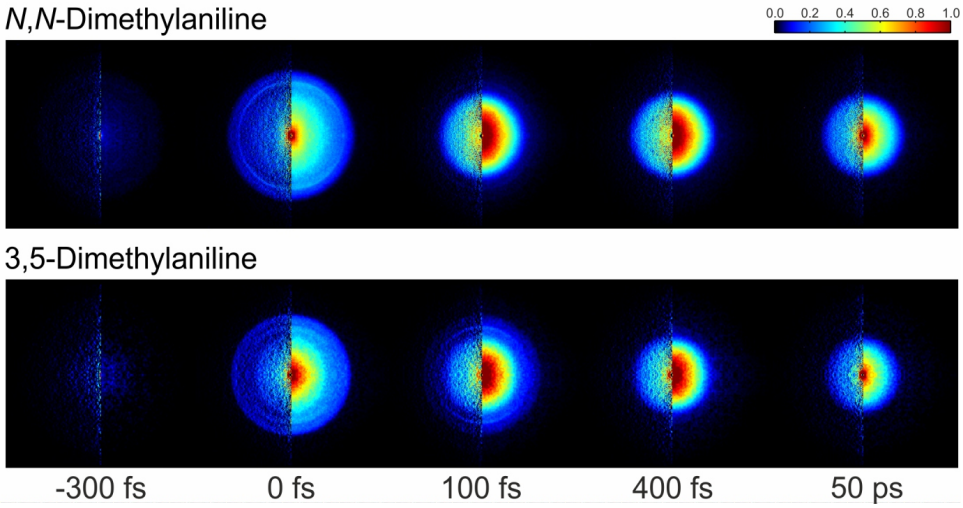

Figure 4.3: *Here the (1 + 1′) photoelectron images of N,N-DMA and 3,5-DMA are shown at selected pump-probe time delays following 240 nm excitation and 308 nm ionisation. The data has been background subtracted by time-invariant pump-alone and probe-alone images and 4-fold symmetrised. Both laser beams have got a vertical polarisation direction with respect to the images. Furthermore the processed data is displayed on the left half of the images, which was gained by applying the Abel matrix inversion.*

After data processing of the complete sets of recorded images (correct energy calibration, pixel weighting and the rapid Abel matrix inversion method) the 3D time-resolved photoelectron spectra are obtained and plotted in Figure 4.4. In Section 3.3 the processing of results is described in more detail. In Figure 4.4 the time axis is (as mentioned in the previous section) on a mixed linear/logarithmic scaling. The comparison of both TRPEI spectra reveals a common long-lived feature that is located in the low kinetic energy region up to $\sim$ 0.8 eV. Furthermore, the data for both N,N-dimethylaniline and 3,5-dimethylaniline look at first very similar, thus there are also additional extremely short lived features in the higher kinetic energy region, although the relative peak intensities vary between the two molecules. The total appearance of the spectra are comparable to the previously recorded data following 250 nm excitation [110], however the shape of the high kinetic energy peaks

differs marginally in shape. This can be explained due to the direct excitation to the $2\pi\pi^*$ state. A detailed discussion will follow later on in this chapter.

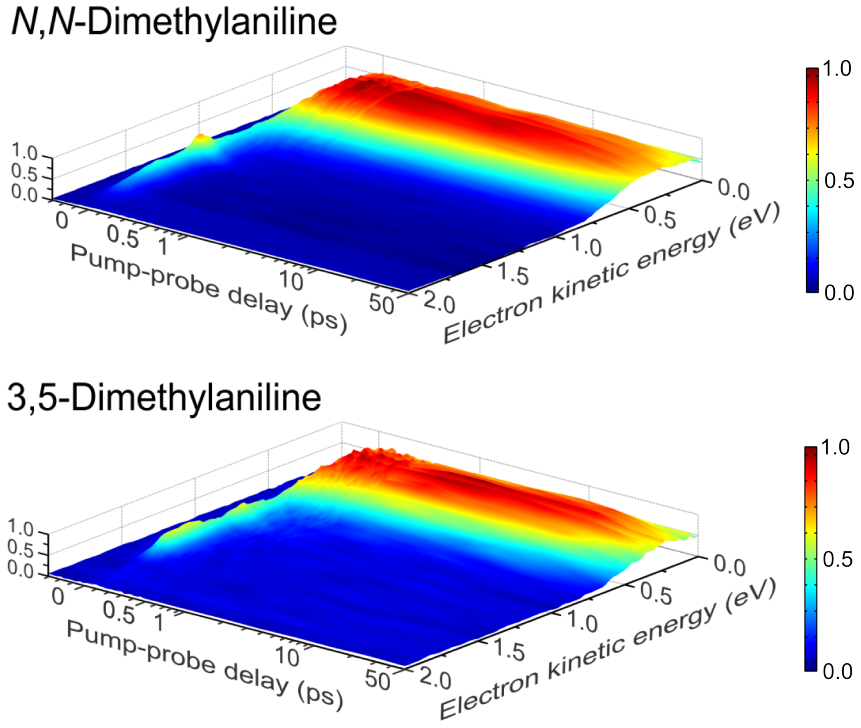

Figure 4.4: *Time-dependent photoelectron spectra of N,N-DMA and 3,5-DMA with a 240 nm excitation and a 308 nm ionisation. The temporal axis is linear until +500 fs and logarithmic between +500 fs and +50 ps and the energy axis is partitioned in 0.025 eV energy bins.*

The total photon energy E_{tot} in this TRPEI measurement of aniline derivatives is a summation of the pump energy $E_{pump} = 5.17$ eV ($\widehat{=}$ 240 nm) and probe energy $E_{probe} = 4.02$ eV ($\widehat{=}$ 308 nm) and is calculated to be $E_{tot} = 9.19$ eV. On the basis of the energy conservation principle the maximum kinetic energy E_{kin,e^-} an electron can gain after the ionisation process is the total photon energy E_{tot} subtracted from the ionisation potential IP of the molecule. The adiabatic $D_0(\pi^{-1})$ ionisation potentials of N,N-DMA and 3,5-DMA are 7.12 eV [124] and ~7.2 eV [125] respectively. These IPs are determined by band edges of low-resolution He (I) photoelectron spectra, therefore they were revised with a high resolution laser based measurement obtained from a 8 resonance-enhanced multiphoton ionization (REMPI) spectra. The new averaged adiabatic $D_0(\pi^{-1})$ IPs are 7.26 ± 0.05 eV for N,N-DMA and 7.48 ± 0.05 eV for 3,5-DMA [110]. Using Equation 4.1

$$E_{kin,e^-} = (E_{pump} + E_{probe}) - IP_{ad} \tag{4.1}$$

the maximum photoelectron kinetic energy cutoff can be calculated to be 1.93 eV (N,N-DMA) and 1.71 eV (3,5-DMA). These calculated values are in good agreement with the TRPEI measurement for both molecules in Figure 4.4. The time-resolved photoelectron spectra of both molecular systems are fitted with the global

Levenberg-Marquardt method in order to determine the temporal evolution of the participating excited states. In Equation 4.2 the 2D fit function $S(E, \Delta t)$ is shown:

$$S(E, \Delta t) = \left[\sum_{i=1}^{4} A_i(E) \cdot P_i(\Delta t) \right] \otimes g(\Delta t) \tag{4.2}$$

Here $A_i(E)$ represents the decay associated photoelectron spectrum of the i^{th} data channel, $g(\Delta t)$ represents the Gaussian cross-correlation function of the pump and probe pulses. The time dependant population, $P_i(\Delta t)$, is given by a series of exponential decay functions, which all originate from $\Delta t = 0$:

$$P_i(\Delta t) = \exp\left(-\frac{\Delta t}{\tau_i}\right) \tag{4.3}$$

Figure 4.5 shows examples the data from 3,5-DMA with the associated 2D global fit and the residuals, that are obtained by subtracting the fit from the raw data.

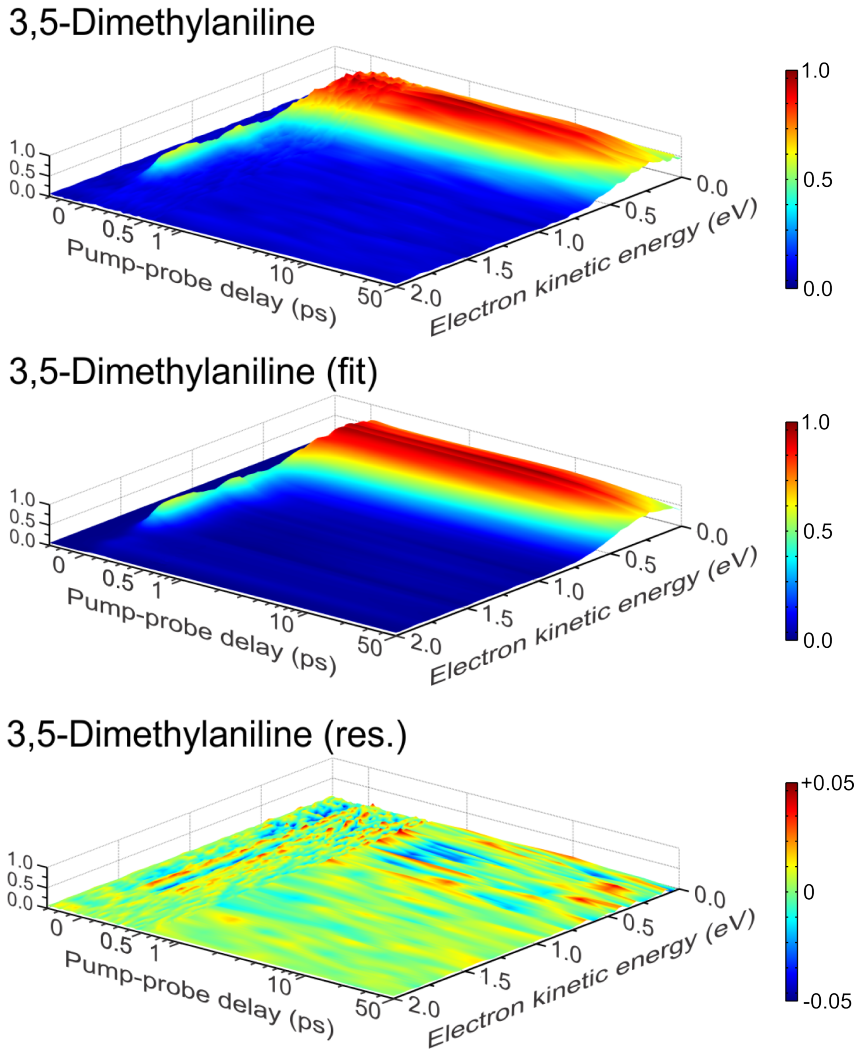

Figure 4.5: *The time-dependent photoelectron spectra of 3,5-DMA (after 240 nm excitation and 308 nm ionisation) as well as the fit of the 3,5-DMA data set with the related residuals are plotted in the same way as above. The fit is in very good agreement with the 3,5-DMA data on the basis of the small amplitude residuals.*

Here the good quality of the fit and the excellent agreement with the data can be seen, as illustrated by the smooth surface of the residuals. In order to fit the TRPEI data of N,N-DMA and 3,5-DMA satisfactorily, four exponential decay functions τ_1 - τ_4 are required in both cases. Here it is worth mentioning that a total number of just three exponents were needed to properly fit the TRPEI data at a excitation wavelength of 250 nm [110].

The global Levenberg-Marquardt fit provides relative amplitudes of each i^{th} exponential decay as a function of photoelectron kinetic energy. The so-called decay associated spectra (DAS) for both molecules are shown in Figure 4.6. Fielding and co-workers also reported four time constants for aniline at similar excitation wavelengths that are comparable to the experimental findings reported here [103, 106, 107].

In Figure 4.6, at high photoelectron kinetic energies > 0.8 eV the spectrum is dominated by the DAS amplitudes of τ_1 and τ_2.

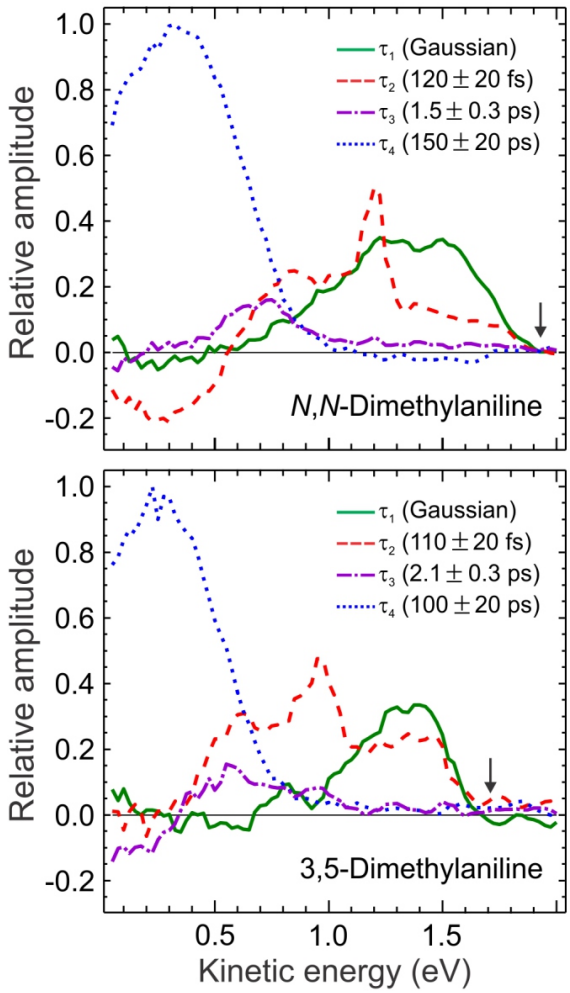

Figure 4.6: *Decay associated spectra for both molecules obtained from the global multi-exponential fit. Uncertainties are given with 1σ and the data are partitioned into 0.025 eV energy bins.The vertical arrows indicate the maximum photoelectron kinetic energy cut-offs based on the central pump and probe wavelengths and the adiabatic IPs = 7.26 eV for N,N-DMA and 7.48 eV for 3,5-DMA.*

In both molecular systems the τ_1 lifetime is extremely short, being essentially zero within the experimental instrument response and resulting in a Gaussian fit component. The second time constant τ_2 is slightly longer with 120 fs for N,N-DMA and 110 fs for 3,5-DMA and displays itself with a mixed amplitude feature in both cases. A narrow, large τ_2 DAS amplitude at 1.2 eV and 0.95 eV for N,N-DMA and 3,5-DMA respectively is superimposed with a broader smaller amplitude spanning a larger energy region.

The lower kinetic energy region of both molecular systems in Figure 4.6 has got just three significant contributions, which are the τ_{2-4} DAS amplitudes. In the N,N-DMA molecule the τ_2 time constant shows negative amplitude between 0.0 eV - 0.5 eV, whereas in 3,5-DMA there is no negative contribution of τ_2 throughout the whole spectrum. In general the spectrum of the τ_{2-4} time constants for N,N-DMA and 3,5-DMA obtained from 240 nm excitation is very similar to the τ_{1-3} DAS plots of both molecules after 250 nm excitation [110] shown in Figure 4.7.

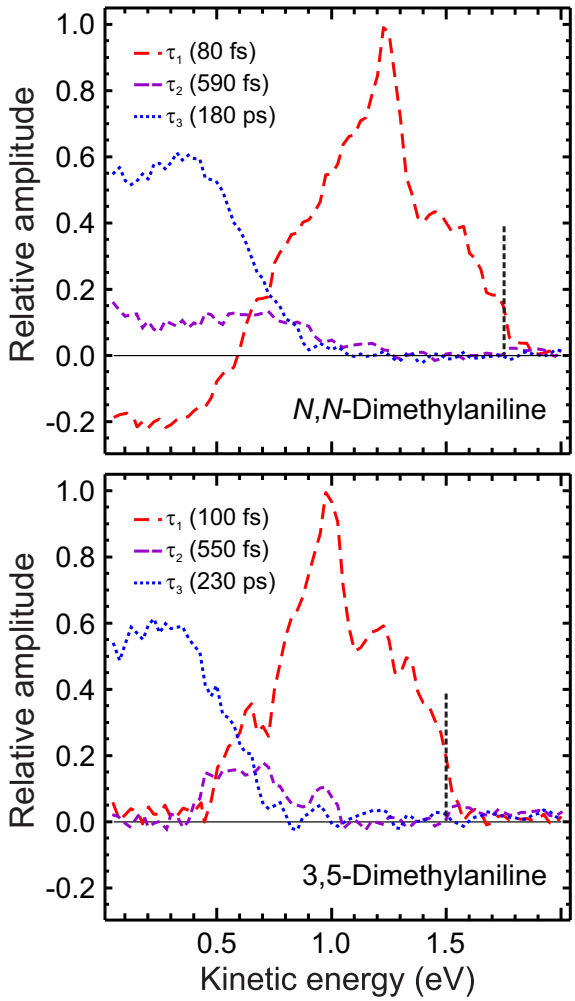

Figure 4.7: *The graph shows the decay associated spectra for N,N-DMA and 3,5-DMA obtained from a global fit to both data sets with a excitation wavelength of 250 nm presented in the literature [110]. Data is partitioned into 0.025 eV energy bins. The τ_{1-3} time constants correspond to the τ_{2-4} constants in the 240 nm excitation data.*

The comparison of Figure 4.6 and Figure 4.7 allows assignment of the τ_{2-4} DAS amplitudes in Figure 4.6 according to the previous data of 250 nm excitation. As such the τ_2 time constant is the decay of the mixed Rydberg/valence $S_2(3s/\pi\sigma^*)$ state, τ_3 describes the intramolecular vibrational redistribution (IVR) on the $S_1(\pi\pi^*)$ energy surface and lastly τ_4 describes the long decay lifetime of the $S_1(\pi\pi^*)$ valence state. The difference in the 240 nm excitation data of N,N-DMA and 3,5-DMA is the additional time constant τ_1, that appears as a Gaussian in the fit. This τ_1 DAS contribution happens to have no significant interaction with the other observed dynamical processes represented by the τ_{2-4} time constants. Thus τ_1 can be assigned to the extremely fast decay of the $2\pi\pi^*$ state, which is populated in both molecular systems due to the 240 nm pump wavelength. An in-depth discussion will be presented in Section 4.4 later in this chapter.
As described above, the total provided photon energy E_{tot} is 9.19 eV ($E_{pump}+E_{probe}$). As a consequence the $D_1(\pi^{-1})$ cation state of N,N-DMA and 3,5-DMA with $D_1(\pi^{-1})$ vertical ionisation energies of 9.00 eV and 8.55 eV respectively, can be in principle reached and observed in the TRPEI data. However, the population of the $S_2(3s/\pi\sigma^*)$ and $S_1(\pi\pi^*)$ excited states after 240 nm excitation is well above their energetic origins, so based on Franck-Condon arguments on vibrational overlap between the excited state and the ion state the conclusion is a lower propensity for $D_1(\pi^{-1})$ ionisation using a 308 nm probe wavelength. From the point of view of total provided photon energy, one could expect to detect the $D_1(\pi^{-1})$ ionisation signal originating from the excited $2\pi\pi^*$ state, which is prepared close to its electronic origin. The fact that neither in the N,N-DMA data and nor in the 3,5-DMA data a positive τ_1 DAS amplitude is recorded in the low photoelectron kinetic energy region leads to the conclusion that the $D_1(\pi^{-1})$ ion state possesses a different geometry than the ion ground state $D_0(\pi^{-1})$, because the Franck-Condon factors of the excited $2\pi\pi^*$ state and the $D_1(\pi^{-1})$ ion state must be quite different from each other.

4.2.2 Photoelecton angular distribution

The dynamical behaviour of the photoelectron angular distributions (PADs) in the recorded TRPEI data of both molecules individually provides further important information about the temporal evolution of the electronic states. As described in detail in the literature [51, 126] the time-resolved evolution of the PAD following a (1 + 1′) ionisation process using parallel linear polarised laser pulses can be described by a function of the photoelectron kinetic energy E, the pump-probe delay time Δt and the angle θ between the laboratory frame z axis and the ejection direction of the photoelectron.

The mathematical description of the PAD intensity is given by Equation 4.4, where $\sigma(E, \Delta t)$ is the time-dependent photoelectron energy distribution, $P_n(cos\theta)$ are the terms of the n^{th}-order Legendre polynomials and β_2 and β_4 are the well-known anisotropy parameters.

$$I(E, \Delta t, \theta) = \frac{\sigma(E, \Delta t)}{4\pi} [1 + \beta_2(E, \Delta t)P_2(cos\theta) + \beta_4(E, \Delta t)P_4(cos\theta)] \tag{4.4}$$

In Figure 4.3 a vertical line going completely through the images via their central points defines the angle $\theta = 180°$. The time-resolved results of the performed fit of the TRPEI data using Equation 4.4 are shown in Figure 4.8.

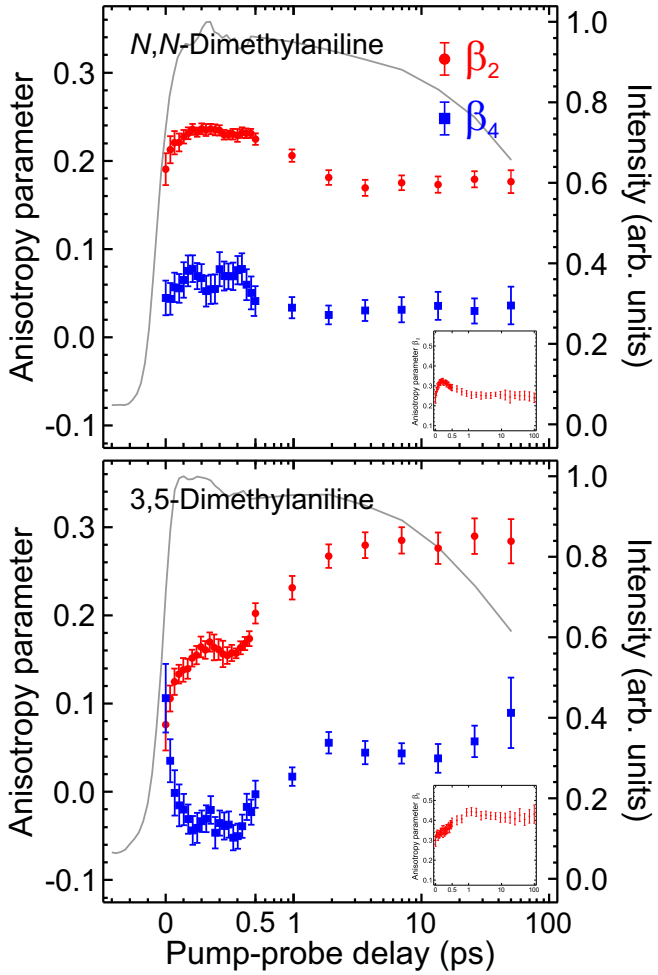

Figure 4.8: *Anisotropy parameters β_2 and β_4 are shown as a function of pump-probe delay Δt averaged over the 0.05 - 0.70 eV photoelectron kinetic energies region following 240 nm excitation/308 nm ionization of N,N-DMA and 3,5-DMA. The time scale is linear up to + 500 fs and logarithmic from + 500 fs onwards. The anisotropy fit was performed to the non-averaged TRPEI data, that is partitioned into 0.025 eV energy bins. The error bars are one standard deviation. The small inserted plots, taken from literature [110], show the dynamical behaviour of β_2 data following 250 nm excitation and are displayed for comparison purposes. The grey line is the time-resolved signal intensity over the same energy region of the spectrum.*

The transients of β_2 and β_4 for both molecular systems show a clear time-dependent variation and are obtained by averaging over the low photoelectron kinetic energy region between 0.05 - 0.70 eV, where the long lived ($\geq$ 100 ps) TRPEI signals are detected. It is valid to average the PAD transients, because for both molecules the temporal behaviour of both β_2 and β_4 parameters is consistent within this selected energy region. Thus the reason for averaging the data is to improve the statistics in the displayed PADs.

In Figure 4.8 the anisotropy parameter β_2 shows a clear and fast rise in both molecules at very short times. In N,N-DMA the rise time is $\sim$ 100 fs, which is somewhat faster than $\sim$ 250 fs in 3,5-DMA. The dynamical evolution of β_2 is different in both molecular systems from that time point onwards. The β_2 parameter of N,N-DMA exhibits a plateau after the initial rise and subsequently shows a small decrease after $\sim$ 1 ps. In 3,5-DMA on the other hand, β_2 shows a second increase on a longer time scale, reaching a maximum value after 2 ps resulting in a plateau that remains for $>$ 50 ps.

The temporal evolution of the anisotropy parameter β_4 of both systems is also plotted in Figure 4.8. In N,N-DMA the behaviour of β_4 matches that seen for β_2 with the only small difference being that the first plateau of β_2 appears to be resolved into two separate peaks in the same time frame. In 3,5-DMA an initial fall is recorded on a time scale of $\sim$ 200 fs (similar time scale as the rise of β_2 in the same molecule). The further temporal evolution of β_4 in 3,5-DMA matches the dynamical behaviour of β_2.

Figure 4.9 displays the β_2 parameter following excitation of 250 nm allowing the direct relation to the dynamics of β_2 in the current 240 nm excitation data [110].

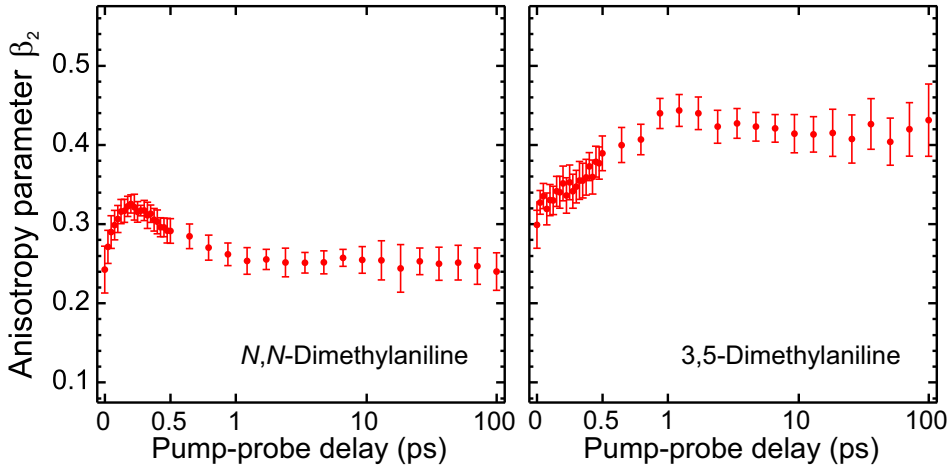

Figure 4.9: *Anisotropy parameters β_2 are plotted as a function of pumpprobe delay Δt averaged over the 0.05 - 0.80 eV (N,N-DMA) and 0.05 - 0.65 eV (3,5-DMA) photoelectron kinetic energies region following 250 nm excitation. The time scale is linear up to + 500 fs and logarithmic from + 500 fs onwards. The data is partitioned into 0.025 eV energy bins. The error bars are one standard deviation. Taken from [110]*

The comparison of both β_2 transients, in Figure 4.8 and 4.9 reveals that both in N,N-DMA and in 3,5-DMA there is an additional feature superimposed over the time dependent curve of the longer excitation wavelength 250 nm. As was the case with the DAS data of both molecules, the additional temporal component in the PADs is assigned to the dynamical process related to the $2\pi\pi^*$ excited state.
It is also worth mentioning that the photoelectron signals at higher kinetic energies (< 0.8 eV) in both molecules exhibit a extremely short life time and as a result no reliable information about their temporal evolution can be extracted.
The photoelectron angular distribution is also dependent on the kinetic energy E and consequently the β_2 and β_4 parameters are plotted as a function of the photoelectron energy E in a region at a pump-probe time delay of $\Delta t = 0$ in Figure 4.10. The grey solid line in the background displays the respective photoelectron spectrum averaged over the time scale Δt close to zero.

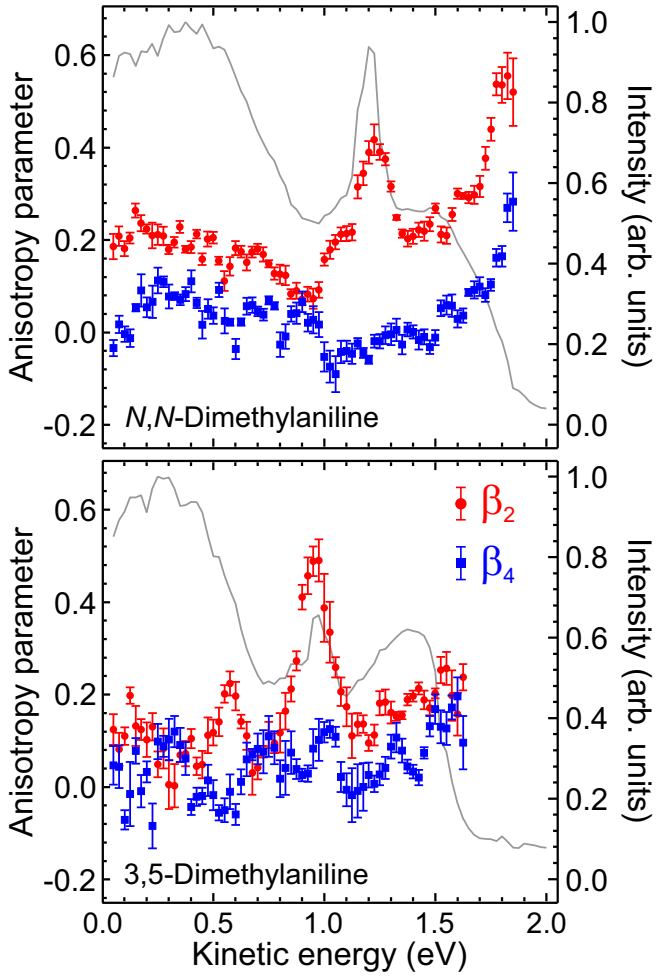

Figure 4.10: *Anisotropy parameters β_2 and β_4 are shown as a function of photoelectron kinetic energy at zero pump-probe delay (data points) following 240 nm excitation/308 nm ionization of N,N-DMA and 3,5-DMA. The PADs are superimposed over the corresponding photoelectron spectrum (grey line). The time scale is linear up to + 500 fs and logarithmic from + 500 fs onwards. The error bars are one standard deviation.*

In N,N-DMA as well as in 3,5-DMA the photoelectron spectra contain a clear sharp peak, at 1.2 eV and 0.95 eV, respectively. This distinct feature is also observed in the τ_2 decay associated spectra of both molecules at the same kinetic energies shown in Figure 4.6. The anisotropy parameter β_2 displays a comparatively high value and simultaneously a small β_4 value is observed in the aforementioned energy region for both molecules. These characteristics are strong evidence of the 3s Rydberg contributon in the mixed $S_2(3s/\pi\sigma^*)$ Rydberg/valence excited state and will be discussed in more detail later in Section 4.4.

The energy dependant PAD data of N,N-DMA also reveals a rapid and distinct increase in both anisotropy parameters β_2 and β_4 in the kinetic energy region close to 1.7 eV. This is possibly a signature of an ionisation signal from a higher lying Rydberg state, which is probably a excited state with a 3p Rydberg component, as seen in the theory later in this chapter. The corresponding photoelectron spectrum (grey line) indicates no apparent strong signature of a Rydberg state implying no significant population to this excited electronic state. An other explanation for the missing signature could be a very small ionisation cross of this state. The fact that the PAD is detecting the presence of the state shows the great advantages of the powerful time-resolved photoelectron imaging technique.

It is known that the $2\pi\pi^*$ state possesses a relative diffuse character and is energetically located above multiple electronically excited Rydberg states, which have been investigated formerly [110, 114]. The electronic population of the $2\pi\pi^*$ excited state is more dominant than of the $S_1(\pi\pi^*)$ state based on the bigger oscillator strength associated with $2\pi\pi^*$. This is in good agreement with the absorption spectra shown in Figure 4.1 at the beginning of this chapter.

4.3 Theoretical framework

The equation of motion (EOM) coupled cluster theory with single and double substitutions in conjunction with an aug-cc-pVDZ basis set was utilised to calculate potential energy surface cuts along the N-CH_3 and the N-H stretching coordinate for N,N-DMA and 3,5-DMA respectively.

The calculations along these coordinates were chosen specifically due to the key importance in the overall non-adiabatic dynamics driven by those coordinates [102, 121, 127].

A B3LYP optimisation with a aug-cc-pVTZ basis set in the C_s symmetry was used to calculate the equilibrium S_0 geometries and the vertical oscillator strengths are calculated with fully relaxed linear response transition densities. The Gaussian 09 program was used throughout in all calculations [128].

All calculated results including the vertical excitation energies and the oscillator strengths are displayed in Table 4.1 and are in very good agreement with the theoretical calculated results of these quantities shown in literature [110].

Table 4.1: *EOM-CCSD/aug-cc-pVDZ vertical excitation energies (ΔE) and oscillator strengths (f) obtained for N,N-DMA and 3,5-DMA, along with corresponding state assignments. The p manifold is heavily mixed with orbitals directed away from the x, y and z molecular axes. As such, no specific assignments are given.*

		ΔE [eV] (CCSD) [a]	f (CCSD)
N,N-Dimethylaniline			
^{1}A′	S_0 [b]	0	-
1 ^{1}A′	$S_2(3s/\pi\sigma^*)$	4.55	0.0231
1 ^{1}A″	$S_1(\pi\pi^*)$	4.59	0.0406
2 ^{1}A′	3p	5.14	0.0007
2 ^{1}A″	3s	5.17	0.0145
3 ^{1}A′	3p	5.41	0.0119
4 ^{1}A′	$2\pi\pi^*$	5.49	0.2441
3,5-Dimethylaniline			
^{1}A′	S_0 [b]	0	-
1 ^{1}A′	$S_1(\pi\pi^*)$	4.68	0.0247
1 ^{1}A″	$S_2(3s/\pi\sigma^*)$	4.80	0.0034
2 ^{1}A′	3s	5.49	0.0089
2 ^{1}A″	3p	5.55	0.0004
3 ^{1}A′	$2\pi\pi^*$	5.65	0.1135
4 ^{1}A′	3p	5.92	0.0037

[a] Aug-cc-pVDZ basis set for response properties
[b] S_0 geometries from B3LYP/aug-cc-pVTZ optimisation in C_s symmetry

In Figure 4.11 potential energy cuts are shown for the S_0 ground state and multiple electronic excited singlet states. As can be clearly seen in both molecular systems, all electronic states are bound along the bond stretching coordinate apart from the special case of $S_2(3s/\pi\sigma^*)$. The potential energy curve of this electronically excited state comprises a small energetic potential barrier before it develops a dissociative asymptotic character. As a consequence the direct N-CH_3/N-H bond fission along this dissociative coordinate is possible in both molecules upon 240 nm excitation.

A conical intersection between the mixed $S_2(3s/\pi\sigma^*)$ Rydberg/valence state and the electronic S_0 ground state is also expected and has been shown by the different computational complete active space self-consistent field (CASSCF) method, referring to the very similar molecular system aniline [121].

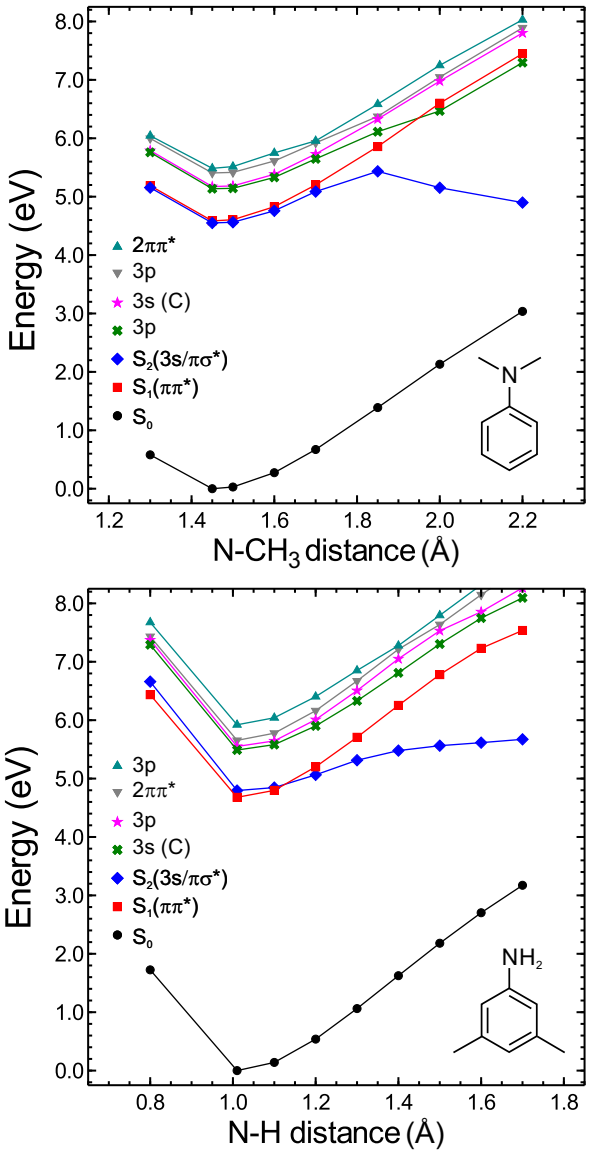

Figure 4.11: *Calculated potential energy cuts of the S_0 ground state and several low-lying electronically excited singlet states along the NH stretching coordinate in 3,5-DMA and the N-CH_3 stretching coordinate in N,N-DMA using EOM-CCSD/aug-cc-pVDZ. The p manifold is heavily mixed with orbitals directed away from the x, y and z molecular axes. As such, no specific assignments are given.*

4.4 Discussion

The results of the decay associated spectra and the photoelectron angular distribution presented in Section 4.2 were obtained from TRPEI data recorded at a excitation wavelength of 240 nm. In N,N-dimethylaniline as well as 3,5-dimethylaniline the dynamical behaviour is composed of two components. Firstly, the relaxation pathways of $S_2(3s/\pi\sigma^*)$ and $S_1(\pi\pi^*)$ (already active at 250 nm excitation) and secondly an additional dynamical feature, which is ascribed to the energetic onset of 240 nm excitation to $2\pi\pi^*$ and its temporal evolution. This is strongly supported by the DAS data, where the spectral characteristics of the τ_{2-4} time constants show remarkable similarities for both excitation wavelengths 240 nm and 250 nm in N,N-DMA and 3,5-DMA. Moreover, the PADs provide additional evidence, since after 240 nm excitation the temporal development of the β_2 anisotropy parameter shows a superposition of the characteristics observed at 250 nm and a new dynamical feature. As a result, firstly the temporal evolution of the first two electronically excited states $S_2(3s/\pi\sigma^*)$ and $S_1(\pi\pi^*)$ will be explained and secondly the role of the energetically higher lying $2\pi\pi^*$ state and its non-adiabatic dynamics will be discussed.

4.4.1 Dynamics of the first two electronic excited states

The DAS time constants τ_2, τ_3 and τ_4 shown in Figure 4.6 of both molecular systems can be attributed to specific electronic states and their dynamical behaviour is based on the comparison with the DAS time constants τ_{1-3} from an earlier TRPEI study at 250 nm, as displayed in Figure 4.7 [110]. In the first instance, all three decay constants exhibit the same spectral and temporal behaviour and absolute energetic peak positions, both for the molecular systems under study and the different excitation wavelengths. This being the case, the τ_3 and τ_4 spectra can be interpreted as direct ionisation from the $S_1(\pi\pi^*)$ state, since the two time constants and their spectral shapes are remarkably similar at both excitation wavelengths 240 nm and 250 nm. In N,N-DMA and 3,5-DMA, the τ_3 DAS is representing a subsequent ultrafast intramolecular vibrational redistribution (IVR) on the time scale of 1.5 ± 0.3 ps and 2.1 ± 0.3 ps, respectively. Ultrafast IVR was previously observed in $S_1(\pi\pi^*)$ of chlorobenzene as well as in S_0 of benzene and difluorobenzene and plays a role in excited electronic states with excitation clearly above the state origin, as it is the case for $S_1(\pi\pi^*)$ [110, 129, 130]. The τ_4 DAS describes the overall decay of $S_1(\pi\pi^*)$ with 150 ± 20 ps in N,N-DMA and 100 ± 20 ps in 3,5-DMA. The final fate of the $S_1(\pi\pi^*)$ excited state can not be determined within the scope of this experiment, but due to previous work several options are feasible including intersystem crossing to energetically lower lying triplet states [131], fluorescence [132] or population transfer back to the electronic ground state S_0 [104, 121].

The τ_2 DAS shown in Figure 4.6 describes the temporal decay of the $S_2(3s/\pi\sigma^*)$ excited state, with an observed decay time of 120 ± 20 fs in N,N-DMA and 110 ± 20 fs in 3,5-DMA. In both molecules the τ_2 DAS exhibits specific characteristics at photoelectron kinetic energies > 0.8 eV such as a superposition of a narrow spectral peak (at 1.2 eV in N,N-DMA and 0.95 eV in 3,5-DMA) on a broader spectral background of lower amplitude. The same behaviour has been observed previously in these systems at the excitation wavelength of 250 nm. This narrow and sharp peak is linked with a relatively high anisotropy parameter β_2 and simultaneously a low β_4 value, as depicted in Figure 4.10. The broader feature, on the contrary, is associated with a low value for both anisotropy parameter β_2 and β_4.
Theoretical calculations support the view of an S_2 excited state with 3s Rydberg character in the vertical Franck-Condon region and $\pi\sigma^*$ valence character at longer N-X bond distances in both molecular systems (in N,N-DMA X = H and in 3,5-DMA X = CH_3). Figure 4.12 shows the excited-state second-moment of the electronic charge distribution $\Delta\langle r_{iso}^2\rangle$ in aniline as a function of N-H distance (left side) and in N,N-DMA dependent on N-CH_3 distance (right side) with respect to the ground state size and geometry.

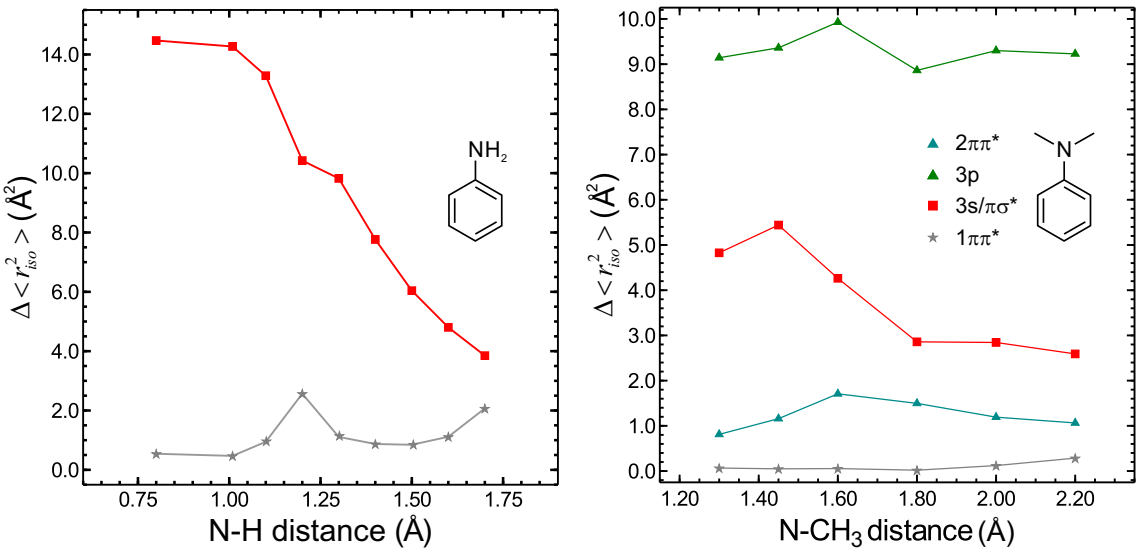

Figure 4.12: *Evolution of the excited-state second-moment of the electronic charge distribution $\Delta\langle r_{iso}^2\rangle$ with respect to the ground state S_0 as a function of N-H distance in aniline and N-CH_3 distance in N,N-DMA. Note that both plots are displaying slightly different ranges in $\Delta\langle r_{iso}^2\rangle$ and bond distances. The aniline data is taken from literature [110] and the N,N-DMA is from this present study [2].*

In their comprehensive review, Reisler and Krylov state that energetically low-lying Rydberg and valence states can be distinguished by $\Delta\langle r_{iso}^2\rangle$, which is the difference between the $\langle r_{iso}^2\rangle$ values for the excited states and the ground state [133]. $\Delta\langle r_{iso}^2\rangle$ provides a measure of the spatial extent of electronic density in the excited states with respect to the ground state and therefore allows the comparison of different

electronic states independent of the overall molecular size. Characteristic values of $\Delta \langle r_{iso}^2 \rangle$ for excited valence states, that contain n, π^* or σ^* are less than $1 Å^2$, since they are very similar to the ground state geometry. However, 3s and 3p Rydberg states exhibit values of $\Delta \langle r_{iso}^2 \rangle$ up to $12 Å^2$ [133].

In Figure 4.12 the decrease of $\Delta \langle r_{iso}^2 \rangle$ is displayed very clearly in aniline, where at short distances a pronounced Rydberg character is visible and upon N-H bond extension the valence character of that mixed excited state becomes more prominent. The right hand side of Figure 4.12 shows the same trend in N,N-DMA although the decrease is not as distinctive. Overall this evolution takes place on an extremely short time scale, which can be not temporally resolved within this TRPEI study. In a spectrally averaged manner, however, it is most certainly possible to see this evolution of the S_2 excited state character with the current TRPEI setup. The 3s Rydberg element within the mixed excited state is responsible for the narrow and sharp peak at 1.2 eV and 0.95 eV for N,N-DMA and 3,5-DMA, respectively, in the DAS (see Figure 4.6). This arises from the strong tendency for diagonal ionisation. In addition to this the s-orbital character exhibits a high β_2 parameter due to the well-defined orbital angular momentum and a low β_4 value based on the lack of inherent alignment of a mostly s-orbital feature (see Figure 4.10).

At more extended bond distances, the $\pi\sigma^*$ valence character of the S_2 excited state dominates, which is based on the decrease of diagonal ionisation propensity resulting in a broader and lower amplitude feature of the τ_2 DAS. Likewise the anisotropy parameter β_2 is reduced in the energy dependant PAD as a consequence of the less well defined orbital angular momentum. This can be seen in the higher photoelectron kinetic energy region of the DAS and the PAD at > 0.8 eV.

Hereafter the features of both molecules in the lower kinetic energy region < 0.8 eV will be discussed. The decay associated spectra in the lower energy region are very similar apart from one prominent difference in the τ_2 DAS. In N,N-DMA it reveals a negative amplitude until 0.55 eV, while the amplitude for 3,5-DMA in that energy region is zero. All exponential decay functions, described in Equation 4.3 and used to globally fit the TRPEI data using Equation 4.2, originate from pump-probe delay $\Delta\ t = 0$. As a consequence, the negative amplitude in the τ_2 DAS in N,N-DMA is persuasive evidence for a sequential dynamical process between two electronic states.

Mathematically this can be interpreted as a necessary summation of the negative short-lived τ_2 DAS amplitude to the sequential long-lived DAS amplitudes in the same low energy region, since the later mentioned $\tau_{3/4}$ time constants do not really originate from zero and represent the ionisation from the $S_1(\pi\pi^*)$ excited state.

Physically the negative amplitude describes the non-adiabatic coupling of $S_2(3s/\pi\sigma^*)$ and $S_1(\pi\pi^*)$ and the concomitant population loss from the higher lying excited state via internal conversion, as discussed in Chapter 3.

The missing negative amplitude in 3,5-DMA means the absence of this dynamical non-adiabatic coupling and suggests instead a different, yet also extremely fast decay process is responsible for population loss from the $S_2(3s/\pi\sigma^*)$ potential energy surface. Using the TRPEI technique does not allow one to track the alternative pathway of the $S_2(3s/\pi\sigma^*)$ Rydberg/valence state. Nevertheless a direct N-H fission along the dissociated reaction coordinate is expected and this assertion is strengthened by detection of ultra fast H-atom release in the very similar system aniline using complimentary detection methods like H atom photofragment translational spectroscopy [102] and time-resolved velocity map imaging [121].
Moreover, the theoretical calculated potential energy cut of the $S_2(3s/\pi\sigma^*)$ excited state along the NH stretching coordinate in 3,5-DMA and N-CH_3 in N,N-DMA (see Figure 4.11) clearly reveals the dissociative character. Thus, the calculations support the argument for the fragmentation pathway in 3,5-DMA on the one hand and suggest, on the other hand, that this dissociation pathway is an additional decay option in N,N-DMA next to the internal conversion to the energetically lower lying $S_1(\pi\pi^*)$ excited state. The methylation of the original molecule aniline proves to be a good method of gaining new dynamical insights. Exciting with 240 nm is well above the small potential barrier present along the reaction coordinate and the two competing pathways are still active in N,N-DMA. In $S_1(\pi\pi^*)$, however, the methylation slowed down the time scale for internal conversion considerably, so H atom loss is the dominant process.
The highly differential TRPEI approach provides, in addition to the DAS data also information about the photoelectron angular distribution of the involved excited energy states. The physical meaning of non-adiabatic coupling between two different states is the intermixture of their vibronic or purely electronic nature, which can be measured in the time dependent development of their photoelectron angular distribution [18, 134, 135]. In this present study of the excited electronic states in the two aniline derivates following 240 nm excitation the dynamical evolution of their PADs is a convolution of two overlapping processes. These are, firstly, the component already observed at a 250 nm excitation wavelength and, secondly, a new behaviour resulting from the newly excited $2\pi\pi^*$ state. The dynamical evolution of the anisotropy parameters β_2 and β_4 for both molecules, as described above in Section 4.2.2, are shown in Figure 4.8. Since the PAD in this Figure is summed over the low photoelectron kinetic energy region, it is a direct reflection of the electronic $S_1(\pi\pi^*)$ excited state evolution. The geometry change of this state due to for example the approach of a conical intersection and therefore the change of electronic character will effect the β_2 and β_4 parameters.
After comparing the temporal evolution of the anisotropy parameter β_2 following 240 nm excitation (see Figure 4.8) with the 250 nm data (see Figure 4.9), it is clear that at both excitation wavelengths the molecules approach the $S_2(3s/\pi\sigma^*)/S_1(\pi\pi^*)$

conical intersection while changing their molecular geometry. In both molecules, and at both excitation wavelengths, β_2 exhibits an increase, however the rise time in N,N-DMA with $\sim$ 150 fs is clearly faster than the rise in 3,5-DMA with $\sim$ 1.5 ps. The quicker rise time in N,N-DMA can be explained due to two competing decay pathways: internal conversion and bond fission, which are happening on the same ultrafast time scale, since the τ_2 decay lifetime associated with $S_2(3s/\pi\sigma^*)$ is 120 fs. Based on this it can be stated that both channels are open and active. On the contrary in 3,5-DMA, the methylation of the aromatic ring structure increases the time scale to reach the geometry of the $S_2(3s/\pi\sigma^*)/S_1(\pi\pi^*)$ CI drastically, therefore the faster bond fission process is the only dominant decay process. In Figure 4.13 the decay processes in NN-DMA and 3,5-DMA are displayed with the associated time constants.

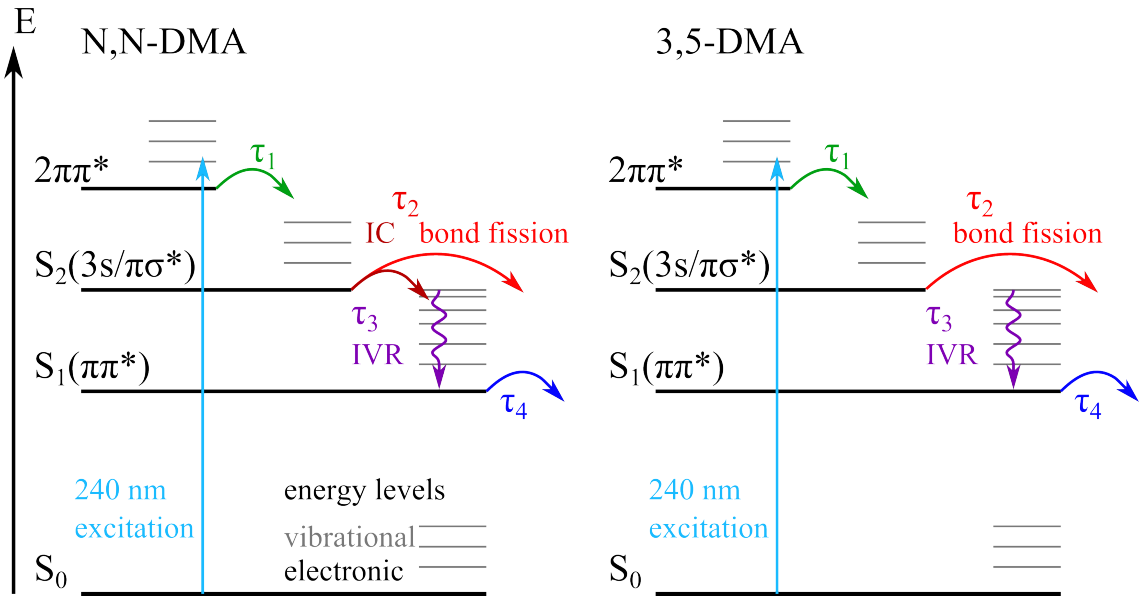

Figure 4.13: *Sketch of energy decays of the three electronic excited states in N,N-DMA and 3,5-DMA after 240 nm excitation.*

4.4.2 $2\pi\pi^*$ dynamics and comparison with aniline

In Section 4.2.1 the τ_1 DAS shown in Figure 4.6 has already been associated with the ionisation from the $2\pi\pi^*$ valence state, which decays extremely quickly on a time scale beyond the resolution of the experimental setup. The Gaussian τ_1 decay constant extracted from the fit of the TRPEI data is plotted against photoelectron kinetic energy in Figure 4.6 and exhibits positive DAS amplitudes throughout the entire spectrum. As discussed above, negative amplitudes in a certain energy region indicate non-adiabatic coupling between two electronic states. The fact that in Figure 4.6 the τ_1 DAS in the lower kinetic energy region of both molecules, N,N-DMA and 3,5-DMA, shows no negative amplitude implies that $2\pi\pi^*$ is not

transferring population to either $S_2(3s/\pi\sigma^*)$ or $S_1(\pi\pi^*)$. This result is remarkable since the case is different in aniline, the very similar base molecule, where the relaxation pathway is calculated to include a three state $2\pi\pi^*/S_2(3s/\pi\sigma^*)/S_1(\pi\pi^*)$ conical intersection [104]. Experimental evidence for population transfer from $2\pi\pi^*$ to $S_2(3s/\pi\sigma^*)/S_1(\pi\pi^*)$ was found after 238 nm excitation [103].

In N,N-DMA and 3,5-DMA the missing negative τ_1 DAS amplitude in the low kinetic energy region can be explained with the help of the photoelectron angular distribution data shown in Figure 4.8. Here both anisotropy parameters β_2 and β_4 exhibit two distinct temporal evolutions, one of which originates from the molecular geometry accessing the $S_2(3s/\pi\sigma^*)/S_1(\pi\pi^*)$ CI. The second evolution may therefore be connected to the different geometry of the $S_1(\pi\pi^*)$ state connecting to the $2\pi\pi^*$ state via an different conical intersection. The time scales for the geometry change in both molecules to reach this $2\pi\pi^*/S_1(\pi\pi^*)$ CI is relatively fast, being $\sim$ 250 fs in N,N-DMA and $\sim$ 350 fs in 3,5-DMA. Nevertheless they are much longer than the recorded $2\pi\pi^*$ lifetime, which is not resolvable within the scope of the TRPEI measurement.

The following conclusions can be drawn for this aforementioned analysis. Firstly, the internal conversion pathway from $2\pi\pi^*$ to $S_1(\pi\pi^*)$ and/or $S_2(3s/\pi\sigma^*)$, although in general electronically accessible and therefore possible, is not active in both molecules, because this decay process is not able to kinetically compete with the operating mechanisms, such as direct dissociation. Secondly, following 240 nm excitation the two low lying $S_2(3s/\pi\sigma^*)$ and $S_1(\pi\pi^*)$ excited states have to be populated directly in the Franck-Condon region.

In aniline, in contrast to the situation mentioned above, the non-adiabatic decay pathway of $2\pi\pi^*$ to $S_1(\pi\pi^*)$ takes place to some extent at similar excitation wavelengths. Here it is interesting to note that in fully deuterated d7-aniline the overall dynamical processes are very similar to the one observed in N,N-DMA, so also here no non-adiabatic population transfer from $2\pi\pi^*$ to $S_1(\pi\pi^*)$ or $S_2(3s/\pi\sigma^*)$ is observed [103]. The vibrational time scales in the molecular systems dictate very crucially which $2\pi\pi^*$ decay pathway becomes the dominant one. Moreover, measurements of aniline at 240 nm excitation have shown no temporal evolution of the β_2 anisotropy parameter in the low kinetic energy region (0.2 - 0.4 eV) [136]. This is an additional argument for the proposed kinetic mechanisms in aniline of temporally being able to access the conical intersection geometry between $2\pi\pi^*$ and $S_2(3s/\pi\sigma^*)/S_1(\pi\pi^*)$ on an ultrafast time scale much shorter than the temporal resolution of the present experiment. Hence internal conversion is now becoming an active decay pathway for the population on the $2\pi\pi^*$ potential energy surface, also observed following 250 nm excitation [110].

If population on the $2\pi\pi^*$ surface is reducing via internal conversion to $S_1(\pi\pi^*)$ and/or $S_2(3s/\pi\sigma^*)$ the molecules have to undergo a significant geometry change re-

quiring motion of the NH_2 group out of the ring plane and distortion of the aromatic ring system suggested by the three state conical intersection in aniline [104] and the $S_1(\pi\pi^*)/2\pi\pi^*$ CI proposed by Stavros and co-workers [108]. The aforementioned kinetics operating in N,N-DMA and 3,5-DMA are in agreement with the literature, since site-selective methylation slows down both described geometry changes, which bring the molecules to the conical intersections. On this basis, the $2\pi\pi^*$ state has to decay via a different pathway than internal conversion to $S_2(3s/\pi\sigma^*)/S_1(\pi\pi^*)$, such as the barrierless decay pathway using conical intersections connecting the $2\pi\pi^*$ state with the electronic ground state S_0, as suggested by Fielding and co-workers [104].

Since geometry changes in the molecules (e.g. out of plane motion of the NH_2 group and considerable aromatic ring distortion) affect the dynamical processes, it is surprising that no significant difference in the $2\pi\pi^*$ decay life time could be observed in the different molecular systems N,N-DMA, 3,5-DMA and aniline. The latter of which has a measured $2\pi\pi^*$ lifetime of 50 ± 10 fs [103]. These ultrafast lifetimes of the three molecules, may in principle different from each other, but are too fast to observe with the current TRPEI setup.

As a result it can be concluded that internal conversion from the $2\pi\pi^*$ excited state directly to the S_0 ground state is a possible relaxation pathway, but another mechanism may be also actively involved in the electronic state decay dynamics. Theoretical excited state calculations for N,N-DMA and 3,5-DMA, shown in Table 4.1, reveal the existence of several Rydberg states lying energetically above $S_2(3s/\pi\sigma^*)$ and just below $2\pi\pi^*$ in the Franck-Condon region. For the purpose of generating a correctly modelled aniline absorption spectrum, the coupling interactions between these Rydberg states and the $2\pi\pi^*$ state have to be included in the simulation [114]. It is therefore more than plausible that these electronic state interactions might play a role in the population decay of the $2\pi\pi^*$ state.

A piece of evidence for the contribution of the Rydberg states to the overall dynamical processes can be seen in Figure 4.10, where the anisotropy parameters β_2 and β_4 are plotted vs. photoelectron kinetic energy at a pump-probe delay time $\Delta t = 0$, shown is section 4.2.2. In N,N-dymethylaniline at high kinetic energies, where the $2\pi\pi^*$ state is located energetically, the β_2 and β_4 parameters exhibit both a high value. This can be caused by a Rydberg state with a p character and should be investigated in future studies.

4.5 Conclusion

The highly differential time-resolved photoelectron imaging technique provides comprehensive insights in the numerous non-adiabatic pathways operating in the aniline derivatives N,N-dimethylaniline and 3,5-dimethylaniline after 240 nm excitation. This site selective methylation method is supported by *ab initio* calculations of state properties in N,N-DMA and 3,5-DMA. These molecules are an excellent basis in a "bottom up" approach to understand the dynamical processes linked to the photoprotective function of bigger biological chromophores.

In this present study several electronic excited states are energetically accessible following 240 nm excitation and their dynamical evolution is observed. In N,N-DMA the mixed $S_2(3s/\pi\sigma^*)$ Rydberg/valence state decays through two competing routes, which are, on the one hand, internal conversion to the longer lived $S_1(\pi\pi^*)$ valence state and, on the other hand, direct bond fission along the N-CH_3 reaction coordinate.

A different picture is painted in the case of 3,5-DMA. Here the only active decay pathway is direct dissociation along the N-H coordinate. The methylation of the aromatic ring alters the relative time scales of the two pathways in a way that internal conversion is slowed down too much to compete kinetically with the dissociation pathway. This statement is greatly underpinned by the temporal evolution of the PADs.

Furthermore, in both molecular systems the energetically higher lying $2\pi\pi^*$ valence state seems not to undergo non-adiabatic coupling with the other excited $S_2(3s/\pi\sigma^*)$ or $S_1(\pi\pi^*)$ states. Instead it is assumed that the $2\pi\pi^*$ excited state is either directly internally converting on a ultrafast time scale to the electronic S_0 ground state (as observed in aniline) or decaying via an other relaxation pathway. Further investigation of the multiple Rydberg states (which are energetically just below the $2\pi\pi^*$ state) might be a key factor and provide more information about the overall relaxation dynamics.

In conclusion it can be seen that site-selective methylation in combination with the highly differential measurement technique provides new and extensive information about the molecular systems under study.

Chapter 5

Time-resolved photoionization spectroscopy of mixed Rydberg-valence states in indole

In this chapter new experimental insights into non-adiabatic relaxation dynamics in gas-phase indole using time resolved photoelectron imaging are presented and were published in the paper M. M. Zawadzki *et al.*, Time-resolved photoionization spectroscopy of mixed Rydberg-valence states: indole case study. *Phys.Chem.Chem.Phys.*, 17, 26659, 2015 [1].

The highly differential spectroscopic technique provides energy and angle-resolved information and reveals subtle details of the complex interplay of several low-lying electronic excited states accessible at a photo-excitation wavelength of 267 nm and 258 nm. Particularly the fate of the mixed Rydberg-valence $3s/\pi\sigma^*$ state was studied, which correspond to the electronic states with a dissociative valence character. Here the experimental data, in combination with various *ab initio* calculations using both coupled cluster and density functional methods, show a population residing on the $3s/\pi\sigma^*$ excited state surface at large N-H bond distances for a comparatively long time period before a dissociation and/or an internal conversion process proceed. Moreover, this chapter addresses some important general information about the nature of mixed Rydberg-valence excited states, such as their spectral fingerprints, the detection sensitivity in photoionization measurements and more generally their significance in vibronic relaxation in small model-chromophore systems.

5.1 Introduction

5.1.1 The indole case study - what happened so far

Indole is the base chromophore in many bio-molecules of interest such as the nucleic acid bases adenine, guanine, aromatic amino acids like tryptophan and eumelanin the pigment in human skin hair and retina [137]. The latter was found to be present already in the Jurassic period [138]. All these molecular systems are the "building blocks" of life and the body's front line defence system against the potentially damaging effects of the ultraviolet radiation using a non-radiative decay mechanism [139, 140]. As such it is of great interest to study and understand the physical processes and dynamical evolution in photoexcited indole in order to subsequently understand the physical mechanisms of larger bio-molecular systems.
The absorption spectrum of a molecular system such as indole is an important piece of evidence for their electronic landscape. In Figure 5.1 the low resolution UV absorption spectrum in the spectral region from 200 nm to 320 nm is shown [141].
One can observe a broad peak spanning from 220 nm to about 280 nm, which originates mainly from the absorption to the ^1L_a excited state. Its electronic origin, although hard to be observed directly, is stated to be located at 273 nm [142, 143]. The narrow peak localised between 280 nm and 295 nm is a signature of the lower situated ^1L_b excited state, the electronic origin of which is known in the literature at 283.8 nm [144, 145]. ^1L_a and ^1L_b are the historical labels by the Platt nomenclature for the two $^1\pi\pi^*$ valence states with a $^1A'$ symmetry [146].

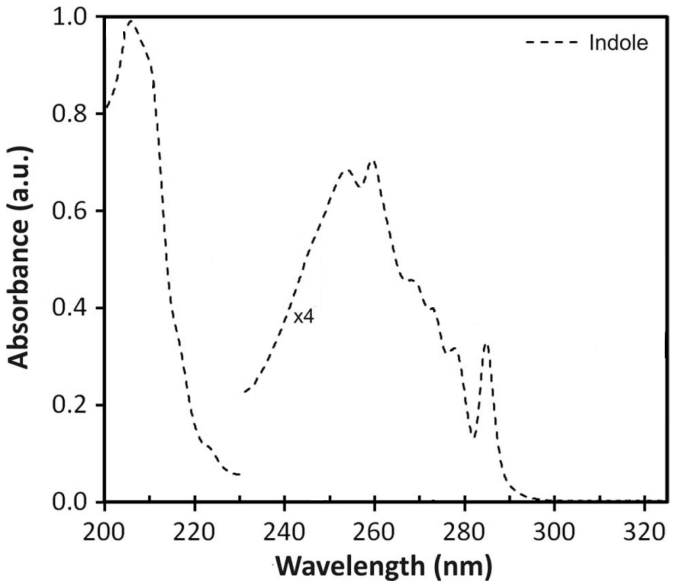

Figure 5.1: *The graph shows a gas phase absorption spectrum of indole. From 230 nm onwards the spectrum was four times magnified for clarity purposes. [24]*

The reason for the slight deviation of the ^1L_b peak position from the literature value can be explained with significant hot-band contributions that can occur in a higher temperature present in the absorption sample cell of the experiment [24]. Finally, the band below 220 nm in the spectrum can be attributed to the absorption of higher lying $^1\pi\pi^*$ valence states ^1B_b and ^1B_a [141, 147].

Next to these optically "bright" electronic excited states in the wavelength region between 200 nm to 300 nm, which are shown in the absorption spectrum in Figure 5.1, exists another electronic excited state, with a mixed $3s/\pi\sigma^*$ Rydberg/valence character. In indole this state is optically "dark" and is dissociative along the N-H bond coordinate [148]. It has $^1A''$ symmetry and the electron density of its 3s Rydberg character is localised on the N-H group, with a node along the N-H bond length [148, 149].

An excited electronic state is essentially optically "dark" for single photon absorption, if its transition from the ground state S_0 carries little or no oscillator strength. In Table 5.1 the oscillator strengths f for the first three excited ^1L_b, ^1L_a and $3s/\pi\sigma^*$ states are shown as well as the calculated vertical excitation energies in eV. Here it is obvious that the two $^1\pi\pi^*$ valence states exhibit a far greater oscillator strength f, than the $3s/\pi\sigma^*$ state and are therefore optically "bright". Sobolewski and Domcke calculated the oscillator strengths for the Rydberg/valence state to be 3×10^{-5} by [148], so even lower than the value in Table 5.1.

Table 5.1: *A list of the calculated vertical excitation energies (in eV) for indole. Theory: coupled cluster response theory in conjunction with an aug-cc-pVDZ one-electron basis set. Also the oscillator strengths f are listed and obtained from LR-CCSD. [24]*

State	E [eV] LR-CCSD	E [eV] CCR(3)	f
$^1\pi\pi^*$ ^1L_b ($^1A'$)	4.823	4.762	0.0280
$^1\pi\pi^*$ ^1L_a ($^1A'$)	5.241	5.117	0.1018
$^1\pi\sigma^*_{NH}$ ($^1A''$)	5.046	5.017	0.0022

Although these Rydberg/valence states hold only little or no oscillator strength for single photon absorption, their repulsive character potentially provides a fast and efficient route for a non-radiative decay pathway in aromatic molecules back to the S_0 electronic ground state. For this reason they have been implicated in playing an important role in "photostability" and are of great interest within the chemical dynamics community [99, 100, 150].

The potential energy functions of the S_0 ground state and the first excited electronic states have a distinctive dependence on the N-H bond distance and are plotted in Figure 5.2. The graph clearly shows the bound nature of the ^1L_a and ^1L_b potential energy functions in terms of the in-plane detachment of the H-atom on the N-H group. The energy curve of the $3s/\pi\sigma^*$ state reveals a dissociative feature along the N-H stretching coordinate due to the repulsive $^1\pi\sigma^*$ character of the overall excited state [120]. Unlike in the literature, where the whole excited state is just called $^1\pi\sigma^*$, the more accurate label $3s/\pi\sigma^*$ substantiates the mixed Rydberg/valence character at short/long N-H bond lengths respectively.

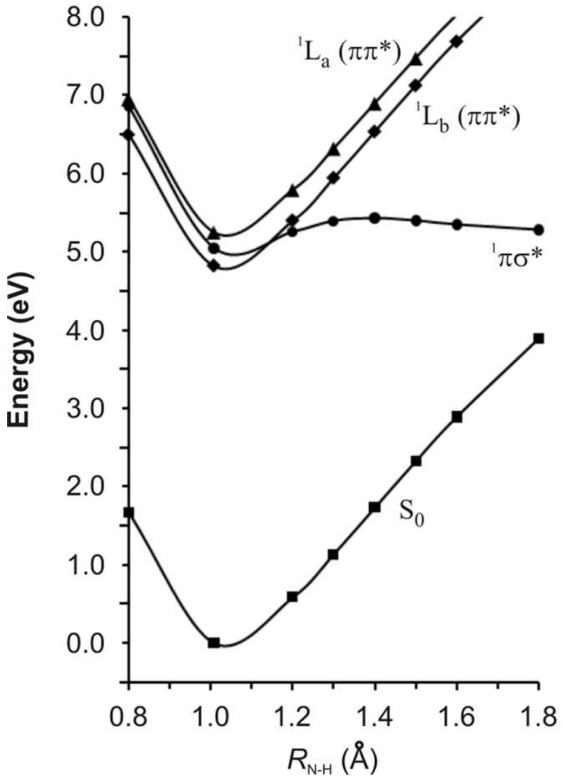

Figure 5.2: *Energy cut along the N-H coordinate in indole obtained using EOM-CCSD theory with a basis set aug-cc-pVDZ. [24]*

The electronic properties of indole have been well studied in the gas phase with various spectroscopic techniques. After initial excitation in the energy region 285 nm - 220 nm both $^1\pi\pi^*$ states are populated, though the ^1L_a is primarily excited based on its bigger oscillator strength. Hereinafter an extremely fast internal conversion from the ^1L_a state via two parallel decay mechanisms takes place on a sub-100 fs time scale [24]. On the one hand, energy can be transferred to the lower lying $^1\pi\pi^*$ singlet state through a conical intersection (CI) that connects the ^1L_a state with this ^1L_b state via different Herzberg-Teller active modes [151, 152]. On the other hand, a non-adiabatic relaxation can take place to the mixed $3s/\pi\sigma^*$ Rydberg/valence state. This is possible, because the potential energy function of the $3s/\pi\sigma^*$ state crosses the functions of the $^1\pi\pi^*$ states, forming a conical intersection located along the

N-H bond stretching coordinate. The formation of the CI is symmetry allowed in the planar system if out-of-plane vibrational modes of A″ symmetry are taken into account and is located at around 5 eV (248 nm) above the S_0 ground state [153]. At an extended N-H bond distance the potential energy curve of the $3s/\pi\sigma^*$ state forms a CI with the S_0 ground state potential allowing an ultrafast internal conversion to S_0 to occur, as has been extensively studied computationally by Sobolewski and Domcke [153].

Alternative to the ground state recovery, N-H bond fission can take place directly on the $3s/\pi\sigma^*$ energy surface, depending on the excitation energy. The lack of observed vibronic structure in the absorption spectrum above the ^1L_a origin may be reasoned in parts with the aforementioned ultrafast decay from the ^1L_a state via the $3s/\pi\sigma^*$ state. The review by Reisler and Krylov from 2009 shows an excellent overview of the Rydberg valence interactions [154].

In the literature there has been some inconsistency in the conclusions about the role and fate of the $3s/\pi\sigma^*$ state. Zwier and co-workers studied the hydride stretch in indole and its derivatives between 284 nm and 273 nm using excited state fluorescence-dip infrared spectroscopy [155]. It was concluded that the $^1\pi\sigma^*$ state was not the main relaxation pathway due to the lack of significant change in the N-H stretching frequency relative to S_0. In other observed indole derivates, however, the $^1\pi\sigma^*$ state was proven to be involved.

A femtosecond time-resolved spectroscopic analysis of indole by Radolff and co-workers examined photoions and photoelectrons in coincidence at excitation wavelengths of 263 nm and 250 nm [156]. A fast internal conversion to the $^1\pi\sigma^*$ state was not detected, because a long lifetime of over several hundred ps of the initially excited $^1\pi\pi^*$ states was observed. The conclusion was no significant connection to the $^1\pi\sigma^*$ state is present at these wavelengths.

Zewail and co-workers [157] also concluded that $^1\pi\sigma^*$ plays no strong role in the relaxations dynamics in indole after investigating the photoexcited molecule at 267 nm with ultrafast electron diffraction. They argued that the initially excited ^1L_a state decays on a timescale of 6.3 ps and is depopulated by the lower lying triplet channels via intersystem crossing (ISC). The $T_1(^3\pi\pi^*)$ state should be responsible for any H-atom loss. The symmetry and parity rule normally predicts long time scales for ISC in a planar geometry, but the authors explain the very short time scale for ISC in indole with the vibronic couplings with the non-planar geometry of the $T_2(^3\pi\pi^*)$ state.

In contrast to these findings, other experimental and theoretical scientists found strong evidence for the important role of $^1\pi\sigma^*$ states. Lee and co-workers investigated the photodissocitation of indole at 193 nm and 248 nm with the multimass ion imaging technique under collision free conditions [158]. They recorded a two-component photofragment translational energy distribution at both wavelengths and

assigned the high kinetic energy component to direct dissociation pathway along the $^1\pi\sigma^*$ state. It was populated through the initially excited $^1\pi\pi^*$ states - the ^1L_a state at 248 nm and the $^1B_a/^1B_b$ states 193 nm. The low energy component is the result of the internal conversion to the highly vibrationally excited S_0 ground state, also called the "hot" ground state.

Ashfold and co-workers did another important experimental study of fragmentation dynamics in indole after excitation at 193 nm and between 240 nm and 286 nm utilising H Rydberg atom photofragment translational spectroscopy [159]. Additional to the findings of Lee and co-workers [158], they found an energetic threshold for the high kinetic energy H atom dissociation channel at excitation wavelengths shorter than 263 nm. This H-atom detachment takes place on the dissociative $^1\pi\sigma^*$ surface along the N-H bond. Ashfold and co-workers also detected low kinetic energy H-atoms that were generated by a unimolecular decay of the "hot" ground state molecule.

The fate of the $3s/\pi\sigma^*$ state was also of great interest for Townsend and co-workers in a recent time-resolved photoelectron spectroscopy (TRPES) study [24], where the relaxation dynamics of indole after 249 nm and 273 nm excitation were investigated. A key finding of this work, as described in detail above, was that at both wavelengths the same parallel relaxation of the initially populated ^1L_a state is taking place decaying either via the ^1L_b or $3s/\pi\sigma^*$ state.

The two techniques, time-resolved photoelectron spectroscopy and photofragment translational spectroscopy, are a great example for complementary tools with their unique observables that can be associated to the same underlying physical processes. In the particular example of indole, the evidence of the high kinetic H atoms after N-H bond fission at shorter wavelengths than 263 nm can be combined with the with the TRPES data enableing to assign specific features to the $3s/\pi\sigma^*$ state. These special features were also observed in the TRPES spectra at 273 nm, which is below the H atom fragment onset, and it was concluded that the relaxation pathway via the $3s/\pi\sigma^*$ state must be still active, although the decay pathway could not be explicitly determined.

A more recent study by Longarte and co-workers measured the relaxation dynamics of the isolated indole molecule with femtosecond time-resolved ionisation [160]. The ion-yield traces were measured after UV excitation in the region between 283 nm to 243 nm. The monitored results also concluded excitation takes place to the $^1\pi\pi^*$ valence states, although mainly to ^1L_a with subsequent parallel exponential decay via ^1L_b or $3s/\pi\sigma^*$. The relaxation pathway via the mixed Rydberg/valence state was, however, just observed for excitation wavelengths above 263 nm, that is in agreement with the H atom elimination threshold in reference [159].

Lindh and co-workers presented a unconstrained theoretical approach to the photophysics of indole confirming the presence of a conical intersection between the

two "bright" $^1\pi\pi^*$ valence states ^1L_a and ^1L_b via a barrierless decay pathway in the Franck-Condon region [137]. Lastly, a very recent study using photoionisation and fragmentation pump-probe spectroscopy was conducted by Ullrich and co-workers studying indole after 200 nm excitation. Due to the high pump energy the higher lying ^1B_b electronic excited state is initially populated and undergoes very fast internal conversion to the ^1L_a state. The subsequent dynamics, although slightly faster due to the shorter excitation wavelength, are the same as in the studies described above. So here the parallel decay process to either ^1L_b or $3s/\pi\sigma^*$ is concluded.
The motivation to investigate photoexcited indole with the time-resolved photoelectron imaging technique at pump wavelengths of 267 nm and 258 nm (below and above the onset threshold for H-atom elimination) was to understand the fate of the mixed $3s/\pi\sigma^*$ Rydberg/valence state. The results of the additional angle-resolved data provided by TRPEI in this chapter give new insights to the dynamical evolution of this state. The experimental results from this very differential spectroscopic tool are supported by information of theoretical ab initio calculations about the $3s/\pi\sigma^*$ state properties.

5.1.2 Experimental details

The experimental setup with all its important components used to collect the data is described in detail in Chapter 3. This section summarises the important details and describes the specific configurations for the indole experiment.
The molecular sample indole with a purity of 99% was purchased from Sigma-Aldrich. In order to introduce the sample into the source chamber of the differentially pumped photoelectron spectrometer it is positioned into the cartridge inside the pulsed molecular beam valve [82]. A carrier gas pressure of 5 bar helium is utilised to enable indole to pass trough a skimmer with a diameter of 1.0 mm and into the main interaction chamber. Here the molecular beam was intersected at 90° with two collinear propagating UV laser beams leading to a $(1 + 1')$ ionisation process of indole, where 267 nm or 258 nm were chosen as pump and 300 nm as a probe wavelength. The reason for a 300 nm probe is the lack of resonant absorption of indole in this spectral region, as shown in Figure 5.1. An evolving "probe-pump" signal in the negative temporal direction can be circumvented guaranteeing a "clean" experiment. This probe wavelength was generated by taking a part of the 800 nm fundamental output of a regeneratively amplified Ti:sapphire laser system, seeding it into a optical parametric amplifier (Light Conversion, TOPAS Prime-U) and doubling the output frequency twice with two thin β-barium borate (BBO) crystals. The fundamental physics of these nonlinear optical processes is described in Section 3.1.2. The result is a probe beam with a wavelength of 300 nm and a pulse energy of ~ 2 μJ. A single-pass fused silica prism compressor is utilised to shorten the temporal duration of the laser pulse after dispersion due to passing though material.

The two different pump wavelengths that are used to study dynamical behaviour upon different excitation are produced as follows. The 267 nm beam was generated in a third harmonic generation process using a portion of the 800 nm fundamental laser output and seeding it into the high harmonics box that is equipped with a pair of thin β-barium borate (BBO) crystals (shown and explained in Figure 3.4). The generation of the other pump wavelength 258 nm also uses two steps, where firstly a separate fraction of the 800 nm fundamental laser output is sum-frequency mixed with the signal beam from a second optical parametric amplifier (Spectra Physics, OPA-800C) in a thin BBO crystal and secondly this light in the visible spectral energy region is frequency doubled with another BBO crystal producing the UV laser light. In both cases the pulse energy of the pump beams is attenuated to 1.2 mJ. Material dispersion is compensated using a single pass calcium fluoride prism compressor to ensure a short fs pulse.

For every time-resolved measurement an accurate temporal delay between pump and probe is needed and is realised in our setup with a precisely operating linear translation stage, which can be automatically controlled with a PC. As mentioned above, pump and probe pulse are co-propagating into the main interaction chamber having been previously combined on a thin dichroic mirror and focussed with a 25 cm fused silica lens into the spectrometer.

Inside the vacuum chamber, between the electrostatic electrodes repeller and lens, which are optimised for velocity-map imaging, the $(1 + 1')$ photoionisation process of indole occurs releasing electrons with specific velocity vectors, a signature of the electronic excited states they originate from. These photoelectrons are detected with a 40 mm MCP/P47 phosphor screen detector, that is used in combination with a CCD camera (640 $\times$ 480 pixels).

The pump-probe signal crosscorrelation (CC) that defines the temporal resolution of the experiment can be optimised by systematically adjusting the length of both prism compressors in each beam line. In this experiment a CC of 120 $\pm$ 10 fs is detected by recording the non-resonant $(1 + 1')$ photonionisation signal of pyrrole, which was also used for energy calibration of the spectrometer [161]. To insure a pure indole monomer detection the spectrometer was changed over to ion detection mode to ensure that no clusters are present in the molecular beam before switching back to photoelectron data collection.

After the system was fully optimised, the translation stage was repeatedly moved in linear pump-probe time delays of 50 fs between -400 fs to +500 fs and from there in 9 exponential steps up to +20 ps. After the two-colour signal collection at each time step a photoelectron image of a one-colour timeinvariant pump and probe signal was detected and used for background subtraction.

5.2 Experimental findings

5.2.1 Time-resolved photoelectron spectra

An overview of representative $(1+1')$ photoelectron images at different pump-probe delay times Δt with a 258 nm excitation and a 300 nm ionization wavelength is shown in Figure 5.3. These images are the result of a couple of processing steps such as subtraction of one colour pump and one colour probe background signal from the original data and four fold symmetrisation. The right hand side of the last data image also shows the rapid Abel matrix inverted data. This inversion technique is described in detail in Section 3.3. The direction of pump and probe laser polarisation is vertical regarding the images.

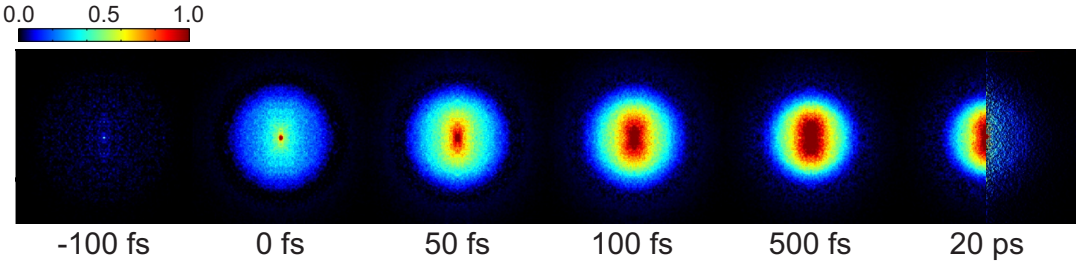

Figure 5.3: *The figure shows a processed sequence of $(1+1')$ photoelectron images at different pumpprobe time delays Δt in indole after excitation at 258 nm and ionization at 300 nm. Here the images are already background subtracted by the pump and probe one colour signal and four fold symmetrised.*

The time-resolved photoelectron spectra of both pump wavelengths (258 nm and 267 nm) are displayed in Figure 5.4 and are generated from a whole set of the fully background substracted and matrix inverted photoeletron images in each case.
The total energy E_{tot} is the sum of the pump energy $E_{pump} = 4.81$ eV (258 nm) or 4.64 eV (267 nm) and the probe energy $E_{probe} = 4.13$ eV (300 nm) and is calculated to be 8.94 eV and 8.77 eV, respectively. Since energy has to be conserved, the kinetic energy of electron E_{kin,e^-} after ionisation can be calculated with Equation 5.1:

$$E_{kin,e^-} = (E_{pump} + E_{probe}) - IP_{ad} \tag{5.1}$$

Here IP_{ad} is the adiabatic ionisation potential for the $D_0(\pi^{-1})$ cation ground state in indole, which is 7.76 eV [162, 163, 164]. The vertical IP_v is known to be 7.9 eV [165, 166]. Consequently the maximum kinetic energy of the electron E_{kin,e^-} is 1.18 eV (with a 258 nm pump pulse) and 1.01 eV (with 267 nm) and is respectively the cut-off energy in both photoelectron spectra in the top half of Figure 5.4.
Here the typical 3D spectrum is plotted as a function of kinetic energy E_{kin,e^-} partitioned into 0.05 eV energy bins and as a function of pump-probe delay times with a linear/logarithmic scale changing at +500 fs. The intensity in each spectrum is normalised with respect to the highest data point. Despite the different signal-to-noise

levels, both spectra show hardly any differences in their spectral and dynamical behaviour. As a consequence, in the 258 nm as well as the 267 nm data, a long-lived pronounced feature is present in the lower kinetic energy region, whereas in the region between 0.8 eV to 1.0 eV a very short-lived peak with a much lower intensity can be detected. In the intermediate energy region a decaying signal with a slightly longer life-time is superimposed and will be also discussed hereafter.

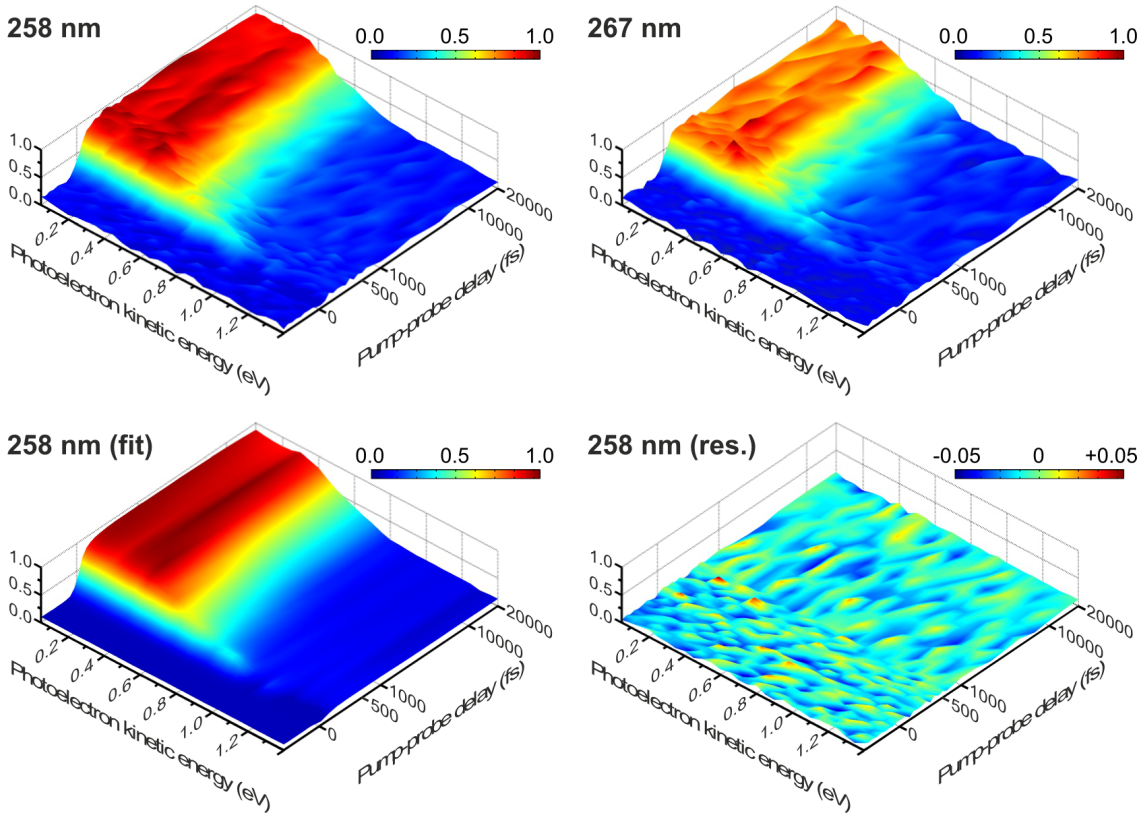

Figure 5.4: *In the top half of the figure the time-dependent photoelectron spectra of indole are shown following excitation at 258 nm and 267 nm and ionisation at 300 nm. The energy axis is binned into 0.05 eV energy steps and the time axes is linear up until +500 fs and from there logarithmic in positive temporal direction. The data was normalised with respect to the highest data point in each spectrum. The lower part of the figure shows the standard Levenberg-Marquardt global fit to the 258 nm data and the corresponding residuals.*

The time constants τ_i of the contributing electronic excited states and their decay associated photoelectron spectra (DAS) in the photoelectron data $S(E, \Delta t)$ are determined with the standard Levenberg-Marquardt global fit function, where the data is 2D fitted dependent on the E_{kin,e^-} and the pump-probe delay time Δt, as explained in Section 3.3:

$$S(E, \Delta t) = \left[\sum_{i=1}^{3} A_i(E) \cdot \exp\left(-\frac{\Delta t}{\tau_i} \right) \right] \otimes g(\Delta t) \tag{5.2}$$

Each i^{th} function is convoluted with the experimental Gaussian cross correlation $g(\Delta t)$ and fixed to originate from $\Delta t = 0$. The fit of the 258 nm TRPEI data are shown in the lower part of Figure 5.4. The corresponding residuals are plotted to confirm the very good quality of the performed fit. In Equation 5.2 $A_i(E)$ is the DAS of the ith data channel with a associated exponential decay function $P_i(\Delta t)$.

$$P_i(\Delta t) = \exp\left(-\frac{\Delta t}{\tau_i}\right) \tag{5.3}$$

This mathematical approach shows the relative amplitude of each time constant as a function of photoelectron kinetic energy E_{kin,e^-} and the data was satisfactory fitted with three exponential decay functions, which are plotted in Figure 5.5. The resultant time constants for the 258 nm spectra are $\tau_1 = 110 \pm 10$ fs, $\tau_2 = 0.9 \pm 0.1$ ps and $\tau_1 = 120 \pm 10$ fs, $\tau_2 = 1.0 \pm 0.1$ ps for the 267 nm data. In both cases the third time constant τ_3 is extremely long and can be considered a step function within the temporal observation window. The maximum $(1 + 1')$ photoelectron kinetic energy cut-off, that is calculated above with Equation 5.1, is marked with vertical arrows in Figure 5.5 and indeed no significant signal can be observed from this point towards higher energies (no observation of a $(1 + 2')$ ionisation signal).

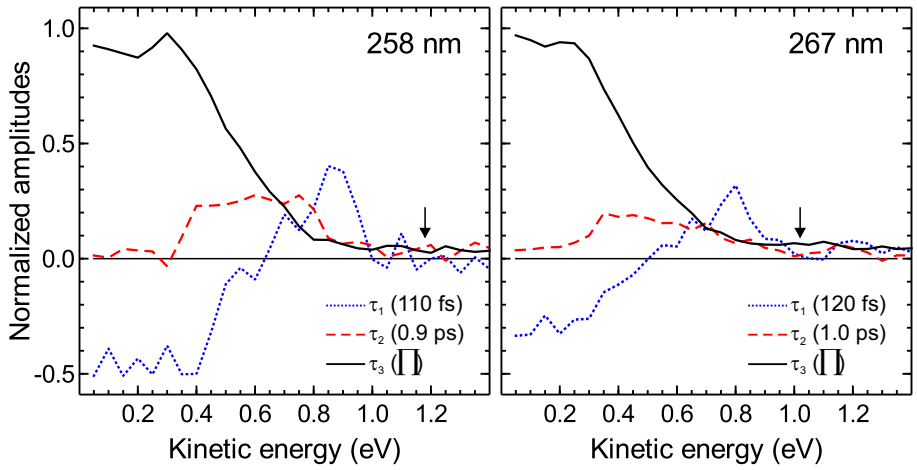

Figure 5.5: *The decay associated spectra are plotted for 258 nm and 267 nm pump wavelength and calculated using the global fit function (see Equation 5.2) to the time-dependent photoelectron spectra from Figure 5.4. The values for* 1σ *uncertainties are* ± 10 *fs and* ± 0.1 *ps for* τ_1 *and* τ_2 *respectively. The vertical arrows indicate the maximum photoelectron kinetic energy cut-off.*

A detailed discussion will be presented in Section 5.4 of this chapter, however a few important features of the decay associated spectra in Figure 5.5 shall be listed now. Firstly, the maximum τ_1 peak position for both excitation wavelength 258 nm and 267 nm is located at $\sim$ 0.8 eV. This peak position for the shortest time constant τ_1 has been previously detected for 273 nm and 249 nm excitation [24]. In the UV energy region there have been published several absorption band studies in crystalline indole [167] as well as in indole doped polymer films [168]. On the basis of

this strong evidence the τ_1 peak can be assigned to a diagonal ionisation from the mainly prepared ^1L_a excited state.
Secondly, in the kinetic energy region up until 0.6 eV the τ_1 decay associated spectrum shows for both measurements a negative feature, which is a persuasive sign of sequential dynamics from the ^1L_a excited state to the ^1L_a state, as illustrated in Section 3.3.2. Thirdly, the middle time constant τ_2 has got no amplitude in the lower energy region (0.0 - 0.3 eV).

5.2.2 Photoelecton angular distribution

Time-resolved photoelectron imaging is a powerful technique and additional dynamical information can be gained by analysing the time-dependence of the photoelectron angular distribution (PAD) of a $(1 + 1')$ ionisation utilising two parallel linear polarised laser pulses. The intensity I of the PAD is a function of the kinetic energy of the electron E_{kin,e^-} and the pump-probe time delay Δt in terms of the anisotropy parameters β_2 and β_4 and can be written as:

$$I(E, \Delta t, \theta) = \frac{\sigma(E, \Delta t)}{4\pi} \left[1 + \beta_2(E, \Delta t) P_2(cos\theta) + \beta_4(E, \Delta t) P_4(cos\theta)\right] \tag{5.4}$$

In this equation $\sigma(E, \Delta t)$ describes the time-dependent electron energy distribution, a vertical line trough the centre point visible in Figure 5.3 defines $\theta = 180°$ and $P_n(cos\theta)$ are the nth-order Legendre polynomials.
The parameters β_2 and β_4 are used, because indole was excited with one and ionised with an other photon originating from linear polarised laser pulses. After applying the fit function in Equation 5.4 to the indole data, β_4 can be determined to be zero within the statistical noise over all spectral regions for both excitation wavelengths 258 nm and 267 nm.
The results of the PAD fit for β_2 as a function of kinetic energy, pump-probe delay time and pump wavelength are plotted in Figure 5.6. The temporal evolution of β_2 as a function of pump-probe delay is plotted in Figure 5.6(a-c). Here the β_2 parameter of each pump wavelength was averaged respectively over the kinetic energy regions (a) 0.05 - 0.30 eV, (b) 0.30 - 0.70 eV and (c) 0.70 - 0.95 eV, because within each energy region the value of β_2 is consistent. These specific regions in Figure 5.6 are also chosen on the basis of decay associated spectra (see Figure 5.5), where region (a) shows just the amplitudes of τ_1 (negative) and τ_3 (positive), (b) is dominated by the positive amplitude of τ_2 and region (c) contains a big portion of the positive amplitude of τ_1.
In Figure 5.6(a) a clear very fast rise in the β_2 data for both wavelengths can be observed followed by a saturation towards later times, reaching a plateau. The rise time constants can be ascertained with rising exponential fits to 140 ± 30 fs (258

nm) and 90 ± 30 fs (267 nm) and assigned to the τ_1 constant, when compared with the corresponding DAS fits.

In the high kinetic energy region displayed in Figure 5.6(c) the β_2 parameter undergoes a quick change from relative high to low values and the two exponential decay constants are calculated to 120 ± 40 fs (258 nm) and 140 ± 50 fs (267 nm). This time scale of this rapid fall matches the rise times in Figure 5.6(a) and will be discussed later in Section 5.4.

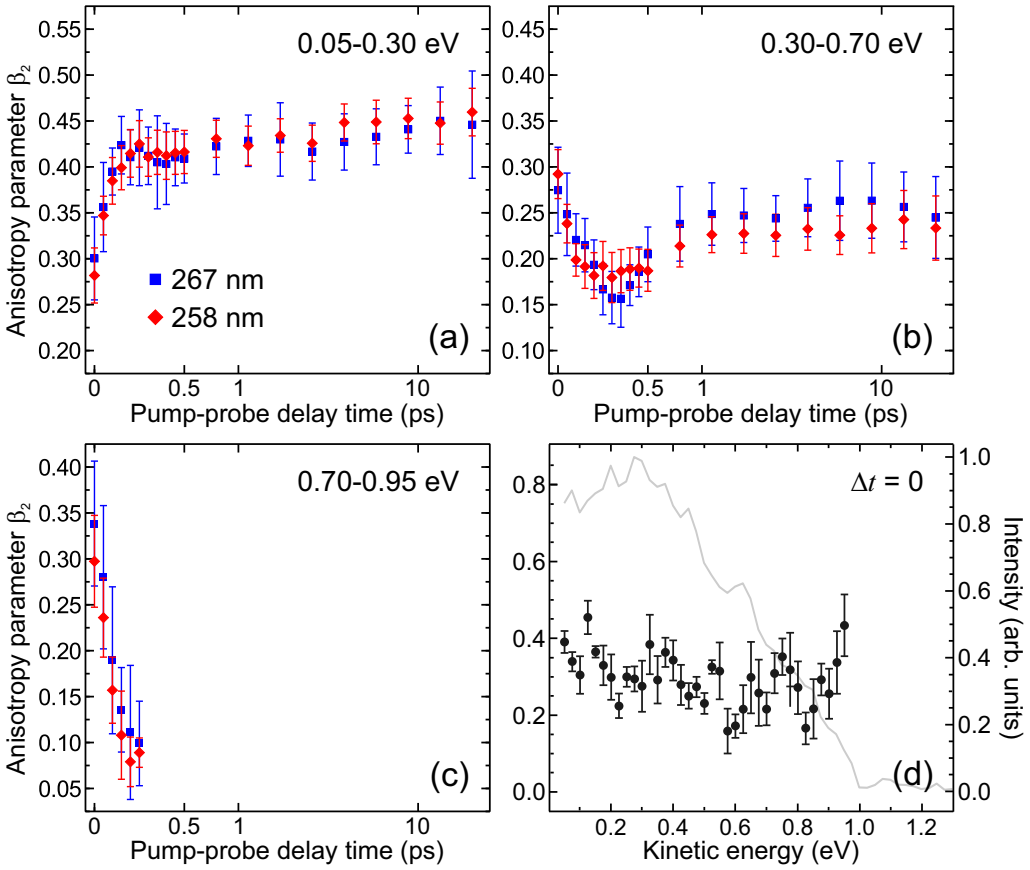

Figure 5.6: *This figure shows the behaviour of the anisotropy parameter β_2. (a-c) Here β_2 is averaged over a specific kinetic energy region and displayed for both pump wavelengths of 258 nm and 267 nm as a function of pump-probe delay time. Like in the photoelectron spectra the timescale is linear until +500 fs and logarithmic from +500 fs to +20 ps. The fits to obtain the data were conducted in a angular region between $5° \leq \theta \leq 90°$ to circumvent uncertainties, which might originate from the noise in the central line of the Abel-inverted images. Subfigure (c) shows β_2 just until 250 fs, because the data is just significantly high in this kinetic energy region. (d) β_2 is ploted together at zero pump-probe delay with the intensity of the photoelectron spectrum (grey line) as a function of electron kinetic energy. All error bars indicate one standard deviation.*

Figure 5.6(b) displays the β_2 data in the region of 0.30 - 0.70 eV. This proves to be more complex, since at small delay times one can observe a fast decrease of the signal very similar to the one in the high energy region (see Figure 5.6(c)). Nevertheless the evolution of β_2 undergoes a subsequent rise with increasing delay time. Due to

these overlapping rising and falling signals no absolute and reliable calculation of decay times can be performed, however, it can be stated that β_2 reaches a plateau in ~ 1 ps. This time constant is significantly longer than the rise time in Figure 5.6(a) and might be compared to the τ_2 decay constant received from the DAS fits for both wavelengths.
The β_2 parameter for 258 nm excitation at $\Delta t = 0$ is plotted in Figure 5.6(d). Also included is the corresponding photoelectron spectrum (grey line) against kinetic energy. The value of β_2 remains relatively constant and small (< 0.45) throughout the whole energy region up to the high-energy signal cut-off. The study of β_2 for 258 nm excitation shows similar behaviour.

5.3 Theoretical framework

State properties vs. N-H bond extension

In this section theoretical investigations are presented in order to support the experimental obtained data and its discussion. Some important former theoretical *ab initio* calculations on indole are summarized in Section 5.1.1, such as excited state energies and oscillator strengths and potential energy cuts along the N-H stretching coordinate [24].
Here the evolution of excited state properties in indole as a function of the N-H bond extension are computationally investigated and plotted in Figure 5.7. For the calculation linear response coupled cluster (LR-CC) theory (aug-cc-pVDZ basis), with the exponential cluster expansion truncated at singles and doubles, i.e., LR-CCSD is used as well as equation of motion coupled cluster theory (EOM-CCSD) to determine the character of the excited states at each particular geometry. The result for the excitation spectrum for both theories is the same, whilst the transition properties are minorly improved with LR-CCSD.
The initial ground state geometry of indole is calculated using density functional theory optimization (B3LYP/aug-cc-pVDZ) from Gaussian09 [128]. Dalton2015 is utilised to calculate all excited state properties [169, 170].
In order to comprehend the differences between pure valence states such as $\pi\pi^*$ and mixed Rydberg/valence states such as $3s/\pi\sigma^*$ in indole and also the differences within these mixed states itself one has to study, additionally, their electronic state properties. Each excited state is a composite of several electronic contributions, however the concise state label is given by the dominant contributor. In Figure 5.7(a) the normalized EOM-CCSD right eigenvector amplitudes for the orbital transition in relation to the $3s/\pi\sigma^*$ contribution to the whole Rydberg/valence state is depicted. The value decreases from 0.62 at 1.01 Å to 0.36 at 1.4 Å.
The specific evolution of the un-normalised LCAO (Linear Combination of Atomic Orbitals) coefficient magnitude for the un-contracted nitrogen 3s basis function in-

side the 3s/$\pi\sigma^*$ state is plotted in Figure 5.7(b). Note that the it is not the whole S_2 Rydberg/valence state, but just the main 3s/$\pi\sigma^*$ state contribution. Here the Rydberg magnitude falls by a factor of $\sim$ 2.5 over the same N-H bond distance than in the previous plot. Consequently, this drop clearly visualizes the substantial reduction of 3s Rydberg character and the augmentation of valence character within the excited state as the N-H bond extends. This evolution is very similar to previously reported in aniline [110] and likely to be of greater importance in similar molecular systems with mixed Rydberg/valence states.

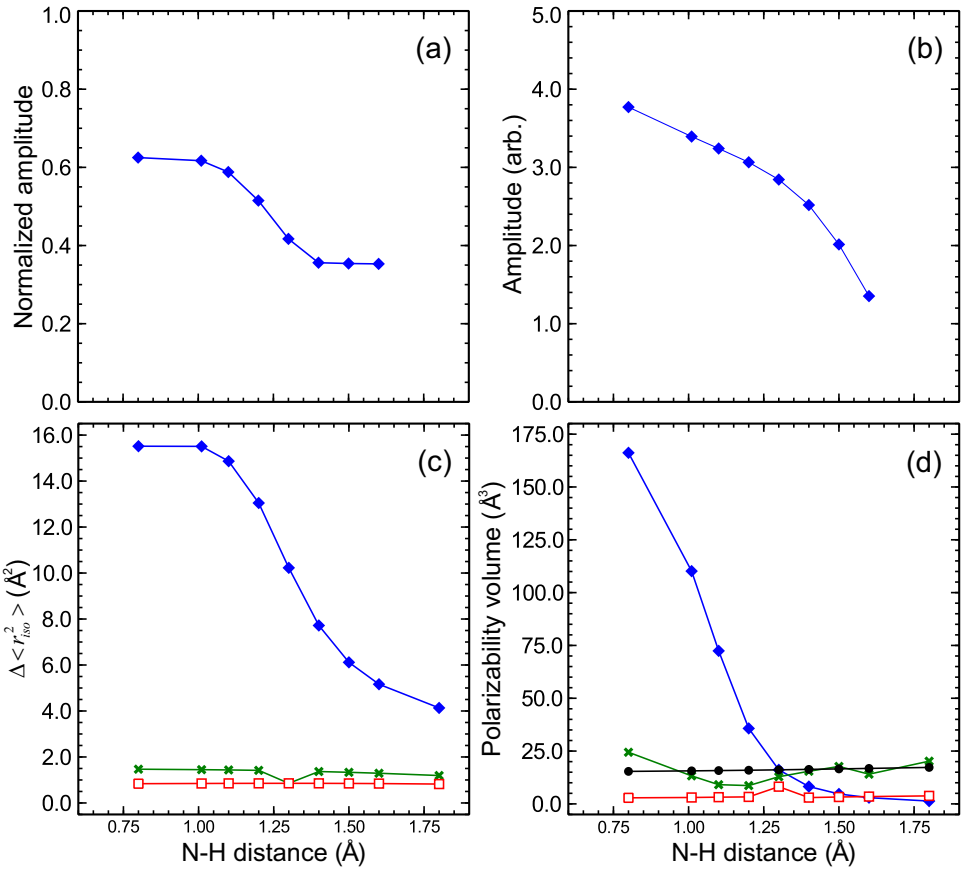

Figure 5.7: *Here the various electronic state properties in indole for the S_0 (black), ^1L_a (green), ^1L_b (red) and 3s/$\pi\sigma^*$ (blue) states as a function of N-H bond extension are plotted. (a) Normalized EOM-CCSD right eigenvector amplitude for the 3s/$\pi\sigma^*$ state, (b) un-normalized LCAO coefficient of the un-contracted nitrogen 3s basis function within the 3s/$\pi\sigma^*$ state, (c) isotropic invariant of the excited-state second-moment of the electronic charge distribution with respect to the ground state S_0, and (d) isotropic electronic polarizability volume. Note that the predicted S_0 equilibrium NH bond length is 1.02 Å and the $\pi\pi^*$ and 3s/$\pi\sigma^*$ states cross at $\sim$ 1.2Å. See main text for more details.*

As already discussed in Chapter 4 the extent of the isotropic invariant of the second-moment electronic charge distribution tensor $\Delta\langle r_{iso}^2\rangle$ with respect to the ground state S_0 is a very good parameter to characterise the excited Rydberg state, as described in the literature by Reisler and Krylov [133]. The change of the $\Delta\langle r_{iso}^2\rangle$ parameter

depending of N-H bond extension for all three excited states ^1L_a, ^1L_b and 3s/$\pi\sigma^*$ is plotted in Figure 5.7(c).
This average of the trace of the second moment tensor can be calculated for each given electronic state with this equation:

$$\langle r_{iso}^2 \rangle = \frac{1}{3} \left(\langle x^2 \rangle + \langle y^2 \rangle + \langle z^2 \rangle \right) \tag{5.5}$$

The typical calculated $\Delta\langle r_{iso}^2 \rangle$ values for valance states are around 1 Å^2, for 3s Rydberg states on the other hand values are an order of magnitude higher [133]. This can be clearly seen in Figure 5.7(c), where the isotropic invariant of the second-moment electronic charge distribution tensor $\Delta\langle r_{iso}^2 \rangle$ is smaller than 1.5 Å^2 for the two excited $\pi\pi^*$ states at all N-H bond distances. The blue curve in this plot corresponding to the 3s/$\pi\sigma^*$ state clearly shows a different behaviour, where $\Delta\langle r_{iso}^2 \rangle$ falls significantly from 15.5 Å^2 to 4.1 Å^2 over the investigated N-H bond length.
This is a very important result, for it shows that the Rydberg character of the mixed 3s/$\pi\sigma^*$ state drops rapidly and significantly with bond extension. Based on this reduction the physical properties of this mixed state will also change dramatically. A relevant example of this property evolution is that in a simple atomic-like approximation the single-photon ionization of a 3s Rydberg character in the vertical Franck-Condon (FC) region would lead to photoelectron partial waves of primarily p character. This would manifest itself as a peaking along the laser polarisation axis in the experimental recorded VMI images and resulting in a high β_2 value close to 2. Moreover, the Rydberg state character appears as a narrow peak in the photoelectron spectrum due to the great propensity for diagonal ionisation from this state. The narrow peak is a distinct and useful tool to identify the 3s/$\pi\sigma^*$ state, which can be clearly seen in the ionisation from the S_2 state in aniline, see Chapter 4 [110].
In indole this strong peaked feature in the 3s/$\pi\sigma^*$ state is not present in the observed photoelectron spectrum in Figure 5.4. In contrast to aniline the 3s/$\pi\sigma^*$ state in indole is only populated indirectly via non-adiabatic decay at already extended N-H bond distances. Once the distance is enlarged the characteristic features of the 3s Rydberg character can not be observed anymore due to its significant reduction and the simultaneously growing σ^* valance character within the 3s/$\pi\sigma^*$ state.
At last in Figure 5.7(d) the isotropic polarisability volume ($\bar{\alpha}$) for each electronic state is displayed and can be calculated using the trace of the electronic polarisability tensor:

$$\bar{\alpha} = \frac{1}{3} \left(\alpha_{xx} + \alpha_{yy} + \alpha_{zz} \right) \tag{5.6}$$

The $\bar{\alpha}$ values for the S_0 ground state (black) and the two $\pi\pi^*$ excited states ^1L_a (green) and ^1L_b (red) are broadly constant over the bond distance in Figure 5.7(d) and it is worth mentioning that the values for ^1L_a and S_0 with ~ 16Å^3 is bigger than the value for ^1L_b with ~ 3Å^3. In contrast to the aforementioned constant polaris-

ability volumes the $\bar{\alpha}$ values for the 3s/$\pi\sigma^*$ state (blue) is dramatically decreasing with increasing N-H bond length, which is again a signature of the change from the 3s Rydberg towards the σ^* valence character within the excited state itself.

Photoionization cross-section vs. isotropic polarizability volume

Time-resolved studies of polyatomic molecules investigate population and energy transfer from initially prepared electronic states to final photoproducts by using photoionisation of reactants performed with state-of-the-art spectroscopy techniques. Due to the complexity of these molecular systems, many non-adiabatic decay pathways between the different electronic states can be energetically accessible and active. However, each of those contributing states along the reaction coordinates has a significantly different ionisation cross-sections and accordingly a distinct detection sensitivity, which is furthermore also dependent on the contributing Franck-Condon factors and influenced by the molecular alignment originating from the excitation of pump pulse.

Time-resolved photoelectron imaging is a powerful and highly differential technique to study the complex intramolecular mechanisms and the subtle details of the various non-adiabatic pathways. Nevertheless even with those state-of-the-art measurements it is very challenging to examine qualitatively much less quantitatively the photoproduct branching ratios of the various decay pathways. Also theoretical approaches to calculate the ionisation cross-section of excited states in bio-molecules like indole are very demanding and up until now not very reliable. This being the case it is desirable to find elementary connections between the photoionisation cross-section and physical properties that are a comparatively easy computationally result.

Vallance and co-workers have found and calculated a robust correlation between ground state electron impact ionisation and isotropic electronic polarisability volume [171]. They combined the experimentally determined ground state ionisation cross-section with calculated electronic polarisability volume for 27 molecular systems [171, 172]. Since this is a good approach to at least qualitatively understand the relative branching ratios of the non-adiabatic decay pathways, the isotropic polarisability volume of 10 more molecules is theoretically investigated in this study. Here the computationally extracted values are compared to a new quantity taken from experimental works - their photoionisation cross-section. The correlation between those two quantities for all 37 molecules at a photon energy of 11.5 eV is visualised in Figure 5.8. The dataset visualises linear behaviour that can be fitted with a correlation factor of 0.93. This clear link might be reasoned with the fact that both polarisability volume and photoionisation cross section are similar dependent on the electronic dipole matrix.

In the context of the present indole study the polarisability volume was computationally calculated for both ^1L_a and ^1L_b valence states and for the mixed $3s/\pi\sigma^*$ Rydberg/valence state. This is plotted in Figure 5.7. The polarisability volume, plotted against N-H bond distance, shows an order of magnitude difference between the pure valence states and the mixed state at short distances, where the Rydberg character of $3s/\pi\sigma^*$ is dominant. Initially, not taking Franck-Condon factors or excited state alignments into consideration, the basic conclusion can be drawn that the ionisation cross section of the Rydberg contribution of the $3s/\pi\sigma^*$ state is at least an order of magnitude bigger than the one of ^1L_a and ^1L_b at the ground state geometry.

Based on no experimental measured evidence of the Rydberg features of the $3s/\pi\sigma^*$ state in the indole data, it can be concluded that $3s/\pi\sigma^*$ is only populated via non-adiabatic relaxation dynamics at extended N-H bond. This manifests itself in the reduced $3s/\pi\sigma^*$ DAS amplitude that originates from the valence character of the excited state.

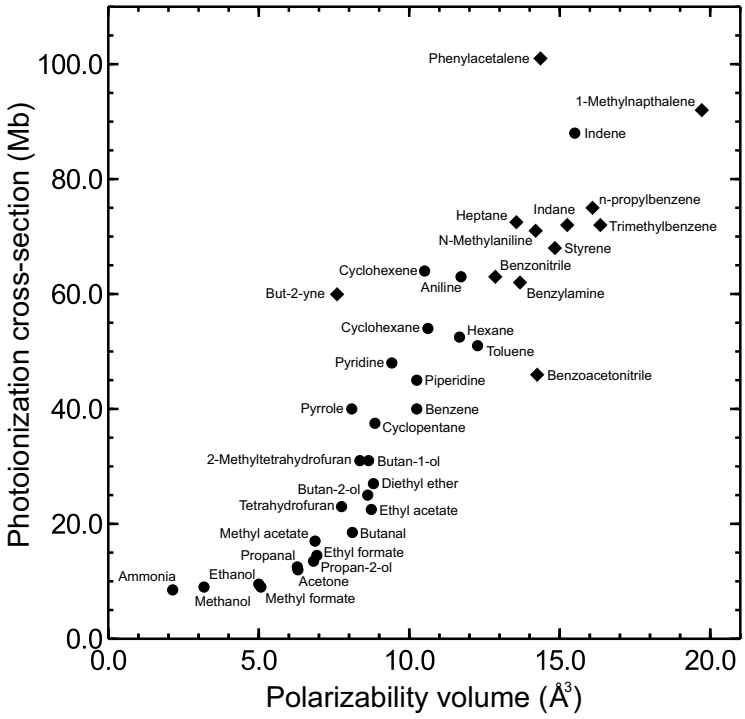

Figure 5.8: *Ground state photoionisation cross-section (at 11.5 eV) vs. isotropic polarisability volume for 37 small molecules.*

5.4 Discussion

The results of the decay associated spectra analysis for both pump wavelengths 267 nm and 258 nm shown in Figure 5.5 are very similar to each other. The decay lifetimes and the related shapes and positions of the spectral characteristics in the DAS plot are also in good agreement with previously recorded TRPES data of indole at 273 nm and 249 nm [24]. Here the time-resolved photoelectron spectrum of gas-phase indole was measured with a magnetic bottle spectrometer and therefore marginal variations in the relative peak amplitude might be resulting from the energy dependent transmission efficiency between the two used techniques.

In Figure 5.5 a positive amplitude feature of the τ_1 DAS can be seen in the region > 0.6 eV. Based on the various studies of band composition in this spectral region performed on crystalline indole [167], indole on polymer films [168] and indole in propylene glycol glass [173] this positive feature of the decay time constant τ_1 can be attributed to the directly excited ^1L_a state.

In the lower kinetic energy region < 0.6 eV the τ_1 DAS displays a pronounced negative amplitude for both excitation wavelengths. Negative features in the decay associated spectrum are a consequence of the fitting procedure applied to the photoelectron data, where all exponential decay functions originate from time zero (pump-probe delay). Here the negative amplitude in the τ_1 DAS is correcting for the positive amplitude corresponding to the longer lived fearture of τ_3 in the low kinetic energy region at small pump-probe delay times, because it does not really originate from time zero. The compensation with the negative amplitudes is clear evidence for sequential dynamics taking place in the molecular system. In this particular case it shows in the low kinetic energy region < 0.6 eV the non-adiabatic population transfer from the initially prepared ^1L_a state to the energeticly lower lying ^1L_b. This process has been theoretically studied and supports these experimental findings [24, 137, 151].

On the grounds of the studies outlined above the τ_3 DAS can be assigned to the ^1L_b state, which proves to have a long lifetime based on the experimentally determined long decay constant τ_3. Since the amplitudes in the lower energy region, especially between 0.05 - 0.3 eV (where just the τ_1 and τ_3 DAS amplitude are present) do not exactly match each other, it has to be concluded that the ^1L_b state is additionally populated directly in the Franck-Condon region besides the population growth following electronic relaxation from ^1L_a. In the case of 267 nm pump DAS spectra this direct excitation of the energetically lower $^1\pi\pi^*$ valence state is more compelling, because of the relative smaller negative τ_1 amplitude compared to the 258 nm pump case. It can be also reasoned with supporting absorption band decomposition studies carried out in indole in solid matrices [173].

In addition to the already outlined evidences for the electronic coupling between the two $^1\pi\pi^*$ valence states $^1L_a/^1L_b$, the angle-resolved data of the time-resolved

photoelectron imaging method provides further confirmation for the non-adiabatic dynamics. The temporal evolution of this photoelectron angular distribution (PAD) proves to be sensitive to changes in the excited state electronic character, as illustrated in the literature for a range of molecular systems [24, 134, 135, 174].
In order to interpret the temporal evolution of the PADs it is judicious to look at specific energy regions in the DAS plot. In both DAS plots in Figure 5.5 three distinct and already mentioned regions (see Section 5.2.2) can be found. In the low kinetic energy region between 0.05 - 0.3 eV, the τ_2 spectrum has an amplitude of zero. Consequently, the whole temporal development of the anisotropy parameter β_2 of the photoelectron is purely based on the temporal evolution of the electronic ^1L_b state character. This fast temporal rise of β_2 is observed for both pump wavelengths and plotted in Figure 5.6(a), where an exponential fitted rise time of $\sim$ 100 fs can determined.
In addition to this result a very fast decaying signal for β_2 in the energy region between 0.70 - 0.95 eV is detected, where the only contributing amplitude of the DAS is given by the τ_1 component that is attributed to the decay of the ^1L_a excited state. Here a fast exponential decay time of β_2 in this high kinetic energy region with $\sim$ 100 fs is observed. This is compatible with the rise time of β_2 in the low energy region. As a consequence, strong electronic $^1L_a/^1L_b$ coupling can be concluded, leading to ultrafast decay of the initially prepared ^1L_a state with subsequent population increase in ^1L_b following electronic relaxation.
Hereafter the experimental information obtained about the τ_2 DAS time constant is described. The lifetimes of τ_2 for the 267 nm and the 258 nm pump wavelengths are extracted from the fit of the photoelectron data to be 1.0 ps and 0.9 ps respectively. In Figure 5.9 the τ_2 lifetimes of this experiment and the ones from the literature [24] are displayed against the photon energy of the excitation pulse. This graph shows a clear linear fall of the τ_2 lifetime taking the two additional data points from the previous TRPES measurement of 1.2 ps (273 nm) and 0.7 ps (249 nm) into account. Formally the τ_2 DAS time constant was found to be corresponding to the decay of the $3s/\pi\sigma^*$ state, that was non-adiabatically populated from the directly excited ^1L_a state on an ultrafast timescale of less then 100 fs. This decay is a competing process to the ultrafast population transfer from ^1L_a to ^1L_b described earlier.
In the H atom photofragment translational spectroscopy study by Ashfold and coworkers, an energetic offset for direct N-H bond breaking along the $3s/\pi\sigma^*$ potential energy curve was recorded to be 263 nm [159]. On the basis of this result the pump wavelengths 258 nm and 267 nm used in this TRPEI study was chosen to excite indole above and below this onset threshold respectively to ultimately understand the role and fate of the $3s/\pi\sigma^*$ state. The assumption for the experimental results was to record a difference in the time-resolved photoelectron spectra for both wavelength, since below the energetic onset the pathway along the $3s/\pi\sigma^*$ potential

energy landscape should be energetically inaccessible. The actual recorded data of indole in this present investigation, however, shows no difference between the two pump energies. In the case of 258 nm excitation one would at least expect that some population on the 3s/$\pi\sigma^*$ surface the would follow the dissociation pathway along the N-H bond. Detecting the same spectral features for 267 nm excitation is at first unexpected. In the previous TRPES study ([24]) this observation was explained by assuming that the activation energy, which had to overcome a small potential hill on the 3s/$\pi\sigma^*$ surface along the N-H bond length, was not high enough and that other decay pathways must be open. Two objective arguments indicate otherwise. For one, a conical intersection at very short N-H bond distances connecting the 3s/$\pi\sigma^*$ state to an other electronic state was not found. A second reason against the assumption of an energetic switch from below the potential barrier to above it and therefore a fully open channel is the linear fall of the τ_2 lifetime with rising pump photon energy, shown in Figure 5.9.

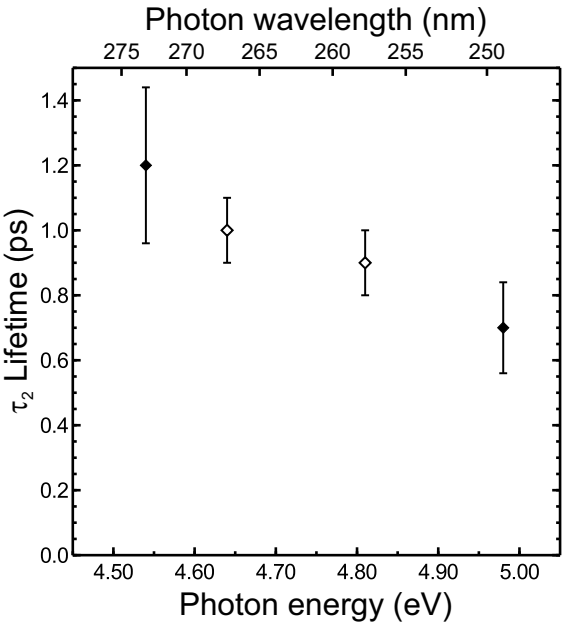

Figure 5.9: *Exponential decay lifetime τ_2 are plotted as a function of pump excitation energy used in this experiment (blank rhombus) and from the literature [24] (filled rhombus).*

In this context, an additional supporting argument disproving the potential barrier hypothesis is the missing features of the 3s Rydberg component from the overall mixed Rydberg/valence state (both in the τ_2 DAS and in the PAD). At short N-H bond distances the 3s Rydberg character is dominant in the overall electronic state, which is supported by theoretical calculations shown in Figure 5.7. This Rydberg state gives rise to an energetically narrow photoelectron feature in the corresponding DAS, as seen in other molecules like aniline [174] and leads to a high positive β_2 anisotropy value in the same energy region. The fact that neither of these features can be detected at either of the investigated pump wavelength leads to the conclu-

sion that the original estimated barrier hight of the $3s/\pi\sigma^*$ along the N-H coordinate must be corrected to lower values. Based on this strong evidence and the fact that all spectral features in the three DAS obtained at 267 nm and 258 nm are identical, it can be validated that for both excitation wavelengths above and below the N-H fission threshold of 263 nm the $3s/\pi\sigma^*$ state is only populated via a non-adiabatic process at extended N-H bond distances.

It is now of interest to understand the H atom photofragmentation process in the context of the data from the complimentary TRPEI study. The current explanation for the wavelength dependent propensity for direct N-H bond separation is the speed and rate with which the electronic wavepacket samples and eventually leaves the conical intersection connecting the $3s/\pi\sigma^*$ state with the electronic S_0 ground state. In the literature this CI is theoretically well established to be located at large N-H bond distances > 1.8 Å[148, 150, 153]. If the motion of the wavepacket transversing the CI is increasing due to the rise in photon energy, non-adiabatic population transfer to S_0 is becoming less likely and leads to an enhanced probability for direct N-H bond fission.

It is worth mentioning that the long τ_2 decay lifetime of ~ 1 ps, which is too long for a pure N-H vibration mode, can be not fully explained with this simple picture. In the very recent literature, however, similar "long" lifetimes for the $3s/\pi\sigma^*$ state have been observed that are compatible with the measured timescales for H-atom detachment in photoexcited indole at 250 - 260 nm [175, 176]. This is also in agreement with the isotropic H atom recoil findings resulting from N-H bond dissociation along the $3s/\pi\sigma^*$ surface [159].

Another explanation for the origin of the τ_2 DAS lifetime (rather than the population of $3s/\pi\sigma^*$) might be an ultrafast intramolecular vibrational redistribution (IVR) on the ^1L_b excited state surface. In other aromatic molecular systems IVR processes have been reported on a sub-ps time scale in the literature [80, 105, 110, 129, 130]. It is also true that this study is done > 2150 cm^{-1} above the ^1L_b origin [177] and therefore higher than the determined IVR thresholds in other similar molecules [178]. Moreover, several studies observing ultrafast IVR have found no link to a significant temporal change in the PAD data [80, 105, 110, 179].

The β_2 values of indole for both excitation wavelengths in the photoelectron energy region between 0.3 - 0.7 eV show a ~ 1 ps rise time (in Figure 5.6(b)). Since IVR does not cause a dynamical change in the PAD, the dynamical increase in β_2 must be a signature of the decaying $3s/\pi\sigma^*$ state contributing to the whole PAD in this middle energy region. Based on this result it can be definitively concluded that the τ_2 DAS ~ 1 ps is the decay constant of the $3s/\pi\sigma^*$ excited state for both pump wavelengths.

In summary, and on the basis of the comprehensive experimental and theoretical present studies in this chapter one can summarise that the initial population, the

dynamical process and ultimate fate of the 3s/$\pi\sigma^*$ excited state in indole is as follows. First, 3s/$\pi\sigma^*$ is populated non-adiabatically at extended N-H bond distances (not in FC region) via the optically "bright" and initially (in the Franck-Condon region) excited ^1L_a valence state. After this population transfer, the further pathway is determined by the overall photon energy in the molecular system affecting the wavepacket dynamics in the region of the conical intersection connecting 3s/$\pi\sigma^*$ and S_0. At a pump wavelength of 258 nm the molecule experiences N-H bond fission and/or relaxation to the ground state and at 267 nm it most likely undergoes internal conversion to S_0.

The long τ_2 decay lifetime of 3s/$\pi\sigma^*$ ($\sim$ 1 ps) might be explained with a population firstly circulating in the upper conical part of the CI between 3s/$\pi\sigma^*$ and S_0 at extended N-H bond distance before continuing to relax via one of the suggested pathways. Comparable behaviour has been previously reported in the $\tilde{A}$ state dissociation of ammonia [180, 181] and another supporting analogy from the recent literature is the "roaming" mechanism [182, 183].

The eventual fate of the 3s/$\pi\sigma^*$ can not be determined conclusively without extensive computational dynamical multi-state simulations. However, also due to the detection sensitivity debate it can be stated that although the amplitude of τ_2 DAS for 3s/$\pi\sigma^*$ is relatively little based on small polarisability volume and the disadvantageous FC factors for ionisation, the mixed 3s/$\pi\sigma^*$ Rydberg/valence state might nevertheless play an important role in the relaxation process in UV excited indole.

5.5 Conclusion

The experimental study of gas-phase indole was conducted with the highly differential time-resolved photoelectron imaging technique using a $(1 + 1')$ excitation (258 nm or 267 nm) and ionisation (300 nm) process and was supported by theoretical ab initio calculations. The comprehensive and complimentary energy- and angle-resolved data of indole reveals new details about the dynamical physical processes that are potentially responsible for the photostability of the molecule.

Initially the ^1L_a valence state is populated by direct one-photon absorption undergoing a subsequent ultrafast decay process of $\sim$ 100 fs. Two competing non-adiabatic pathways are energetically possible, to the energetically lower lying and long lived ^1L_b valence state or to the mixed $3s/\pi\sigma^*$ Rydberg/valence state, which has a decay lifetime of $\sim$ 1 ps. On the latter potential energy surface population remains on the upper cone of the CI at extended N-H bond distances for a relatively long time, before indole dissociates an H atom and/or relaxes into the electronic ground state.

The theoretical calculations of this study support, on the one hand, the complex experimental results and their interpretation by revealing the drastic change in electronic character of the $3s/\pi\sigma^*$ Rydberg/valence state with N-H bond extension. On the other hand they address the challenges of spectroscopic detection of highly mixed Rydberg/valence states generally in a wide range of molecules. As a consequence, investigating these mixed electronic states with less differential spectroscopic techniques and determine their total relevance in the overall relaxation dynamics has to be done with great care in order to fully understand the photostability and protection function of "model-chromophore" systems.

Finally, these aforementioned experimental challenges to determine the ultimate fate of the Rydberg/valence states can be solved by mapping the full dynamical relaxation process to the electronic ground state. This is possible if time-resolved photoelectron imaging is performed using a higher energetic photon to probe also the non-adiabatic relaxation to S_0. The generation of these so called "vacuum ultra violet" (VUV) high energy photons is done in a challenging four wave frequency mixing (FWFM) process in noble gases and the results of the endeavours are explained in details in Chapter 6.

Chapter 6

Generation of vacuum ultraviolet light - the new tool in the lab

This chapter presents the generation and characterisation of new light source in the laboratory - the fifth harmonic frequency of the Ti:Sapphire laser. Firstly, the fundamental underlying third order nonlinear processes of the vacuum ultraviolet (VUV) light generation will be described in detail. Here four wave frequency mixing in noble gases was deployed to create VUV laser pulses. Secondly, the construction of the newly built interaction gas cell and vacuum chamber will be explained. This was used for the VUV light generation, characterisation and propagation into the main interaction chamber of the existing TRPEI spectrometer. The highest frequency conversion efficiency of the VUV light was achieved in a non-collinear beam geometry of both pump beams. Furthermore the first results of photoelectron imaging in combination with the new light source will be outlined at the end of this chapter, which demonstrates the functionality and the performance of the new tool in the laboratory.

6.1 Motivation

Time-resolved photoelectron imaging unites the possibility of measuring the temporal evolution of molecular energy states, by simultaneously mapping all their characteristics by collecting spectral and angular resolved information. This can be obtained by detecting the recoiling photoelectrons after excitation and ionisation with two pump and probe femtosecond laser pulses. Nevertheless, this highly differential spectroscopic technique is limited by the energy of the probe pulse which restricts the observation of the full dynamical process from reactants to final products. The vibrational transition strength between the ground state and the excited state of the molecular system is defined by the overlap of the vibrational wavefunctions of these two states. The square of the pure vibrational overlap integral is called the Franck-Condon factor [184] (a detailed description of the Franck-Condon principle can be found in chapter 2). These vibrational transitions are dependent on the pulse energy leading to the potential restricted view of the TRPES technique. An example of this is displayed in Figure 6.1

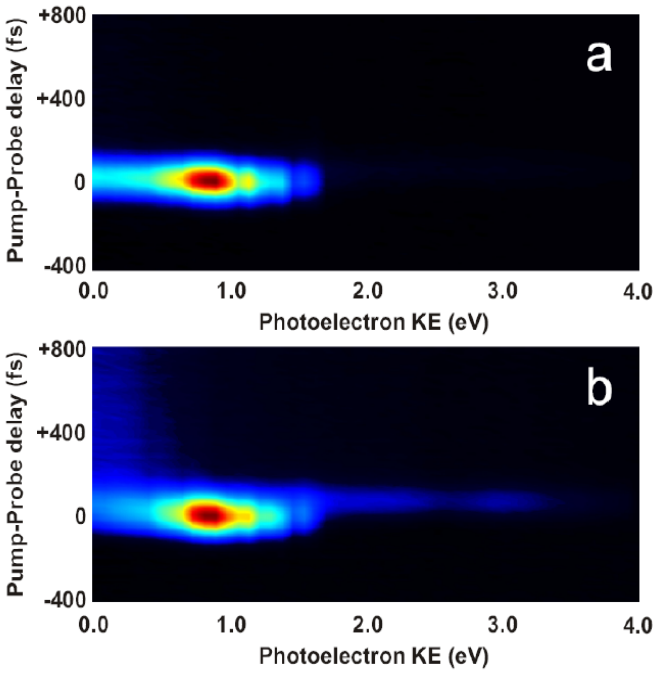

Figure 6.1: *TRPES data (colour-map intensity plot) from 1,3-butadiene obtained at two different probe intensities, namely in a) 350 nJ of a 267 nm probe pulse for a $(1+1')$ process and in b) 2.5 μJ for a $(1+2')$ process. [Spectra recorded by D.Townsend]*

The TRPES spectrum is plotted as a function of pump-probe time delay in fs and the photoelectron kinetic energy in electron volts (eV). In Figure 6.1 (a) and (b) the TRPES spectrum from 1,3-butadiene is acquired by using a 200 nm pump pulse of energy 20 nJ to excite the molecule from the electronic ground state, S_0, to the electronic excited state, S_2. The difference between the two obtained spectra is the

pulse energy in the 267 nm probe pulse. In Figure 6.1(a) the spectrum was recorded with a lower pulse energy of $E = 350$ nJ, leading to a photoelectron spectrum, which only shows the fast (< 100 fs) non-adiabatic decay of the S_2 excited state and is unable to map the S_1 excited state, into which the S_2 state couples. Although the energy of the 267 nm probe pulse (4.64 eV) is high enough to ionise the S_1 excited state in principle, the Franck-Condon (FC) overlap of the S_1 state, which is highly vibrationally excited, and the accessible vibrational levels of the first cation state D_0, is very small. As a result, the probability of a transition between S_1 and D_0 is negligible. The dominating $(1 + 1')$ process from the ground state, across S_2, to D_0 is illustrated in Figure 6.2 with the arrows a) by showing a good FC overlap due to the same vibrational wavefunctions.

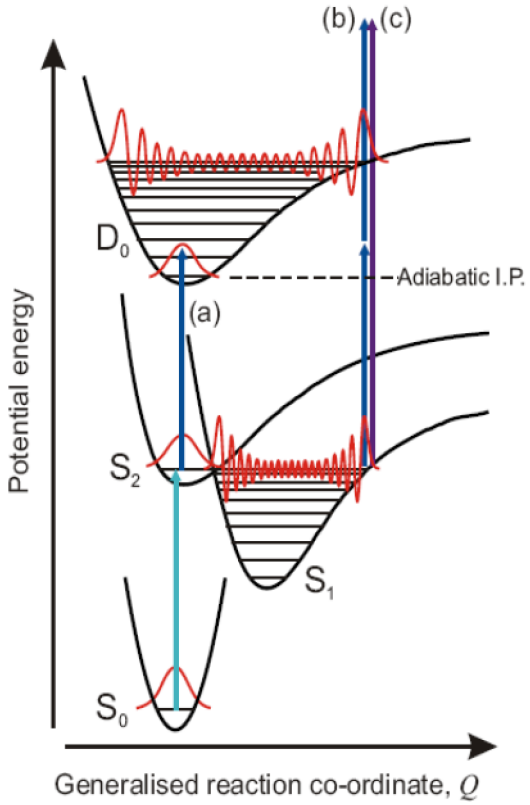

Figure 6.2: *Sketch of the Franck-Condon principle leading to the transitions between electronic states displayed by vertical arrows. The schematic vibrational wavefunctions are shown in red. For simplicity reasons, a stationary state representation is used in place of a wavepacket picture.*

In Figure 6.1(b) the TRPES spectrum was acquired with a higher pulse energy of E = 2.5 μJ, leading to more spectral features due to the significant increase of the two photon absorption probability of the 267 nm probe pulse. The $(1 + 2')$ process, illustrated with the arrows b) in Figure 6.2, allows ionization to a higher vibronic state in the cation D_0 from the highly vibrational excited state S_1, leading to the display of the temporal evolution of S_1 in the spectral region between 1.7 - 3.4 eV. Also, the long lived electronic ground state is now visible in the energy region below

0.5 eV, with a matching rise time compared to the decay time of the S_1 excited state. In 1,3-butadiene, the cross-section for a two photon ionization is sufficiently high to result in the $(1+2')$ process, which allows the whole dynamical process from reactants to products to be revealed. The cross-section for a two photon ionization is relatively weak compared to a one photon absorption leading to low signal levels in the requested spectral area. Another argument against the use of $(1+2')$ process is the possibility of spectrally overlapping the signals of the two processes which then leads to difficulties in the data analysis. Based on these reasons, the use of a femtosecond vacuum ultraviolet (fs VUV) photon for the probe pulse in the TRPES setup is essential. With a fs VUV pulse, a measurement of the complete dynamical "landscape" would be possible with the simultaneous advantage of the bigger one photon absorption cross-section. The use of these higher photon probe energies opens up the possibilities to examine a diverse range of new molecules.

6.2 VUV light generation in isotropic media

The fifth harmonic generation (FHG) of the fundamental frequency ω of a Ti:sapphire laser uses a specific case of four wave frequency mixing (FWFM). In Section 2.5 the fundamental principles of nonlinear optical effects such as frequency conversion and phase matching based on the conservation of energy and momentum have been discussed. The third order nonlinear principles now outlined in this section are extensively described in the book "Nonlinear optical parametric processes in liquids and gases" by J. Reintjes [185] and were previously studied by Bjorklund in 1975 [186]. The interested reader is directed to this body of literature for further information.

The propagation of a light wave passing through a nonlinear optical medium can be described with the well-established wave equation, which is derived from the Maxwell equations under the assumption of a vanishing magnetic polarisation [59]

$$\nabla^2 \mathbf{E}(r,z,t) - \frac{\epsilon_r}{c^2}\frac{\partial^2}{\partial t^2}\mathbf{E}(r,z,t) = \frac{1}{\epsilon_0 c^2}\frac{\partial^2}{\partial t^2}\mathbf{P}(r,z,t) \tag{6.1}$$

This wave equation shows that the nonlinear response of the medium $\mathbf{P}(r,z,t)$ acts like a source term. Here, a light wave with different frequency components of an electric field strength $\mathbf{E}(r,z,t)$, defined in Equation 2.39, travels through an optical medium inducing a polarisation that leads to the generation of electromagnetic radiation at a new frequency. This nonlinear process is the well known four wave frequency mixing.

Four wave difference frequency mixing is a special case of FWFM, which is utilised for the fifth harmonic generation. Here three incoming waves of the frequencies 3ω (λ_{TH} = 267 nm) and ω (λ_{FF} = 800 nm) interact in a $\chi^{(3)}$ nonlinear process,

generating a fourth wave of the frequency 5ω. Since energy has to be conserved the FWDFM process can be explained with the sum of two photons of energy 3ω subtracted by one photon energy of ω creating a new photon with the energy of 5ω ($\lambda_{FH} = 160$ nm).

$$\hbar(2\omega_{\mathrm{TH}} - \omega_{\mathrm{FF}}) = \hbar\omega_{\mathrm{VUV}} \tag{6.2}$$

Considering the quasistatic approximation, the behaviour of the amplitude envelope of the generated field can be expressed as

$$\nabla_{\perp}^2 A_{\mathrm{VUV}} + 2ik_{\mathrm{VUV}}\frac{\partial A_{\mathrm{VUV}}}{\partial z} = -\frac{4\pi\omega_{\mathrm{VUV}}^2}{c^2}\mathbf{P}(\omega_{\mathrm{VUV}})e^{-i\Delta k_{\mathrm{VUV}}z} \tag{6.3}$$

Here A_{VUV} is the electric field amplitude and k_{VUV} is the wave vector. The corresponding nonlinear polarisation amplitude, $\mathbf{P}(\omega_{\mathrm{VUV}})$, for the FWDFM process can be expressed with the electric field strength defined in Equation 2.39

$$\mathbf{P}(\omega_{\mathrm{VUV}} = 2\omega_{\mathrm{TH}} - \omega_{\mathrm{FF}}) = 3\epsilon_0\chi^{(3)}\mathbf{E}_{\mathrm{TH}}^2\mathbf{E}_{\mathrm{FF}}^* \tag{6.4}$$

and is quadratically dependent on the electric field strength of the third harmonic $\mathbf{E}_{\mathrm{TH}}$ and linearly dependent on the electric field at the fundamental frequency $\mathbf{E}_{\mathrm{FF}}$. The intensity I_{VUV} of the generated vacuum ultraviolet radiation for an incident plane wave can be written as

$$I_{\mathrm{VUV}} = \frac{72\pi^4}{n_{\mathrm{TH}}^2 n_{\mathrm{FF}} n_{\mathrm{VUV}}\lambda_{\mathrm{VUV}}^2 c^2\epsilon_0^2}|\chi^{(3)}|I_{\mathrm{TH}}^2 I_{\mathrm{FF}}\frac{L^2 sin^2(\Delta kL/2)}{(\Delta kL/2)^2} \tag{6.5}$$

Equation 6.5 clearly shows that the generated VUV intensity, I_{VUV}, is a function of the $\chi^{(3)}$ of the nonlinear medium and is quadratically dependent on the third harmonic input intensity, I_{TH}, and linearly dependent on the intensity of the fundamental wave I_{FF}. Furthermore it is quadratically dependent on the interaction length L of the two beams if a perfect phase matching condition is achieved. The wave vector mismatch of the contributing waves is defined by Δk, which is

$$\Delta k = k_{\mathrm{VUV}} - (2k_{\mathrm{TH}} - k_{\mathrm{FF}}) \tag{6.6}$$

For the plane wave solution, Δk has to be zero, which leads to the phase matching condition of the FWDFM nonlinear process

$$\frac{n_{\mathrm{VUV}}}{\lambda_{\mathrm{VUV}}} = \frac{2n_{\mathrm{TH}}}{\lambda_{\mathrm{TH}}} - \frac{n_{\mathrm{FF}}}{\lambda_{\mathrm{FF}}} \tag{6.7}$$

and based on this, to an intensity maximisation of the generated vacuum ultraviolet radiation. In a variety of applications, such as the example of FWDFM in nonlinear media, the use of focused Gaussian beams is favoured over the collimated beam approach. This offers the advantage of the significant enhancement of the frequency

conversion due to the higher intensities along the interaction length L. Furthermore, with the plane wave solution, which is a good approximation for collimated waves, dictates that maximum conversion efficiency is realised only for perfect phase matching, i.e. when $\Delta k = 0$.

In the general case of FWFM with focused beams this condition is not a necessity any longer. The focused beam gains an additional phase shift by passing through the focus, which is the so-called "Gouy phase shift" [187, 188]. This phase is defined as

$$\phi_G(z) = -\arctan\frac{z}{z_R}, \tag{6.8}$$

whereby $z = 0$ is the position of the beam waist and z_R is the Rayleigh length. This length, z_R, is defined as the distance from the beam waist, w_0, in the propagation direction over which the beam radius increases by a factor of $\sqrt{2}$ [189]

$$z_R = \frac{\pi w_0^2}{\lambda_0} n(\lambda). \tag{6.9}$$

The Rayleigh length is also dependent on the refractive index $n(\lambda)$. It can be seen by Equation 6.8 that a Gaussian beam passing through the focus from $z = -\infty$ to ∞ obtains a phase shift of $\phi_G = \pi$.

In the nonlinear FWFM process waves of different frequencies, such as the incident and the generated waves, will experience a phase shift based on dispersion and the "Gouy phase shift", which causes a phase mismatch, Δk. The conversion efficiency of the four wave frequency mixing can be maximised if both effects compensate for each other. For the special case of four wave difference frequency mixing, the generated power, P_{VUV}, of the newly created wave was calculated in great detail by Bjorklund in 1975 [186] and summarised by J. Reintjes [185]. It will be just recited here:

$$P_{\mathrm{VUV}} = \frac{18 n_{\mathrm{VUV}}}{c^2 \epsilon_0^2} \frac{k_0^2 k_{\mathrm{TH}}^2 k_{\mathrm{FF}}}{k' n_{\mathrm{TH}}^2 n_{\mathrm{FF}}} |\chi^{(3)}|^2 P_{\mathrm{TH}}^2 P_{\mathrm{FF}} |F_2|^2 \tag{6.10}$$

By comparison with Equation 6.5 (intensity of the generated wave, that is based on the plane wave approximation) a lot of similarities can be observed. The VUV power here is derived from the non-depleted pump approximation and is dependent on the contributing wave vectors, $k_0 = \omega_{\mathrm{VUV}}/c$ and $k' = 2k_{\mathrm{TH}} - k_{\mathrm{FF}}$. P_{TH} and P_{FF} are the respective input powers of the third harmonic and fundamental waves which interact in the $\chi^{(3)}$ nonlinear medium. F_2 is the efficiency function that is defined by a phase matching integral. In the case of FWDFM with tightly focused beams, this phase matching condition is the same as in the plane wave approximation namely $\Delta k = 0$, if collinear propagating incident waves are considered.

6.3 The new tool in the lab - VUV light

The up-conversion of the fundamental frequency output of a Ti:sapphire laser system has been of increasing interest in recent years since a variety of pump-probe spectroscopic techniques use UV and VUV pulses to study a range of molecular systems. Previously, the frequency conversion from the infrared to the ultraviolet (or even vacuum ultraviolet) was achieved using nonlinear optical crystals and gases. Sum frequency generation in a BBO crystal (largest birefringence) is just possible down to 189 nm due to its transparency [190]. Frequency conversion with low intensity is possible down to 166 nm in different nonlinear optical crystals such as $KB_5O_8 \cdot 4H_2O$ (KB5) [191]. The creation of shorter wavelengths are restricted by the transparency of the optical crystals.
Generation of higher harmonics of the fundamental frequency of a Ti:sapphire laser in gases were produced and published in the literature. The fifth harmonic was created, with a pulse energy in the nano joule regime, within an argon filled cell by Fuss and co-workers [192]. Noack and co-workers were able to enhance the energy conversion of the FHG up to micro joules [193, 194, 195, 196].
In this section a new tool is presented for the laboratory (based on the work on Noack and co-workers) - VUV laser pulses generated in a FWDFM process in an argon filled gas cell and utilised as pump or probe beam for the spectroscopic measurements. The generation of VUV requires high input intensities of the TH and the FF wave, as can be seen in Eq. 6.5 and 6.10, whilst also requiring the suppression of other third order nonlinear effects that would quench the frequency conversion of the VUV wave.

6.3.1 Generation of the third harmonic

The efficient generation of vacuum ultraviolet radiation, in this particular case the fifth harmonic of the Ti:sapphire laser of wavelength $\lambda = 160$ nm, requires an intense UV laser radiation of 3ω frequency. This third harmonic field should be created efficiently while simultaneously maintaining the short pulse duration of the fundamental pump. The theoretical principles of second and third harmonic generation are explained in section 2.5.1. The experimental setup used for the third harmonic generation is displayed in Figure 6.3 and comprises of a combination of four optical elements.
Firstly, the fundamental p-polarised wave ω ($\lambda_{FF} = 800$ nm) passes through a 0.5 mm thick BBO crystal, which is AR-coated for 400 - 800 nm. The crystal is manufactured with a $\theta = 29°$ cut with respect to its optical axes for a maximised second harmonic generation conversion efficiency. The efficiency amounts to 35% of the fundamental pump wave, which was confirmed experimentally. The created wave at 2ω ($\lambda_{SH} = 400$ nm) is s-polarised, since it was generated in a Type I nonlinear

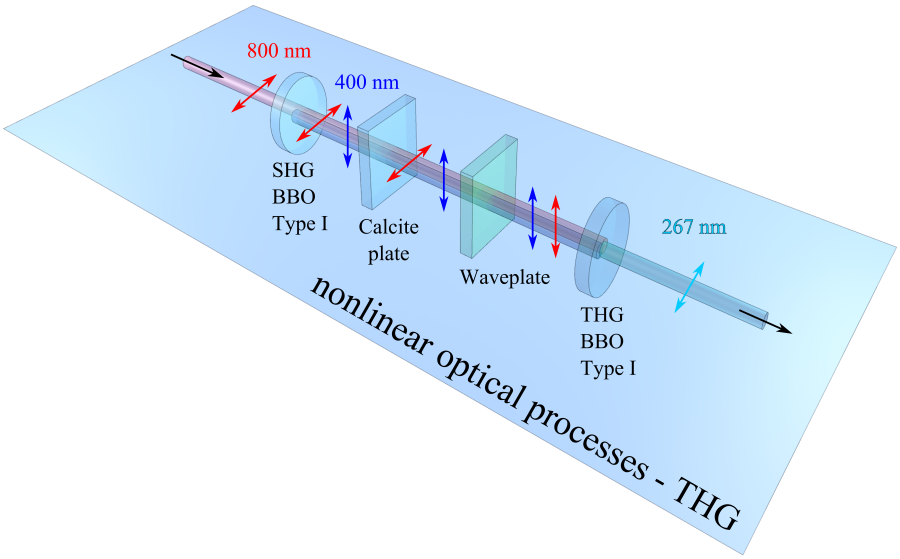

Figure 6.3: *Setup of third harmonic generation using four specific optical components. SHG is generated in the first nonlinear optical crystal. The calcite plate functions as a group velocity delay compensator between the fundamental and the second harmonic wave. The waveplate rotates both polarisations to be parallel and in order to increase the frequency conversion of the third harmonic generation in a type I mixing process within the second BBO crystal.*

process (o + o = e). Both waves are spatially co-propagating, since spacial walk-off can be neglected here. In Figure 6.3 the ω beam and 2ω beams are drawn slightly offset from each other for illustrative purposes.

A calcite plate (CP) then acts as a group velocity delay compensator between the fundamental and the second harmonic waves. Calcite is a negative uniaxial crystal with a high birefringence, where the group velocity, v_o, of the ordinary wave is greater than the group velocity, v_e, of the extraordinary wave [197]. The coarse adjustment of the group velocity delay compensation is achieved by carefully selecting the thickness of the calcite plate ($d = 2.0$ mm) and the fine adjustment is done choosing the correct incidence angle with respect to the propagation direction of the waves. Consequently, the CP compensates the velocity delay caused by the other optical components.

The third component is a zero-order dual waveplate (WP), which acts as a $\lambda/2$-plate for 800 nm and a λ-plate for 400 nm. Thus it rotates the polarisation of the fundamental wave by 90° and by 180° for the second harmonic. Both waves therefore co-propagate with the same polarisation direction.

The third harmonic wave is generated in a 0.1 mm thick BBO crystal which is cut for a Type I phase matched interaction angle of $\theta = 44°$. The created third harmonic has a wavelength of $\lambda = 267$ nm and is p-polarised. This will become necessary for the generation process of the p-polarised fifth harmonic in argon, used as the isotropic nonlinear medium.

6.3.2 Generation of the fifth harmonic

The Ti:sapphire laser system used for the four wave difference frequency mixing process of the fifth harmonic is presented in section 3.1.1. In this FWDFM process, which is explained in detail in Section 6.2, two waves of the third harmonic and one of the fundamental frequency are mixed in order to create a fourth wave with a frequency, 5ω corresponding to a wavelength of $\lambda = 160$ nm.
Since nitrogen absorbs electromagnetic radiation of wavelengths $\lambda \leq 190$ nm, the newly created 160 nm laser light needs to travel in argon, or under vacuum conditions, within a new built vacuum chamber. The experimental setup for the fifth harmonic generation is displayed in Figure 6.4, where the laser system, the important optical components and the photoelectron spectrometer are sketched.

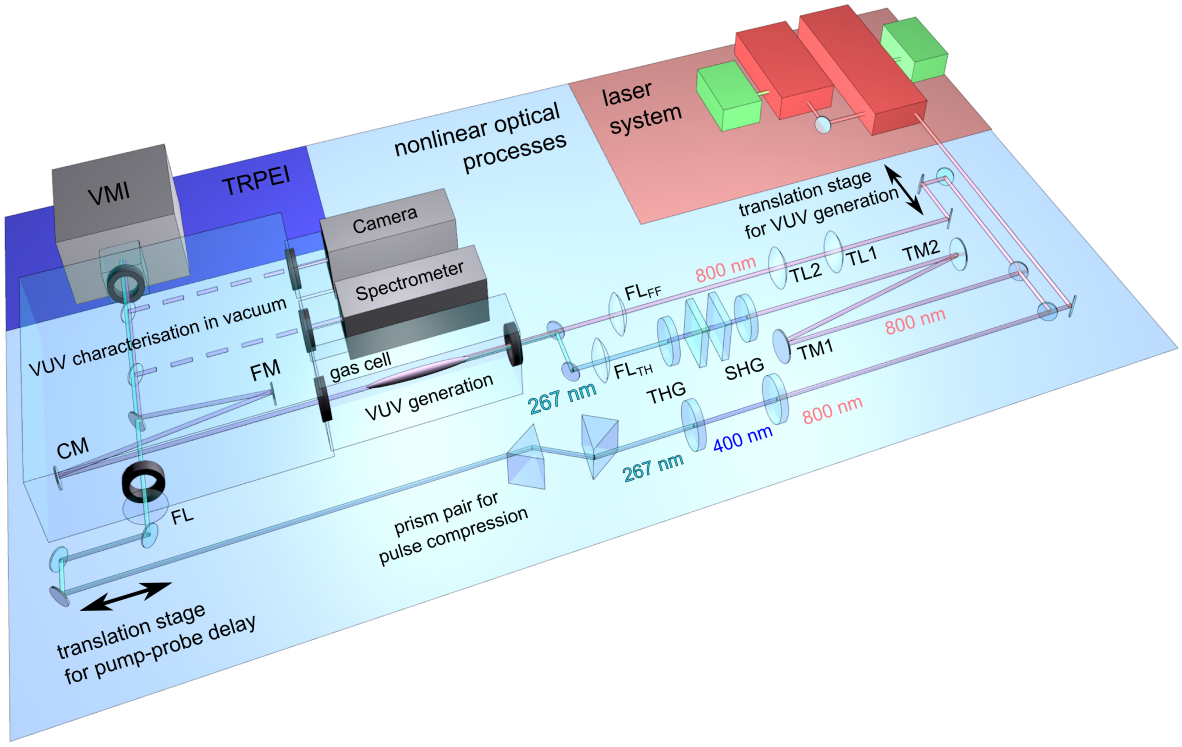

Figure 6.4: *Experimental setup of the VUV generation comprising the laser system, the nonlinear optical processes and the TRPEI spectrometer. The laser output is split into three parts of different initial intensities. The first one is used for a THG Type II generation, where the 267 nm pulse is compressed with a pair of prisms and used as a "probe" pulse for TRPEI. The second beam is telescoped down and frequency converted to 267 nm with the THG kit described in Section 6.3.1 and focused into the argon-filled gas cell. The third beam is focused into the same cell, after travelling through a translations stage, used for optimisation of temporal overlap of the TH and the FF participating in the VUV pulse generation in the FWDFM process. Characterisation tools within the new vacuum chamber allow the investigation of the created fifth harmonic wave, before it enters the TRPEI spectrometer as a "pump" wave.*

The Ti:sapphire laser output of pulse duration 55 fs, repetition rate 1 kHz and pulse energy 4 mJ, is split into three beam paths of different energies. Two parts of the output are used for the VUV generation, whilst the other one functions as the second beam for the pump-probe TRPEI spectrometer. The latter beam, displayed in Figure 6.4 in the front, has a pulse energy of 0.4 mJ (and is called the "red beam line"). This 800 nm beam is been focused through a Type I BBO crystal for SHG and subsequently travels through a second BBO crystal optimised for Type II THG, as described above. After recollimation, the pulse travels through a prism pair for optimal pulse compression and, ultimately, maximisation of the TRPEI signal of the molecular sample. The UV beam is focused with a lens (FL) into the VMI interaction chamber after having passed through two optics on a translation stage, which optimise the temporal overlap between the two femtosecond pulses of the TRPEI experiment. As mentioned above the main energy of the laser output is divided in two beam paths used for the FWDFM process that generates the fifth harmonic. In Figure 6.4 the middle beam path (called the "gold beam line") uses 50% of the fundamental laser output, so $E_{\text{pulse}}(800\text{ nm}) = 2$ mJ, to generate 267 nm with the THG kit, described in detail in Section 6.3.1. Before passing through the nonlinear optical crystals the fundamental beam is telescoped down in a ratio 3:1 using a mirror telescope (TM1: CC = 3 m and TM2: CX = 1 m). This generated third harmonic is then focused with a lens, $\text{FL}_{\text{TH}} = 0.5$ m, into the argon filled gas cell passing through a 1 mm CaF entrance window, in order to frequency mix with a "fresh" 800 nm fundamental beam.

The last beam path is called the "silver beam line" and is the third part of the fundamental laser output with a pulse energy of $E_{\text{pulse}}(800\text{ nm}) = 1.6$ mJ. This 800 nm pulse travels through a 2:1 ratio reducing lens telescope and is focused with a lens, $\text{FL}_{\text{FF}} = 0.6$ m, into the interaction gas cell, where the fifth harmonic is generated. In this "silver beam line", a translation stage with two mirrors is used to optimise the temporal delay between the two pump pulses of the FWDFM nonlinear process.

The telescope ratios and focal lengths of the lenses were chosen for two reasons. Firstly, the mirror telescope optimises the THG in the "gold line", since the power is important for the FHG, which is quadratically dependent on it. Secondly the focal lengths of the telescope mirrors and the lenses were carefully selected to maximise the generation of the 160 nm pulse. As this is dependent on the interaction lengths of the two pump pulses of frequencies 3ω ("gold beam line") and ω ("silver beam line"), which depends on the Rayleigh lengths of both input beam. The focused diameter of the fundamental beam is calculated to be 110 μm and 85 μm for the third harmonic.

Both beams generate a filamentation within the region of their foci, which is a few cm in length. Once both beams are spatially and temporally perfectly overlapped,

the filamentation region increases in length and intesity due to the interaction of the two beams, causing frequency conversion to occur. The newly generated fifth harmonic pulse 5ω travels alongside the two pump pulses, 3ω and ω, through the 0.5 mm CaF_2 exit window of the gas cell and into the newly built vacuum chamber. This is sketched in Figure 6.4 and displayed larger and from the top down in Figure 6.5. The whole VUV vacuum chamber is pumped with a turbomolecular pump from Edwards Vacuum that is backed with a rotary pump. In Figure 6.4 it is nicely shown that the vacuum chamber is separated from the gas cell with a window. The argon filled gas cell is separately pumped, this is very convenient due to the radical reduction of the evacuation time.

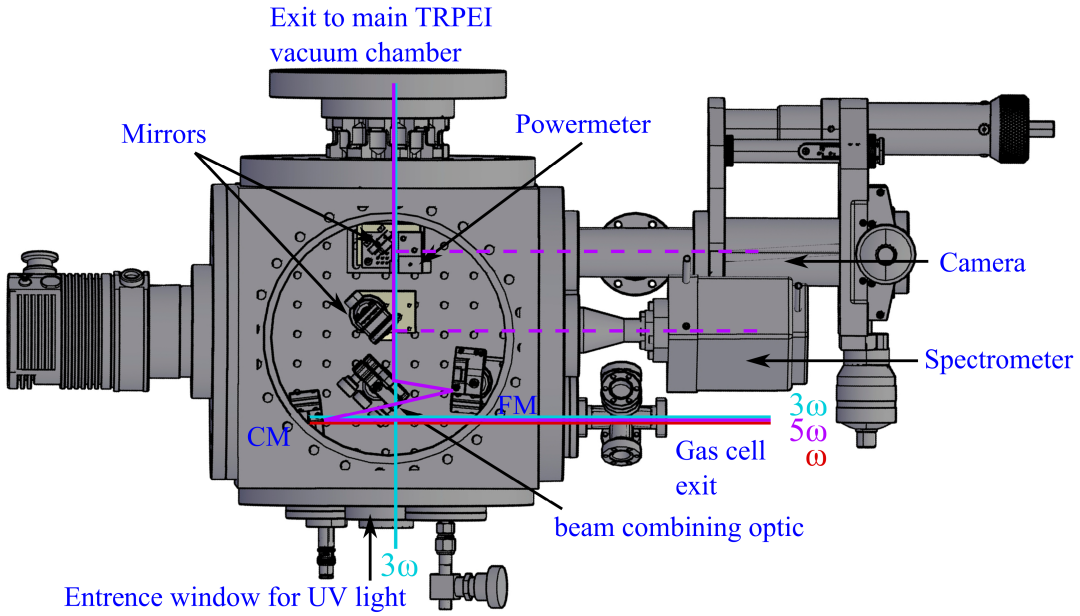

Figure 6.5: *Technical drawing of the newly designed and built VUV Chamber with all the characterisation tools and the important optical components within the chamber. The solid line beam paths represent the situation during a pump probe TRPEI measurement. The dashed lines are alternative beam pathways for characterisation purposes of the fifth harmonic pulse. The spectrum and the power of the VUV pulse can be recorded by moving the corresponding translation stages into the beam path. Vacuum pumps and tubing are not displayed based on overview reasons.*

In the four wave difference frequency mixing nonlinear process, focused input beams are used, because perfect phase matching cannot be achieved with collimated beams. With the aid of the aforementioned Gouy phase, defined in Equation 6.8, the k-vector mismatch due to dispersion can be compensated for. After the generation region, the VUV beam, alongside the two pump beams, diverge in the VUV chamber and hit the first optic. This is a curved mirror, custom coated for 155 - 160 nm, which only reflects the VUV pulse and collimates it simultaneously.
A second mirror then focuses the VUV beam into the TRPEI spectrometer directly in between the ion optics within the main interaction chamber (see Section 3.2). Before the fifth harmonic reaches the spectrometer it gets reflected off of a third

optic, which acts as a combiner of the VUV pulse and another UV pulse travelling through the optic in a perpendicular geometry directly into the spectrometer. These are the two pulses that are needed as "pump" and "probe" pulses in the time resolved measurement performed in the spectrometer. A sketch of the VUV chamber, attached to the main interaction chamber of the spectrometer, can be seen in Figure 6.6. The chamber at the front is the VUV chamber, where the fifth harmonic enters from the diagonal top right hand side.

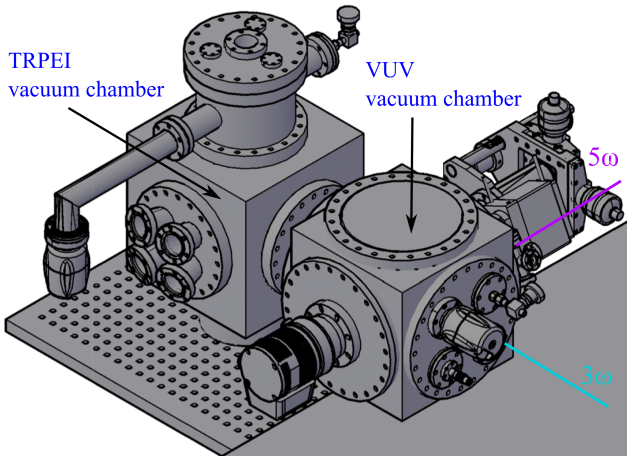

Figure 6.6: *Sketch of the VUV chamber attached to the main interaction chamber of the TRPEI spectrometer.*

Inside the VUV chamber (see Figure 6.5) there are two motorised mini translation stages. The first one holds a pick-off mirror into an argon purged VUV/UV spectrometer VS7550 from Resonance Ltd with a spectral resolution of $\lambda/\Delta\lambda = 1200$. Another pick-off mirror, and a VUV power meter (XR-16-G VUV energy probe) from Star Tech Instruments, are mounted on the second translation state, which is combined with a standard oscilloscope GW Instek with 70 MHz and 1 Gsa/s. The mirror directs the beam to a mirco USB camera, which was used for finding a rough spatial overlap of both "pump" and "probe" beam. The fine tuning was done with the TRPEI spectrometer itself in spatial focusing mode. The dashed lines in Figures 6.4 and 6.5 symbolise the alternative fifth harmonic beam pathways within the chamber.

6.3.3 Ultrashort VUV pulse generation - a closer look

The fifth harmonic generation, as previously mentioned, is performed through the aforementioned filamentation in gases using the four wave difference frequency mixing process. In the presence of a high laser intensity causing the creation of filament, several nonlinear processes can occur.
The phase matching condition is related to the dispersion in the nonlinear medium (argon), which is based on the refractive index of the medium. The intensity dependent nonlinear refractive indices n_2, defined in Equation 2.45, is based on the

temperature and the pressure of the gas used as nonlinear medium. A pressure dependent measurement of the nonlinear refractive index n_2 in several inert gases, including argon, was done by Börzsönyi *et al.* who quote $n_2 = 19.4 \pm 1.9 \times 10^{-19} \mathrm{cm}^2/\mathrm{W}$ at p = 1 bar [198]. An earlier theoretical study by the same group investigated the dispersion of 800 nm pulses in gases related to the nonlinear refractive index. This is defined by the Sellmeier coefficients (B_1, B_2, C_1 and C_2), the temperature T of the gas and its pressure p [199].

$$n^2(\lambda, p, T) - 1 = \frac{p}{p_0} \cdot \frac{T_0}{T} \cdot \left[\frac{B_1 \lambda^2}{\lambda^2 - C_1} + \frac{B_2 \lambda^2}{\lambda^2 - C_2} \right]_{p_0, T_0} \tag{6.11}$$

In Equation 6.11 the parameter λ is the vacuum wavelength, the pressure was p_0 = 1 bar and the temerature was T_0 = 273 K. In order to compensate for the dispersion in argon and achieve phase matching for the nonlinear FWDFM process, high intensity focused laser beams are used for the fifth harmonic generation with the aid of filamentation in the third order nonlinear gas dependent on the pressure regime [200, 201]. Here, three pressure regimes could be identified and examined in this study. The low pressure regime of p $\lesssim$ 1 atm is dictated by plasma effects and defocusing. The high pressure regime of p $\gtrsim$ 1 atm is dominated by high intensity nonlinear effects, such as self-focusing and its collapse due to group velocity dispersion. In the transitional pressure regime both phenomena of plasma effects and self-focusing result in a stabilised pulse propagation over a longer distance.
In 2006 Theberge *et al.* successfully performed FWDFM during filamentaion of near-infrared and infrared laser pulses in air using the aforementioned effects in the plasma. Here, the phenomena of intensity clamping and nonlinear phase locking effects were used for the generation of a stable pulse, with a good quality mode [202]. The desired goal for four wave mixing processes (in our case fifth harmonic generation) is to perform stable frequency conversion during filamentation in this above mentioned intermediate pressure regime. Here, a dynamical quasi equilibrium is governed by the interaction between the intensity dependent optical Kerr effect and low-density plasma phenomena. Specifically, the high intensity ultrashort laser pulse self focuses inside the third order nonlinear medium causing plasma formation, which then induces a defocusing of this particular laser pulse. This phenomena is called intensity clamping and this alternating self-and defocusing results in an extended filamentation length. [200, 202, 203].
In our results of the FHG in argon, this extended region of a bright filament is observed, when both femtosecond pump pulses are spatially and temporally overlapped. If both pulses exhibit a slight delay or spatial display two weak filaments can be observed, which are shorter in length. Moreover, a phase locking effect providing phase matching over a long pulse propagation length in the third harmonic generation, is predicted to occur in all other third order nonlinear processes including four wave frequency mixing [204].

6.4 Characterization and Optimization of fifth harmonic

The efficiency of the fifth harmonic generation is dependent on several parameters discussed above, that, when optimised, will lead to the highest VUV pulse energy. Figure 6.7 shows the recorded VUV spectrum generated with the FWDFM process in argon using the newly designed experimental setup that is described above. The spectrum was recorded with the VUV spectrometer from Resonance ltd. The settings for the optimal VUV data acquisition are a grating angle of -13 deg and the aperture and slit were adjusted according to the incoming intensity of the generated fifth harmonic.

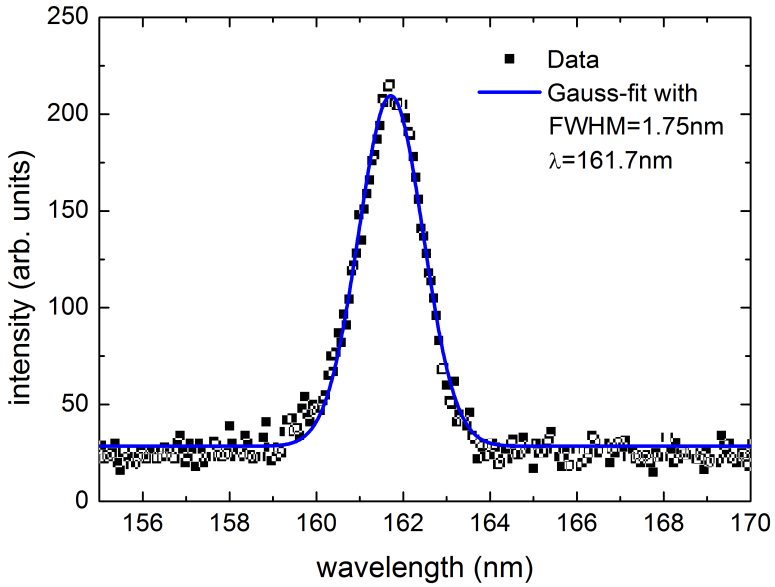

Figure 6.7: *Recorded VUV spectrum of the fifth harmonic that was generated in the FWDFM nonlinear process using the third harmonic and the fundamental of the laser output. A Gaussian fit is applied to the data with a central wavelength of λ = 161.7 nm and a FWHM = 1.75 nm.*

In Figure 6.7 it can be seen, that the generated fifth harmonic pulse exhibits a Gaussian form in the spectral domain. The central wavelength, λ_0, can be extracted from the fit centred at 161.7 nm with a full width at half maximum FWHM = 1.75 nm. Under the assumption that the generated VUV pulse is transform limited, the $\tau_{\mathrm{VUV}} = \Delta t$, for a Gaussian pulse shape with the time-bandwidth product $K = 0.441$ can be calculated with

$$\Delta t \geq \frac{K \cdot \lambda_0^2}{c \cdot \Delta\lambda} \quad \text{using} \quad \Delta\nu \cdot \Delta t \geq K \tag{6.12}$$

On the basis of the VUV spectrum in Figure 6.7 and considering the best case scenario of a transform limited pulse, the pulse duration (transform-limited) of the generated fifth harmonic is calculated with Equation 6.12 to be $\tau_{\mathrm{VUV}} = 22$ fs.

Another piece of evidence for the short pulse duration can be taken from the fundamental pump pulse ($\lambda = 800$ nm), which is generating the higher harmonics. Figure 6.8 shows the measured autocorrelation signal of the fundamental pump beam, that was recorded with a single shot auto correlator and the ACore acquisition software. The FWHM of the curve is 84.5 fs (provided during the measurement by the software) and combined with the deconvolution factor for a Gaussian pulse, $D_{\mathrm{Gauss}} = \frac{1}{\sqrt{2}}$ the pulse duration τ can be calculated with

$$\tau = \mathrm{FWHM} \cdot D_{\mathrm{Gauss}} \tag{6.13}$$

Here the 800 nm fundamental pulse has a pulse duration τ_{FF} of 59.7 fs.

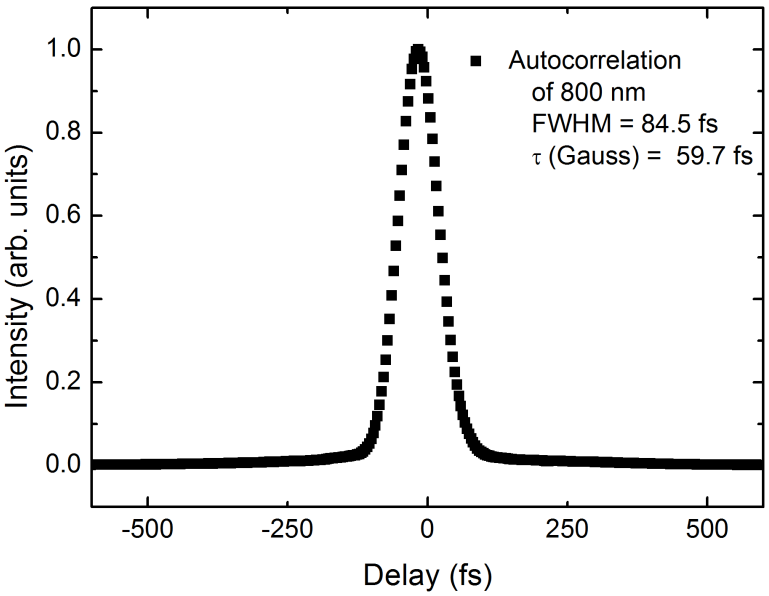

Figure 6.8: *Recorded autocorrelation signal of the 800 nm input beam of the THG and subsequent FHG with a single shot auto correlator and the ACore acquisition software. The temporal duration of the Gaussian pulse can be calculated to $\tau_{FF} = 59.7$ fs.*

The product of the envelopes of the pump pulses τ_{FF} determines the FWHM and therefore the temporal duration of the generated fifth harmonic. Starting from an simple example of the second harmonic generation, the Gaussian envelope function of both fundamental waves has to be multiplied with each other. This results in a relationship between the temporal duration of the SH and the FF pulse

$$\tau_{\mathrm{SH}} = \frac{\tau_{\mathrm{FF}}}{\sqrt{2}} \tag{6.14}$$

This relationship shows, that the multiplication of two Gaussian pulses leads to a new Gaussian pulse with a more narrow temporal width. For the fifth harmonic generation, two third harmonic pulses and a pulse at the fundamental wavelength are used in the FWDFM nonlinear process. On this basis, the total number of Gaussian

envelope functions is seven and the temporal duration of the fifth harmonic can be rated using a modification to Equation 6.14

$$\tau_{\mathrm{VUV}} = \frac{\tau_{\mathrm{FF}}}{\sqrt{7}} \tag{6.15}$$

The temporal duration of the VUV pulse can be calculated using Equation 6.15 and the results of the measured autocorrelation signal in Figure 6.8 under the assumption that all pulses exhibit similar temporal durations. To this first approximation the result is $\tau_{\mathrm{VUV}} = \frac{59.7\mathrm{fs}}{\sqrt{7}} = 22.6$ fs. This value of 22.6 fs is in very good agreement with the above calculated transform limited pulse duration $\tau_{\mathrm{VUV}} = 22$ fs of the fifth harmonic. For the results discussed above, the assumption was made that the all the fundamental input pulses exhibit the measured temporal duration of ~ 60 fs, since τ could not be recorded and verified for the third harmonic pump pulse.

6.4.1 Collinear four wave frequency mixing

The fifth harmonic wave can be generated in a beam geometry where both pump beams travel collinearly and focus at the same spot in the argon filled gas tube. The phase matching conditions can be optimised by choosing suitable focusing conditions and input peak powers of both pump beams combined with the correct pressure adjustment in the argon gas cell.

The experimental results in this section where obtained with the focusing conditions and the experimental setup described in Section 6.3.2, except for the "silver beam line". Here, the 800 nm input beam was not telescoped down, but instead two windows were used to control the chirp and therefore optimise the pulse compression as the compressor position of the regenerative amplifier was set for maximal THG power output. The input fundamental beam possesses a focus diameter of $d_{\mathrm{FF}} = 55$ μm and a Rayleigh range of $L_{\mathrm{R,FF}} = 6.1$ mm. The input pulse energy of the fundamental wave was determined to $E_{\mathrm{FF}} = 700$ μJ. The parameters for the third harmonic input beam are a focused diameter of $d_{\mathrm{TH}} = 46$ μm, a Rayleigh range of $L_{\mathrm{R,TH}} = 12.6$ mm and a pulse energy $E_{\mathrm{TH}} = 96$ μJ.

As explained above in Section 6.3.3, the pressure regime has to be selected accordingly to the focusing conditions in order to balance the high pressure physical mechanisms such as intensity induced self focusing, normal GVD and multiphoton ionisation with the low pressure effects like plasma defocusing and tunneling ionisation [200, 205]. In a single component gas such as argon the increase of frequency conversion efficiency varies monotonically according to the tightness of the beam focus [185]. A pressure dependent study of the frequency conversion efficiency was done by measuring the pulse energy of the generated VUV pulse as a function of the pressure within the gas cell. The input parameters were constant throughout the measurement, and the fundamental beam and the third harmonic beam were

focused at the same spot and temporally overlapped. Figure 6.9 shows the results of the collinear pressure dependent VUV generation in the nonlinear medium argon.

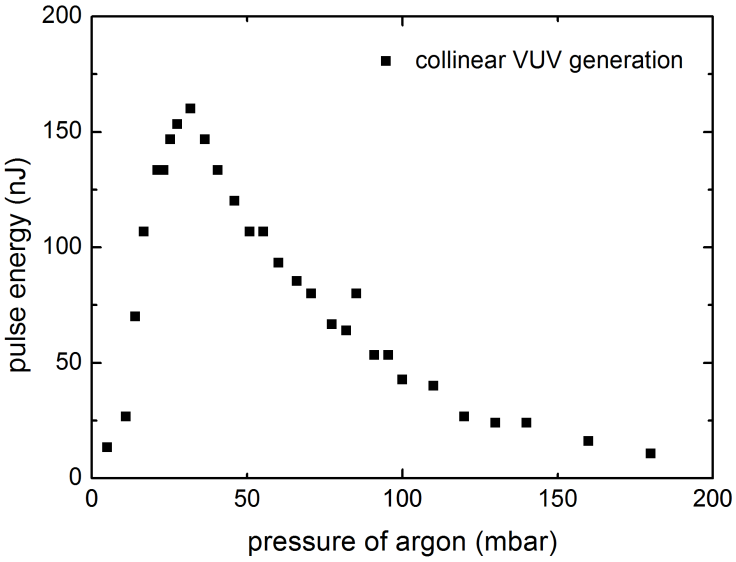

Figure 6.9: *Pulse energy of the generated fifth harmonic in nJ plotted over the argon pressure in mbar. This measurement was conducted in a collinear FWFM geometry of the two pump beams.*

The pulse energy of the generated VUV beam was determined by measuring the VUV power with a power meter combined with a standard digital storage oscilloscope (see Section 6.3.2). From the measured and background subtracted voltage, V, the generated VUV power can be calculated by also using the resistance $R = 15000\ \Omega$ and the detector responsivity $R_{res} = 0.005\ \frac{A}{W}$ for 160 nm.

$$P_{\mathrm{VUV}} = \frac{V}{R \cdot R_{res}} \tag{6.16}$$

The VUV energy can be ascertained with this power, P_{VUV}, and the repetition rate of the laser, which was set to 1 kHz. Figure 6.9 displays a fast rise in the lower pressure regime, where the interaction between the pulses and nonlinear material increases with increasing pressure. The optimum conversion efficiency in the collinear input beam geometry is found at $p = 32$ mbar. During the measurement a clear filamentation in both pump beams can be observed, which increases in length up to 10 cm if both pump beams are overlapped in space and time. This observation is a signature of the so called intensity clamping or alternating self-and defocusing effect [200, 202, 203]. The critical power, P_{cr}, for self focusing can be calculated for a Gaussian pulse dependent on the applied pressure in the following way:

$$P_{cr} = \frac{3.77 \cdot \lambda_0^2}{8\pi n_0 n_2} \tag{6.17}$$

In Equation 6.17, λ_0 is the vacuum wavelength and n_0 and n_2 the linear and nonlinear refractive index, respectively. For argon, $n_0 = 1.000357$ and the nonlinear

refractive index $n_2 = 1.27 \cdot 10^{-23} \frac{\mathrm{m}^2}{\mathrm{W \cdot bar}}$ [206]. The critical pressure for the fundamental and the third harmonic waves are $P_{cr}(\mathrm{FF}) \cong 200$ GW and $P_{cr}(\mathrm{TH}) \cong 20$ GW, respectively. The actual input peak powers of both beams in this collinear experiment are calculated with each pulse energy E_{FF} and E_{TH} to be $P_{\mathrm{FF,peak}} \cong 10$ GW and $P_{\mathrm{TH,peak}} \cong 3$ GW. It can be seen that both the input peak powers are below the threshold for self focusing, which might be the reason for the low conversion efficiency and therefore the low pulse energy. Nevertheless it can be assumed that a balancing effect, such as self focusing, also takes place in this lower pressure regime due to the observation of the extended filamentation.

6.4.2 Noncollinear four wave frequency mixing

Noncollinear four wave frequency mixing can be used in order to increase the efficiency of the third order nonlinear process in isotropic media. Here, the noncollinear phase matching makes use of the actual vector properties of the involved waves with their wavevectors $\mathbf{k}_{\mathrm{VUV}}$, $\mathbf{k}_{\mathrm{TH}}$, $\mathbf{k}_{\mathrm{FF}}$ and their vectorial mismatch $\Delta\mathbf{k}$ [185].

$$\Delta\mathbf{k} = \mathbf{k}_{\mathrm{VUV}} - (2\mathbf{k}_{\mathrm{TH}} - \mathbf{k}_{\mathrm{FF}}) \tag{6.18}$$

The Gouy phase shift that is experienced by focused beams leads to the minimisation of the wave vector mismatch $\Delta\mathbf{k}$, as described in Section 6.4.1. However in the presence of normal dispersion a fully vanishing wavevector mismatch cannot be achieved. It is therefore advantageous to introduce an angle between the two pump beams and therefore a noncollinear propagation geometry, as shown in Figure 6.10.

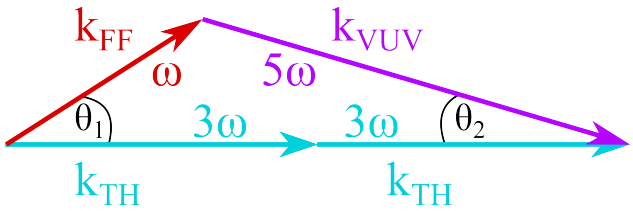

Figure 6.10: *Wave vector diagram for perfect noncollinear phase matching condition with positive dispersion. Here the geometry between the two input waves, the fundamental ω and the third harmonic 3ω and the generated fifth harmonic 5ω has no wave vector mismatch $\Delta\boldsymbol{k}$.*

In this wavevector diagram the **k**-vectors of the fundamental and the third harmonic wave propagate in different directions defined by the angle θ_1 between them. The second angle, θ_2, defines the difference of propagation direction between the fifth and the third harmonic.

Where dispersion is present, a mismatch between the **k**-vectors generally occurs. In order to achieve perfect phase matching the correct pressure has to be found

for a certain set of angles. In other words both of the phase matching angles, θ_1 and θ_2, are dependent on the type of gas, the pressure, the temperature and the wavelength of the incident beams. These angles are defined within the small angle limit by Equation 6.19 and 6.20 and are dependent on the refractive indices n and wavelengths λ of the contributing waves [185].

$$\theta_1 = \left(\frac{(n_{\mathrm{VUV}}/\lambda_{\mathrm{VUV}})^2 - [(2n_{\mathrm{TH}}/\lambda_{\mathrm{TH}}) - (n_{\mathrm{FF}}/\lambda_{\mathrm{FF}})]^2}{2n_{\mathrm{TH}}n_{\mathrm{FF}}/(\lambda_{\mathrm{TH}}\lambda_{\mathrm{FF}})} \right)^{\frac{1}{2}} \tag{6.19}$$

$$\theta_2 = \left(\frac{(n_{\mathrm{FF}}/\lambda_{\mathrm{FF}})^2 - [(2n_{\mathrm{TH}}/\lambda_{\mathrm{TH}}) - (n_{\mathrm{VUV}}/\lambda_{\mathrm{VUV}})]^2}{2n_{\mathrm{TH}}n_{\mathrm{VUV}}/(\lambda_{\mathrm{TH}}\lambda_{\mathrm{VUV}})} \right)^{\frac{1}{2}} \tag{6.20}$$

A study by Noack and co-workers shows the pressure dependency of the noncollinear phase matching angle in mrad, displayed in Figure 6.11 [207]. Here, for each given angle the pressure was adjusted to obtain maximal VUV intensity.
The curve is dependent on the focusing conditions of the fundamental and the third harmonic waves which are somewhat different to the parameters presented in this chapter. Nevertheless the graph is a good guideline for experimental measurements and it clearly shows, that with increasing pressure the phase matching angle between the fundamental and the third harmonic has to rise as well. The insert shows the pressure dependent VUV intensity at a given phase matching angle of 15 mrad [207].

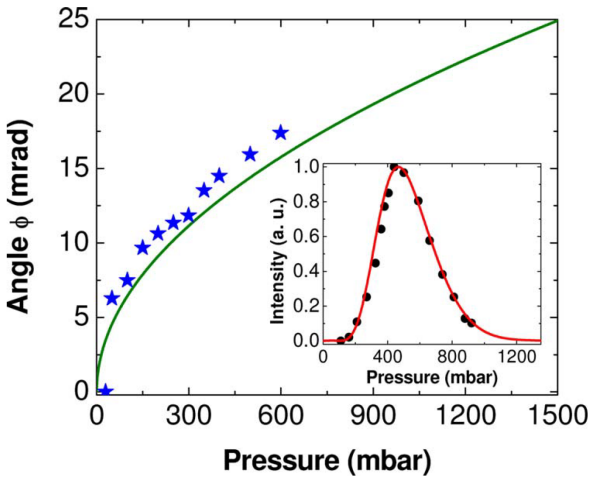

Figure 6.11: *The phase matching angle between the two incident beams is plotted over the pressure of argon used as a nonlinear medium in the FWDFM process [207]. The insert shows the VUV generation for a noncollinear angle of 15 mrad.*

The experimental approach to achieve phase matching for the nonlinear FWDFM process is to alter the pressure within the gas cell filled with argon whilst simultaneously maintaining a constant angle between the two incident waves of fixed wavelengths, 267 nm and 800 nm.
In order to set the small phase matching angle θ_1 between the incident beams correctly, basic trigonometry was utilised with the known separation, $2s$, of the middle

points of the two beam spots at the entrance window of the cell and the distance, d, from that point to the focus.

$$\theta_1 = 2\alpha = 2\tan\left(\frac{s}{d}\right) \tag{6.21}$$

The noncollinearly generated VUV pulse was realised with an experimental setup that is described in Section 6.3.2. Due to the phase matching angle, the interaction length L_{eff} of the fundamental and the third harmonic wave is reduced. It can be assumed that in the plane wave approximation L_{eff} is indirectly proportional to the phase matching angle.

The input parameters for the fundamental wave are a focus diameter $d_{\text{FF}} = 110\ \mu\text{m}$, a Rayleigh length of $L_{\text{R,FF}} = 24$ mm and an input pulse energy $E_{\text{FF}} = 1$ mJ. The incident third harmonic wave of a pulse energy $E_{\text{TH}} = 170\ \mu\text{J}$ has got a focus diameter of $d_{\text{TH}} = 57\ \mu\text{m}$ and a Rayleigh length of $L_{\text{R,TH}} = 18$ mm. A pressure dependent measurement of the VUV pulse energy generated in a noncollinear FWDFM geometry was conducted at two different fixed phase matching angles and compared with the collinear pulse energy curve. The results are plotted in Figure 6.12.

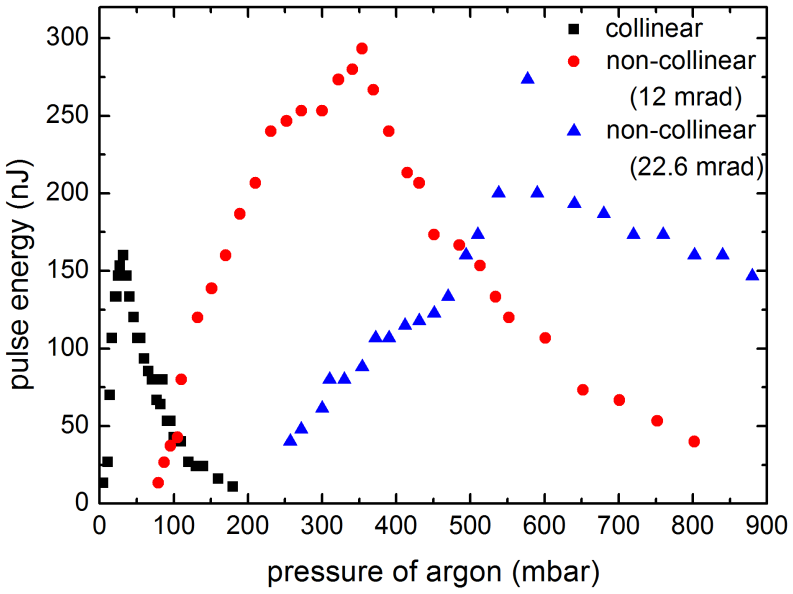

Figure 6.12: *Pressure dependent measurement of the VUV pulse energy generated in a collinear geometry (black) and noncollinear geometry of the two input beams at a phase matching angle $\theta_1 = 12.5$ mrad (red) and $\theta_1 = 22.6$ mrad (blue).*

In the noncollinear geometrical setup, the focused input pulses produce maximal frequency conversion if they are directly spatially overlapped at their foci and arrive at the same time at this position (temporal overlap). In this case there is a specific pressure matching condition for the chosen angle θ_1 between the two beams. In Figure 6.12 the maximum VUV generation at $\theta_1 = 12.5$ mrad is achieved at an argon pressure of $p = 350$ mbar. The VUV pulse energy was measured to be $E_{\text{VUV}} = 300$ nJ. The second measurement, that was performed at an angle of $\theta_1 = 22.6$

mrad, resulted in a generated VUV pulse energy of $E_{\mathrm{VUV}} = 273$ nJ at a gas pressure of $p = 577$ mbar. The graph clearly shows that higher pulse energies of the fifth harmonic can be generated using the noncollinear FWFM process compared to the collinear geometry. This is due to the fact that total phase matching condition is achieved at higher gas pressures and that the conversion efficiency is quadratically dependent on the number of argon atoms N or, equivalently, the gas pressure p [207].

$$I_{\mathrm{VUV}} \propto N^2 |\chi^{(3)}|^2 \frac{I_{\mathrm{TH}}^2 I_{\mathrm{FF}} L^2 \mathrm{sinc}^2(\Delta k L/2)}{n_{\mathrm{TH}}^2 n_{\mathrm{FF}} \lambda_{\mathrm{VUV}}^2} \tag{6.22}$$

The asymmetric pressure behaviour of the VUV pulse energy in Figure 6.12 can be explained with the quadratic pressure dependence (with a wavevector mismatch $\mathbf{\Delta k} = 0$) in Equation 6.22 and has been previously observed in the literature [207].

In the third order nonlinear medium, argon, the fifth harmonic can be generated not only by four wave difference frequency mixing ($\omega_V UV = 2\omega_{TH} - \omega_{FF}$), but also with sum frequency mixing ($\omega_V UV = \omega_{TH} + 2\omega_{FF}$). Based on phenomenological evidence the observed intensity of the VUV pulse is more strongly dependent on the third harmonic intensity than on the fundamental input intensity. Based on this fact, it can be concluded that the fifth harmonic is generated with the nonlinear difference frequency mixing process.

It is also important to consider the pressure regime where phase matching is achieved in argon for the given angles. The critical power for self focusing to occur at a gas pressure of $p = 500$ mbar is calculated with Equation 6.17 to be $P_{cr}(\mathrm{FF}) \cong 15$ GW and $P_{cr}(\mathrm{TH}) \cong 2$ GW. The actual input peak powers of the fundamental $P_{\mathrm{FF,peak}} \cong 17$ GW and the third harmonic $P_{\mathrm{TH,peak}} \cong 5$ GW are above this self focusing threshold. During the FHG in the noncollinear geometry, a clear bright filament can be observed, that is shorter in length that the one in the collinear case but is, however, slightly more intense. Based on the comparison of critical power and input power of both incident waves it is evident that the balancing effect of the intensity dependent Kerr focusing and the low pressure plasma defocusing is controlling the VUV frequency generation [202].

Further optimisation of the third harmonic generation resulted in a pulse energy $E_{\mathrm{TH}} = 220$ μJ. Using this new optimised third harmonic and the same input pulse energy of the fundamental wave of $E_{\mathrm{FF}} = 1$ mJ in the FWFM process a new record of the VUV pulse energy could be achieved. At a phase matching angle $\theta_1 = 17.7$ mrad and a gas pressure of $p = 422$ mbar the highest fifth harmonic pulse energy was measured to be $E_{\mathrm{FH}} = 613$ nJ. The energy of this generated VUV pulse is sufficient to use it as a pump or a probe pulse to perform time-resolved spectroscopic experiments.

6.5 Combination of the new light source and TR-PEI spectrometer

The time-resolved photoelectron spectrometer was augmented with the implementation of the novel femtosecond vacuum ultraviolet (VUV) light source. The functionality and performance of the combined VUV plus TRPEI imaging technique was investigated and preliminary experimental data from xenon and butadiene are presented.

The general experimental setup, which was used for the measurement of both molecules, is outlined in detail in Chapter 3. The newly generated femtosecond VUV laser pulse of $\lambda_{pump} = 160$ nm was used as a pump beam for the excitation of the systems under study. A second fs UV pulse of $\lambda_{probe} = 267$ nm was utilised for the ionisation process.

In principle, the experiment was conducted with the experimental setup that is displayed in Figure 6.4 with a minor change inside the VUV vacuum chamber. The pathway geometry inside the VUV chamber, as shown in Figure 6.5, was altered by changing the focusing mirror (FM) from a long focal length to a shorter one ($f_{FM} =$ 10 cm). Thus, the position of the mirror had to be changed as well and it is located now at the other end of the main vacuum chamber of the VMI spectrometer. The laser beam pathway for the fifth harmonic ($\lambda_{pump} = 160$ nm) now runs through the VMI interaction chamber and hits the focusing mirror, which then back-focuses the pump beam onto the molecular sample. The beam pathway of the third harmonic ($\lambda_{probe} = 267$ nm) also changed in the same way.

TRPEI measurement of xenon

The noble gas xenon was measured in a two-colour $(1 + 1')$ photoionisation process in order to evaluate the performance and calibrate the spectrometer.

Figure 6.13 shows the recorded xenon photoelectron image accumulated over a range of pump-probe time delays from Δt = -150 fs to 150 fs in 25 fs steps. The ionisation potential IP_{Xe} of xenon is 12.13 eV [208] and the total energy provided by the pump and the probe pulse is $E_{tot} = E_{pump} + E_{probe} = 7.75$ eV + 4.64 eV = 12.39 eV. The bright ring in Figure 6.13 corresponds to the two-colour signal, with the radius size being proportional to the kinetic energy of the ionised electrons $E_{kin,e^-} = E_{tot} - IP_{Xe}$.

The faint outer ring in the photoelectron image of xenon is generated by the small one-colour signal originating from three photon ionisation of the 267 nm probe pulse. The total energy provided by three 267 nm photons is $E_{tot,1colour} = 3 \cdot E_{probe} = 13.2$ eV.

Both ionisation processes are non-resonant, which means that the transition from the initial ground state to the final cation state occurs without an intermediate ex-

cited electronic state. Based on this the xenon two-colour $(1 + 1')$ photoionisation image can be used as a calibration for the system response and a cross-correlation measurement of pump and probe pulse.

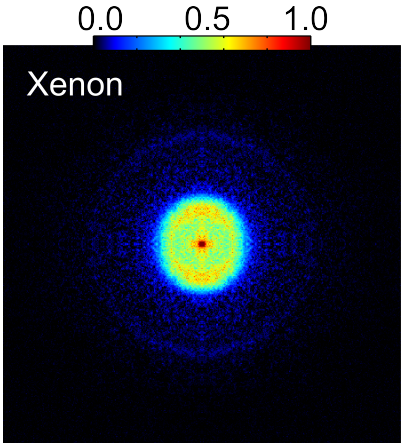

Figure 6.13: *Summation of $(1 + 1')$ photoelectron images of xenon over a range of pump-probe time delays from Δt = -150 fs to 150 fs following 160 nm excitation and 267 nm ionisation.*

The time-resolved photoelectron spectra of xenon can be obtained from the complete set of photoelectron images at different pump-probe delay times Δt applying the rapid matrix Abel inversion method (described in Section 3.3). This xenon 3D spectrum is plotted against photoelecton kinetic energy and pump-probe time delay in Figure 6.14.

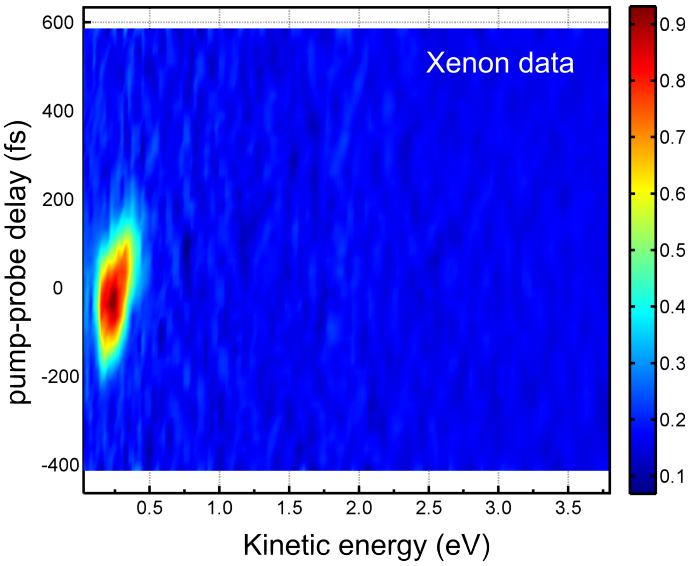

Figure 6.14: *Time-dependent photoelectron spectrum of xenon dependent on the electron kinetic energy and the pump-probe time delay obtained with 160 nm excitation and 267 nm ionisation. This data set is used for characterisation of the VUV pulse and for system calibration purposes in order to be able to analyse further data.*

The time-dependent photoelectron spectrum of xenon can be used to characterise the performance of the spectrometer, because the two-colour $(1+1')$ photoionisation process is non-resonant. The utilisation of the spectrometer in a non-resonant configuration enables a type of frequency-resolved optical gating (FROG) measurement, where detection of the cross-correlation of two laser pulses is spectrally resolved. In Figure 6.14 a FROG-type measurement between the pump pulse of $\lambda_{pump} = 160$ nm and the probe pulse of $\lambda_{probe} = 267$ nm was conducted. In an ideal case, one well-characterised laser pulse is used in order to measure the properties of the second pulse. In the xenon experiment the characteristics, such as pulse durations of both laser pulses, are not fully known. However the pulse duration of the probe pulse (267 nm) was compressed with an external prism pair by maximising the one-colour ionisation signal levels of xenon. The xenon data exhibits, as can be seen in Figure 6.14, a small spectral tilt. Since the 267 nm pulse was optimally compressed, the tilt is a signature of a slight chirp in the 160 nm pulse.
From the time dependent photoelectron spectrum in Figure 6.14 the intensity in the low kinetic energy region was plotted against pump-probe delay, which can be seen in Figure 6.15. Since the xenon data shows a non-resonant photoionisation signal, it has to be fitted with a Gaussian function. The extracted full width at half maximum FWHM = 210 fs and corresponds to the convolution of both pump and probe pulse durations.

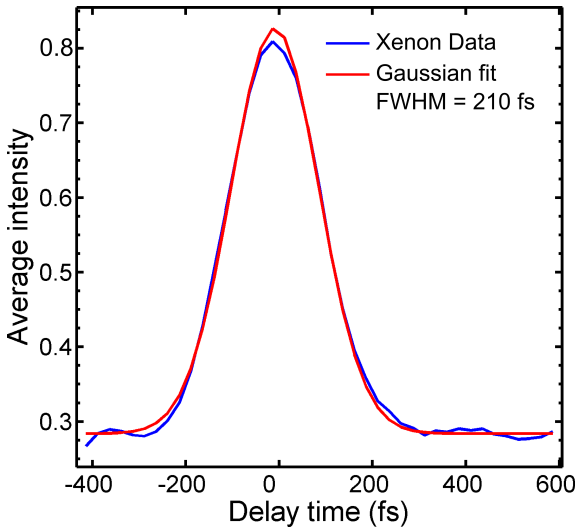

Figure 6.15: *Transient of xenon summed over the low kinetic energy region from 0.05 eV to 0.50 eV, which was fitted with a Gaussian function with a full width at half maximum of 210 fs.*

As the exact pulse duration of the probe pulse (267 nm) is unknown, no absolute value for the pulse duration can be extracted. However, it can be assumed that the fs VUV laser pulse is getting a chirp after the generation process. The CaF_2 window between gas cell and VUV vacuum chamber introduces a small positive chirp to the

VUV pulse, but the bigger contribution to the chirp most likely originates from the collimation mirror inside the VUV vacuum chamber. Although the reflectivity of the mirrors was optimised for 160 nm, the group velocity dispersion of the CaF_2 mirror substrate leads to the chirp in the pulse.
Improvements to the setup can be done with the optimisation of the beam path geometry and the minimisation of the angle of incidence at each mirror used in the VUV vacuum chamber.

TRPEI measurement of butadiene

A proof-of-concept study was undertaken by investigating the molecular system 1,3-butadiene. It is a good prototype of conjugated molecules and an excellent starting point for a performance test for the newly implemented VUV light source in combination with the TRPEI spectrometer. Its optical absorption spectrum of butadiene was studied in the ultraviolet spectrum [209, 210, 211] and its ionisation potential is 9.08 eV [212].
The first and preliminary results of $(1 + 1')$ photoionised 1,3-butadiene following a 160 nm excitation and a 267 nm ionisation step are displayed hereafter. In Figure 6.16 the summation of $(1+1')$ photoelectron images is shown in a pump-probe time delays region at $\Delta t = 0$ fs. The data was created by subtracting the one-colour pump alone and one-colour probe alone background from the overall recorded signal. It exhibits a bright intensity inner ring, which corresponds to lower kinetic energy electrons and a pair of larger, less intense rings that are a signature of faster photoelectrons.

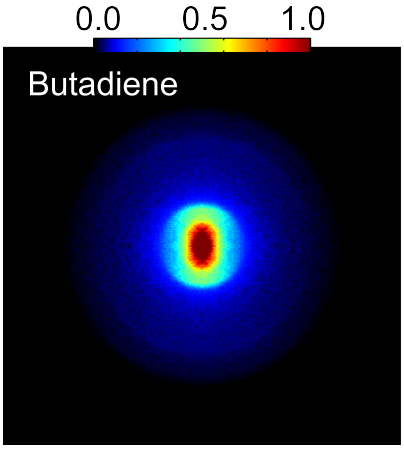

Figure 6.16: *Summation of $(1 + 1')$ photoelectron images of butadiene in the pump-probe time delays region at $\Delta t = 0$ fs following 160 nm excitation and 267 nm ionisation.*

After background subtraction the rapid Abel inversion, described in detail in Section 3.3, was applied to the photoelectron image of butadiene. The time-resolved and

kinetic energy dependent photoelectron spectrum is plotted and displayed in the top half of Figure 6.17. The bottom half of Figure 6.17 shows the 2D Levenberg-Marquardt fit to the butadiene data set using one exponential function convoluted with the Gaussian cross-correlation. The fitting routine is explained in detail in Section 3.3.2. The dashed lines in the spectrum and the fit symbolise the $(1+1')$ photoionisation cut-off energy of the 160 nm pump pulse and the 267 nm probe pulse. The total energy provided by both photons is $E_{tot} = E_{pump} + E_{probe} = 7.75$ eV + 4.64 eV = 12.39 eV. The maximal electron kinetic energy in a $(1+1')$ process is calculated with $E_{kin,e^-} = E_{tot} - IP_B = 12.39$ eV - 9.08 eV = 3.31 eV.

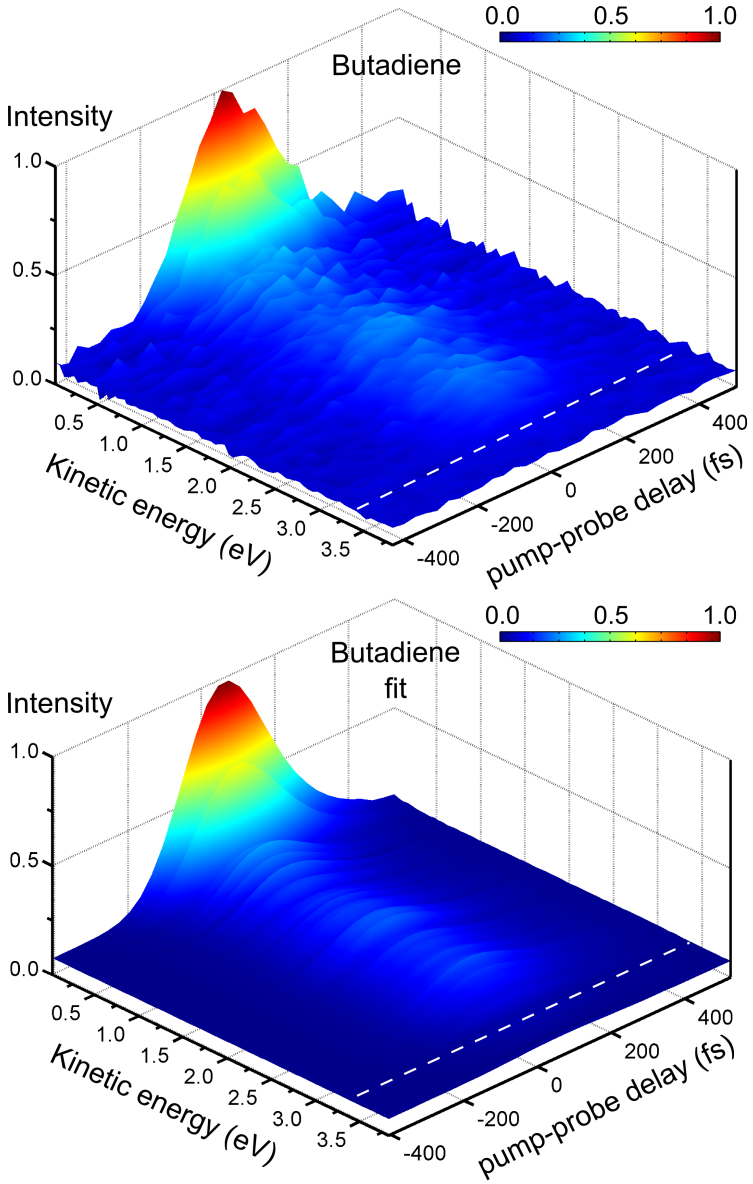

Figure 6.17: *Time-dependent photoelectron spectrum of butadiene dependent on the electron kinetic energy and the pump-probe time delay obtained with 160 nm excitation and 267 nm ionisation. The data was fitted with a single exponential 2D global fit function. The fit is displayed below the data set and the dashed lines represent the $(1+1')$ photoionisation energy cut-off.*

The spectrum of butadiene exhibits, over the whole electron kinetic energy range, ultra fast decaying signals. Using an excitation wavelength of 160 nm a manifold of several excited states can be excessed up to the $3d/\pi$ or even the $4p/\pi$ electronic state [210]. The weak intensity signal, which extends until the $(1 + 1')$ photoionisation cut-off energy, is a signature of the projection to the D_0 ground state of the butadiene cation. The strong intensity signal at low kinetic energies is originating from projections to energetically higher lying excited cation states of the butadiene (D_1 and D_2). The reason for the intense signal might be a higher projection propensity from the electronic excited states of the neutral molecule to the excited cation states based on Franck-Condon arguments and this should be investigated further. The high intensity feature in the low electron kinetic energy region between 0.05 eV and 0.50 eV and the corresponding single exponential fit are plotted against pump-probe delay time in Figure 6.18. A time constant of $\tau = 120$ fs could be extracted, despite the relatively long cross-correlation of the measurement. It has previously been shown that time constants of approximately half the cross-correlation value may be reliably extracted from mono-exponential fits to transient data [213].

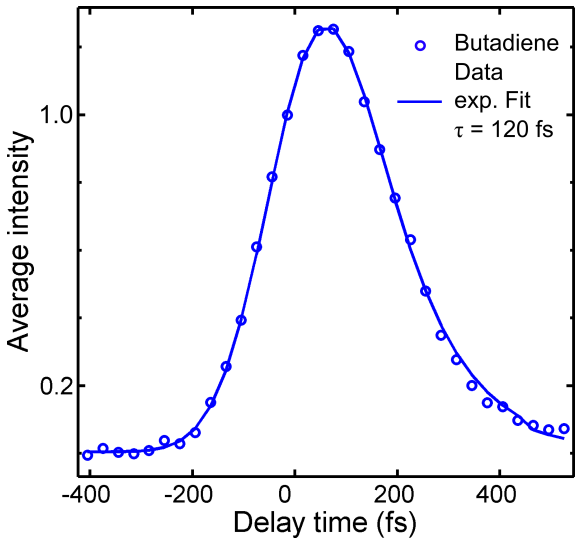

Figure 6.18: *Time-dependent section of butadiene summed over the low kinetic energy region from 0.05 eV to 0.50 eV. A single exponential lifetime of $\tau = 120$ fs could be extracted from the 2D global fit applied to the data.*

Overall, the butadiene data presented above provides as successful first demonstration of a TRPEI measurement using our newly developed VUV light source. Future work will begin to exploit the VUV capability further and some possible avenues of investigation will be discussed briefly in Chapter 7.

6.6 Conclusion

The goal was to design and construct a compact femtosecond vacuum ultraviolet light source, which can be used for time-resolved spectroscopic measurements.
The generation of fs VUV laser pulses is conducted in a nonlinear medium with a third order nonlinearity $\chi^{(3)}$ using a four wave frequency mixing process. In this work the generation of the fifth harmonic of wavelength $\lambda_{\mathrm{FH}} = 160$ nm from a Ti:sapphire laser was produced by frequency mixing the fundamental wave ($\lambda_{\mathrm{FF}} = 800$ nm) and the third harmonic ($\lambda_{\mathrm{TH}} = 267$ nm) in the noble gas argon used as a nonlinear medium. For this purpose a gas cell for the nonlinear interaction process and an attached completely new VUV vacuum chamber, containing optics and diagnostic tools, were designed and built within the scope of this work.
At first the VUV pulse was generated in a FWFM process with a collinear geometry. Here both pump pulses (fundamental and third harmonic) were co-propagating and focused into the interaction region. The conversion efficiency of the generated VUV pulse depends on the intensities of both pump beams and also on the pressure and the temperature of the nonlinear gas. The maximum pulse energy of 160 nJ of the VUV pulse in this configuration was achieved at $p = 32$ mbar.
In order to enhance the conversion efficiency of the VUV pulse a non-collinear geometry of both input pulses was chosen, to avoid wavevector mismatch of all beams and establish perfect phase matching. The phase matching is achieved for higher pressures of the nonlinear medium argon, which enhances the frequency conversion process. A maximal VUV pulse energy of $E_{\mathrm{FH}} = 613$ nJ was generated at a phase matching angle of $\theta_1 = 17.7$ mrad and a gas pressure of $p = 422$ mbar. This VUV energy is sufficient to conduct TRPEI experiments in combination with the newly generated VUV laser source.
In order to demonstrate the functionality and the performance of the combined VUV light source and the time-resolved photoelectron imaging spectrometer the noble gas xenon was investigated with a pump wavelength of $\lambda_{pump} = 161$ nm and a probe wavelength of $\lambda_{probe} = 267$ nm. Here a cross correlation of 210 fs was measured. Furthermore, as a proof-of-concept study, the conjugated molecule butadiene was investigated using the new VUV laser light as a pump pulse to study higher lying excited states and a lifetime of 120 fs was determined.
Conclusively, it can be stated that the successful implementation of this new fs VUV light source enables the study of a variety of different molecular systems. Using the VUV pulse as a probe in the TRPEI technique allows us to potentially detect the full dynamical relaxation process of molecules back to their electronic ground state, and this will be the subject of future work within the group.

Chapter 7

Summary and Outlook

7.1 General conclusions

In this thesis, the nonadiabatic molecular dynamics of model chromophores, which form the basis of biologically important molecular systems, were investigated with ultrafast nonlinear optics in conjunction with photoelectron imaging spectroscopy. In order to comprehend the photoprotective function of DNA, eumelanin and biomolecules, the dynamical processes and physical functionality of the basic heteroaromatic molecules have to be first understood. This "bottom up" methodology is often used in the femtochemistry community and was part of this work.

The molecule aniline is an excellent starting point, since it is a constituent part of three out of the four nuclear bases of DNA and has been therefore widely investigated in recent years. Nevertheless open questions about its excited state dynamics remain and therefore its potential photoresistivity is not fully understood. The chemical structure of a molecular system is responsible for the dynamical operating mechanism, because it defines the critical coordinates that drive the nonradiative relaxation process. Hence, site-selective methylation of a molecule is a useful tool to gain additional in depth information about the dynamical process. The non-adiabatic relaxation pathways in the derivatives of aniline, N,N-dimethylaniline (N,N-DMA) and 3,5-dimethylaniline (3,5-DMA), have been thoroughly studied with time-resolved photoelectron imaging. Upon 240 nm excitation several electronic excited states in both molecules are energetically accessible and are populated in the Franck-Condon region, such as the $2\pi\pi^*$, $S_2(3s/\pi\sigma^*)$ and $S_1(\pi\pi^*)$ states. Due to the structural difference of both molecules, the temporal evolution and the fate of the participating electronic states are not the same. The critical relaxation coordinates that dominate the non-adiabatic state coupling in both molecules are the distortion of the molecular ring-system and N-X bond stretching. In N,N-DMA the $S_2(3s/\pi\sigma^*)$ excited state decays via two pathways, which are internal conversion due to non-adiabatic coupling with the $S_1(\pi\pi^*)$ state and direct bond fission. In 3,5-DMA this $S_2(3s/\pi\sigma^*)$ state just decays via direct dissociation, because of the structural

changes on the aromatic ring-system that effectively slow down the non-adiabatic coupling mechanism. The energetically higher lying $2\pi\pi^*$ excited state decays on an ultrafast timescale without the interaction of the other involved states.
Much like aniline, the relaxation dynamics of the base molecule indole were studied within the scope of this thesis. Indole is particularly interesting since it is the aromatic sub-component of many bio-molecules, like two DNA bases, amino acids and the pigment eumelanin, which are all extremely photoresistant. Specifically eumelanin is the body's front line defence system against potential harmful UV radiation, therefore it is of great interest to understand the underlying temporal decay mechanisms in the base chromophore indole. Next to the relaxation dynamics of the $\pi\pi^*$ excited states, the role of the $(3s/\pi\sigma^*)$ excited state in indole is of particular significance. These dissociative $\pi\sigma^*$ states were the focus of many experimental and theoretical investigations, since they supposedly mediate the non-radiative decay pathway back to the molecular ground state. Utilising the highly differential pump-probe TRPEI approach, which provides time-, energy- and angle-resolved information, the ultrashort non-adiabatic dynamics and the population transfer from the energetically higher lying $\pi\pi^*$ excited state to the $(3s/\pi\sigma^*)$ state and the second, lower lying $\pi\pi^*$ state were analysed. However, the ultimate fate of the $(3s/\pi\sigma^*)$ state remains unclear, since the pulse energy of the employed probe pulse restricts the detection of the full dynamical process.
In order to be able to study the complete relaxation pathway back to the electronic ground state of a molecular system, a new ultrafast vacuum ultraviolet light source has been built in the laboratory and combined with the TRPEI spectrometer. These ultrashort laser pulses of the new light source were created in a nonlinear four wave frequency mixing process in noble gas with a high third order nonlinearity. Here the input frequencies involved the fundamental ($\lambda_{FF} = 800$ nm) and third harmonic ($\lambda_{TH} = 267$ nm) frequency of a Ti:Sapphire laser system. At first a collinear geometry between the two input pulses were used for the generation process in a gas filled cell. The generation efficiency of the outcoming fifth harmonic frequency was dependent on the pressure and the temperature of the noble gas within the home built cell. In order to increase the energy conversion efficiency of the generated VUV pulse, the FWFM process was changed to a non-collinear geometry of the input waves. Here, perfect phase matching was achieved at higher gas pressures, which enhanced the frequency conversion. The highest vacuum ultraviolet light generation using the FWFM nonlinear process was achieved using an argon pressure $p = 422$ mbar and a phase matching angle $\theta_1 = 17.7$ mrad. This yielded an efficient fifth harmonic freuqency pulse with a wavelength $\lambda_{FH} = 161$ nm and pulse energy $E_{\mathrm{FH}} = 613$ nJ. This energy was sufficient to perform time-resolved photoelectron imaging experiments. The functionality and performance of the combined TRPEI spectrometer with the newly developed VUV light source was evaluated with the noble gas

xenon that was also used for calibration purpose and a proof-of-concept study on the molecule 1,3-butadiene was performed. Summarising, the novel state-of-the-art spectroscopic technique including the fs vacuum ultraviolet light source opens possibilities to study molecular photophysics on a larger dimension. New insight to the full non-adiabatic dynamical process of biomolecules as well as their "molecular structure - dynamics - protection function" relationship can be revealed.

7.2 Future directions

The work in this thesis explored how modifications in molecular structure as well as changes of the excitation energies influenced the overall relaxation dynamics of molecular systems. This newly gained insights and the availability of the newly designed and build femtosecond vacuum ultraviolet light source in combination with the TRPEI spectroscopic technique opens new possibilities to study and understand a variety of different biologically relevant model molecules.

7.2.1 Important biomolecular model systems

Future spectroscopic TRPEI measurements, employing the fs VUV laser pulse as a pump step, can examine important molecular systems of interest such as diethylether (DEE) and tetrahydrofuran (THF), shown in Figure 7.1. The molecular structure of THF is comparable to ribose, which is a part of DNA [214]. Hence a detailed understanding about the dynamical mechanisms of these molecules is of great interest, which is motivated once again by the photoresistance of the molecules after ultraviolet light absorption.

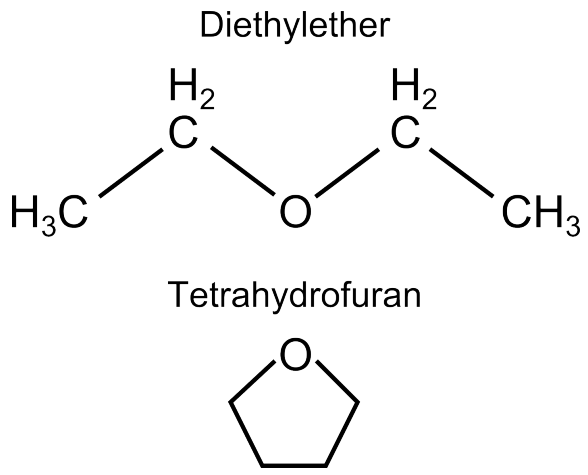

Figure 7.1: *Structural formula of diethylether (DEE) and tetrahydrofuran (THF)*

Equally interesting is the study of ultrafast dynamics in acetylacetone (chemical name: 2,4-pentanedione), which exhibits keto - enol tautomerim. Its common molecular form in the gas phase is the enolic acetylacetone and the its stability originates from the intramolecular H-bond, which is abundant in many biomolecules [215]. Hence acetylacetone is an excellent starting point for the study of intramolecular H-atom transfer, which is a common and important reaction pathway mediated by UV excitation.

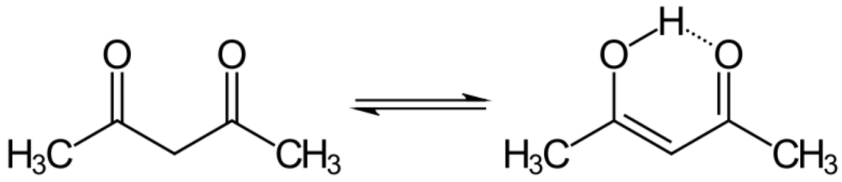

Figure 7.2: *Keto-enol tautomerism of Acetylacetone*

7.2.2 Novel optical and spectroscopic techniques

Further directions for the diversification of the spectroscopic technique is the performance of TRPEI with tunable VUV light. The general feasibility of tunable fs VUV pulses was demonstrated by Noack and co-workers [196]. A generation and implementation of tunable fs pulses in the vacuum ultraviolet spectral region can be done with the current experimental setup. The four wave sum- or difference frequency mixing process in a third order nonlinear gas can be used to generate fs-VUV laser pulses of wavelengths λ = 112 - 164 nm. The input pump pulses of this nonlinear FWFM process are the tunable output of an OPA (wavelength range: signal 1.1 - 1.6 μm or idler 1.6 - 2.6 μm) combined with frequency converted UV pulses (wavelength range: 273 - 260 nm, second order nonlinear processes in crystals). The pulse energy of the tunable fs VUV pulses is below the one photon ionisation potential of most molecular systems of interest and will therefore allow the complete study of their complex dynamical behaviour. Another efficient way of generating tunable deep-ultraviolet radiation is the utilisation of hollow-core crystal fibres, which enable pressure adjusted normal and anomalous dispersion [216]. Their ability to generate gas-based radiation of enormous tunablility, from near infrared to vacuum ultraviolet light, and the subsequent utilisation of the tunable generated radiation with spectroscopic techniques, potentially offers a great improvement over our current approach.

In order to further facilitate the “bottom up” methodology of investigation of biologically relevant molecules, these bigger systems have to be efficiently put into the gas-phase. Laser induced acoustic desorption (LIAD) is a alternative method of preparing molecules with a low vapour pressure from the solid-phase into the gas-phase [217, 218]. Here a solid molecular sample is coated on the front surface of a

thin metal foil. These molecules desorb from this surface, due to laser pulses hitting the back surface of this foil. Subsequently the pure molecular systems can be studied using a time-of-flight experiment or a particle imaging spectroscopic technique.
An extremely differential spectroscopic method to investigate the complete photodissociation process of polyatomic molecules is the photoelectron-photoion coincidence technique (PEPICO). In the photoionisation process of molecules, two types of particles are generated, which are cationic photofragments and photoelectrons. The intrinsic properties of both species are correlated and the energy and angular distribution of the electrons and the ions will be observed as a function of pump-probe delay [219, 220]. The utilisation of the PEPICO technique with new light sources in the UV and VUV spectral region provide, in principle, the detection of the complete non-adiabatic process of the molecular system.

Bibliography

[1] M. M. Zawadzki, J. O. F. Thompson, E. A. Burgess, M. J. Paterson, and D. Townsend, Time-resolved photoionization spectroscopy of mixed Rydberg-valence states: indole case study, *Phys. Chem. Chem. Phys.*, 2015, **17**, 26659–26669.

[2] M. M. Zawadzki, M. Candelaresi, L. Saalbach, S. W. Crane, M. J. Paterson, and D. Townsend, Observation of multi-channel non- adiabatic dynamics in aniline derivatives using time-resolved photoelectron imaging, *Faraday Discuss.*, 2016, **194**, 185 – 208.

[3] S. W. Crane, M. M. Zawadzki, J. O. F. Thompson, N. Kotsina, O. Ghafur, and D. Townsend, Caveats in the interpretation of time-resolved photoionization measurements: A photoelectron imaging study of pyrrole, *J. Chem. Phys.*, 2016, **145**(23), 234304.

[4] M. Barbatti, A. C. Borin, and S. Ullrich, *Photoinduced Phenomena in Nucleic Acids II: DNA Fragments and Phenomenological Aspects*, Topics in Current Chemistry, Springer International Publishing, 2014.

[5] G. P. Pfeifer, Y. H. You, and A. Besaratinia, Mutations induced by ultraviolet light, *Mutat. Res. Mol. Mech. Mutagen.*, 2005, **571**(12), 19–31.

[6] C. E. Crespo-Hernandez, B. Cohen, P. M. Hare, and B. Kohler, Ultrafast Excited-State Dynamics in Nucleic Acids, *Chem. Rev.*, 2004, **104**, 1977–2019.

[7] C. Cockell and J. Knowland, Ultraviolet radiation screening compounds, *Biol. Rev.*, 1999, **74**(3), 311–345.

[8] M. Bixon and J. Jortner, Intramolecular Radiationless Transitions, *J. Chem. Phys.*, 1968, **48**, 715.

[9] J. Jortner, S. A. Rice, and R. M. Hochstrasser, Radiationless Transitions in Photochemistry, in Advances in Photochemistry, *Adv. Photochem.*, 1969, **7**, 149.

[10] S. R. Henry and W. Siebrand in *Org. Mol. Photophysics*, ed. J. B. Birks, Vol. 1; Wiley, London, 1973; p. 152.

[11] K. F. Freed in *Radiationless Process. Mol. Condens. Phases*, ed. F. K. Fong; Springer-Verlag, Berlin, 1976; p. 23.

[12] T. H. Maiman, Optical and microwave-optical experiments in ruby, *Phys. Rev. Lett.*, 1960, **4**(11), 564–566.

[13] D. E. Spence, P. N. Kean, and W. Sibbett, 60-fsec pulse generation from a self-mode-locked Ti: sapphire laser, *Opt. Lett.*, 1991, **16**(1), 42–44.

[14] M. Dantus, M. J. Rosker, and A. Zewail, Real-time femtosecond probing of "transition states" in chemical reactions, *J. Chem. Phys.*, 1987, **87**(4), 2395–2397.

[15] T. S. Rose, M. J. Rosker, and A. H. Zewail, Femtosecond realtime observation of wave packet oscillations (resonance) in dissociation reactions, *J. Chem. Phys.*, 1988, **88**, 6672.

[16] A. H. Zewail, Femtochemistry: Atomic-Scale Dynamics of the Chemical Bond, *J. Phys. Chem. A*, 2000, **104**(24), 5660–5694.

[17] A. Stolow, A. E. Bragg, and D. M. Neumark, Femtosecond time-resolved photoelectron spectroscopy., *Chem. Rev.*, 2004, **104**(4), 1719–57.

[18] G. Wu, P. Hockett, and A. Stolow, Time-resolved photoelectron spectroscopy: from wavepackets to observables., *Phys. Chem. Chem. Phys.*, 2011, **13**(41), 18447–67.

[19] T. Oliver, G. King, and M. N. R. Ashfold, Position matters: competing O-H and N-H photodissociation pathways in hydroxy- and methoxy-substituted indoles., *Phys. Chem. Chem. Phys.*, 2011, **13**(32), 14646–62.

[20] M. Born and R. Oppenheimer, Zur Quantentheorie der Molekeln, *Ann. Phys.*, 1927, **389**(20), 457–484.

[21] NIST, proton-electron mass ratio, http://physics.nist.gov/cgi-bin/cuu/Value?mpsme, 2017.

[22] P. W. Atkins and R. S. Friedman, *Molecular quantum mechanics*, Oxford University Press, Oxford, 5rd ed., 2011.

[23] D. Townsend, Lecture: Atomic & Molecular Spectroscopy, Molecular Electronic Structure, 2015.

[24] R. Livingstone, O. Schalk, A. E. Boguslavskiy, G. Wu, T. L. Bergendahl, A. Stolow, M. J. Paterson, and D. Townsend, Following the excited state relaxation dynamics of indole and 5-hydroxyindole using time-resolved photoelectron spectroscopy, *J. Chem. Phys.*, 2011, **135**(19), 1–12.

[25] J. D. Young *The Effect of Increasing Molecular Complexity on the Dynamics of Biologically Relevant Chromophores* PhD thesis, 2016.

[26] L. Chai, Fluoreszenzmikroskopische Untersuchung on CellROX Green https://prezi.com/fljx-tlvza36/fluoreszenzmikroskopische-untersuchung-on-cellrox-green/, 2015.

[27] M. Brouard and C. Vallance, *Tutorials in Molecular Reaction Dynamics*, The Royal Society of Chemistry, 2012.

[28] H. H. Jaffe and A. L. Miller, The fates of electronic excitation energy, *J. Chem. Educ.*, 1966, **43**(9), 469.

[29] R. G. Gilbert and S. C. Smith, *Theory of unimolecular and recombination reactions*, Blackwell Scientific Publications, Oxford, 1990.

[30] C. M. Marian, Spinorbit coupling and intersystem crossing in molecules, *Comput. Mol. Sci.*, 2012, **2**(2), 187–203.

[31] P. Ankins and J. De Paula, *Physical Chemistry for the Life Sciences*, 2006.

[32] J. R. Lakowicz, *Principles of Fluorescence Spectroscopy*, Springer Science & Business Media, 3rd ed., 2007.

[33] M. A. Robb, M. Garavelli, M. Olivucci, and F. Bernardi, A Computational Strategy for Organic Photochemistry, *Rev. Comput. Chem.*, 2007, **15**, 87–146.

[34] G. A. Worth and L. S. Cederbaum, Beyond Born-Oppenheimer: molecular dynamics through a conical intersection., *Annu. Rev. Phys. Chem.*, 2004, **55**, 127–58.

[35] B. G. Levine and T. J. Martínez, Isomerization through conical intersections., *Annu. Rev. Phys. Chem.*, 2007, **58**, 613–34.

[36] D. R. Yarkony, Diabolical conical intersections, *Rev. Mod. Phys.*, 1996, **68**(4), 985–1013.

[37] W. Domcke and D. R. Yarkony, Role of conical intersections in molecular spectroscopy and photoinduced chemical dynamics., *Annu. Rev. Phys. Chem.*, 2012, **63**, 325–352.

[38] S. Matsika and P. Krause, Nonadiabatic events and conical intersections., *Annu. Rev. Phys. Chem.*, 2011, **62**, 621–643.

[39] E. Teller, The Crossing of Potential Surfaces, *J. Phys. Chem.*, 1937, **41**(1), 109–116.

[40] G. Wu, P. Hockett, and A. Stolow, Time-resolved photoelectron spectroscopy: from wavepackets to observables., *Phys. Chem. Chem. Phys.*, 2011, **13**(41), 18447–67.

[41] A. Stolow and J. G. Underwood, Time-resolved photoelectron spectroscopy of nonadiabatic dynamics in polyatomic molecules, *Adv. Chem. Phys.*, 2008, **139**, 497–583.

[42] G. M. Roberts and V. G. Stavros, The role of $\pi\sigma^*$ states in the photochemistry of heteroaromatic biomolecules and their subunits: insights from gas-phase femtosecond spectroscopy, *Chem. Sci.*, 2014, **5**(5), 1698.

[43] I. Fischer, D. M. Villeneuve, M. J. J. Vrakking, and A. Stolow, Femtosecond wave-packet dynamics studied by time-resolved zero-kinetic energy photoelectron spectroscopy, *J. Chem. Phys.*, 1995, **102**(13), 5566.

[44] M. J. J. Vrakking, D. M. Villeneuve, and A. Stolow, Observation of fractional revivals of a molecular wave packet, *Phys. Rev. A*, 1996, **54**(1), R37–R40.

[45] W. Domcke and G. Stock in *Adv. Chem. Phys.;* John Wiley & Sons, Inc., Hoboken, NJ, USA, 1997; chapter 1, pp. 1–169.

[46] H. Köppel, W. Domcke, and L. S. Cederbaum, Multimode molecular dynamics beyond the Born-Oppenheimer approximation, *Adv. Chem. Phys.*, 1984, **57**, 59–246.

[47] V. Blanchet, M. Z. Zgierski, T. Seideman, and A. Stolow, Discerning Vibronic Molecular Dynamics using Time-Resolved Photoelectron Spectroscopy, *Nature*, 1999, **401**(6748), 52–54.

[48] M. Schmitt, S. Lochbrunner, J. P. Shaffer, J. J. Larsen, M. Z. Zgierski, and A. Stolow, Electronic continua in time-resolved photoelectron spectroscopy. II. Corresponding ionization correlations, *J. Chem. Phys.*, 2001, **114**(3), 1206–1213.

[49] T. Suzuki, Femtosecond Time-Resolved Photoelectron Imaging, *Annu. Rev. Phys. Chem. .*, 2006, **57**, 555–592.

[50] C. N. Yang, On the angular distribution in nuclear reactions and coincidence measurements, *Phys. Rev.*, 1948, **74**(7), 764–772.

[51] K. L. Reid, Photoelectron Angular Distributions, *Annu. Rev. Phys. Chem.*, 2003, **54**(1), 397–424.

[52] N. G. Jablonski and G. Chaplin, Human skin pigmentation, migration and disease susceptibility., *Philos. Trans. R. Soc. Lond. B. Biol. Sci.*, 2012, **367**(1590), 785–92.

[53] A. L. Sobolewski and W. Domcke, Photophysics of eumelanin: ab initio studies on the electronic spectroscopy and photochemistry of 5,6-dihydroxyindole., *Chemphyschem*, 2007, **8**(5), 756–62.

[54] M. N. R. Ashfold, G. A. King, D. Murdock, M. G. D. Nix, T. Oliver, and A. G. Sage, Pi sigma* excited states in molecular photochemistry., *Phys. Chem. Chem. Phys.*, 2010, **12**(6), 1218–38.

[55] A. L. Sobolewski and W. Domcke, Computational studies of the photophysics of hydrogen-bonded molecular systems., *J. Phys. Chem. A*, 2007, **111**(46), 11725–35.

[56] A. Sobelewski and W. Domcke, On the mechanism of nonradiative decay of DNA bases: ab initio and TDDFT results for the excited states of 9H-adenine, *Eur. Phys. J. D - At. Mol. Opt. Plasma Phys.*, 2002, **20**, 369–374.

[57] A. L. Sobolewski, W. Domcke, C. Dedonder-Lardeux, and C. Jouvet, Excited-state hydrogen detachment and hydrogen transfer driven by repulsive $1\pi\sigma^*$ states: A new paradigm for nonradiative decay in aromatic biomolecules, *Phys. Chem. Chem. Phys.*, 2002, **4**(7), 1093–1100.

[58] P. A. Franken, A. E. Hill, C. W. Peters, and G. Weinreich, Generation of optical harmonics, *Phys. Rev. Lett.*, 1961, **7**(4), 118–119.

[59] R. W. Boyd, *Nonlinear Optics*, Academic Press, Elsevier Inc., London, 3rd ed., 2008.

[60] P. D. Maker, R. W. Terhune, M. Nisenoff, and C. M. Savage, Effects of Dispersion and Focusing on the Production of Optical Harmonics, *Phys. Rev. Lett.*, 1962, **8**(1), 21–22.

[61] N. Bloembergen and B. E. A. Saleh in *Fundam. Photonics;* John Wiley & Sons, Inc., 1991; chapter 21.

[62] F. Traeger, *Handbook of Lasers and Optics*, 2003.

[63] T. H. Maiman, Stimulated Optical Radiation in Ruby, *Nature*, 1960, **187**, 493–494.

[64] C. Rullière, *Femtosecond Laser Pulses: Principles and Experiments*, Springer Science+Business Media, Inc., New York, 2nd ed., 2003.

[65] R. Thomson, C. Leburn, and D. Reid, *Ultrafast Nonlinear Optics*, Springer Science+Business Media, Inc., London, 2013.

[66] P. F. Moulton, Spectroscopic and laser characteristics of Ti:Al2O3, *J. Opt. Soc. Am. B*, 1986, **3**(1), 125–133.

[67] F. Salin, J. Squier, and M. Piché, Mode locking of Ti:AI(2)O(3) lasers and self-focusing: a Gaussian approximation., *Opt. Lett.*, 1991, **16**(21), 1674–1676.

[68] N. Sarukura, Y. Ishida, and H. Nakano, Generation of 50-fsec pulses from a pulse-compressed, cw, passively mode-locked Ti:sapphire laser, *Opt. Lett.*, 1991, **16**(3), 153–155.

[69] R. Paschotta, Encyclopedia of Laser Physics and Technology - group velocity dispersion, www.rp-photonics.com/group_velocity_dispersion.html, 2016.

[70] J. A. Valdmanis, R. L. Fork, and J. P. Gordon, Generation of optical pulses as short as 27 femtoseconds directly from a laser balancing self-phase modulation, group-velocity dispersion, saturable absorption, and saturable gain, *Opt. Lett.*, 1985, **10**(3), 131–133.

[71] D. Strickland and G. Mourou, Compression of amplified chirped optical pulses, *Opt. Commun.*, 1985, **56**(3), 219–221.

[72] Https://en.wikipedia.org/wiki/Chirped_pulse_amplification, Chirped pulse amplification, 2016-03-17.

[73] R. Paschotta, Encyclopedia of Laser Physics and Technology regenerative amplifier, www.rp-photonics.com/regenerative_amplifiers.html, *RP Photonics Consult. GmbH*, 2016.

[74] K. Yamakawa, P. H. Chiu, A. Magana, and J. D. Kmetec, Generation of high peak and average power femtosecond pulses at a 10 Hz repetition rate in a titanium-doped sapphire laser, *IEEE J. Quantum Electron.*, 1994, **30**(11), 2698 – 2706.

[75] H. H. Telle, A. G. Ureña, and R. J. Donovan, *Laser Chemistry: Spectroscopy, Dynamics and Applications*, John Wiley & Sons Ltd, London, 1st ed., 2007.

[76] R. Paschotta, Encyclopedia of Laser Physics and Technology - Supercontinuum generation, https://www.rp-photonics.com/supercontinuum_generation.html, 2017.

[77] A. H. Zewail, Femtochemistry: Atomic-scale dynamics of the chemical bond [Review], *J. Phys. Chem. A*, 2000, **104**, 5660–5694.

[78] A. Stolow, A. E. Bragg, and D. M. Neumark, Femtosecond time-resolved photoelectron spectroscopy, *Chem. Rev.*, 2004, **104**(4), 1719–1757.

[79] D. M. Neumark, Time-resolved Photoelectron Spectroscopy of Molecules and Clusters, *Annu. Rev. Phys. Chem.*, 2001, **52**, 255–277.

[80] R. A. Livingstone, J. O. F. Thompson, M. Iljina, R. J. Donaldson, B. J. Sussman, M. Paterson, and D. Townsend, Time-resolved photoelectron imaging of excited state relaxation dynamics in phenol, catechol, resorcinol, and hydroquinone, *J. Chem. Phys.*, 2012, **137**(18), 184304.

[81] A. Stolow, Minimum profile ultrahigh vacuum gate valve based on linear/rotary motion feedthrough, *J. Vac. Sci. Technol. A-Vacuum Surfaces Film.*, 1996, **14**(4), 2669–2670.

[82] U. Even, J. Jortner, D. Noy, N. Lavie, and C. Cossart-Magos, Cooling of large molecules below 1 K and He clusters formation, *J. Chem. Phys.*, 2000, **112**(18), 8068.

[83] U. Even, Pulsed Supersonic Beams from High Pressure Source: Simulation Results and Experimental Measurements, *Adv. Chem.*, 2014, **2014**, 1–11.

[84] S. Y. T. van de Meerakker, H. L. Bethlem, and G. Meijer, Taming molecular beams, *Nat. Phys.*, 2008, **4**(8), 595–602.

[85] A. T. J. B. Eppink and D. H. Parker, Velocity map imaging of ions and electrons using electrostatic lenses: Application in photoelectron and photofragment ion imaging of molecular oxygen, *Rev. Sci. Instrum.*, 1997, **68**, 3477–3484.

[86] D. H. Parker and A. T. J. B. Eppink, Photoelectron and photofragment velocity map imaging of state-selected molecular oxygen dissociation/ionization dynamics, *J. Chem. Phys.*, 1997, **107**(7), 2357.

[87] A. J. R. Heck and D. W. Chandler, Imaging Techniques for the Study of Chemical Reaction Dynamics, *Annu. Rev. Phys. Chem.*, 1995, **46**(1), 335–372.

[88] J. Solomon, Photodissociation as Studied by Photolysis Mapping, *J. Chem. Phys.*, 1967, **47**(1967), 889.

[89] D. Townsend, M. Minitti, and A. G. Suits, Direct current slice imaging, *Rev. Sci. Instrum.*, 2003, **74**(4), 2530.

[90] Y. Ogi, H. Kohguchi, D. Niu, K. Ohshimo, and T. Suzuki, Super-resolution photoelectron imaging with real-time subpixelation by field programmable gate array and its application to NO and benzene photoionization, *J. Phys. Chem. A*, 2009, **113**(52), 14536–14544.

[91] D. Townsend, Time-Resolved Photoelectron Imaging as a Probe of UV Relaxation Dynamics, *Invit. Talk, Univ. Warwick*, 2016, p. 30.

[92] Y. T. Cho and S.-J. Na, Application of Abel inversion in real-time calculations for circularly and elliptically symmetric radiation sources, *Meas. Sci. Technol.*, 2005, **16**, 878–884.

[93] B. J. Sussman *Quantum control using the nonresonant dynamic stark effect* PhD thesis, Queens University Kingston, 2007.

[94] B. J. Whitaker in *Imaging Chem. Dyn.*, ed. A. G. Suits and R. E. Continetti; American Chemical Society, Washington, D.C., 2000; pp. 68–86.

[95] B. J. Whitaker, *Imaging in molecular dynamics Technology and Applications*, Cambridge University Press, 2003.

[96] G. M. Roberts, J. L. Nixon, J. Lecointre, E. Wrede, and J. R. R. Verlet, Toward real-time charged-particle image reconstruction using polar onion-peeling, *Rev. Sci. Instrum.*, 2009, **80**, 053104.

[97] J. O. F. Thompson, L. B. Klein, T. I. Sølling, M. J. Paterson, and D. Townsend, The role of novel Rydberg-valence behaviour in the non-adiabatic dynamics of tertiary aliphatic amines, *Chem. Sci.*, 2016, **00**, 1–14.

[98] C. E. Crespo-Hernández, B. Cohen, P. M. Hare, and B. Kohler, Ultrafast Excited-State Dynamics in Nucleic Acids, *Chem. Rev.*, 2004, **104**(4), 1977 – 2020.

[99] M. N. R. Ashfold, G. A. King, D. Murdock, M. G. D. Nix, T. Oliver, and A. G. Sage, Pi sigma* excited states in molecular photochemistry., *Phys. Chem. Chem. Phys.*, 2010, **12**(6), 1218–38.

[100] G. M. Roberts and V. G. Stavros, The role of $\pi\sigma^*$ states in the photochemistry of heteroaromatic biomolecules and their subunits: insights from gas-phase femtosecond spectroscopy, *Chem. Sci.*, 2014, **5**(5), 1698.

[101] I. Cnossen, J. Sanz-Forcada, F. Favata, O. Witasse, T. Zegers, and N. F. Arnold, Habitat of early life: Solar X-ray and UV radiation at Earth's surface 4-3.5 billion years ago, *J. Geophys. Res. E Planets*, 2007, **112**(2), 1–10.

[102] G. King, T. Oliver, and M. N. R. Ashfold, Dynamical insights into 1pi sigma* state mediated photodissociation of aniline., *J. Chem. Phys.*, 2010, **132**(21), 214307.

[103] O. M. Kirkby, M. Sala, G. Balerdi, R. de Nalda, L. Bañares, S. Guérin, and H. H. Fielding, Comparing the electronic relaxation dynamics of aniline and d 7 -aniline following excitation at 272238 nm, *Phys. Chem. Chem. Phys.*, 2015, **21**(2).

[104] M. Sala, O. M. Kirkby, S. Guérin, and H. H. Fielding, New insight into the potential energy landscape and relaxation pathways of photoexcited aniline from CASSCF and XMCQDPT2 electronic structure calculations., *Phys. Chem. Chem. Phys.*, 2014, **16**(7), 3122–33.

[105] J. O. F. Thompson, R. A. Livingstone, and D. Townsend, Following the relaxation dynamics of photoexcited aniline in the 273-266 nm region using time-resolved photoelectron imaging., *J. Chem. Phys.*, 2013, **139**(3), 034316.

[106] R. Spesyvtsev, O. M. Kirkby, M. Vacher, and H. H. Fielding, Shedding new light on the role of the Rydberg state in the photochemistry of aniline., *Phys. Chem. Chem. Phys.*, 2012, **14**(28), 9942–7.

[107] R. Spesyvtsev, O. M. Kirkby, and H. H. Fielding, Ultrafast dynamics of aniline following 269238 nm excitation and the role of the S2(π3s/$\pi\sigma$*) state, *Faraday Discuss.*, 2012, **157**, 165.

[108] G. M. Roberts, C. Williams, J. D. Young, S. Ullrich, M. J. Paterson, and V. G. Stavros, Unraveling ultrafast dynamics in photoexcited aniline., *J. Am. Chem. Soc.*, 2012, **134**(30), 12578–89.

[109] R. Montero, Á. Peralta-Conde, V. Ovejas, R. Martínez, F. Castaño, and A. Longarte, Ultrafast dynamics of aniline in the 294-234 nm excitation range: The role of the pi sigma* state, *J. Chem. Phys.*, 2011, **135**(5).

[110] J. O. F. Thompson, L. Saalbach, S. W. Crane, M. J. Paterson, and D. Townsend, Ultraviolet relaxation dynamics of aniline, N, N-dimethylaniline and 3,5-dimethylaniline at 250 nm, *J. Chem. Phys.*, 2015, **142**(11), 114309.

[111] K. Kimura, H. Tsubomura, and S. Nagakura, The Vacuum Ultraviolet Absorption Spectra of Aniline and Some of Its N-Derivatives, *Bull. Chem. Soc. Jpn.*, 1964, **73**(9), 1336–1346.

[112] K. Kimura and S. Nagakura, Vacuum ultra-violet absorption spectra of various mono-substituted benzenes, *Mol. Phys. An Int. J. Interface Between Chem. Phys.*, 1964, **9**(2), 117 – 135.

[113] Y. Honda, M. Hada, M. Ehara, and H. Nakatsuji, Excited and ionized states of aniline: Symmetry adapted cluster configuration interaction theoretical study, *J. Chem. Phys.*, 2002, **117**(5), 2045–2052.

[114] F. Wang, S. P. Neville, R. Wang, and G. Worth, Quantum dynamics study of photoexcited aniline., *J. Phys. Chem. A*, 2013, **117**(32), 7298–307.

[115] T. Ebata, C. Minejima, and N. Mikami, A new electronic state of aniline observed in the transient IR absorption spectrum from S1 in a supersonic jet, *J. Phys. Chem. A*, 2002, **106**(46), 11070–11074.

[116] G. Herzberg, *Molecular Spectra and Molecular Structure III*, 1966.

[117] H. Tsubomura and T. Sakata, A new electronic transition found for the aniline derivatives, *Chem. Phys. Lett.*, 1973, **21**(3), 511–512.

[118] A. Davidsson and B. Nordén, A new electronic transition in the polarized spectrum of dimethyl aniline, *Chem. Phys. Lett.*, 1974, **28**(1), 39–40.

[119] K. Fuke and S. Nagakura, Rydberg transitions of aniline and N,N-diethylaniline, *J. Mol. Spectrosc.*, 1977, **64**(1), 139–146.

[120] A. L. Sobolewski and W. Domcke, Conical intersections induced by repulsive $1\pi\sigma^*$ states in planar organic molecules: Malonaldehyde, pyrrole and chlorobenzene as photochemical model systems, *Chem. Phys.*, 2000, **259**(2-3), 181–191.

[121] G. M. Roberts, C. Williams, J. D. Young, S. Ullrich, M. J. Paterson, and V. G. Stavros, Unraveling ultrafast dynamics in photoexcited aniline., *J. Am. Chem. Soc.*, 2012, **134**(30), 12578–89.

[122] L. Lagesson-Andrasko and V. Lagesson, *Handbook of Ultraviolet Spectra Vapour Phase 168-330 nm*, 2005.

[123] R. Spesyvtsev, O. M. Kirkby, and H. H. Fielding, Ultrafast dynamics of aniline following 269238 nm excitation and the role of the S2(π3s/$\pi\sigma^*$) state, *Faraday Discuss.*, 2012, **157**, 165.

[124] J. P. Maier and D. W. Turner, Steric inhibition of resonance studied by molecular photoelectron spectroscopy. Part 3.Anilines, phenols and related compounds, *J. Chem. Soc., Faraday Trans. 2*, 1973, **69**, 521 –531.

[125] L. Szepes, G. Distefano, and S. Pignataro, Steric Inhibition Of Resonance In Acetanilides By UV Photoelectron-Spectroscopy, *Ann. Chim.*, 1974, **64**, 159 – 167.

[126] T. Suzuki, Femtosecond time-resolved photoelectron imaging., *Annu. Rev. Phys. Chem.*, 2006, **57**, 555–92.

[127] M. Sala, O. M. Kirkby, S. Guérin, and H. H. Fielding, New insight into the potential energy landscape and relaxation pathways of photoexcited aniline from CASSCF and XMCQDPT2 electronic structure calculations., *Phys. Chem. Chem. Phys.*, 2014, **16**(7), 3122–33.

[128] G. E. S. M. J. Frisch, G. W. Trucks, H. B. Schlegel, V. B. M. A. Robb, J. R. Cheeseman, G. Scalmani, M. C. B. Mennucci, G. A. Petersson, H. Nakatsuji, G. Z. X. Li, H. P. Hratchian, A. F. Izmaylov, J. Bloino, R. F. J. L. Sonnenberg, M. Hada, M. Ehara, K. Toyota, O. K. J. Hasegawa, M. Ishida, T. Nakajima, Y. Honda, J. E. P. H. Nakai, T. Vreven, J. A. Montgomery, Jr., K. N. K. F. Ogliaro, M. Bearpark, J. J. Heyd, E. Brothers, J. N. V. N. Staroverov, R. Kobayashi, S. S. I. K. Raghavachari, A. Rendell, J. C. Burant, M. K. J. Tomasi, M. Cossi, N. Rega, J. M. Millam, J. J. J. E. Knox, J. B. Cross, V. Bakken, C. Adamo, A. J. A. R. Gomperts, R. E. Stratmann, O. Yazyev, R. L. M. R. Cammi, C. Pomelli, J. W. Ochterski, P. S. K. Morokuma, V. G. Zakrzewski, G. A. Voth, O. F. J. J. Dannenberg, S. Dapprich, A. D. Daniels, J. C. J. B. Foresman, J. V. Ortiz, and D. J. Fox, GAUSSION 09, Revision D.01, Gaussian, Inc., 2009.

[129] Y. Z. Liu, C. C. Qin, S. Zhang, Y. M. Wang, and B. Zhang, Ultrafast dynamics of the first excited state of chlorobenzene, *Wuli Huaxue Xuebao/ Acta Phys. - Chim. Sin.*, 2011, **27**(4), 965–970.

[130] R. S. von Benten, Y. Liu, and B. Abel, Dynamical consequences of symmetry breaking in benzene and difluorobenzene, *J. Chem. Phys.*, 2010, **133**(13), 134306.

[131] B. Kim, C. P. Schick, and P. M. Weber, Time-Delayed Two-Color Photoelectron Spectra of Aniline, 2-Aminopyridine, and 3-Aminopyridine - Snapshots of the Nonadiabatic Curve Crossings, *J. Chem. Phys.*, 1995, **103**, 6903–6913.

[132] R. Scheps, D. Florida, and S. Rice, Influence of large amplitude vibrational motion on the rate of intersystem crossing : A study of single vibronic level, *J. Chem. Phys.*, 1974, **61**(5), 1730.

[133] H. Reisler and A. Krylov, Interacting Rydberg and valence states in radicals and molecules: experimental and theoretical studies, *Int. Rev. Phys. Chem.*, 2009, **28**(2), 267–308.

[134] Y.-I. Suzuki, T. Horio, T. Fuji, and T. Suzuki, No TitleTime-resolved photoelectron imaging of S2 S1 internal conversion in benzene and toluene, *J. Chem. Phys.*, 2011, **134**(18), 184313.

[135] C. Z. Bisgaard, O. J. Clarkin, G. Wu, A. M. D. Lee, O. Gessner, C. C. Hayden, and A. Stolow, Time-Resolved Molecular Frame Dynamics of Fixed-in-Space CS2 Molecules, *Science (80-.).*, 2009, **323**(5920), 1464–1468.

[136] R. Spesyvtsev *PhD Thesis* PhD thesis, University College London, 2013.

[137] A. Giussani, M. Merchán, D. Roca-Sanjuán, and R. Lindh, Essential on the Photophysics and Photochemistry of the Indole Chromophore by Using a Totally Unconstrained Theoretical Approach, *J. Chem. Theory Comput.*, 2011, **7**, 4088.

[138] K. Glass, S. Ito, P. R. Wilby, T. Sota, A. Nakamura, C. Bowers, J. Vinther, S. Dutta, R. Summons, D. E. Briggs, K. Wakamatsu, and J. D. Simon, Direct chemical evidence for undegraded eumelanin pigment from the Jurassic period, *PNAS*, 2012, **109**(26), 10218–10223.

[139] P. Meredith and J. Riesz, Radiative relaxation quantum yields for synthetic eumelanin., *Photochem. Photobiol.*, 2004, **79**(2), 211–216.

[140] A. Huijser, A. Pezzella, and V. Sundström, Functionality of epidermal melanin pigments: current knowledge on UV-dissipative mechanisms and research perspectives., *Phys. Chem. Chem. Phys.*, 2011, **13**(20), 9119–27.

[141] H. Lami, On the possible role of a mixed valenceRydberg state in the fluorescence of indoles, *J. Chem. Phys.*, 1977, **67**(7), 3274.

[142] B. J. Fender, D. M. Sammeth, and P. R. Callis, Site selective photoselection study of indole in argon matrix: location of the 1L a origin, *Chem. Phys. Lett.*, 1995, **239**, 31 – 37.

[143] V. A. Povedailo and D. L. Yakovlev, Electronic energy of the 1La level of supersonic jet-cooled indole, *J. Appl. Spectrosc.*, 2008, **75**(3), 336–340.

[144] J. Hager and S. C. Wallace, Laser Spectroscopy and Photodynamics, 1983, **439**(1982), 2121–2127.

[145] J. W. Hager, D. R. Demmer, and S. C. Wallace, Electronic Spectra of Jet-Cooled Indoles : Evidence for the ' La State, 1987, (13), 1375–1382.

[146] J. R. Platt, Classification of Spectra of Cata-Condensed Hydrocarbons, *J. Chem. Phys.*, 1948, **17**(5), 484.

[147] H. Lami, Presence of a low-lying Rydberg band in the vapour phase absorption spectra of indole and 1-methyl indole, *Chem. Phys. Lett.*, 1977, **48**(3), 447 – 450.

[148] A. L. Sobolewski and W. Domcke, Ab initio investigations on the photophysics of indole, *Chem. Phys. Lett.*, 1999, **315**(3), 293–298.

[149] L. Serrano-Andrés and B. O. Roos, Theoretical Study of the Absorption and Emission Spectra of Indole in the Gas Phase and in a Solvent, *J. Am. Chem. Soc.*, 1996, **118**(1), 185 – 195.

[150] A. L. Sobolewski, W. Domcke, C. Dedonder-Lardeux, and C. Jouvet, Excited-state hydrogen detachment and hydrogen transfer driven by repulsive $1\pi\sigma^*$ states: A new paradigm for nonradiative decay in aromatic biomolecules, *Phys. Chem. Chem. Phys.*, 2002, **4**(7), 1093–1100.

[151] C. Brand, J. Küpper, D. W. Pratt, W. L. Meerts, D. Krügler, J. Tatchen, and M. Schmitt, Vibronic coupling in indole: I. Theoretical description of the 1La-1Lb interaction and the electronic spectrum., *Phys. Chem. Chem. Phys.*, 2010, **12**(19), 4968–79.

[152] J. Küpper, D. W. Pratt, W. L. Meerts, C. Brand, J. Tatchen, and M. Schmitt, Vibronic coupling in indole: II. Investigation of the 1La-1Lb interaction using rotationally resolved electronic spectroscopy., *Phys. Chem. Chem. Phys.*, 2010, **12**(19), 4980–8.

[153] A. L. Sobolewski and W. Domcke, Computational studies of the photophysics of hydrogen-bonded molecular systems., *J. Phys. Chem. A*, 2007, **111**(46), 11725–35.

[154] H. Reisler and A. Krylov, Interacting Rydberg and valence states in radicals and molecules: experimental and theoretical studies, *Int. Rev. Phys. Chem.*, 2009, **28**(2), 267–308.

[155] B. C. Dian, A. Longarte, and T. S. Zwier, Hydride stretch infrared spectra in the excited electronic states of indole and its derivatives: Direct evidence for the [sup 1]$\pi\sigma$[sup] state, *J. Chem. Phys.*, 2003, **118**(6), 2696.

[156] H. Lippert, H.-H. Ritze, I. Hertel, and W. Radloff, Femtosecond time-resolved analysis of the photophysics of the indole molecule, *Chem. Phys. Lett.*, 2004, **398**(4-6), 526–531.

[157] S. T. Park, A. Gahlmann, Y. He, J. S. Feenstra, and A. H. Zewail, Ultrafast electron diffraction reveals dark structures of the biological chromophore indole., *Angew. Chem. Int. Ed. Engl.*, 2008, **47**(49), 9496–9.

[158] M.-F. Lin, C.-M. Tseng, Y. T. Lee, and C.-K. Ni, Photodissociation dynamics of indole in a molecular beam, *J. Chem. Phys.*, 2005, **123**(12), 124303.

[159] M. G. D. Nix, a. L. Devine, B. Cronin, and M. N. R. Ashfold, High resolution photofragment translational spectroscopy of the near UV photolysis of indole: dissociation via the 1pi sigma* state., *Phys. Chem. Chem. Phys.*, 2006, **8**(22), 2610–8.

[160] R. Montero, Á. P. Conde, V. Ovejas, F. Castaño, and A. Longarte, Ultrafast photophysics of the isolated indole molecule., *J. Phys. Chem. A*, 2012, **116**(11), 2698–703.

[161] R. Montero, V. Ovejas, M. Fernandez-Fernandez, A. Peralta Conde, and A. Longarte, Revisiting the relaxation dynamics of isolated pyrrole, *J. Chem. Phys.*, 2014, **141**(1).

[162] T. Vondrak, S.-I. Sato, and K. Kimura, Cation Vibrational Spectra of Indole and Indole Argon van der Waals Complex . A Zero Kinetic Energy Photoelectron Study, 1997, **5639**(96), 2384–2389.

[163] J. Braun, T. Grebner, and H. Neusser, Van Der Waals versus Hydrogen-Bonding in Complexes of Indole with Argon, Water, and Benzene by Mass-Analyzed Pulsed Field Threshold Ionization, *J. Phys. Chem. A*, 1998, **102**(19), 3273–3278.

[164] M. de Groot, J. Broos, and W. J. Buma, Tagging multiphoton ionization events by two-dimensional photoelectron spectroscopy., *J. Chem. Phys.*, 2007, **126**(20), 204312.

[165] L. N. Domelsmith, L. L. Munchausen, and K. N. Houk, Photoelectron spectra of psychotropic drugs. 1. Phenethylamines, tryptamines, and LSD, *J. Am. Chem. Soc.*, 1977, **99**(13), 4311–4321.

[166] M. Kubota and T. Kobayashi, E lectronic structures of melatonin and related compounds studied by photoelectron spectroscopy, 2003, **128**, 165–178.

[167] Y. Yamamoto and J. Tanaka, Polarized Absorption Spectra of Crystals of Indole and Its Related Compounds, *Bull. Chem. Soc. Jpn.*, 1972, **45**(5), 1362–1366.

[168] E. Jalviste and N. Ohta, Stark absorption spectroscopy of indole and 3-methylindole., *J. Chem. Phys.*, 2004, **121**(10), 4730–9.

[169] L. B. K. Aidas, C. Angeli, K. L. Bak, V. Bakken, R. Bast, P. D. O. Christiansen, R. Cimiraglia, S. Coriani, J. J. E. E. K. Dalskov, U. Ekstrom, T. Enevoldsen, H. F. P. Ettenhuber, B. Fernandez, L. Ferrighi, H. H. L. Frediani, K. Hald, A. Halkier, C. Hattig, E. H. T. Helgaker, A. C. Hennum, H. Hettema, H. J. A. J. S. Høst, I.-M. Høyvik, M. F. Iozzi, B. Jansik, S. K. D. Jonsson, P. Jørgensen, J. Kauczor, R. K. T. Kjærgaard, W. Klopper, S. Knecht, A. L. H. Koch, J. Kongsted, A. Krapp, K. Kristensen, R. H. M. O. B. Lutnæs, J. I. Melo, K. V. Mikkelsen, J. M. H. O. C. Neiss, C. B. Nielsen, P. Norman, J. Olsen, T. B. P. A. Osted, M. J. Packer, F. Pawlowski, T. A. R. P. F. Provasi, S. Reine, Z. Rinkevicius, C. C. M. S. K. Ruud, V. Rybkin, P. Salek, B. S. A. S. d. Meras, T. Saue, S. P. A. Sauer, P. R. T. K. Sneskov, A. H. Steindal, K. O. Sylvester-Hvid, A. J. T. A. M. Teale, E. I. Tellgren, D. P. Tew, D. J. D. W. L. Thøgersen, O. Vahtras, M. A. Watson, M. Z. Ågren, and H., Dalton, *Wiley Interdiscip. Rev. Comput. Mol. Sci.*, 2014, (4), 269.

[170] Http://daltonprogram.org, Dalton, a molecular electronic structure program, release Dalton2015.0, 2015.

[171] J. N. Bull, P. W. Harland, and C. Vallance, Absolute total electron impact ionization cross-sections for many-atom organic and halocarbon species, *J. Phys. Chem. A*, 2012, **226**(1), 767.

[172] J. N. Bull, J. W. L. Lee, and C. Vallance, Absolute electron total ionization cross-sections: molecular analogues of DNA and RNA nucleobase and sugar constituents, *Phys. Chem. Chem. Phys.*, 2014, **16**, 10743 – 10752.

[173] M. R. Eftink, L. A. Selvidge, P. R. Callis, and A. A. Rehms, Photophysics of Indole Derivatives: Experimental Resolution of La and Lb Transitions and Comparison with Theory, 1990, **94**, 3469–3479.

[174] J. O. F. Thompson, L. Saalbach, S. W. Crane, M. J. Paterson, and D. Townsend, Ultraviolet relaxation dynamics of aniline, N, N -dimethylaniline and 3,5-dimethylaniline at 250 nm, *J. Chem. Phys.*, 2015, **142**(11).

[175] R. Montero, Á. P. Conde, V. Ovejas, F. Castaño, and A. Longarte, Ultrafast photophysics of the isolated indole molecule., *J. Phys. Chem. A*, 2012, **116**(11), 2698–703.

[176] T. J. Godfrey, H. Yu, M. S. Biddle, and S. Ullrich, A wavelength dependent investigation of the indole photophysics via ionization and fragmentation pump-probe spectroscopies., *Phys. Chem. Chem. Phys.*, 2015, **17**(38), 25197–209.

[177] G. Berden and W. L. M. E. Jalviste, Rotationally resolved ultraviolet spectroscopy of indole, indazole, and benzimidazole: Inertial axis reorientation in the S1(1Lb)S0 transitions, *J. Chem. Phys.*, 1995, **103**(22), 9596.

[178] R. Matsumoto, K. Sakeda, Y. Matsushita, T. Suzuki, and T. Ichimura, Spectroscopy and relaxation dynamics of photoexcited anisole and anisole-d3 molecules in a supersonic jet, *J. Mol. Struct. TheoChem*, 2005, **735**, 153–167.

[179] S. E. Greenough, M. D. Horbury, J. O. F. Thompson, G. M. Roberts, T. N. V. Karsili, B. Marchetti, D. Townsend, and V. G. Stavros, Solvent induced conformer specific photochemistry of guaiacol, *Phys. Chem. Chem. Phys.*, 2014, **16**(30), 16187–16195.

[180] J. Biesner, L. Schnieder, G. Ahlers, X. Xie, K. H. Welge, M. N. R. Ashfold, and R. N. Dixon, State selective photodissociation dynamics of A state ammonia. II, *J. Chem. Phys.*, 1989, **91**(5), 2901.

[181] A. S. Chatterley, G. M. Roberts, and V. G. Stavros, Timescales for adiabatic photodissociation dynamics from the A state of ammonia., *J. Chem. Phys.*, 2013, **139**(3), 034318.

[182] D. Townsend, S. Kyoung Lee, and A. G. Suits, Orbital polarization from DC slice imaging: S(1D2) alignment in the photodissociation of ethylene sulfide, *Chem. Phys.*, 2004, **301**(2-3), 197–208.

[183] A. G. Suits, Roaming Atoms and Radicals: A New Mechanism in Molecular Dissociation, *Acc. Chem. Res.*, 2008, **41**(7), 873 – 881.

[184] E. U. Condon, Nuclear Motions Associated with Electron Transitions in Diatomic Molecules, *Phys. Rev.*, 1928, **32**(6), 858—-872.

[185] J. F. Reintjes, *Nonlinear Optical Parametric Processes in Liquids and Gases*, Academic Press Inc., New York, 1984.

[186] G. Bjorklund, Effects of focusing on third-order nonlinear processes in isotropic media, *Quantum Electron. IEEE J.*, 1975, **QE-11**(6).

[187] A. Rubinowicz, On the Anomalous Propagation of Phase in the Focus, *Phys. Rev.*, 1938, **54**(11), 931–936.

[188] R. W. Boyd, Intuitive explanation of the phase anomaly of focused light beams, *J. Opt. Soc. Am.*, 1980, **70**(7), 877–880.

[189] R. Paschotta, Rayleigh Length https://www.rp-photonics.com/rayleigh_length.html, 2017.

[190] J. Ringling, O. Kittelmann, F. Noack, G. Korn, and J. a. Squier, Tunable femtosecond pulses in the near vacuum ultraviolet generated by frequency conversion of amplified Ti:sapphire laser pulses., *Opt. Lett.*, 1993, **18**(23), 2035.

[191] V. Petrov, F. Rotermund, F. Noack, J. Ringling, O. Kittelmann, and R. Komatsu, Frequency conversion of Ti:sapphire-based femtosecond laser systems to the 200-nm spectral region using nonlinear optical crystals, *IEEE J. Sel. Top. Quantum Electron.*, 1999, **5**(6), 1532–1542.

[192] K. Kosma, S. a. Trushin, W. E. Schmid, and W. Fuss, Vacuum ultraviolet pulses of 11 fs from fifth-harmonic generation of a Ti:sapphire laser., *Opt. Lett.*, 2008, **33**(7), 723–5.

[193] M. Beutler, M. Ghotbi, F. Noack, and I. Hertel, Generation of sub-50-fs vacuum ultraviolet pulses by four-wave mixing in argon, *Opt. Lett.*, 2010, **35**(9), 1491 – 1493.

[194] M. Ghotbi, M. Beutler, and F. Noack, Generation of 2.5 μJ vacuum ultraviolet pulses with sub-50 fs duration by noncollinear four-wave mixing in argon., *Opt. Lett.*, 2010, **35**(20), 3492–4.

[195] M. Beutler, M. Ghotbi, and F. Noack, Generation of intense sub-20-fs vacuum ultraviolet pulses compressed by material dispersion, *Opt. Lett.*, 2011, **36**(19), 3726–3728.

[196] M. Ghotbi, P. Trabs, M. Beutler, and F. Noack, Generation of tunable sub-45 femtosecond pulses by noncollinear four-wave mixing, *Opt. Lett.*, 2013, **38**(4), 486–8.

[197] Calcite Crystals http://www.newlightphotonics.com/Birefringent-Crystals/Calcite-Crystals, 2017.

[198] Á. Börzsönyi, Z. Heiner, A. P. Kovács, M. P. Kalashnikov, and K. Osvay, Measurement of pressure dependent nonlinear refractive index of inert gases, *Opt. Express*, 2010, **18**(25), 25847–25854.

[199] A. Börzsönyi, Z. Heiner, M. P. Kalashnikov, A. P. Kovacs, and K. Osvay, Dispersion measurement of inert gases and gas mixtures at 800 nm, *Appl. Opt.*, 2008, **47**(27), 4856–4863.

[200] M. Mlejnek, E. Wright, and J. Moloney, Femtosecond pulse propagation in argon: A pressure dependence study, *Phys. Rev. E*, 1998, **58**(4), 4903–4910.

[201] N. Akozbek, C. Bowden, A. Talebpour, and S. Chin, Femtosecond pulse propagation in air: variational analysis, *Phys. Rev. E. Stat. Phys. Plasmas. Fluids. Relat. Interdiscip. Topics*, 2000, **61**(4), 4540–9.

[202] F. Théberge, N. Aközbek, W. Liu, A. Becker, and S. L. Chin, Tunable Ultrashort Laser Pulses Generated through Filamentation in Gases, *Phys. Rev. Lett.*, 2006, **97**(2), 1–4.

[203] A. Brodeur, C. Chien, F. Ilkov, S. Chin, O. Kosareva, and V. Kandidov, Moving focus in the propagation of ultrashort laser pulses in air, *Opt. Lett.*, 1997, **22**(5), 304–306.

[204] N. Aközbek, A. Iwasaki, A. Becker, M. Scalora, S. L. Chin, and C. M. Bowden, Third-Harmonic Generation and Self-Channeling in Air Using High-Power Femtosecond Laser Pulses, *Phys. Rev. Lett.*, 2002, **89**(14), 143901.

[205] S. C. Rae, Ionization-induced defocusing of intense laser pulses in high-pressure gases, *Opt. Commun.*, 1993, **97**(1), 25–28.

[206] C. Brée, A. Demircan, and G. Steinmeyer, Saturation of the All-Optical Kerr Effect, *Phys. Rev. Lett.*, 2011, **106**(18), 183902.

[207] M. Ghotbi, M. Beutler, and F. Noack, Generation of 2.5 μJ vacuum ultraviolet pulses with sub-50 fs duration by noncollinear four-wave mixing in argon., *Opt. Lett.*, 2010, **35**(20), 3492–4.

[208] D. R. Lide, *Ionization potentials of atoms and atomic ions - Handbook of Chem. and Phys.*, 1992.

[209] R. McDiarmid, On the ultraviolet spectrum of trans-1,3-butadiene, *J. Chem. Phys.*, 1976, **64**(2), 514.

[210] L. Serrano-Andres, M. Merchan, I. Nebot-Gil, R. Lindh, and B. O. Roos, Towards an accurate molecular orbital theory for excited states: Ethene, butadiene, and hexatriene, *J. Chem. Phys.*, 1993, **98**(4), 3151.

[211] D. M. P. Holland, M. A. MacDonald, M. A. Hayes, P. Baltzer, B. Wannberg, M. Lundqvist, L. Karlsson, and W. von Niessen, An experimental and theoretical study of the valence shell photoelectron spectrum of butadiene, *J. Phys. B At. Mol. Opt. Phys.*, 1996, **29**(14), 3091.

[212] W. Mallard, J. Miller, and K. Smyth, The ns Rydberg series of 1,3-trans-butadiene observed using multiphoton ionization, *J. Chem. Phys.*, 1983, **79**, 5900.

[213] S.-H. Lee, K.-C. Tang, I.-C. Chen, M. Schmitt, J. P. Shaffer, T. Schultz, J. G. Underwood, M. Z. Zgierski, and A. Stolow, Substituent Effects in Molecular Electronic Relaxation Dynamics via Time-Resolved Photoelectron Spectroscopy: $\pi\pi^*$ States in Benzenes, *J. Phys. Chem. A*, 2002, **106**(39), 8979–8991.

[214] S.-H. Lee, Dynamics of multi-channel dissociation of tetrahydrofuran photoexcited at 193 nm: distributions of kinetic energy, angular anisotropies and branching ratios, *Phys. Chem. Chem. Phys.*, 2010, **12**(11), 2655–63.

[215] L. Poisson, P. Roubin, S. Coussan, B. Soep, and J. M. Mestdagh, Ultrafast dynamics of acetylacetone (2,4-pentanedione) in the S2 state, *J. Am. Chem. Soc.*, 2008, **130**(10), 2974–2983.

[216] P. S. J. Russell, P. Holzer, W. Chang, A. Abdolvand, and J. C. Travers, Hollow-core photonic crystal fibres for gas-based nonlinear optics, *Nat. Photonics*, 2014, **8**(4), 278–286.

[217] C. R. Calvert, L. Belshaw, M. J. Duffy, O. Kelly, R. B. King, a. G. Smyth, T. J. Kelly, J. T. Costello, D. J. Timson, W. a. Bryan, T. Kierspel, P. Rice, I. C. E. Turcu, C. M. Cacho, E. Springate, I. D. Williams, and J. B. Greenwood, LIAD-fs scheme for studies of ultrafast laser interactions with gas phase biomolecules, *Phys. Chem. Chem. Phys.*, 2012, **14**(18), 6289.

[218] V. V. Golovlev, S. L. Allman, W. R. Garrett, N. I. Taranenko, and C. H. Chen, Laser-induced acoustic desorption, *Int. J. Mass Spectrom. Ion Process.*, 1997, **169**, 69–78.

[219] S. Lochbrunner, J. J. Larsen, J. P. Shaffer, M. Schmitt, T. Schultz, J. G. Underwood, and A. Stolow, Methods and applications of femtosecond time-resolved photoelectron spectroscopy, *J. Electron Spectros. Relat. Phenomena*, 2000, **112**, 183–198.

[220] A. Bodi, M. Johnson, T. Gerber, Z. Gengeliczki, B. Sztáray, and T. Baer, Imaging photoelectron photoion coincidence spectroscopy with velocity focusing electron optics, *Rev. Sci. Instrum.*, 2009, **80**(3).